

Technische Universität München

Fakultät für Chemie

Festkörper-NMR-Spektroskopie

Structural Characterization of Interactions between the Alzheimer's Disease Amyloid- β Peptide and Small Molecules and Peptide Inhibitors

Elke Martha Prade

Vollständiger Abdruck der von der Fakultät für Chemie der Technischen
Universität München zur Erlangung des akademischen Grades eines

Doktors der Naturwissenschaften (Dr. rer. nat.)

genehmigten Dissertation.

Vorsitzender: Univ.-Prof. Dr. Michael Sattler

Prüfer der Dissertation:

1. Univ.-Prof. Dr. Bernd Reif
2. Univ.-Prof. Dr. Aphrodite Kapurniotu

Die Dissertation wurde am 27.10.2015 bei der Technischen Universität
München eingereicht und durch die Fakultät für Chemie am 07.12.2015
angenommen.

Summary

Despite extensive research and numerous therapeutic approaches, Alzheimer's disease remains an untreatable disorder with increasing prevalence. The peptide amyloid- β ($A\beta$) is the main culprit responsible for plaque formation, a pathological hallmark of Alzheimer's disease, and its exerted toxicity contributes significantly to neurodegeneration. Like all amyloidogenic proteins, $A\beta$ exists in various aggregations states including monomers, oligomers and fibrils, making it difficult to characterize. Magic angle spinning solid-state NMR spectroscopy is the unique tool available to capture molecular details of amyloids in their aggregated fibrillar states. Various potential drug candidates have been described in the literature, which are targeted to interfere with aggregation properties of $A\beta$. However, the molecular mechanisms of such interactions are not understood. The aim of this study is to elucidate structural details of $A\beta$ in complex with inhibitory molecules by using a combination of solution-state and solid-state NMR spectroscopy. The molecules investigated include the nonsteroidal anti-inflammatory drug sulindac sulfide and peptide inhibitors mimicking the cross-amyloid surface. It was found that sulindac sulfide is able to interact with $A\beta$ in two mechanisms. Firstly, promiscuous binding of sulindac sulfide as colloids interferes with $A\beta$ solubility and redirects $A\beta$ into off-pathway oligomers with reduced neurotoxicity. Secondly, individual sulindac sulfide molecules intercalate between β -strands formed in fibrillar $A\beta$. By this specific binding mechanism, sulindac sulfide may prevent oxidation of $A\beta$ M35, and can thereby serve as a protective factor against reactive oxygen species in the brain. In both binding scenarios, sulindac sulfide does not interfere with the formation of characteristic structural elements of $A\beta$, such as the salt bridge connecting D23 and K28, or the typical β -strand motif. The peptide inhibitors investigated induce $A\beta$ aggregation and form insoluble structurally homogeneous complexes with the amyloid. It was determined that the peptide inhibitors adopt a loop structure in solution, which may facilitate its interaction with $A\beta$. This study contributes to unraveling the mechanism of action in which small molecules interact with amyloid proteins structurally, and the resulting biochemical consequences. It is crucial to

II | SUMMARY

understand such mechanisms on a molecular level, as they will facilitate structure based drug design in the fight against Alzheimer's disease and other amyloidogenic disorders.

Zusammenfassung

Bis zum heutigen Zeitpunkt ist Morbus Alzheimer trotz umfangreicher Forschung und Entwicklung zahlreicher therapeutischer Ansätze eine unheilbare Erkrankung mit steigender Prävalenzrate, dessen pathologisches Merkmal unter anderem die Ablagerung des β -Amyloid Peptides ($A\beta$) in Form von senilen Plaques ist. Die durch $A\beta$ bewirkte Toxizität trägt signifikant zu einem progressiven Krankheitsverlauf und zur Neurodegeneration bei Alzheimer-Patienten bei. Wie alle Amyloid-Proteine kann $A\beta$ in unterschiedlichen Aggregationszuständen vorliegen, beispielsweise als lösliches Monomer, Dimer oder als unlösliche Fibrillen, wodurch eine strukturelle Charakterisierung dieser Zustände eine Herausforderung darstellt. Mithilfe der Festkörper-Kernspinresonanz (NMR)-Spektroskopie können Amyloidproteine in ihrem unlöslichen Zustand molekular aufgelöst werden. Zahlreiche, in der Literatur beschriebene, Wirkstoffe verändern die Aggregationseigenschaften von $A\beta$. Die molekularen Details solcher Wechselwirkungen sind jedoch nicht bekannt. In der vorliegenden Arbeit werden durch den Einsatz von Lösungs- und Festkörper-NMR-Spektroskopie die Interaktionen von $A\beta$ mit verschiedenen Inhibitoren, welche als potentielle Wirkstoffe gelten, untersucht. Der Fokus liegt hierbei auf dem nichtsteroidalen Antirheumatikum Sulindac Sulfid, sowie einiger Peptidinhibitoren. Es konnte gezeigt werden, dass Sulindac Sulfid durch zwei unterschiedliche Mechanismen mit $A\beta$ interagieren kann. Zum einen kann Sulindac Sulfid als unspezifische kolloidale Strukturen die Löslichkeit von $A\beta$ herabsetzen, wodurch $A\beta$ Moleküle in Aggregate überführt werden, welche keine Fibrillenstruktur mehr ausbilden können und zudem eine verringerte Neurotoxizität zeigen. Des Weiteren kann Sulindac Sulfid zwischen den zwei charakteristischen β -Strängen vorgeformter $A\beta$ Fibrillen eingelagert werden. Durch diesen spezifischen Bindungsmechanismus verringert Sulindac Sulfid die M35 Oxidation von $A\beta$, und schützt somit das Gehirn vor reaktiven Sauerstoffspezien. In beiden Modellen bleiben trotz der Bindung von Sulindac Sulfid die charakteristischen Strukturmerkmale von $A\beta$ erhalten. Diese beinhalten die Ausbildung der Salzbrücke zwischen D23 und K28, sowie das typische β -Faltblatt. Die untersuchten Peptidinhibitoren fördern $A\beta$ Aggregation und verbinden sich mit $A\beta$ zu unlöslichen, jedoch strukturell homogenen, Komplexen. Es

IV | ZUSAMMENFASSUNG

konnte gezeigt werden, dass sich die inhibitorischen Peptide in Lösung zu einer Schleife falten. Es wird vermutet, dass die Ausbildung dieses Strukturelementes erst die Wechselwirkung mit A β ermöglicht. Die vorliegende Arbeit gibt Einblicke in die molekularen Mechanismen der Interaktion von A β mit inhibitorisch wirkenden Molekülen und zeigt die hierbei entstehenden biochemischen Auswirkungen. Eine Aufklärung dieser molekularen Abläufe ist ausschlaggebend für ein strukturbasiertes Wirkstoffdesign für die Entwicklung von Medikamenten gegen Morbus Alzheimer und weiterer amyloido gener Erkrankungen.

Table of Contents

Summary	I
Zusammenfassung	III
List of Figures	VIII
List of Tables	X
1. Introduction	1
1.1 NMR spectroscopy	1
1.1.1 Basic concepts of NMR spectroscopy	1
1.1.1.1 The origin of the NMR signal	1
1.1.1.2 Relaxation.....	3
1.1.1.3 Multidimensional NMR and structure calculation.....	5
1.1.2 Solid-state NMR.....	7
1.1.2.1 Magic angle spinning (MAS).....	7
1.1.2.2 Dipolar recoupling.....	8
1.1.2.2.1 Cross Polarization (CP).....	8
1.1.2.2.2 Rotational echo double resonance (REDOR).....	9
1.1.2.3 Structure determination by solid-state NMR.....	10
1.1.3 Applications and advances of biomolecular NMR.....	11
1.2 Alzheimer’s Disease (AD)	13
1.2.1 Background of AD	13
1.2.2 Genetics of AD	14
1.2.3 Treatment of AD.....	15
1.2.4 Inflammation in AD	15
1.3 The AD peptide Amyloid-β (Aβ)	16
1.3.1 Generation of the A β peptide	16
1.3.2 Oxidation of the A β peptide	18
1.4 Amyloidogenesis	18
1.4.1 Amyloid self-assembly	18
1.4.2 The amyloid hypothesis	19
1.4.3 Self-propagation and cross-seeding.....	20
1.5 NMR studies of Aβ	21
1.5.1 Solution-state NMR characterization of A β monomers and intermediates.....	21
1.5.2 Solid-state NMR characterization of A β fibrils	22
1.5.3 Solution-state NMR studies of A β interactions with inhibitory molecules.....	26
1.5.4 Solid-state NMR studies of A β interactions with inhibitory molecules.....	27
1.6 Aβ inhibitors investigated in this study	27
1.6.1 The γ -secretase modulator sulindac sulfide.....	27
1.6.1.1 γ -secretase modulators	27
1.6.1.2 Sulindac sulfide interactions with A β	28
1.6.1.3 Colloid formation of sulindac sulfide.....	29
1.6.2 Peptide inhibitors.....	30
1.6.2.1 Diabetes mellitus.....	30
1.6.2.2 Islet amyloid polypeptide (IAPP)	31
1.6.2.3 The link between Type 2 Diabetes and Alzheimer’s disease	31
1.6.2.4 Design of IAPP based inhibitors.....	31
1.7 Scope of this study	33
2. Materials and Methods	34
2.1 Materials	34

2.1.1 Chemicals.....	34
2.1.2 Equipment and software.....	34
2.1.3 Bacterial strains and plasmids	34
2.1.4 Bacterial growth media	35
2.2 Methods.....	35
2.2.1 Molecular biology.....	35
2.2.1.1 Plasmid purification.....	35
2.2.1.2 Heat shock transformation	36
2.2.1.3 Glycerol stocks.....	36
2.2.2 Recombinant expression and purification of A β ₁₋₄₀	36
2.2.2.1 Expression of recombinant A β ₁₋₄₀	36
2.2.2.1.1 Test expression.....	37
2.2.2.1.2 Main expression	37
2.2.2.1.3 Cell harvesting	37
2.2.2.2 Purification of recombinant A β ₁₋₄₀	37
2.2.3 Protein analytical methods	39
2.2.3.1 Tricine sodium dodecyl sulfate polyacrylamide gel electrophoresis (SDS-PAGE).....	39
2.2.3.2 Mass spectrometry	40
2.2.3.3 Transmission electron microscopy (TEM).....	40
2.2.3.4 Dynamic light scattering (DLS)	40
2.2.4 Sample preparation	40
2.2.4.1 NSAID stocks	40
2.2.4.2 Dissolving monomeric A β ₁₋₄₀	41
2.2.4.3 Probing equilibrium of aggregated A β ₁₋₄₀	41
2.2.4.4 Oxidation assays of A β ₁₋₄₀ and NSAIDs	41
2.2.4.5 Preparation of A β ₁₋₄₀ fibrils	42
2.2.4.6 Preparation of ISMs in combination with A β ₁₋₄₀	42
2.2.4.7 Preparation of the ISM R3-GI.....	42
2.2.5 NMR spectroscopy	43
2.2.5.1 Data analysis.....	43
2.2.5.1.1 Plotting and resonance assignment of NMR data.....	43
2.2.5.1.2 Peak integration	43
2.2.5.1.3 Prediction of secondary structures.....	43
2.2.5.1.4 Chemical shift perturbations (CSPs)	44
2.2.5.2 Solution-state NMR sample preparations	44
2.2.5.3 Solution-state NMR measurements.....	44
2.2.5.4 Solid-state NMR sample preparations	45
2.2.5.4.1 Packing of rotors.....	45
2.2.5.4.2 Sulindac sulfide incubated A β ₁₋₄₀ fibrils	46
2.2.5.4.3 Sulindac sulfide induced A β ₁₋₄₀ aggregates	46
2.2.5.4.4 K3L3K3-GI induced A β ₁₋₄₀ aggregates.....	46
2.2.5.5 MAS Solid-state NMR measurements.....	46
2.2.5.5.1 Conventional 2D and 3D assignment spectra.....	47
2.2.5.5.2 Detecting the A β salt bridge.....	48
2.2.5.5.3 Detecting ¹³ C- ¹⁹ F dipolar couplings in A β aggregated by sulindac sulfide	48
2.2.5.5.4 Detecting ¹³ C- ¹⁹ F dipolar couplings in A β fibrils.....	48
2.2.6 Structure calculation.....	49
3. Results	50
3.1 Expression, purification and characterization of monomeric A β ₁₋₄₀	50
3.2 The effect of sulindac sulfide on aggregation and biochemical properties of monomeric A β ₁₋₄₀	54
3.3 Solid-state NMR investigations of A β ₁₋₄₀ aggregates induced by sulindac sulfide.....	60
3.4 Interactions of sulindac sulfide with fibrillar A β ₁₋₄₀	67
3.5 Oxidation of A β ₁₋₄₀	78
3.6 Interaction of ISMs with A β ₁₋₄₀	87

3.7 Solution-state NMR structure of R3-GI.....	94
4. Discussion.....	108
4.1 A β interactions with sulindac sulfide.....	108
4.2 Interactions of A β with ISMs.....	117
4.3 Conclusions	120
5. Appendix.....	XI
5.1. Biophysical and biochemical properties of peptides.....	XI
5.1.1 A β_{1-40} peptide:.....	XI
5.1.2 Cross-Amyloid Interaction Surface Mimics (ISMs) ^[378]	XII
5.2 Chemical shifts	XIII
5.2.1 Chemical shifts of monomeric A β_{1-40} in solution	XIII
5.2.2 Chemical shifts of sulindac sulfide induced A β_{1-40} aggregates	XV
5.2.3 Chemical shifts of sulindac sulfide incubated and reference A β_{1-40} fibrils.....	XVI
5.2.4 Chemical shift assignment of R3-GI.....	XVII
5.3 Pulse sequences.....	XVIII
5.4 Comparison of A β_{1-40} chemical shifts to sulindac sulfide incubated and reference A β_{1-40} fibrils	XIX
6. Abbreviations.....	XXIII
References	XXV
Curriculum Vitae	XLIII
List of Publications.....	XLIV
Acknowledgements.....	XLV

List of Figures

Figure 1.1 Basic concepts of NMR.....	3
Figure 1.2: NMR relaxation properties.....	5
Figure 1.3: Schematic illustration of magic angle spinning.....	7
Figure 1.4: CP pulse scheme.....	9
Figure 1.5: REDOR pulse scheme.....	10
Figure 1.6.: Hallmarks of AD pathology.....	14
Figure 1.7: Processing of the amyloid precursor protein (APP) and generation of A β ₁₋₄₀ and A β ₁₋₄₂	17
Figure 1.8: Kinetics and intermediates of amyloidogenesis.....	19
Figure 1.9: Details of A β fibril structures.....	23
Figure 1.10: Chemical structures of the NSAIDs sulindac, sulindac sulfide and sulindac sulfone.....	28
Figure 1.11: Electron microscopy images of colloidal aggregates.....	30
Figure 1.12: Design of IAPP-based amyloid inhibitors.....	33
Figure 2.1: MAS rotor filling tool for ultracentrifuges.....	45
Figure 3.1: Expression and purification of A β ₁₋₄₀	50
Figure 3.2: Solution-state NMR analysis of monomeric A β ₁₋₄₀	52
Figure 3.3: Solution-state NMR ¹ H- ¹³ C HSQC of monomeric A β ₁₋₄₀	53
Figure 3.4: The effect of NSAIDs on monomeric A β by solution-state NMR.....	55
Figure 3.5: Properties of monomeric A β in the presence of sulindac sulfide and DMSO-d ₆	56
Figure 3.6: Solubility of NSAIDs analyzed by solution-state NMR.....	58
Figure 3.7: The effect of sulindac sulfide on morphological and neurotoxic properties of A β	59
Figure 3.8: MAS solid-state NMR spectra of sulindac sulfide induced A β aggregates.....	60
Figure 3.9: Overlay of 2D ¹³ C- ¹³ C PDS correlation spectra of sulindac sulfide induced A β aggregates.....	61
Figure 3.10: Structural elements of A β aggregated by 10-X sulindac sulfide determined by solid-state NMR.....	63
Figure 3.11: ¹³ C- ¹⁹ F TEDOR spectra of A β aggregated by 10-X sulindac sulfide.....	64
Figure 3.12: A β ¹³ C atoms interacting with sulindac sulfide.....	66
Figure 3.13: MAS solid-state NMR spectra of sulindac sulfide incubated A β fibrils.....	67
Figure 3.14: Overlay of 2D ¹³ C- ¹³ C PDS correlation spectra of sulindac sulfide incubated A β fibrils.....	68
Figure 3.15: Strip plot of sulindac sulfide incubated A β fibrils.....	69
Figure 3.16: Structural details of sulindac sulfide incubated A β fibrils.....	70
Figure 3.17: The effect of sulindac sulfide on the salt bridge in A β fibrils.....	71
Figure 3.18: Solid-state NMR restraints collected for sulindac sulfide incubated A β fibrils.....	72
Figure 3.19: Dipolar coupling based ¹⁹ F- ¹³ C spectra of different A β samples.....	74
Figure 3.20: Docking of sulindac sulfide to A β fibrils.....	77
Figure 3.21: Oxidation of monomeric A β	78
Figure 3.22: Comparison of oxidized monomeric and fibrillar A β	80
Figure 3.23: Oxidation of fibrillar A β by a variety of oxidizing agents.....	81
Figure 3.24: Oxidation of fibrillar A β in the presence of sulindac sulfide.....	83
Figure 3.25: Oxidation of NSAIDs.....	85
Figure 3.26: The oxidized state of fibril bound NSAIDs.....	86
Figure 3.27: Interactions of L3-GI with A β	87
Figure 3.28: Interactions of K3L3K3-GI with A β in an HFIP film.....	88
Figure 3.29: Interactions of K3L3K3-GI with A β in the absence of HFIP.....	89
Figure 3.30: Interactions of K3L3K3-GI with A β in the presence of HFIP.....	91
Figure 3.31: MAS solid-state NMR spectra of K3L3K3-GI induced A β aggregates.....	92
Figure 3.32: A β incubated with K3L3K3-GI.....	93
Figure 3.33: 2D ¹ H- ¹ H NOESY of R3-GI including assignments.....	95

<i>Figure 3.34: Long range NOEs observed for R3-GI.....</i>	<i>96</i>
<i>Figure 3.35: Residue interaction map and secondary structure of R3-GI.....</i>	<i>97</i>
<i>Figure 3.36: DLS of 1mM R3-GI.....</i>	<i>98</i>
<i>Figure 3.37: Residue specific r.m.s.d. values for preliminary monomeric and dimer R3-GI structures.....</i>	<i>99</i>
<i>Figure 3.38: R3-GI confirmed long distance NOEs.....</i>	<i>102</i>
<i>Figure 3.39: Preliminary solution-state NMR structure of monomeric R3-GI conformer 1.....</i>	<i>103</i>
<i>Figure 3.40: Preliminary solution-state NMR structure of monomeric R3-GI conformer 2.....</i>	<i>104</i>
<i>Figure 3.41: Preliminary solution-state NMR structure of dimeric R3-GI conformer 1.....</i>	<i>105</i>
<i>Figure 3.42: Preliminary solution-state NMR structure of dimeric R3-GI conformer 2.....</i>	<i>106</i>
<i>Figure 4.1: Schematic representation of mechanism of interaction between sulindac sulfide and Aβ monomers and fibrils.....</i>	<i>116</i>
<i>Figure 5.1: Solid-state NMR pulse sequences.....</i>	<i>XVIII</i>
<i>Figure 5.2: Residue specific CS differences; structures.....</i>	<i>XIX</i>
<i>Figure 5.3: Residue specific CS differences; models.....</i>	<i>XX</i>
<i>Figure 5.4: CS correlations; structures.....</i>	<i>XXI</i>
<i>Figure 5.5: CS correlations; models.....</i>	<i>XXII</i>

List of Tables

<i>Table 1.1: NMR relevant properties of selected nuclei.....</i>	<i>2</i>
<i>Table 1.2: Anisotropic interactions found in proteins.....</i>	<i>8</i>
<i>Table 1.3: Structural details of wild type and mutant Aβ₁₋₄₀ and Aβ₁₋₄₂ structures and wild type Aβ₁₋₄₀ models and CS.</i>	<i>25</i>
<i>Table 2.1: Recipes for bacterial growth media and their components.....</i>	<i>35</i>
<i>Table 2.2: Recipes for tricine SDS-PAGE buffers and gels.....</i>	<i>39</i>
<i>Table 3.1: ¹³C-¹⁹F REDOR restraints of fibrillar Aβ.....</i>	<i>73</i>
<i>Table 3.2: Comparison of sulindac sulfide incubated Aβ fibrils to literature.</i>	<i>75</i>
<i>Table 3.3 DLS of 1 mM R3-GI.....</i>	<i>98</i>
<i>Table 3.4: r.m.s.d. values of preliminary monomeric and dimeric R3-GI structures</i>	<i>100</i>
<i>Table 3.5: R3-GI long range NOEs observed in 2D ¹H-¹H NOESY.....</i>	<i>101</i>
<i>Table 3.6: Hydrogen bonds in preliminary monomeric R3-GI structure of conformer 1.</i>	<i>103</i>
<i>Table 3.7: Hydrogen bonds in preliminary monomeric R3-GI structure of conformer 2.</i>	<i>104</i>
<i>Table 3.8: Intermolecular hydrogen bonds in preliminary dimeric R3-GI structure of conformer 1.....</i>	<i>105</i>
<i>Table 3.9: Intermolecular hydrogen bonds in preliminary dimeric R3-GI structure of conformer 2.</i>	<i>106</i>
<i>Table 3.10: NMR restraints and statistics of preliminary R3-GI structures calculated by ARIA.</i>	<i>107</i>
<i>Table 5.1: Solution-state NMR chemical shifts of monomeric Aβ₁₋₄₀ at 277 K.</i>	<i>XIV</i>
<i>Table 5.2: Solid-state NMR chemical shifts of Aβ₁₋₄₀ aggregates induced by a 10-X molar excess of sulindac sulfide.</i>	<i>XV</i>
<i>Table 5.3: Solid-state NMR chemical shifts of Aβ₁₋₄₀ fibrils incubated with a 5-X molar excess of sulindac sulfide.</i>	<i>XVI</i>
<i>Table 5.4: Solution-state NMR chemical shifts of R3-GI at 277 K.</i>	<i>XVII</i>

1. Introduction

1.1 NMR spectroscopy

1.1.1 Basic concepts of NMR spectroscopy

The theoretical concepts of Nuclear Magnetic resonance (NMR) spectroscopy are a huge topic on their own and a comprehensive introduction is beyond the scope of this thesis. A brief outline of the fundamental concepts of NMR spectroscopy will be presented here, which is only directly related to the understanding of the NMR experiments employed in this thesis. Excellent textbooks and reviews are available in the literature describing the principles of NMR spectroscopy in depth^[1-4].

1.1.1.1 The origin of the NMR signal

The basic principles of spectroscopy rely on the detection of transitions between energy levels of an atom or molecule. NMR spectroscopy exploits the energy of transitions experienced by the magnetic moment μ of nuclei with a nonzero nuclear spin angular momentum in a magnetic field. The NMR signal is proportional to magnetogyric ratio of the detected nucleus and its natural abundance, among other parameters (Table 1.1). Nuclei with spin $\frac{1}{2}$ include ^1H , ^{13}C , ^{15}N , ^{19}F and ^{31}P , which are among some of the most frequently occurring nuclei in biomolecules. Although natural abundances of ^{13}C and ^{15}N are relatively low, their abundance in biomolecules can be enhanced by isotopic labeling, for instance by supplementing growth media with the appropriate isotopes. NMR spectroscopy provides direct access to the structure and molecular dynamics of biomacromolecules with atomic resolution. This makes NMR spectroscopy one of the most powerful techniques to characterize the structure and dynamics of proteins or RNA^[5,6] in soluble and insoluble states.

Nucleus	Spin quantum number I	Magnetogyric ratio γ ($10^7 \text{ rad T}^{-1} \text{ s}^{-1}$)	Natural abundance (%)
^1H	$\frac{1}{2}$	26.7522	99.98
^2H	1	4.1066	0.0156
^{13}C	$\frac{1}{2}$	6.7283	1.108
^{14}N	1	1.9338	99.63
^{15}N	$\frac{1}{2}$	-2.7126	0.365
^{19}F	$\frac{1}{2}$	25.1815	100.0
^{31}P	$\frac{1}{2}$	10.8394	100.0

Table 1.1: NMR relevant properties of selected nuclei.

A spin $\frac{1}{2}$ nucleus possesses angular momentum P , which in combination with the magnetogyric ratio γ accounts for the magnetic moment, as described by the following equation:

$$\mu = \gamma P \quad (1)$$

When placed in a magnetic field B_0 , the magnetic moment of spin $\frac{1}{2}$ nuclei aligns to the field in two discrete orientations, which corresponds to the α and the β spin states (Zeeman splitting) (Figure 1.1a). A nucleus possessing spin quantum number I has $2I+1$ eigenstates, where the equilibrium populations among the eigenstates are established according to the Boltzmann distribution. The spins precess around the B_0 field direction with frequency ν_0 (Hz) or ω_0 (rad s^{-1}) (2), also known as the Larmor frequency of the nucleus. Signals in the resulting NMR spectrum originate from the difference in frequency between the two energy states for a spin $\frac{1}{2}$ nucleus.

$$\omega_0 = -\gamma B_0 \quad \nu_0 = \frac{-\gamma B_0}{2\pi} \quad (2)$$

Transition between different eigenstates can be driven by radiofrequency (RF) pulses generated by the transmitter coil of the spectrometer, whose frequency corresponds to the energy gap between the states, ω_0 . If the applied frequency corresponds to the Larmor frequency, the RF is considered on resonance for the respective spins. The RF pulse provides an oscillating B_1 field in the transverse plane, creating phase coherence of all spins and thus net magnetization in the x-y plane (Figure 1.1b). It is this transverse magnetization, which induces a current detectable by the coil and ultimately results in the signal observed in NMR experiments.

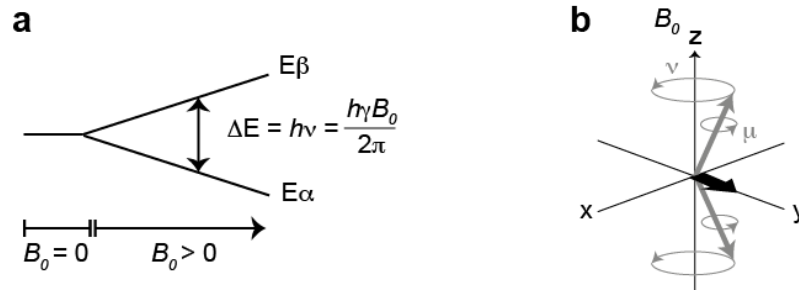


Figure 1.1 Basic concepts of NMR. (a) Nuclear spin states α and β adopted by nuclei with spin $\frac{1}{2}$ in a magnetic field B_0 . ΔE grows with increasing field strength of B_0 . Energy provided by the RF coil corresponding to the Larmor frequency fulfills the resonance condition of the respective spins. h = Planck's constant (b) Spins will align to the magnetic field and precess around B_0 direction according to their Larmor frequency ν_0 . Bold arrows represent net magnetization. If the α and β states are equally populated, no net magnetization is found along the z -axis (gray arrows). Following a $\pi/2$ RF pulse along x , spins are phase coherent causing transverse net magnetization (black arrow) aligned to the y -axis.

Individual nuclei in a system experience variations in their effective magnetic fields due to their chemical environment, causing them to precess at slightly different Larmor frequencies. More specifically, surrounding circulating electrons induce local magnetic fields, thereby shielding the nucleus from the external B_0 . This effect is known as chemical shift (CS, δ), and enables NMR spectroscopists to discriminate between nuclei in the system of interest and to study their chemical surroundings. As the chemical shift is small relative to the Larmor frequencies, it is expressed as parts per million (ppm).

1.1.1.2 Relaxation

RF pulses perturb the ground state by introducing spin coherence and deviations to net macroscopic magnetizations. The system returns to equilibrium by recovering magnetization along the direction of B_0 in time T_1 (longitudinal relaxation time constant), as well as by coherence loss in the x - y plane in time T_2 (transverse relaxation time constant). As magnetization is restored along the z -axis, energy is lost to the surrounding, thus the process is also termed spin-lattice relaxation. Transverse magnetization is lost due to spins precessing at different frequencies, thus due to their δ , thereby leading to a fanning out of the bulk magnetization. Energy is distributed among spins, coining the term spin-spin relaxation. The loss of phase coherence is measured as an oscillating, time-dependent free induction decay (FID), which is the direct observable in NMR experiments. The FID decays exponentially

4 | INTRODUCTION

with the effective transverse relaxation time T_2^* and can be described by the following relation:

$$\text{FID} \propto \exp\left(-\frac{t}{T_2^*}\right) \quad (3)$$

As the FID is measured as a function of time, Fourier transformation needs to be applied to the FID in order to yield the frequency domain components. Fourier transformation of an exponential decay results in Lorentzian line-shapes, whose linewidths are inversely proportional to T_2^* . Hence, a system relaxing slowly to the thermal equilibrium yields narrower NMR resonances than a rapidly relaxing system.

In general, a time-dependent fluctuating magnetic field at a spin's Larmor frequency is required for longitudinal relaxation to occur. Dipole-dipole interactions, chemical shift anisotropy (CSA), spin rotation and quadrupolar mechanisms induce local fields, and random motions of the molecule, such as tumbling, are responsible for their time dependence. The molecular motion is quantified by the rotational correlation time τ_c , the time it takes a molecule to rotate by one radian. The spectral density function $J(\omega)$ (Figure 1.2a) describes the frequency distribution of molecular motion, which can be expressed as:

$$J(\omega) = \frac{\tau_c}{1 + \omega^2 \tau_c^2} \quad (4)$$

For globular proteins, τ_c is approximated by Stoke's law. This implies that the rate of tumbling increases as a function of solvent viscosity and the hydrodynamic radius, i.e. the size of the protein. As described above, the relaxation time constant T_1 is directly dependent on τ_c (Figure 1.2b). T_1 is most severely affected by intermediate motions, and insensitive to very slow or very fast motions, as described by the spectral density function. Transverse magnetization vanishes with the same rate (liquids) or a slower rate (solids) than longitudinal magnetization, therefore $T_2 \leq T_1$. Hence, T_2 is also limited by τ_c . However unlike T_1 , T_2 relaxation is enhanced by slow motions typical for molecules of large molecular weight, ultimately resulting in resonance broadening in the NMR spectrum.

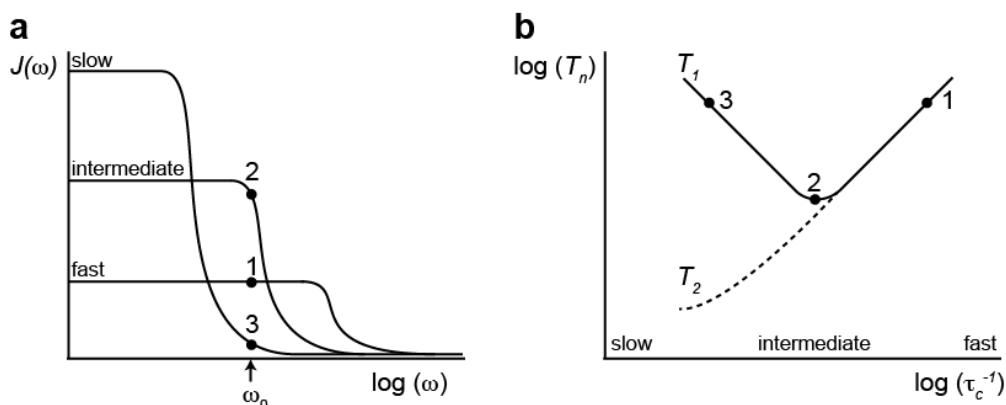


Figure 1.2: NMR relaxation properties. (a) Spectral density as a function of frequency. $J(\omega)$ is indicated for slow, intermediate and fast motions at the Larmor frequency ω_0 . (b) Dependence of T_1 and T_2 on the correlation time τ_c . T_1 values are shown for slow, intermediate and fast motions at ω_0 as indicated in (a).

All functional activities exerted by proteins, including enzymatic catalysis, protein folding, and binding to other proteins or ligands, rely on dynamic processes. Hereby, the protein exchanges between multiple conformational states on a μs - ms timescale. Such states, though biologically relevant, may not be accessible by conventional NMR techniques, as they may not resemble the lowest energy conformer^[7]. For soluble proteins, such dynamic exchange processes may be probed by Carr-Purcell-Meiboom-Gill (t) and $R_{1\rho}$ relaxation dispersion experiments, which allow the extraction of relaxation rates, and thermodynamic and kinetic parameters^[8-10]. Studies of internal dynamics in solids has been limited to the ps- μs range, due to their intrinsically rapid relaxation rates^[11], and mobile residues are typically unobservable by conventional experiments^[12]. Due to recent methodological advances, it is possible to quantitatively detect slower conformational exchange processes by solid-state NMR^[11,13-15]. As there is no overall tumbling in solids, relaxation is solely due to internal motions. This facilitates sensitive detection of local, site-specific relaxation-rates by solid-state NMR^[14,16,17]. Perdeuteration of the protein assists this process, as strong ^1H - ^1H dipolar interactions are suppressed^[18-21].

1.1.1.3 Multidimensional NMR and structure calculation

A number of parameters influence the signal to noise ratio (S/N) of NMR spectra. In general, S/N is given by the following relation:

$$\frac{S}{N} \propto n\gamma_e \sqrt{\gamma_d^3 B_0^3 t} \quad (5)$$

In order to improve S/N in NMR experiments, it is therefore crucial to consider the number of spins n , the magnetogyric ratios of the excited (γ_e) and the detected nuclei (γ_d), the magnetic field strength B_0 and the measurement time t , i.e. the number scans accumulated. Due to its high γ , ^1H is most frequently utilized as the nucleus for excitation and detection in solution-state NMR experiments. After initial excitation, magnetization is transferred from ^1H to spin-coupled nuclei, which are allowed to evolve under their chemical shifts, and subsequently magnetization is transferred back to ^1H for detection. These coherence transfers are commonly achieved through INEPT (Insensitive Nuclei Enhanced by Polarization Transfer) steps, which employs scalar (J) couplings mediated through chemical bonds. The resulting multi-dimensional heteronuclear correlations allow sequential resonance assignment to chemical shifts of directly bonded nuclei. The most prominent 2D spectrum is the ^1H - ^{15}N HSQC (heteronuclear single quantum coherence), which correlates ^1H to its directly bonded ^{15}N , and is considered the fingerprint spectrum of a protein.

The measurement of chemical shifts provide information about secondary structure^[22] and torsion angles, which can be predicted by TALOS+ (Torsion Angle Likelihood Obtained from Shift and Sequence Similarity)^[23,24]. Structural elucidation of proteins relies strongly on the nuclear Overhauser effect (NOE), which is based on through-space homonuclear magnetization transfers facilitated by dipolar couplings. The NOE originates from a redistribution of spin populations of coupled nuclei, as induced by dipole-dipole relaxation, and provides distance information.

NOE data is an essential contribution to solution-state NMR structures. As gathering NOE data can be tedious, Monte-Carlo algorithms like CS-Rosetta are being developed to predict protein structures solely from chemical shift data^[25]. Traditionally, solution-state NMR structures are calculated from restraints provided by CS, torsion angles, hydrogen bonds and NOEs. Additionally, restraints obtained from paramagnetic relaxation enhancement (PRE) and residual dipolar couplings (RDC) can contribute to structure determination. Upon insertion of a paramagnetic ligand, PREs are observable for nuclei within 30 Å^[26]. In order to detect RDCs, partial molecular alignment must be induced, as dipolar couplings are averaged out in isotropic solutions^[27]. RDCs provide information about the orientation of bonds relative to the external magnetic field.

1.1.2 Solid-state NMR

Due to the absence of tumbling in solids, there is no restriction imposed by molecular weight in solid-state NMR. The rigid orientation of atoms in solids is the origin for severe line broadening, and at the same time a source of valuable structural restraints. The following section introduces basic principles of approaches to overcome the anisotropy induced line broadenings, as well as to exploit the information contained in anisotropic interactions.

1.1.2.1 Magic angle spinning (MAS)

Nuclear spin interactions can be categorized into isotropic (orientation independent) and anisotropic (orientation dependent) interactions. The latter are typically negligible in solutions, as they are averaged to zero due to molecular mobility. However, in solids, nuclei have a rigid orientation with respect to B_0 as well as to the neighboring nuclei, which gives rise to large anisotropic interactions. Although anisotropic interactions contain information on the local geometry, they cause severe line broadening and loss of resolution in solid-state NMR. The sample is spun along the rotor axis, which makes an angle θ with respect to the external magnetic field B_0 (Figure 1.3). Sample spinning is routinely used to average out the anisotropic interactions in solid-state NMR. The spinning frequency ω_r should ideally be set to a few times larger than the size of the anisotropic interaction for complete averaging. The angle θ between the rotor axis and the main magnetic field is known as the magic angle and defined as $\text{Arctan}\sqrt{2} \approx 54.74^\circ$. Magic angle spinning (MAS) leads to significant line narrowing in solid-state NMR.

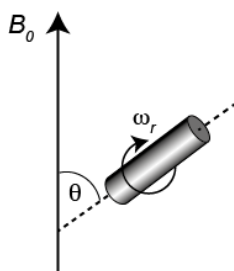


Figure 1.3: Schematic illustration of magic angle spinning. Spinning the rotor at frequency ω_r at angle $\theta = 54.74^\circ$ with respect to B_0 , leading to removal of dipolar interactions.

The Hamiltonian operator for a heteronuclear dipolar interaction between two spins I and S under secular approximation, is given by the following equation:

$$\hat{H}_{IS}^{DD} = b_{IS} \frac{3\cos^2\theta - 1}{2} 2I_z S_z, \quad \text{where } b_{IS} = -\mu_0 \frac{\gamma_I \gamma_S \hbar}{4\pi r_{IS}^3} \quad (6)$$

where r corresponds to the distance between the two spins, μ_0 is the magnetic constant, and $\hbar = h/2\pi$. When θ is set to the magic angle, the Hamiltonian operator equals zero. Modern NMR probes allow spinning of 3.2 mm rotors up to 24 kHz and 4.0 mm rotors up to 18 kHz. Some relevant anisotropic interactions frequently encountered in biological solid-state NMR are summarized in Table 1.2.

Spins	Type of interaction	b_{IS}
$^1\text{H}-^1\text{H}$	dipole-dipole	~ 60 kHz
$^1\text{H}-^{13}\text{C}$	dipole-dipole, direct bond	~ 23 kHz
$^1\text{H}-^{15}\text{N}$	dipole-dipole, direct bond	~ 11 kHz
^{13}C (aliphatic)	CSA @ 800 MHz	~ 6 kHz
^{15}N	CSA @ 800 MHz	~ 20 kHz

Table 1.2: Anisotropic interactions found in proteins. Values are taken from Barbet-Massin *et al*^[28].

The strongest dipolar couplings in biomolecules are among ^1H s. The $^1\text{H}-^1\text{H}$ dipolar coupling Hamiltonian is homogeneous in the sense of Maricq and Waugh^[29]. Therefore, it is impossible to demolish this interaction only by MAS. Hence, conventional solid-state NMR spectroscopy relies on the acquisition of ^{13}C nuclei, even after taking into account its lower γ . In addition, constant high power ^1H decoupling has to be applied throughout the pulse sequence to eliminate the strong heteronuclear dipolar couplings to ^1H nuclei.

1.1.2.2 Dipolar recoupling

As anisotropic interactions contain structurally relevant information, such as distance restraints, it is of interest to reintroduce such interactions during a solid-state NMR experiment^[30]. This method is termed as recoupling and provides the basis for experiments employing cross polarization (CP)^[31,32], rotational echo double resonance (REDOR)^[33], and various others^[34].

1.1.2.2.1 Cross Polarization (CP)

Signal enhancement in solid-state NMR can be obtained by employing the high γ of

spin I (typically ^1H) for initial excitation and subsequent polarization transfer to low- γ spins S (mostly ^{13}C and ^{15}N in biological systems), as similarly done in solution NMR. In the case of solid-state NMR, this magnetization transfer is achieved via heteronuclear dipolar interactions to neighboring spins through space by CP (Figure 1.4). CP steps reintroduce dipolar couplings, which are otherwise removed by MAS. A $\pi/2$ RF pulse creating transverse magnetization of I spins is followed by simultaneous, on-resonance RF irradiation on both spins (I and S).

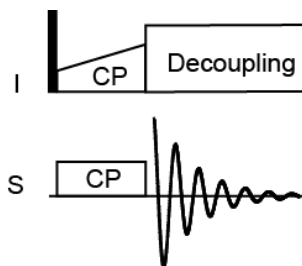


Figure 1.4: CP pulse scheme. The black rectangle represents a $\pi/2$ pulse.

For efficient magnetization transfer, the spin-locked frequencies of I and S ω_I and ω_S , respectively, must fulfill the Hartmann-Hahn-condition^[35]. Under magic angle spinning, with ω_r , the Hartmann-Hahn condition is satisfied when

$$\gamma_I B_{1I} = \gamma_S B_{1S} \pm n\omega_r \quad (7)$$

1.1.2.2.2 Rotational echo double resonance (REDOR)

REDOR building blocks in NMR pulse sequences consist of rotor-synchronized π -pulses on the S channel, reintroducing I-S dipolar couplings, inducing dephasing of the I spins (Figure 1.5). The dependence of this signal attenuation on I-S dipolar coupling facilitates measurement of heteronuclear distance restraints^[36].

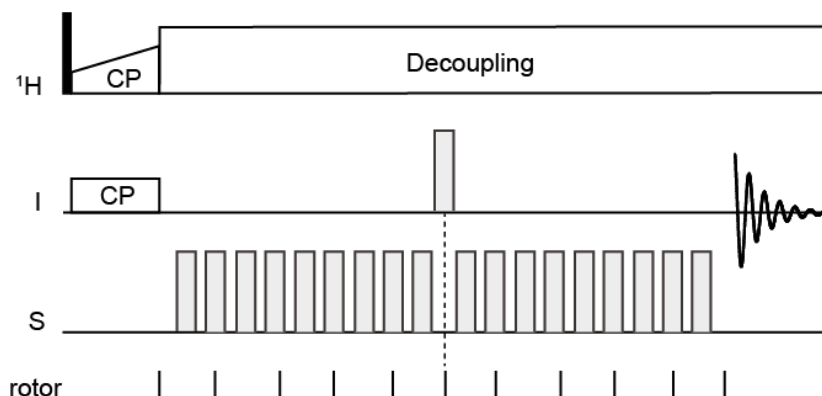


Figure 1.5: REDOR pulse scheme. The black rectangle represents a $\pi/2$ pulse. White rectangles represent π -pulses.

The closely related transferred echo double resonance (TEDOR)^[37,38] consists of two REDOR blocks. The initial REDOR block is followed by simultaneous $\pi/2$ pulses on both channels to transfer magnetization from I to S. Typically, CS is allowed to evolve on the S spin, before magnetization is transferred back to I by another pair of $\pi/2$ pulses and the second REDOR block. The magnitude of coherence transfer to the S spin is dependent on I-S dipolar interactions. Application of the TEDOR sequence demonstrated the ability to simultaneously measure multiple heteronuclear distances^[39].

1.1.2.3 Structure determination by solid-state NMR

CP and TEDOR constitute two powerful methods for heteronuclear coherence transfers via dipolar interactions. Most conventional solid-state NMR spectra rely on dipolar-based homonuclear mixing schemes. ^{13}C - ^{13}C recoupling sequences such as proton-driven spin diffusion (PDSD)^[40] or dipolar assisted rotational resonance (DARR)^[41] allow the identification and assignment of spin systems within a protein. Homonuclear long-range contacts may be measured by proton-assisted recoupling (PAR)^[42]. Mixing schemes applicable to fast MAS include the phase-alternated recoupling irradiation scheme (PARIS)^[43] and mixed rotational and rotary resonance recoupling (MIRROR)^[44]. In addition, proton assisted insensitive nuclei cross polarization (PAIN)^[45] is a heteronuclear recoupling schemes enabling the detection of long-range distance restraints.

Specific labeling patterns in proteins alleviate various challenges in resonance assignment and measurements of restraints and may be achieved by the use of selectively labeled precursors^[46-48]. MAS solid-state NMR spectroscopy has been successfully employed in the past to solve structures of large protein assemblies. Examples include micro-crystals of the α -spectrin Src-homology 3 domain (SH3)^[48], amyloids of the *Podospora anserina* HET-s prion^[49,50], oligomers of the small heat shock protein α B-crystallin^[51] and *Shigella* type III secretion needles^[52].

1.1.3 Applications and advances of biomolecular NMR

NMR spectroscopy and X-ray crystallography are the two most prominent techniques available for high-resolution structural characterization of biomolecules. It is often of great benefit to use combinatorial approaches of NMR, X-ray crystallography, cryo-EM or small angle scattering to address specific structural problems, as each technique provides unique information about different biological aspects. The main advantage of NMR over X-ray crystallography is that it represents the protein in a natural, soluble environment, and is able to capture its dynamic properties and kinetic details of ligand interactions. An increasing number of biological aspects become amenable to solution-state NMR characterization due to recent advances in the field. For instance, major progress has been made in the characterization of sparsely populated “NMR invisible” states, which are crucial in various biological processes^[53,54]. Methods capable of capturing such states include PRE, relaxation dispersion and dark state exchange saturation transfer (DEST)^[54,55]. Such methods allow the characterization of transient invisible “dark” states, which are based on a dynamic equilibrium with visible states^[56]. These states may occupy only 0.5-5% of the protein population and range from ns to ms lifetimes^[54]. For instance, PRE measurements have been successfully applied to follow conformational changes of the maltose binding protein^[57] and calmodulin^[58] upon ligand binding, as well as to describe transient binding of a transcription factor to its target DNA^[59]. Relaxation dispersion and DEST experiments probe dynamic exchange processes of amyloid monomers interacting with the GroEL chaperone^[60], and with other amyloid species^[61,62] (Section 1.5.1). Similarly, membrane proteins constitute a group of biomolecules elusive to various biophysical techniques due to their insolubility. The introduction of nanodisc technology facilitates analysis of membrane proteins by solution-state NMR^[63-65]. The target protein forms self-assemblies with phospholipids into discoidal bilayers termed nanodiscs, which keep the membrane soluble and available to NMR investigations. This method has been successfully applied to gain

insight to functional properties of various membrane proteins such as cytochrome P450^[66,67] and G-protein coupled receptors^[68]. In-cell NMR is another rapidly developing field, which enables *in situ* characterization of proteins in their natural environment^[69,70]. This method facilitates the observation of numerous cellular processes, such as posttranslational modifications^[71], metabolic processes^[72], as well as protein-protein^[73] and protein-ligand interactions^[74].

One of the major drawbacks of solution-state NMR spectroscopy is its dependence on molecular weight, restricting most applications to protein sizes below 50 kDa. Proteins beyond this weight generate spectral overlap and broadened NMR lines due to their high τ_c , making spectra inapplicable for further analysis. This limit was pushed to higher molecular weights by protein perdeuteration, as this procedure slows down transverse relaxation rates^[75]. The development of transverse relaxation-optimized spectroscopy (TROSY) allows the analysis of protein complexes up to 1 MDa^[76-78]. The TROSY technique exploits the differential cross-correlated relaxation processes between either dipole-dipole and CSA or two different dipole-dipole relaxation mechanisms of two *J*-coupled spins, which gives rise to four multiplet components as a result of constructive or destructive interference. TROSY experiments select one of the four multiplet components for observation, thereby attenuating T_2 relaxation effects. The method is particularly powerful when applied to methyl groups^[79-81], as these groups are typically dynamic and yield higher signals compared to backbone resonances due to the contribution of three protons. The availability of precursors^[82] in combination with specific labeling schemes^[83,84] facilitates selective labeling of methyl groups. Application of TROSY in the solid-state enables the detection of dynamic residues undergoing intermediate exchange, inaccessible to conventional solid-state NMR experiments^[85].

Solid-state NMR spectroscopy is applicable to biological systems, which are difficult to access by solution-state NMR. Large protein complexes and proteins of limited solubility like amyloids and membrane proteins are a few examples of such systems. A rapidly emerging field in solid-state NMR spectroscopy concerns ^1H detection for structural elucidations. Introducing deuterons chemically dilutes the strong ^1H - ^1H dipolar network, thereby reducing spectral overlap and narrowing linewidths^[86]. However, as these dipolar contacts yield structural restraints^[87], a compromise must be found to back-exchange protons without forfeiting resolution^[88,89]. An approach named reduced adjoining protonation (RAP) allows selectively reducing proton density in nonexchangeable proton sites, in particular aliphatic side chains^[90].

Additionally, high MAS and stronger B_0 fields can be used to overcome the strong ^1H induced anisotropies, enabling high resolution ^1H detection for fully protonated samples^[91-93], paving the way for resonance assignment^[94,95] and structural elucidations^[96].

NMR is hindered by long experimental acquisition times due to its low intrinsic sensitivity. Non uniform sampling (NUS) and non Fourier transform based processing methods result in significant reduction of experimental time^[97-99], facilitating acquisition of 4D spectra in solid-state NMR^[100]. Furthermore, sensitivity of solid-state NMR can be enhanced by a factor 10^2 - 10^3 by dynamic nuclear polarization (DNP)^[101,102]. In DNP experiments, polarization is transferred from electrons of a polarizing agent to nuclear spins via microwave irradiation^[103,104]. Application of DNP enabled the study of membrane proteins^[105-107] and amyloids^[108-110].

The permanent NMR methodological developments are assisted by technological advances, for instance the availability of high magnetic field spectrometers. Furthermore, NMR probes featuring MAS frequencies up to 100 kHz for 0.8 mm rotors have been introduced^[111]. A further benefit of utilizing these small rotors is the significant reduction of sample volume, which is often a major bottleneck.

In summary, recent progress in sample preparation combined with methodological and technological developments will assist to overcome obstacles faced by NMR spectroscopy, granting access to yet inapproachable biological systems.

1.2 Alzheimer's Disease (AD)

1.2.1 Background of AD

The increasing global prevalence of dementia places heavy social and economic burdens on society. Approximately 35.6 million people worldwide were affected by dementia in 2010, and the number is estimated to double every 20 years^[112]. Alzheimer's disease (AD) is the most common cause of dementia and accounts for 60-80% of all cases^[113]. The condition was first reported in 1906 by the German neuropathologist Alois Alzheimer^[114], and is a progressive neurodegenerative disorder associated with a decline in cognitive function. The two pathological hallmarks of AD in brain tissue include the extracellular deposition of the amyloid- β

(A β) peptide into diffuse and neuritic plaques, as well as the intraneuronal accumulation of hyperphosphorylated tau (p-tau) protein into neurofibrillar tangles (NFTs)^[115,116] (Figure 1.6). AD is further associated with a damage to neurons and synapses, as well as gliosis and white matter lesions^[115]. Risk factors of AD include cardiovascular problems such as hypertension, diabetes and high cholesterol levels, cerebrovascular diseases such as infarcts, lifestyle-related factors like smoking, alcohol and low physical activity and education, as well as genetic predisposition^[115,117].

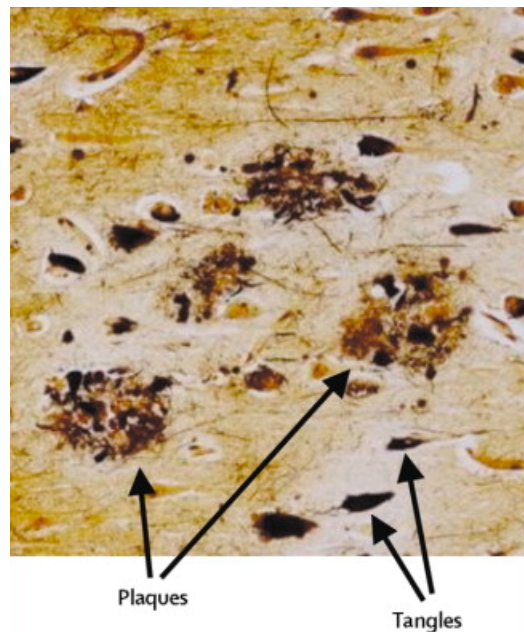


Figure 1.6.: Hallmarks of AD pathology: Plaques and neurofibrillary tangles. A β is deposited in extracellular deposits called senile plaques. They are associated with an increasing number of astrocytes, microglia and dystrophic neurons. Aggregates of the hyperphosphorylated microtubule-associated protein tau form intracellular tangles. The figure was adapted from Blennow *et al*^[118].

1.2.2 Genetics of AD

AD can be categorized into two types, the rapidly progressing early-onset AD (EOAD), developing before the age of 65 and accounting for >1% of all AD cases, and sporadic late-onset AD (LOAD), occurring at ≥ 65 years and affecting the majority of patients^[113,119]. Clinically, these two forms are indistinguishable, as they are phenotypically and pathologically similar^[115,120]. They are however based on genetic differences^[121]. EOAD follows a Mendelian pattern of inheritance, and is mainly

caused by A β overproduction^[122]. It arises due to mutations in three autosomal dominant genes: amyloid precursor protein (*APP*), presenilin 1 (*PSEN1*) and presenilin 2 (*PSEN2*), the last two being components of the γ -secretase complex responsible for APP cleavage and A β metabolism^[122,123]. AD caused by such mutations is also referred to as familial AD (FAD). The gene for APP is located on chromosome 21, and A β toxicity is linked to trisomy 21 (Down syndrome), in addition to AD^[124]. The strongest genetic risk factor for developing LOAD is the inheritance of the ϵ 4 allele of the apolipoprotein (*APOE*) gene^[122]. ApoE is involved in lipid homeostasis and transport and is encoded by three polymorphic alleles ϵ 2, ϵ 3, and ϵ 4. The presence of two ϵ 4 alleles will increase LOAD risk by a factor 9 or more^[125].

1.2.3 Treatment of AD

Neuropathological progression and therapeutic intervention can be monitored by the use of biomarkers^[126]. AD is typically diagnosed by magnetic resonance imaging (MRI) assessing brain atrophy, positron emission tomography (PET) measurements of glucose metabolites and the retention of the amyloid binding Pittsburgh compound B (PIB), as well as biomarkers in the cerebrospinal fluid (CSF)^[127]. Immunoassays allow the detection of A β , p-tau and A β -antibodies as biomarkers in the CSF^[128].

Although neurotransmitter-based approaches such as cholinesterase inhibitors and memantine help in controlling cognitive AD symptoms, no therapeutic strategy for curing or prevention of the disorder is currently available^[129,130]. Most clinical trials target pathways in A β metabolism and clearance^[131]. Promising fields of research include the design of small molecule inhibitors interfering with A β plaque formation, and active and passive immunization strategies^[132]. However, several antibodies including bapineuzumab and solanezumab have shown disappointing primary results in late clinical phase trials^[133].

1.2.4 Inflammation in AD

The progression and development of AD are closely associated with and caused by neuroinflammation^[134-137]. During AD pathogenesis, A β deposits co-localize with chronic inflammatory mediators such as activated microglia and astrocytes^[138], which show a strong immune response towards A β ^[139]. In addition, an excessive production of inflammatory chemokines and cytokines, complement system components and reactive oxygen species (ROS) by brain cells cause damage to synapses and hence,

cognitive impairment^[139,140]. This elevated inflammatory response contributes further to A β deposition and tau phosphorylation^[141]. Due to these inflammatory processes, nonsteroidal anti-inflammatory drugs (NSAIDs) have been suggested to exert beneficial effects on AD pathogenesis^[142]. Indeed, epidemiological studies point to a protective influence of NSAIDs for AD^[143,144], although other studies do not support these findings^[137,145]. Further investigations are required to elucidate details of the effects of NSAID on AD risk^[145]. Instead of inhibiting cyclooxygenase (COX) activity, in AD, NSAIDs act directly on A β production^[142].

1.3 The AD peptide Amyloid- β (A β)

1.3.1 Generation of the A β peptide

The deposition of amyloidogenic proteins and their inherent toxicity is the cause of numerous degenerative diseases^[146-148] and more than 100 human diseases^[149]. Examples are aggregates of prions in spongiform encephalopathies^[148], antibody light chains in systemic amyloidosis^[150], α -synuclein (α S) in Parkinson's disease^[151] and islet amyloid polypeptide (IAPP) in type 2 diabetes (T2D)^[152]. A β peptides have been identified as the main constituent of senile plaques in AD brain tissue in 1985^[153]. The approximately 40 residues long A β peptides are derived by proteolytic cleavage of the amyloid precursor protein (APP)^[154-156]. APP is a type I transmembrane glycoprotein found in nearly all subcellular compartments of various cell types^[157]. In a nonamyloidogenic pathway, the ectodomain of APP is cleaved by the α -secretase, followed by further cleavage of the C-terminal membrane-bound fragment (C83) by the γ -secretase in the transmembrane sequence (TMS)^[155,158]. This normal metabolic event results in the secretion of soluble p3 peptides of ca. 3 kDa^[159], comprising only the C-terminal part of the A β sequence. In the amyloidogenic pathway APP is cleaved by the β -secretase (BACE-1 for β -site APP-cleaving enzyme) at a more N-terminal site^[160,161]. Cleavage of the retaining C99 fragment by the γ -secretase will result in release of the amyloidogenic A β peptides^[162]. A schematic representation of the generation of A β peptides from APP and the sequences of A β ₁₋₄₀ and A β ₁₋₄₂ are displayed in Figure 1.7.

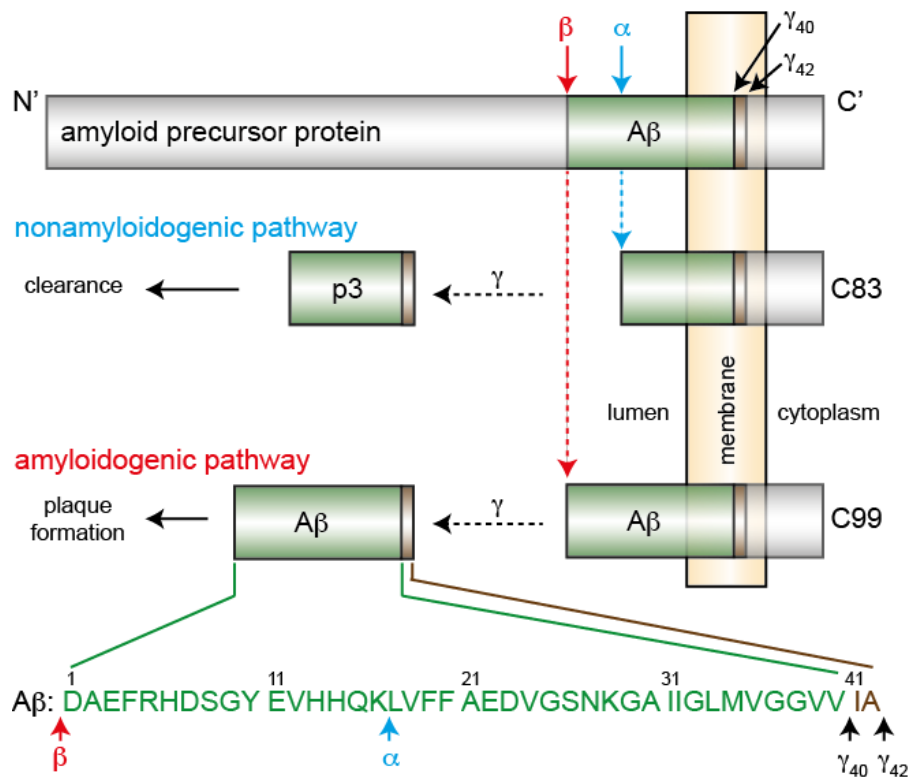


Figure 1.7: Processing of the amyloid precursor protein (APP) and generation of A β ₁₋₄₀ and A β ₁₋₄₂. The membrane bound APP undergoes sequential proteolytic cleavage by the α - and β -secretases, resulting in C-terminal membrane bound fragments C83 in the nonamyloidogenic (blue), and C99 in the amyloidogenic pathway (red), respectively. These fragments are further cleaved by the γ -secretase, generating soluble p3 or amyloidogenic A β peptides. The cleavage site of the γ -secretase determines the lengths of A β peptides. The sequences of A β ₁₋₄₀ and A β ₁₋₄₂ are shown in the lower part of the figure. Arrows indicate cleavage sites of the secretases. The figure is adapted from Steiner *et al.*^[163].

In general, γ -secretase activity is facilitated by PSEN1 and PSEN2^[163] and is associated with determining the lengths of A β peptides. As the cleavage site of the γ -secretase is rather imprecise, an ensemble of A β peptides with varying lengths is produced ranging from 30 to 51 residues^[164]. A β ₁₋₄₀ and A β ₁₋₄₂ (40 and 42 residues, respectively) are the predominantly produced peptides^[165-167]. They differ only by two additional residues in the C-terminus of A β ₁₋₄₂ (Figure 1.7). The C-terminus of A β peptides is particularly critical for aggregation^[168]. A β ₁₋₄₂ is the pathological relevant peptide^[158], as it is the major component of senile plaques in brain tissue^[169] and more aggregation-prone^[163,170,171]. However, not the total A β content, but rather an increasing A β ₁₋₄₂ to A β ₁₋₄₀ ratio enhances AD pathology and defers the age of onset^[172,173].

1.3.2 Oxidation of the A β peptide

Oxidative stress contributes to pathogenesis of numerous diseases, including neurodegenerative diseases^[174]. It is caused by an imbalance in redox homeostasis, hence a reduction of antioxidants, and an increase of ROS like the hydroxyl radical ($\cdot\text{OH}$) and reactive nitrogen species (RNS) such as nitric oxide ($\text{NO}\cdot$). These radicals contain an unpaired electron and tend to react with other biomolecules, thereby causing oxidative damage to DNA, RNA, proteins, lipids and other cellular components^[175,176]. Within proteins, methionine residues are particularly susceptible to oxidation and function as endogenous antioxidants^[177]. Reversible oxidation of the thioether will result in methionine sulfoxide^[178]. A second irreversible oxidation will produce methionine sulfone.

The brain is particularly vulnerable to oxidative stress due to its elevated levels of redox transition metal ions and limited amounts of antioxidants^[175]. Oxidative stress contributes significantly to AD disease progression^[179]. The A β peptide plays an important role in this process, although the exact mechanism is unclear^[180]. Oxidative stress seems to be mediated by residue M35 of the A β peptide^[181], which is found in its oxidized form in 10-50% of total A β in AD plaques^[182]. In addition, M35 is critical for the neurotoxicity of A β ^[181]. However, M35 oxidation also facilitates reduction of the neurotoxic A β -bound Cu^{II} to Cu^{I} ^[183]. Oxidation of M35 interferes with aggregation properties of A β ^[175]. A large amount of literature suggests that it hinders fibrillation and oligomer formation by preventing hydrophobic and electrostatic interactions^[184-187], although there are controversial reports^[188].

1.4 Amyloidogenesis

1.4.1 Amyloid self-assembly

Amyloidogenesis describes the self-assembly of soluble monomeric protein into insoluble protein aggregates. The formation of fibrils can be monitored by the dye Thioflavin T (ThT), which exhibits enhanced fluorescence upon binding to insoluble amyloid species^[189]. The process occurs in a sigmoidal fashion and consists of three phases, a lag phase, exponential growth, and a stationary phase^[190] (Figure 1.8). The lag phase is a thermodynamically unfavorable rate-limiting step, in which low-n oligomeric intermediates are formed as nuclei. In the exponential growth phase, the generated nuclei act as seeds for rapid elongation and growth into larger oligomers

and protofibrils and finally association into mature fibrils^[190-193]. The size of amyloid fibrils is in the range of MDa. The stationary phase is reached once the monomeric population is depleted, and larger species will remain in assembly/disassembly equilibrium^[61,192]. Fibril growth is believed to be a template-dependent process, in which accreting monomers associate with the end of the growing fibrils^[194,195].

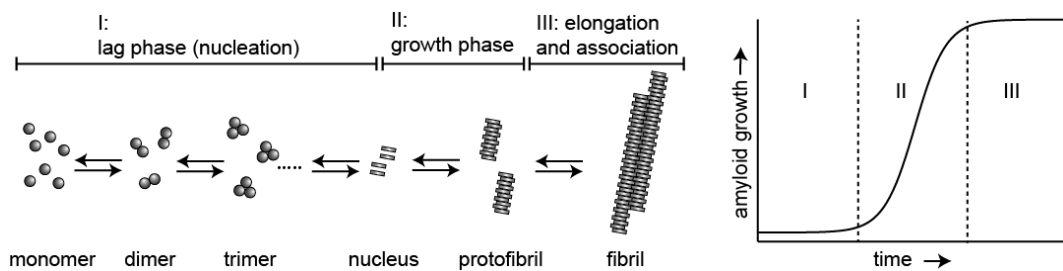


Figure 1.8: Kinetics and intermediates of amyloidogenesis. Amyloid formation is a nucleation-dependent process. In the lag phase (I), nuclei are generated which serve as seeds for fibril growth in the exponential phase (II) until the monomer population is depleted. In the stationary phase (III) protofibrils elongate and associate to form mature fibrils. The figure is adapted from Ghosh *et al*^[193].

The nucleation dependent amyloid fibrillation process resembles the crystallization behavior of solutes at concentrations above their solubility limit^[196,197]. Under such conditions solutes often form crystals. However supersaturated solutions are stable and retained, as crystallization underlies a high free-energy barrier^[198]. Similarly, in a metastable supersaturated solution, amyloidogenic proteins are kinetically trapped and will remain soluble^[199]. Supersaturation can be interrupted by ultrasonication, as it accelerates spontaneous fibrillation by triggering nucleation and introducing seeds to overcome the lag phase of amyloidogenesis^[197,200-202].

1.4.2 The amyloid hypothesis

The amyloid hypothesis postulates that A β is the fundamental factor that triggers a downstream cascade of events ultimately responsible for AD pathology^[203,204]. Original reports describe that synaptic dysfunction, neurofibrillary tangles of p-tau, neuronal loss, vascular damage and dementia are direct consequences of A β deposition into plaques^[203]. Concerns of the hypothesis first arose when it was found that not amyloid deposits, but rather soluble A β species correlate with cognitive impairment^[205]. These findings gave rise to a hypothesis emphasizing the role of soluble oligomers in AD^[206]. Although it is well established that soluble A β oligomers

constitute the toxic amyloid species, there are still many unresolved issues concerning the amyloid hypothesis^[207]. Indeed, AD therapeutic approaches have been strongly guided by the amyloid hypothesis in the past and have mostly failed in late clinical phases^[207,208].

Substantial evidence suggests that low-n A β oligomers are responsible for amyloid toxicity^[205,209-211]. *In vitro* studies demonstrated that neurotoxicity initially observed for A β aggregates is actually mediated by A β soluble oligomers, also termed A β -derived diffusible ligands (ADDLs)^[212], in a greater extent than by mature fibrils^[213]. In addition, oligomeric A β contribute to AD pathogenesis by inducing tau hyperphosphorylation^[214]. In particular, low-n oligomers impair synaptic plasticity by inhibiting hippocampal long term potential (LTP) of rats *in vivo* ^[215]. The importance of low-n oligomers in AD is further stressed by evidence that they cause synapse loss^[216], alterations to synapse composition^[217] and are found in elevated levels in AD brains in an age-dependent manner^[218], although there are controversial reports^[217,219]. There are ongoing debates regarding the correlation between size of the oligomers and toxicity^[211], as low-n oligomers may act as seeds for high-n oligomers^[220] and protofibrils^[221]. The mechanism by which oligomers mediate neurotoxicity is unclear^[211], although data suggests that they act by binding multi-protein receptor complexes on neuronal surfaces and thereby trigger synapse failure^[206] or neurotoxic pathways^[217].

1.4.3 Self-propagation and cross-seeding

Fibrils have the ability to propagate their own structure by recruiting free peptide from their surrounding solution, a concept known as self-propagation^[222]. This can be demonstrated by seeded fibrillation, where the presence of seeds results in omitting the lag phase of amyloidogenesis^[223]. Hereby, the structure of the seed determines the structure of the final fibril^[224,225]. Cross-seeding, an event where one type of amyloid species serves as a seed for a different type of amyloid protein, is highly sequence and conformation dependent^[222]. For instance, α S seeds induce tau fibril formation^[226]. A β_{1-40} seeds are able to efficiently cross-seed elongation of IAPP, while IAPP are poor seeds for A β_{1-40} growth^[227]. There is controversial data about the ability of A β_{1-40} and A β_{1-42} to cross-seed each other. On one hand, A β_{1-40} inhibits A β_{1-42} aggregation when present as a monomer^[228-230], however fibril formation of both peptides can be seeded by the other form^[229] and mixtures of the two peptides^[231]. On the other hand, *in vitro* fibrils of A β_{1-40} and A β_{1-42} are unable to

cross-seed each other efficiently^[232,233]. The factors underlying cross-seeding remain elusive, but are most likely determined by molecular structures^[222].

1.5 NMR studies of A β

All A β species along the pathway to fibrillogenesis constitute potential drug targets. It is crucial to understand the internal molecular structure of amyloid assemblies as a basis for pharmacological approaches. It is however difficult to study amyloid aggregates using conventional structural biology methods, as they are inherently noncrystalline, insoluble and of high molecular weight, making them inaccessible for X-ray crystallography and solution-state NMR spectroscopy^[222]. MAS solid-state NMR spectroscopy has emerged to be the most powerful technique for structural determination of insoluble macromolecular complexes^[234,235]. Amyloid deposits can also be visualized by electron microscopy (EM)^[236]. Structural details are available for monomeric and fibrillar A β , although oligomer structures remain elusive^[237].

1.5.1 Solution-state NMR characterization of A β monomers and intermediates

The monomeric entity of A β peptides adopts mainly unstructured, random coil conformations in aqueous solutions, although they contain transient secondary structure propensities^[238,239], a typical feature of intrinsically disordered proteins (IDPs)^[240]. Monomers may fold into partially helical intermediates on the way to fibrillogenesis^[241].

The structural characterization of amyloid intermediates is challenging, as they are heterogeneous in size, structure and morphology^[242]. Moreover, low-n oligomers occur early in the amyloidogenic pathway and convert into larger oligomers, protofibrils and fibrils. Therefore it is crucial to prepare kinetically stable intermediates^[243]. Attempts to capture A β oligomers include freeze-trapping^[244], photo-induced cross-linking^[245,246], or glutaraldehyde cross-linking of SDS stabilized globulomers^[247], among others^[248-251]. Oligomeric species have also been extracted from brain tissue of affected human individuals^[237]. Analogous studies exist for protofibrils^[252-254]. The sample preparations yield heterogeneous oligomers, however

they have the common feature of containing β -sheet elements, and the β -sheet content increases with oligomer size^[255].

In addition to structural determination, dynamic processes in which $A\beta$ species undergo on the path to fibrillogenesis can be probed by solution-state NMR, for instance by DEST experiments^[54,56]. Exchange species on protofibrillar surfaces constitute a sparsely populated state. Transferring and detecting their properties on the observable monomeric state, enabled the description of a kinetic exchange regime between the two species^[256]. Furthermore, NMR relaxation measurements determined that 3% of the total $A\beta$ peptide undergoes dynamic exchange between oligomeric and monomeric states^[61].

1.5.2 Solid-state NMR characterization of $A\beta$ fibrils

$A\beta$ fibers can reach up several microns in length and have a width between 5-15 nm^[222] (Figure 1.9). The macroscopic fibril morphology depends heavily on the growth conditions during fibrillogenesis^[234]. For instance, when subject to gentle agitation, $A\beta_{1-40}$ will fold into straight protofibrils which associating laterally into “striated ribbons”^[225]. Quiescent conditions during growth will yield $A\beta_{1-40}$ fibrils with a periodic twist termed “twisted-pair”^[257]. Structural characterizations of different fibril polymorphs revealed that although amyloid fibrils contain common secondary and tertiary structural elements, they differ in their overall symmetry and quaternary structure^[257,258].

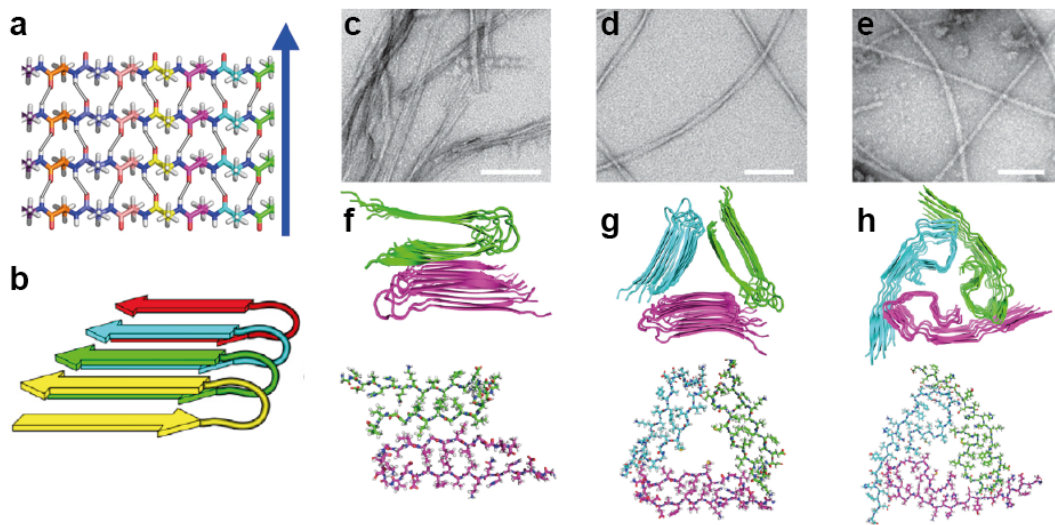


Figure 1.9: Details of A β fibril structures. (a) in-register parallel cross- β arrangements of adjacent peptide strands with β -strand conformation. The β -strands are perpendicular to the fibril axis (blue arrow), whereas the hydrogen bonds (gray) are approximately parallel. (b) cross- β structures formed by peptides in β -arch conformation. (c-e) EM images and (f-h) structural models of A β ₁₋₄₀ fibrils. Individual peptide strands will assemble into (c, f) a 2-fold symmetric structure with striated ribbon morphology in the presence of agitation, (d, g) a 3-fold symmetric structure with a twisted morphology under quiescent conditions, or (e, h) an alternative 3-fold symmetric structure when seeded from brain tissue. White scale bar = 100 nm. Images are adapted from Tycko *et al*^[222,234].

The formation of β -sheets is the most characteristic secondary structural elements of self-assembled A β . The high propensity for cross- β structures found in fibrils can be observed in X-ray diffraction measurements^[259]. In cross- β structures, β -sheets are formed which align perpendicular to the fibril axis, and are connected by interstrand hydrogen bonds parallel to the fibril axis^[258] (Figure 1.9a-b). Except for monomeric A β , β -sheet content is found in most A β species to different extents^[236].

Currently, there are several MAS solid-state NMR structures^[232,257,260-263] and numerous models^[264-267] available for wild type and mutant A β ₁₋₄₀ fibrillar assemblies. Details of A β structures and models are summarized in Table 1.3. The most commonly observed structures consist of in-register parallel cross- β structures consisting of U-shaped β -arches (β -loop- β), although exceptions have been found^[263,268]. In addition, a salt bridge connecting side chains of D23 and K28 is frequently observed^[232,260,266]. The structures and models differ mainly in the number of monomers forming the basic fibrillar subunit, residues involved in β -strands, as well as the flexibility of the N-terminus. It is consensus that the C-terminus, consisting

of mainly hydrophobic residues, is the driving force for aggregation and forms the fibrillar core^[168]. Several models do not feature the N-terminus^[261,263,264], as it is absent in solid-state NMR spectra due to dynamic disorder and flexibility. Experimental mass-per-length (MPL) measurements of fibrils by EM allow determining the number of monomers contributing to the subunit^[234]. Wild type A β ₁₋₄₀ structures are available for 2-fold symmetric “striated-ribbon” fibrils^[260] (Figure 1.9c, f), 3-fold symmetric “twisted-pair” fibrils^[257] (Figure 1.9d, g), as well as 3-fold symmetric fibrils seeded from AD patient brain tissue^[232] (Figure 1.9e, h). Differing quaternary structures are found within one fibril morphology, depending on side chain orientation^[260]. In the calculated structures, symmetric dimers/trimers form the subunit of the fibrils. However, asymmetric dimer formation has been described to form the basis for one A β ₁₋₄₀ polymorph^[264]. In addition, structures have been solved for the Osaka mutant Δ E22^[262] and the Iowa mutant D23N^[261,263] of A β ₁₋₄₀.

In contrast to A β ₁₋₄₀, little is known about A β ₁₋₄₂ structural details at an atomic level. This may be attributed to its higher aggregation propensity^[163] and heterogeneous fibril assemblies^[150], making sample preparation challenging. Hydrogen/deuterium (H/D) exchange^[269-271] and EM studies^[269,272] on A β ₁₋₄₂ fibrils have provided valuable insight to overall morphology, symmetry and dynamics. Two recent MAS solid-state NMR studies characterize A β ₁₋₄₂ fibrils at a molecular level^[233,273]. Xiao *et al* present a structural model of A β ₁₋₄₂ fibrils featuring the formation of an alternative salt bridge connecting K28 N ζ and A42 CO, and the presence of three β -strands^[233], which are confirmed by Colvin *et al*^[273].

	Description	Author, year	PDB-ID	Symmetry	Production	Fibril preparation	Residues observed	Salt-bridge	Motif
Structures	1-40, wild type	Petkova <i>et al.</i> 2005 ^[225] , Pektova <i>et al.</i> 2006 ^[260]	2LMN/ 2LMO	2-fold	synthetic	agitation	A02, D07-V39	D23-K28	U
	1-40, wild type	Paravastu <i>et al.</i> 2008 ^[257]	2LMP/ 2LMQ	3-fold	synthetic	quiescent, sonication	A02, G09-E22, V24-V40	no	U
	1-40, wild type, brain-tissue seeded	Lu <i>et al.</i> 2013 ^[232]	2M4J	3-fold	synthetic/ recombinant	n/a	D01-H13, Q15-V40	D23-K28	U/S
	1-40, Osaka mutant, Δ E22	Schütz <i>et al.</i> 2015 ^[262]	2MVX	2-fold	recombinant	agitation	n/a	E03-K28	other
	1-40, Iowa mutant, D23N	Qiang <i>et al.</i> 2012 ^[263]	2LNQ	n/a, antiparallel	synthetic	agitation	Q15-K16, V18-N23, K28, A30-I32, L34-M35, V36, G38-V40	no	U
	1-40, Iowa mutant, D23N	Sgourakis <i>et al.</i> 2015 ^[261]	2MPZ	3-fold	synthetic	agitation	K16-L17, F19-V24, K28-V40	no	U
	1-42, wild type	Xiao <i>et al.</i> 2015 ^[233]	2MXU	n/a	synthetic	n/a	A02, F04, G09, V12-H14, L17-A21, D23-S26, K28-L34, V36-A42	K28-A42	S
Models and CS	1-40, wild type	Petkova <i>et al.</i> 2005 ^[225]	-	n/a	synthetic	quiescent	A02, D07-V39	weak D23-K28, potential K16-E22	n/a
	1-40, wild type, asymmetric dimer conformer 1	Lopez del Amo <i>et al.</i> 2012 ^[264]	-	2-fold	recombinant	agitation	Q15-V40	n/a	double- β
	1-40, wild type, asymmetric dimer conformer 2	Lopez del Amo <i>et al.</i> 2012 ^[264]	-	2-fold	recombinant	agitation	A21-G38	n/a	double- β
	1-40, wild type	Petkova <i>et al.</i> 2002 ^[266]	-	2-fold	synthetic	agitation	A02, D07, G09-V12, K16-A21, D23-G25, K28-I32, L34-V36	D23-K28	U
	1-40, wild type	Bertini <i>et al.</i> 2011 ^[265]	-	2-fold	recombinant	agitation	A02-V40	n/a	U
	1-40, wild type, phospholipid reference	Niu <i>et al.</i> 2014 ^[267]	-	n/a	recombinant	agitation	A02-R05, D07-A21, V24-V40	n/a	other
	1-42, wild type	Colvin <i>et al.</i> 2015 ^[273]	-	n/a	recombinant	n/a	M0-R05, D07-V12, K16-V40	n/a	triple- β

Table 1.3: Structural details of wild type and mutant A β ₁₋₄₀ and A β ₁₋₄₂ structures and wild type A β ₁₋₄₀ models and CS.

1.5.3 Solution-state NMR studies of A β interactions with inhibitory molecules

Even though our understanding of AD pathology has improved in the past years, AD remains an untreatable disease^[133]. Various initially promising treatment strategies have failed in clinical trials^[132]. In current AD research, strong emphasis is placed on small molecules able to interfere with amyloid aggregation properties or A β production, toxicity and clearance^[132]. In addition, further development of amyloid binding diagnostic compounds such as PIB will facilitate earlier AD detection^[274]. A large number of multidisciplinary approaches combining NMR with biophysical methods like isothermal titration calorimetry (ITC), circular dichroism (CD) spectroscopy, dynamic light scattering (DLS), small angle X-ray scattering (SAXS), atomic force microscopy (AFM) and EM have set out to explain the mechanism of action in which such small molecules inhibit amyloids, however, the details of the molecular interactions remain to be solved^[275].

A plethora of amyloid binding compounds has been probed by solution-state NMR. Valuable information nature of the interaction can be extracted from monitoring NMR variables like chemical shift perturbations (CSP), signal intensities and line widths, as well as NOEs^[276,277]. These NMR properties give insight about the binding site, size, and stoichiometry. For instance, solution-state NMR was employed to study associations of A β species to substances like CR^[278,279], lacmoid and lacmoid-like compounds^[279-281], peptide inhibitors^[282,283], nanoparticles^[284], Zn²⁺ ions^[285-287], and the phenolic compounds (-)-epigallocatechin-3-gallate (EGCG)^[288], resveratrol^[289] and others^[290].

In aggregating systems such as amyloids, insoluble species and bound ligands are not observable by traditional solution-state NMR methods. More advanced solution-state NMR experiments provide details of exchange rates and dynamics of the complex, as well as the free (“visible”) and bound (“invisible”) state of the ligand^[56]. For example, CPMG relaxation dispersion experiments may be employed to study equilibrium chemical exchange processes on a ms timescale^[10,291]. This technique has been successfully applied to investigate CR^[279,292] and lacmoid^[279] binding to A β . Furthermore, in transferred NOE (trNOE) experiments, NOE properties of the target-ligand complex are transferred back to the free state, which is detectable in the spectra^[293]. This approach yields information about the conformation of the ligand in the bound state, and has been employed to study α S

bound CR^[292], ThT bound to insulin fibrils^[294], and the interaction of various small molecules with A β ^[294].

1.5.4 Solid-state NMR studies of A β interactions with inhibitory molecules

Solid-state NMR spectroscopy has emerged as the most powerful tool to investigate insoluble amyloid-small molecule complexes at atomic resolution^[295]. The first study on such a protein-ligand complex allowed a high-resolution mapping of the CR-HET-s fibril binding site^[296]. This was achieved by monitoring CSPs of HET-s fibrils in the presence of Congo Red (CR) and polarization-transfer from ¹H of CR to ¹³C of the [²H, ¹³C, ¹⁵N] labeled protein. EGCG-induced oligomers formed by A β ₁₋₄₀ yield well-resolved solid-state NMR spectra^[288]. Analysis of secondary chemical shifts and REDOR spectra indicated the presence of the typical β -sheets and the D23-K28 salt bridge. Two studies investigate the binding of curcumin to A β ₁₋₄₂ fibrils and highlight the binding site^[297] as well as alterations of the D23-K28 salt bridge and disturbance of the fibrillar character^[298]. Similarly, Zn²⁺ has been demonstrated to disrupt the salt bridge, although leaving the cross- β structure intact^[299]. A combination of solid-state NMR data and molecular dynamics (MD) were employed to determine the binding site of Cu²⁺ to A β ₁₋₄₀ fibrils^[300].

1.6 A β inhibitors investigated in this study

1.6.1 The γ -secretase modulator sulindac sulfide

1.6.1.1 γ -secretase modulators

A β ₁₋₄₂ production is increased in FAD, as the underlying mutations affect γ -secretase activity and cleavage site^[162,301]. The γ -secretase is therefore considered a prime drug target for AD therapy^[302]. However, it is involved in various pathways, such as Notch signaling^[303], and attempts to inhibit its full activity have failed in clinical trials^[164]. Instead, allosteric γ -secretase-modulators (GSMs) provide a more promising attempt to alter A β production. Instead of diminishing A β production, GSMs shift the profile of A β peptides generated^[304]. These so-called 1st generation GSMs act by reducing levels of the disease-relevant A β ₁₋₄₂ and enhancing production of shorter, less toxic peptides^[304,305]. This class of GSMs includes mainly NSAIDs and

their derivatives^[304]. This work focuses on the interaction of the NSAID sulindac sulfide with A β .

1.6.1.2 Sulindac sulfide interactions with A β

Sulindac is a pro-drug and contains a methyl sulfoxide group, which is reduced to its active metabolite sulindac sulfide or oxidized to sulindac sulfone in the body^[306] (Figure 1.10). The reduction reaction of sulindac to sulindac sulfide is catalyzed by the methionine sulfoxide reductase (Msr) and oxidation to sulindac sulfone is metabolized by cytochrome P450^[306,307]. Sulindac sulfide inhibits COX 1 and 2 activity, thereby reducing the production of prostaglandins^[308]. Sulindac metabolites are promising anti-tumor agent^[309,310], especially for colorectal cancer^[311]. Sulindac sulfide has further pleiotropic effects, for instance, by inhibiting tumor cell invasion and down-regulating NF- κ B mediated microRNA transcription^[312].

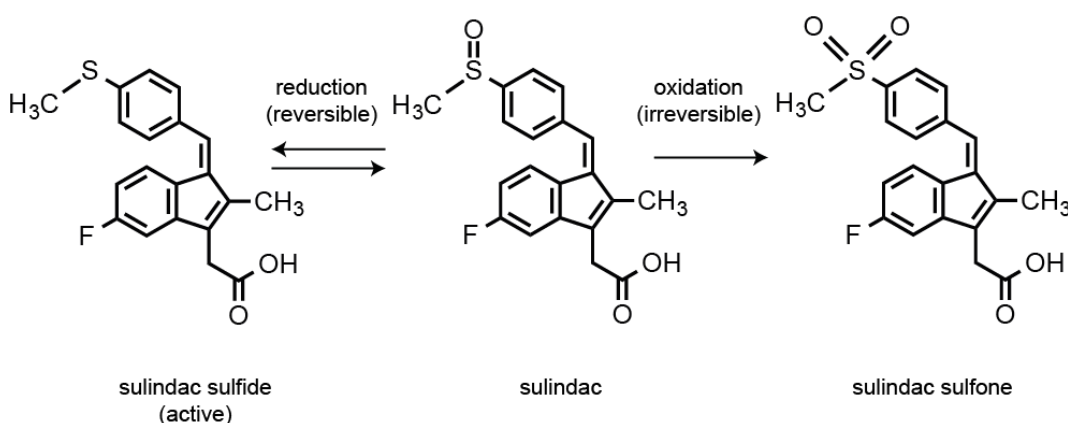


Figure 1.10: Chemical structures of the NSAIDs sulindac, sulindac sulfide and sulindac sulfone. Biotransformation of sulindac involving the oxidation state of the sulfoxide substituent. Sulindac (center) can be reduced to its active metabolite sulindac sulfide (left) in a reversible reaction, or irreversibly oxidized to sulindac sulfone (right)^[308].

The NSAIDs ibuprofen, indomethacin and sulindac sulfide^[305], as well as *R*-flurbiprofen^[313,314] are able to inhibit A β ₁₋₄₂ release in cultured cells, although others raise A β ₁₋₄₂ concentrations *in vivo*^[315]. The mechanism of action is still a topic of discussion^[316], as these GSMs may target either the γ -secretase^[317-319] or APP^[320,321]. Sulindac sulfide is reported to interfere with APP dimerization^[164,322], a process influencing the specificity of γ -secretase cleavage. Cellular APP exists as a homodimer^[323], and dimerization is mediated by the G₂₉xxxG₃₃ motif of the A β sequence in the APP-TMS^[324]. Loss of the GxxxG motif weakens APP dimerization

and increases levels of shorter A β peptides^[324]. NSAIDs including sulindac sulfide target A β ₁₋₄₂ production by binding to the GxxxG motif, thereby attenuating APP dimerization^[320,322,325].

The mechanism involved in NSAID activity are yet undefined. Efficacy of 1st generation GSMs in AD could not be verified in clinical trials^[326]. 2nd generation GSMs aim at improving potency and bioavailability in the brain^[316]. However, it is crucial to elucidate details of the NSAID-APP interaction. The GxxxG motif is involved in cholesterol binding^[327]. NSAIDs have been suggested to interact with lipids in phospholipid complexes^[328-330]. These findings contribute to understanding how NSAIDs behave in membrane environments. Solution-state NMR structures of dimeric APP-TM are available for the wild type^[331] and for a familial mutant^[332], and will provide further insight of APP processing and small molecule interference.

The binding of sulindac sulfide to APP is well known and accepted. However, the interaction of sulindac sulfide to the A β peptide itself is still a matter of debate, as there are reports that support its binding to monomeric^[322,333], oligomeric^[334] and fibrillar A β ^[333], and those, which refute a direct interaction^[335]. Similarly, the effect of sulindac sulfide on A β aggregation properties remains elusive. Hirohata *et al* demonstrated anti-fibrillogenic and fibril destabilizing effects exerted by sulindac sulfide towards A β ^[336] and α S^[337], while Yesuvadian *et al* reported no influence of sulindac sulfide on the aggregation process of A β ^[333]. These discrepancies may arise due to the colloidal character of sulindac sulfide.

1.6.1.3 Colloid formation of sulindac sulfide

The solubility of sulindac sulfide is limited in aqueous solutions, and it aggregates into micelle-like colloidal aggregates above a certain critical micelle concentration (CMC)^[335]. This phenomenon of aggregate formation is a common mechanism responsible for nonspecific and promiscuous activity of numerous compounds^[338]. Such self-assemblies lead to protein aggregation and inhibition of protein function in a nonspecific manner^[338-341]. Colloidal aggregates are formed mainly by hydrophobic small molecules with few polar groups and may reach submicrometer sizes^[338]. The organization of such macromolecular assemblies is unclear, however they can be highly ordered and driven by aromatic π -stacking, as suggested for the amyloid dye CR^[342]. Representative EM images of tetraiodophenolphthalein and CR colloids are shown in Figure 1.11.

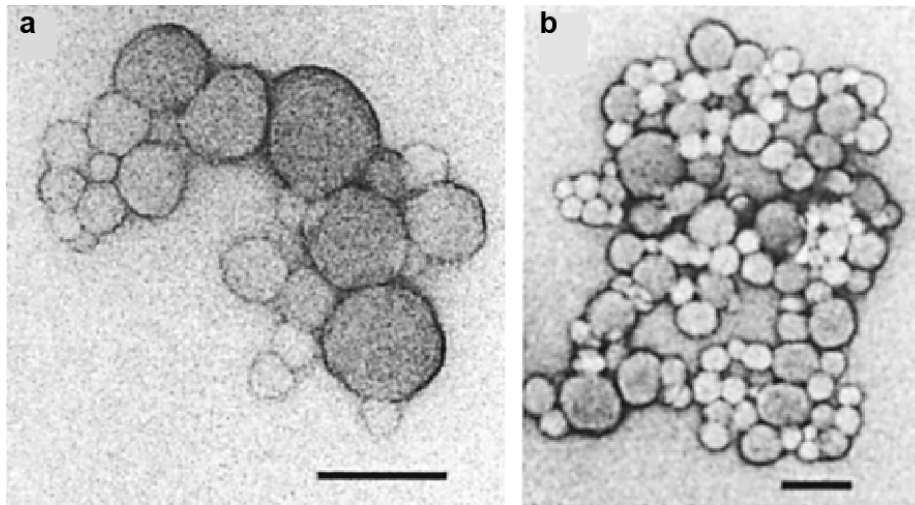


Figure 1.11: Electron microscopy images of colloidal aggregates. (a) 100 μM tetraiodophenolphthalein in 20 mM Tris and (b) 50 μM CR in 20 mM Tris. Scale bar = 100 nm. The figure is adapted from McGovern *et al.*^[338].

Colloidal species of small organic molecules are able to interact nonspecifically with $\text{A}\beta$ and inhibit its aggregation into fibrils^[343] and oligomers^[290]. It has been suggested that the binding of sulindac sulfide to APP and $\text{A}\beta$ is based on a nonspecific interaction^[344], which is further supported by the observation of colloids formed by sulindac sulfide^[335]. Interestingly, its oxidized derivative sulindac sulfone is significantly more soluble and does not form colloids^[335]. The promiscuous mode of action characteristic for colloidal inhibitors must be taken into account when assessing the efficiency of GSM-amyloid interactions.

1.6.2 Peptide inhibitors

1.6.2.1 Diabetes mellitus

Diabetes mellitus is a metabolic disorder caused by an impairment of insulin-regulated glucose uptake leading to chronic hyperglycaemia^[345]. The disease can be categorized into type 1 diabetes (T1D), an autoimmune disorder caused by a lack of insulin production^[346], and the more common type 2 diabetes (T2D), characterized by insulin resistance and strongly associated with obesity^[347] and cardiovascular disease^[348]. 347 million patients were affected by diabetes in 2008

and the prevalence, as predicted by the World Health Organization (WHO), is to double between 2000 and 2030 to 4.4%^[349].

1.6.2.2 Islet amyloid polypeptide (IAPP)

Islet amyloid is found in the islets of Langerhans in the pancreas and is a pathological hallmark of T2D^[350]. These deposits are constituted of fibrils formed by a 37 amino acid long peptide called islet amyloid polypeptide (IAPP), also named amylin^[351-353]. IAPP is co-secreted with insulin from β -cells^[354]. Its physiological role is not understood, but it has been suggested to be a neuroendocrine modulator in glucose metabolism^[355]. A causative role of IAPP has been proposed in T2D, as islet amyloid depositions correlate with loss of β -cells and a lack of insulin secretion^[350,356]. Similar to other amyloidogenic disorders, early oligomeric intermediates constitute the toxic species of IAPP^[357,358].

1.6.2.3 The link between Type 2 Diabetes and Alzheimer's disease

There is increasing evidence suggesting a link between AD and T2D^[359-363]. AD patients have an increased risk for developing T2D^[359]. Similarly, insulin resistance can cause memory impairment^[362]. $A\beta$ was found to co-localize with IAPP in pancreatic tissue of T2D patients^[364]. Besides aggregation of amyloidogenic peptides and cell death, AD and T2D share further physiological processes, including high cholesterol levels and risk of cardiovascular disease^[365], increased oxidative stress and inflammation^[366,367] and association with *APOE- ϵ 4*^[368,369]. Impairment of insulin signaling seems to be the main common underlying problem in both diseases^[361]. Insulin receptors are found on neurons in the brain and mediate numerous cellular processes such as cell growth, hence, a misregulation will induce neurodegeneration^[361]. Furthermore, insulin signaling triggers phosphorylation of tau^[370].

1.6.2.4 Design of IAPP based inhibitors

The peptide sequences of $A\beta_{1-40}$ and IAPP are ca. 25% identical and 50% similar, where some regions share even higher identity^[371], and cross-seeding of the two peptides has been described^[227]. These observations triggered the design of IAPP based peptide inhibitors targeting AD and T2D^[371,372]. An IAPP mimic (IAPP-GI) was designed containing N-methylations at G24 and I26 of the amyloid core of full-length IAPP, which is soluble, nonamyloidogenic and noncytotoxic^[372]. The N-methylations

prevent interstrand hydrogen bond formation necessary for amyloid self-assembly^[372]. Indeed IAPP-GI disassociates and blocks the formation of oligomers and fibrils of IAPP^[372] and A β ₁₋₄₀^[371], binds their prefibrillar entities, and is a potent inhibitor of insulin aggregation^[373]. IAPP-GI has contributed to the design of further peptide inhibitors^[374,375].

Within the IAPP-GI sequence, regions A08-H18 and N22-S28 have been identified as hot regions responsible for high affinity interaction between amyloid peptides^[376]. However, neither A08-S28, nor each hot segment alone is sufficient to inhibit A β ₁₋₄₀ aggregation, suggesting the necessity of topological features for inhibition^[377]. The two segments were connected by various linkers consisting of three identical amino acids and tested for their efficiency to block A β and IAPP aggregation^[378] (Figure 1.12). Such peptide inhibitors are termed IAPP cross-amyloid interaction surface mimics (ISMs). The advantage of ISMs over IAPP-GI is that they lack IAPP bioactivity and may thus be used for development of AD drugs. The hot segments connected by a leucine linker (L3-GI) adapts β -strand character in solution and is the most potent inhibitor of A β ₁₋₄₀ and IAPP aggregation and cytotoxicity. The resulting co-aggregates also contain β -strand elements. An arginine linker (R3-GI) has similar effects on A β ₁₋₄₀, although it contains less β -sheet content judged by far-UV CD spectroscopy. ISMs containing an alanine (A3-GI) or glycine linker (G3-GI) are unable to suppress A β ₁₋₄₀ or IAPP fibrillation, and contain high amounts of unordered structures. In the current work, we elucidate structural characteristics of ISM interactions with A β ₁₋₄₀.

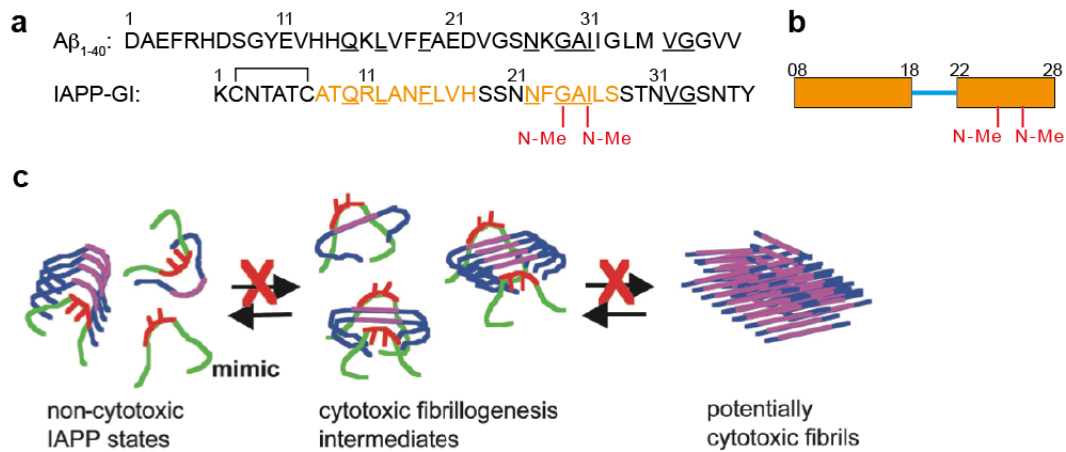


Figure 1.12: Design of IAPP-based amyloid inhibitors. (a) Sequences of $A\beta_{1-40}$ and IAPP. Identical residues are underlined. G24 and I26 of IAPP-GI are N-methylated (red). Physiological post-translational modifications of IAPP include disulfide bond formation between C02 and C07 and amidation the C-terminus^[379]. Sequences A08-H18 and N22-S28 were identified as hot regions for $A\beta$ -IAPP interactions^[376] (orange). (b) Structure of ISMs. The hot regions of IAPP-GI were connected by various linkers (blue) and tested for their inhibitory efficiency^[378]. (c) Mechanism of interaction action between IAPP-GI and IAPP. IAPP-GI binds IAPP monomers and intermediates, inhibiting further self-assembly to cytotoxic species. N-methylations (red) prohibit hydrogen bond formation on one side of the assembly. At the same time, IAPP-GI dissociates cytotoxic intermediates. (c) is reproduced from Yan *et al*^[372].

1.7 Scope of this study

Understanding the mechanism in which inhibitory molecules interact with amyloidogenic proteins is crucial for structure-based drug design. In the current study, we investigate interactions of the AD peptide $A\beta$ with the NSAID and GSM sulindac sulfide, as well as several ISM peptide inhibitors. In particular, we use solution-state NMR spectroscopy to monitor soluble $A\beta$ and its aggregation behavior, as well as MAS solid-state NMR spectroscopy to characterize insoluble $A\beta$ aggregates. Using a combination of solid-state NMR methods such as chemical shifts and distance restraints, we gather information about structural details of $A\beta$ within the aggregate. As sulindac sulfide forms complexes with $A\beta$, the NMR active properties of its ^{19}F atom were employed to localize the binding site of the NSAID on $A\beta$. In addition, solution-state NMR studies were carried out on the ISM K3L3K3-GI to characterize its structural details, and to understand how they facilitate binding to $A\beta$.

2. Materials and Methods

2.1 Materials

2.1.1 Chemicals

Chemicals were supplied by Carl Roth GmbH & Co. KG (Karlsruhe, Germany), SERVA Electrophoresis GmbH (Heidelberg, Germany), VWR International GmbH (Ismaning, Germany), Roche Diagnostics GmbH (Unterhaching, Germany) and Sigma-Aldrich Chemie GmbH (Taufkirchen, Germany), unless stated otherwise. $^{15}\text{NH}_4\text{Cl}$ and U- $^{13}\text{C}_6$ D-glucose and D_2O were purchased from Cambridge Isotope Laboratories, Inc (Tewksbury, USA) and Euriso-top (Saint-Aubin, France). DMSO-d_6 was supplied by Euriso-top and Sigma-Aldrich.

2.1.2 Equipment and software

Equipment for the ÄKTApurifier system, as well as the UNICORN 3.51 software was obtained from GE Healthcare GmbH (Munich, Germany), unless stated otherwise. NMR spectrometers and associated equipment are manufactured by Bruker BioSpin GmbH (Rheinstetten, Germany). Experiments were recorded using TopSpin v 3.2 (Bruker BioSpin). Molecular structures were created with ChemBioDraw 14.0 (PerkinElmer, Inc, Waltham, USA). Figures were created with Adobe Illustrator CS5 (Adobe Systems Inc, San Jose, USA). Protein structures were analyzed with PyMOL^[380]. ARIA2 (ambiguous restraints for iterative assignment) was used for protein structure calculations^[381].

2.1.3 Bacterial strains and plasmids

The pET28a(+) vector and *E. coli* BL21 (DE3) cells were supplied by Novagen (Merck Millipore, Darmstadt, Germany). *E. coli* XL1-Blue cells were purchased from Stratagene (Agilent Technologies Deutschland GmbH, Waldbronn, Germany).

2.1.4 Bacterial growth media

Lysogeny Broth (LB) (Table 2.1) was used for expression of unlabeled peptide, minipreps or precultures. LB medium was autoclaved prior to use. M9 medium (Table 2.1) was supplemented with $^{15}\text{NH}_4\text{Cl}$ for ^{15}N , and $\text{U-}^{13}\text{C}_6$ D-glucose for ^{13}C isotope labeling, respectively. Otherwise, unlabeled NH_4Cl (Roth) and D-glucose (Roth) were added to the media. Isotopes, biotin (Roth) and thiamin-HCl (Serva) were prepared fresh and sterile filtered. All other M9 components were autoclaved prior to use.

Medium	Amount per 1 L	Reagent (all Roth)
LB pH 7.5	10 g	Tryptone
	10 g	NaCl
	5 g	Yeast extract
M9 (10X)	60 g	Na_2HPO_4
	30 g	KH_2PO_4
	5 g	NaCl
Trace elements (100X)	5 g	EDTA, pH 7.5
	0.83 g	$\text{FeCl}_3 \cdot 6 \text{H}_2\text{O}$
	84 mg	ZnCl_2
	13 mg	$\text{CuCl}_2 \cdot 2 \text{H}_2\text{O}$
	10 mg	$\text{CoCl}_2 \cdot 6 \text{H}_2\text{O}$
	10 mg	H_3BO_3
M9 (1X)	1.6 mg	$\text{MnCl}_2 \cdot 6 \text{H}_2\text{O}$
	100 ml	M9 (10X)
	10 ml	Trace elements (100X)
	1 ml	1 M MgSO_4
	0.3 ml	1 M CaCl_2
	10 ml	Biotin (0.1 mg/ml)
	1 ml	Thiamin-HCl (1 mg/ml)
10 ml	20% (w/v) D-glucose or $\text{U-}^{13}\text{C}_6$ D-glucose	
5 ml	10% (w/v) NH_4Cl or $^{15}\text{NH}_4\text{Cl}$	

Table 2.1: Recipes for bacterial growth media and their components.

2.2 Methods

2.2.1 Molecular biology

2.2.1.1 Plasmid purification

Plasmids were purified from *E. coli* XL1-Blue LB o/n cultures using the Wizard® Plus SV Miniprep kit (Promega GmbH, Mannheim, Germany). The DNA was sequenced at GATC Biotech AG (Konstanz, Germany) and stored at $-20\text{ }^\circ\text{C}$. Pure plasmid concentration was determined by measuring the UV absorbance at 260 nm.

2.2.1.2 Heat shock transformation

A 100 μ l aliquot of cells were thawed on ice. Around 40 ng of the plasmid DNA was added to the cells and mixed gently. The mixture was incubated for 30 min on ice, heat shocked for 40 sec at 42 °C and immediately incubated on ice for 5 min. 1 ml of LB was added to the cells, followed by incubation for 1 h at 37 °C with 450 RPM. 50 μ l of the suspension was spread on LB agar plates containing kanamycin (Roth) (50 μ g/ml). Cells were allowed to grow o/n at 37 °C.

2.2.1.3 Glycerol stocks

75 μ l of an o/n LB culture of BL21 (DE3) cells were mixed with 25 μ l of sterile 80% glycerol (Roth). The mixture was gently vortexed, immediately flash frozen in liquid nitrogen and stored at -80 °C.

2.2.2 Recombinant expression and purification of A β ₁₋₄₀

The A β ₁₋₄₀ sequence was cloned into pET28a(+) vector (Appendix 5.1.1) containing a gene for kanamycin resistance. The construct was preceded by an N-terminal methionine, which does not alter the biochemical properties of the peptide^[382]. The A β ₁₋₄₀ peptide is expressed into inclusion bodies (IB) and purified following a washing protocol and reversed-phase HPLC (RP-HPLC) based on a protocol described previously^[383].

2.2.2.1 Expression of recombinant A β ₁₋₄₀

A β ₁₋₄₀ was recombinantly expressed in *E. coli* BL21 (DE3) cells. The cultures were grown in LB or M9 media supplemented with the desired isotopes for isotope-labeled peptide. All cultures were inoculated with a single colony picked from a plate containing BL21 (DE3) cells harboring the A β ₁₋₄₀ sequence prepared by heat shock transformation or from glycerol stocks. Bacterial cultures were grown in flasks using media supplemented with kanamycin (50 μ g/ml) at 37 °C and 150 RPM. Cell growth was monitored by measuring the OD₆₀₀. Protein expression was induced at an OD₆₀₀ of 0.7-0.8 by the addition of isopropyl- β -D-thiogalactopyranoside (IPTG) (SERVA) to a final concentration of 1 mM. After induction, the cultures were incubated for 4 h at 37 °C and 150 RPM.

2.2.2.1.1 Test expression

Prior to big scale expressions, test expressions were carried out at a smaller scale to screen for efficiently expressing colonies. 5-10 colonies were picked from the plates and added to 20 ml LB medium. The precultures were allowed to grow o/n. On the following day, appropriate amounts of cells were centrifuged 10 min at 4000 g and resuspended in unlabeled M9 medium to yield an OD₆₀₀ of 0.1. The cells were grown to an OD₆₀₀ of 0.7-0.8 and protein expression was induced for 4 h. Afterwards, cell pellets were collected by centrifuging 500 µl of each culture for 10 min at 21100 g. Protein expression was analyzed by tricine SDS-PAGE.

2.2.2.1.2 Main expression

200 ml LB medium was inoculated with 5 ml of the o/n LB culture of the colony showing the highest protein expression levels. Cells in LB medium were allowed to grow 5-6 h and used to inoculate the M9 o/n preculture. For this purpose, appropriate amounts of cells were centrifuged 10 min at 4000 g and resuspended in 300 ml M9 medium to yield an OD₆₀₀ of 0.1. The M9 precultures were allowed to grow o/n. On the following day, the cells were diluted in M9 to an OD₆₀₀ of approximately 0.1-0.2. The cells were grown to an OD₆₀₀ of 0.7-0.8 and protein expression was induced for 4 h. Before harvesting the cells, 500 µl of each culture was centrifuged for 10 min at 21100 g and used as a sample to check for protein expression by tricine SDS-PAGE.

2.2.2.1.3 Cell harvesting

The cells were harvested by centrifuging the cultures 30 min at 6000 RPM and 4 °C. The pellets were resuspended on ice in 20 mM Tris (Roth) pH 8.0. Subsequently, the cells were again centrifuged for 40 min at 6000 g and 4 °C. The cell pellets were immediately flash frozen in liquid nitrogen and stored at -80 °C until further use.

2.2.2.2 Purification of recombinant Aβ₁₋₄₀

Cell pellets were thawed on ice and pellets of 2 L culture were resuspended in 50 ml 20 mM Tris pH 8.0 supplemented with 20 µg/ml Deoxyribonuclease I (SERVA) and 1 cComplete EDTA-free Protease Inhibitor Cocktail tablet (Roche). The suspension was stirred for 20 min at RT. Cells were lysed by sonication on ice (30% amplitude, 1 s pulse on, 1 s pulse off, total sonication time 3-5 min). This step was repeated until cells were fully lysed. The lysate was centrifuged for 30 min at 24000 g and 4 °C and the supernatant was discarded. The pellet containing IB were washed three times,

once with buffer A (20 mM Tris pH 8.0 supplemented with 0.4% Triton X-100 (Roth)) and twice with buffer B (20 mM Tris pH 8.0). To wash the IB, the pellet was resuspended in 30 ml of buffer A by sonication on ice until no particles remained (typically 30% amplitude, 1 s pulse on, 1 s pulse off, total sonication time 2-3 min). The suspension was centrifuged for 15 min at 24000 g at 4 °C. The washing step was repeated twice with buffer B. IB were stored o/n at -80 °C. On the following day, IB were dissolved in 20 ml 8 M guanidinium hydrochloride (Roth) in 20 mM Tris pH 8.0 by sonication at RT (30% amplitude, 1 s pulse on, 1 s pulse off, total sonication time 1-2 min). The suspension was centrifuged at 24000 g for 20 min at 20 °C.

The IB extraction was further purified using an ÄKTApurifier system (GE Healthcare). The extract was loaded onto an ECO^{PLUS} HPLC column (TAC15/500, Kronlab Chromatography Technology, Dinslaken, Germany) home-packed with the reversed-phase separation material SOURCE 30RPC (GE Healthcare). The following buffers (filtered and degased) were used for the RP-HPLC runs:

Buffer A: 10 mM ammonia solution (Roth)

Buffer B: 80% acetonitrile (VWR), 0.3% trifluoroacetic acid (TFA) (Roth)

Initially, the column was equilibrated with 20% B for 5 column volumes (CV). The sample was loaded in 0.6 CV, and the column was washed for 4 CV, both at 20% B. This was followed by a gradient from 20% B to 60% B over 15 CV, in which A β ₁₋₄₀ usually elutes at around 42% B. Fractions of 11 ml were collected throughout the gradient. The concentration of B was increased to 100% in 1.5 CV and remained at 100% B for 1.5 CV until the completion of the run. A constant flow of 4 ml/min was used for the entire HPLC run. Protein elution was monitored by UV at 280 nm.

The protein content of the fractions was analyzed by SDS-PAGE. Fractions containing A β ₁₋₄₀ were gathered in glass tubes, flash frozen in liquid nitrogen, lyophilized for at least 3 days and stored at -80 °C until further use.

2.2.3 Protein analytical methods

2.2.3.1 Tricine sodium dodecyl sulfate polyacrylamide gel electrophoresis (SDS-PAGE)

In order to analyze protein content of samples, tricine SDS-PAGE was carried out according to the protocol described by Schagger^[384] (Table 2.2). This method is optimized for the separation of small (<30 kDa) and hydrophobic proteins.

Bacterial cell pellets from cultures were dissolved in 40 µl sample loading buffer (1X) by vigorous vortexing. For fractions collected in the RP-HPLC run, 30 µl of the fractions were mixed 10 µl of sample loading buffer (4X). The samples were incubated at 95 °C for 15 min with 800 RPM.

Around 5 µl of samples from bacterial cell pellet samples and 10 µl of samples from RP-HPLC fractions were loaded onto the gels. The Ultra-low Range Molecular Weight Marker (Sigma-Aldrich) was loaded onto the gels as a reference for molecular weight. Gels were run with a constant voltage of 100 V. After the run was completed, gels were incubated in fixing solution (20% ethanol (Roth), 10% acetic acid (Roth)) for 30 min, transferred to staining solution (0.025% Coomassie (Serva), 10% acetic acid) for at least 1 h and incubated in destaining solution (10% acetic acid).

Buffer / gel	Concentration / amount	Reagent
Gel buffer (3X) pH 8.45	3 M 1 M 0.3% (w/v)	Tris HCl (Roth) SDS (Serva)
16% gel (30 ml)	12 ml 10 ml 3 g 5 ml 200 µl 8 µl	40% Acrylamide (Serva) Gel buffer (3X) Glycerol (Roth) H ₂ O 10% (w/v) Ammonium persulfate (APS) (Sigma-Aldrich) Tetramethylethylenediamine (TEMED) (Roth)
loading buffer (4X)	200 mM 400 mM 8% 0.4% (w/v) 40%	Tris-HCl pH 6.8 (Roth) Dithiothreitol (DTT) (Roth) SDS Bromophenol blue (Sigma-Aldrich) Glycerol
Anode buffer (10X) pH 8.9	1 M 0.225 M	Tris HCl
Cathode buffer (10X) pH ~ 8.25	1 M 1 M 1%	Tris Tricine (Roth) SDS

Table 2.2: Recipes for tricine SDS-PAGE buffers and gels

2.2.3.2 Mass spectrometry

Lyophilized peptide was dissolved in 50% acetonitrile and analyzed by mass spectrometry. The analysis was carried out on a Thermo Finnigan LTQ-FT (ESI-ICR) spectrometer (Thermo Fisher Scientific, Inc., Waltham, USA), operating between 50-2000 m/z. Deconvolution of spectra was done using the program ProMass 2.8 (Thermo Fisher Scientific, Inc.).

2.2.3.3 Transmission electron microscopy (TEM)

Protein samples were prepared for TEM visualization by negative staining on a formvar coated grids stabilized with carbon film containing 300 meshes (Electron Microscopy Sciences, Hatfield, USA). The hydrophilization of the grids was enhanced by glow discharging in argon atmosphere for 30 s and 3 mA, to increase sample adsorption on the grids. 10 μ l of protein sample was placed on the grid and incubated for 60 s. The protein solution was carefully removed using filter paper. The grid was stained with 5 μ l 2% (w/v) uranyl acetate for 30 s. The stain was again removed using a filter paper. Images were recorded on a JEM-100CX transmission electron microscope (JEOL, Freising, Germany) at a magnification of 33000.

2.2.3.4 Dynamic light scattering (DLS)

The R3-GI peptide was dissolved to a concentration of 1 mM as described in Section 2.2.4.7 and subject to DLS measurement on a DynaPro NanoStar instrument (Wyatt Technology Europe GmbH, Dernbach, Germany). Three measurements consisting of 10 acquisitions each were carried out at 25 °C. Acquisition times of 60 s were used. The data was analyzed by the DYNAMICS V7 software (Wyatt Technology Europe GmbH). DLS measurements were carried out under the guidance of Dr. Philipp Baer (Technische Universität München, Chair of Biochemistry, Garching, Germany).

2.2.4 Sample preparation

2.2.4.1 NSAID stocks

Stocks of sulindac sulfide (Sigma-Aldrich) and sulindac sulfone (Sigma-Aldrich) were prepared in DMSO- d_6 at concentrations of 50 mM or 100 mM. The amount of the NSAID was determined by weight (error: 2.35 mM at a concentration of 50 mM).

Appropriate amounts of the NSAID stocks were added to aqueous solutions. The final concentration of DMSO in aqueous solutions typically did not exceed 1%.

2.2.4.2 Dissolving monomeric A β ₁₋₄₀

To avoid aggregation, it is crucial to obtain a purely monomeric solution free of nucleation seeds^[385]. Lyophilized A β ₁₋₄₀ was dissolved in 10 mM NaOH (Roth) in a glass vial^[386]. Appropriate amounts of NaOH were added until all particles were dissolved and a clear solution was obtained. In order to remove potential seeds for aggregation, the solution was centrifuged for 10 min at 21100 g. The supernatant was transferred to a new glass vial. The concentration of A β ₁₋₄₀ was determined by measuring the UV absorbance at 280 nm. The A β ₁₋₄₀ peptide was then diluted to the desired concentration (typically 50 μ M or 100 μ M) with 2-X buffer (100 mM Na-phosphate, 100 mM NaCl, pH 7.4). Monomeric A β ₁₋₄₀ was freshly prepared for all further steps.

2.2.4.3 Probing equilibrium of aggregated A β ₁₋₄₀

Monomeric A β ₁₋₄₀ at a concentration of 50 μ M was incubated with a 6-X molar excess of sulindac sulfide (300 μ M), which causes aggregation of a significant amount of the peptide. The sample was centrifuged for 30 min at 21100 g. The soluble and aggregated fractions were separated and the pellet was resuspended in 50 mM Na-phosphate, 50 mM NaCl, pH 7.4. 1D-¹H NMR experiments were carried out at all steps.

2.2.4.4 Oxidation assays of A β ₁₋₄₀ and NSAIDs

Monomeric or fibrillar A β ₁₋₄₀ or NSAIDs were incubated with H₂O₂ (Sigma-Aldrich), T-chloramine (Sigma-Aldrich), N-chlorosuccinimide (NCS) (Sigma-Aldrich) or N-bromosuccinimide (NBS) (Sigma-Aldrich) under the desired conditions in the dark and at RT in glass vials. The oxidation reactions of fibrils were terminated by centrifuging the fibrils for 10 min at 21100 g, and redissolving them in DMSO-d₆ supplemented with 25 mM ascorbic acid (Sigma-Aldrich) and 0.2% TFA, as described previously^[383]. To terminate oxidation of monomeric A β ₁₋₄₀, 25 mM ascorbic acid was added to the solution. As a reference, soluble monomeric A β ₁₋₄₀ was oxidized, lyophilized and redissolved as described for fibrillar A β ₁₋₄₀.

2.2.4.5 Preparation of A β ₁₋₄₀ fibrils

A β ₁₋₄₀ fibrils were prepared based on a protocol described earlier^[383]. Monomeric A β ₁₋₄₀ at a concentration of 50 μ M was incubated with 5-10% (w/w) seeds and incubated in glass vials under agitation until all monomeric material was fibrillized. Seeds were obtained from sonicated fibrils. The seeding step was repeated for 11 generations until fibril morphology was consistent.

2.2.4.6 Preparation of ISMs in combination with A β ₁₋₄₀

All peptide inhibitors were provided by the group of Prof. Dr. Aphrodite Kapurniotu (Technische Universität München, Group of Peptide Biochemistry, Weihenstephan, Germany). Sequences of all ISMs used are shown in Appendix 5.1.2. The peptides were synthetically produced and purified and provided in a film evaporated from hexafluoroisopropanol (HFIP). Measurements were performed on A β ₁₋₄₀ at a concentration of 20 μ M incubated with ISMs at 1-X (20 μ M) or 10-X (200 μ M) molar excesses. All steps were carried out on ice and in glass vials. The peptide inhibitors and A β ₁₋₄₀ (lyophilized) were dissolved in HFIP at 1 μ l/ μ g until a clear solution was obtained. The solutions containing ISMs were then transferred to the A β ₁₋₄₀ solution, and incubated for 30 min. The HFIP was evaporated by a weak flow of N₂ gas. The resulting film was dissolved in 500 μ l of 10 mM Na-phosphate pH 7.5 supplemented with 1 % HFIP and measured.

Alternatively, as a preparation of solid-state NMR samples, monomeric A β ₁₋₄₀ was prepared as described in Section 2.2.4.2, however using a stronger buffer (200 mM Na-P, 10 mM NaCl, pH 7.4). As indicated at the experimental figure captions, the final buffer contained 1% HFIP. The ISMs were dissolved in 50 μ l of 1mM HCl (10% final concentration), added to A β ₁₋₄₀ and measured immediately. For all ISMs and experimental setups, reference experiments using A β ₁₋₄₀ treated under the same conditions were carried out.

2.2.4.7 Preparation of the ISM R3-GI

The R3-GI peptide was synthetically produced and purified by the group of Prof. Dr. Aphrodite Kapurniotu (Technische Universität München) and provided in a film evaporated from HFIP. Peptides for DLS and NMR measurements including ¹H-¹⁵N and ¹H-¹³C HSQCs contained U-¹³C, ¹⁵N isotope labeling at A06, V10, L20 and S21. 450 μ l of 10 mM Na-phosphate pH 7.5 supplemented with 1 % HFIP was added to

the peptide, and incubated for several minutes. Concentrations of 500 μM and 1 mM were obtained for solution-state NMR and DLS measurements, respectively.

2.2.5 NMR spectroscopy

2.2.5.1 Data analysis

2.2.5.1.1 Plotting and resonance assignment of NMR data

1D spectra were plotted using nmrglue^[387] and 2D as well as strips from 3D spectra were plotted using Sparky^[388]. NMR spectra were assigned using CcpNmr Analysis 2.4.1^[389].

2.2.5.1.2 Peak integration

1D spectra were integrated using nmrglue and 2D spectra were integrated using CcpNmr. A β_{1-40} amide signals were integrated in the region between 7.65 ppm to 8.5 ppm in 1D-¹H spectra.

2.2.5.1.3 Prediction of secondary structures

Secondary structural elements were predicted by TALOS+^[24], and by secondary chemical shift $\Delta\delta\text{C}\alpha$ (ppm) and $\Delta\delta\text{C}\alpha-\Delta\delta\text{C}\beta$ (ppm).

Secondary chemical shifts were calculated using the following equation:

$$\Delta\delta C = \delta C_{observed} - \delta C_{random\ coil}$$

Random coil values were taken from Wishart *et al*^[390]. The values are specified within a range of ± 0.7 ppm ($\Delta\delta\text{C}\alpha$) and ± 1.4 ppm ($\Delta\delta\text{C}\alpha-\Delta\delta\text{C}\beta$). Hence, $\Delta\delta$ values within this range are considered insignificant and are indicated by a gray bar in the data.

Negative values for $\Delta\delta\text{C}\alpha$ (ppm) and $\Delta\delta\text{C}\alpha-\Delta\delta\text{C}\beta$ (ppm) indicate β -strand and positive values indicate α -helical structural elements. At least 4 consecutive positive values are required to define a helix and at least 3 consecutive negative values are required to define a β -strand.

2.2.5.1.4 Chemical shift perturbations (CSPs)

For solution-state NMR studies, CSPs are extracted from ^1H and ^{15}N chemical shifts of sulindac sulfide (sul) incubated A β and reference A β (ref) using the following equation:

$$\Delta\delta = \frac{1}{2} \left[(\delta H_{sul} - \delta H_{ref})^2 + \left(\frac{1}{10} (\delta N_{sul} - \delta N_{ref}) \right)^2 \right]^{1/2}$$

For solid-state NMR studies, CSPs are extracted from ^{13}C and ^{15}N chemical shifts of sulindac sulfide (sul) incubated A β and reference A β (ref) using the following equations:

$$\Delta\delta_C = \left[(\delta C_{sul} - \delta C_{ref})^2 \right]^{1/2} \quad \text{and} \quad \Delta\delta_N = \left[\left(\frac{2}{5} (\delta N_{sul} - \delta N_{ref}) \right)^2 \right]^{1/2}$$

The following equation was used for calculating CSPs of backbone resonances:

$$\Delta\delta = \frac{1}{3} \left[(\delta C\alpha_{sul} - \delta C\alpha_{ref})^2 + (\delta CO_{sul} - \delta CO_{ref})^2 + \left(\frac{2}{5} (\delta N_{sul} - \delta N_{ref}) \right)^2 \right]^{1/2}$$

2.2.5.2 Solution-state NMR sample preparations

All samples were freshly prepared. For titrations, the molecules of interest were added directly to the NMR tube (DURAN Group GmbH, Wertheim/Main, Germany) and the samples were mixed gently by inversion and measured immediately. Samples contained 10% D₂O.

2.2.5.3 Solution-state NMR measurements

Solution-state NMR experiments were recorded Avance III spectrometers operating at ^1H Larmor frequencies of 900, 750, 600 and 500 MHz. The spectrometers are equipped with cryogenic (except for the 750 MHz) triple resonance gradient probes ($^1\text{H}/^{13}\text{C}/^{15}\text{N}$). The ^1H CS scale was referenced by setting the signal of 2,2-dimethyl-2-silapentane-5-sulfonate (DSS) to 0.00 ppm, and ^{13}C as well as ^{15}N CS scales were referenced according to their frequency ratios^[391]. All measurements were carried out at 277 K, unless stated otherwise.

All 1D- ^1H spectra contained a watergate pulse sequence for solvent suppression^[392]. 2D ^1H - ^{15}N correlations were recorded as SOFAST heteronuclear multiple quantum coherence (HMQC) experiments^[393]. 2D ^1H - ^{13}C correlations were recorded as HSQC experiments employing constant-time homonuclear ^{13}C decoupling^[394]. Band-selective excitation short-transient (BEST) pulse sequence versions were recorded for 3D assignment spectra HNCA, HNC O ^[395] and HNCACB^[396]. In addition, sequential assignment was achieved by a 3D HNCANNH spectrum^[397]. 2D ^1H homonuclear NOESYs^[398] were recorded using a watergate pulse sequence for solvent suppression.

2.2.5.4 Solid-state NMR sample preparations

Approximately 12-15 mg of $\text{A}\beta_{1-40}$ was used in all solid-state NMR studies. Samples packed into rotors were stored at 4 °C.

2.2.5.4.1 Packing of rotors

Aggregated material was centrifuged into NMR MAS rotors (Bruker BioSpin). The rotor packing step varied depending on the sample volume. For volumes <20 ml, 2 ml aliquots were pelleted for 15 min at 21100 g. The pellets were resuspended in 200 μl of buffer, and spun into the rotor for 30 min at 21100 g. For larger sample volumes, ~ 20 ml were sedimented into the NMR rotor^[399] for 1 h at 28000 RPM using a filling tool (Bruker BioSpin, Figure 2.1) and a L-100 XP Ultracentrifuge and a SW 32 Ti rotor (Beckman Coulter GmbH, Krefeld, Germany). The supernatant was carefully removed after each step and replaced by another ~ 20 ml of sample material.

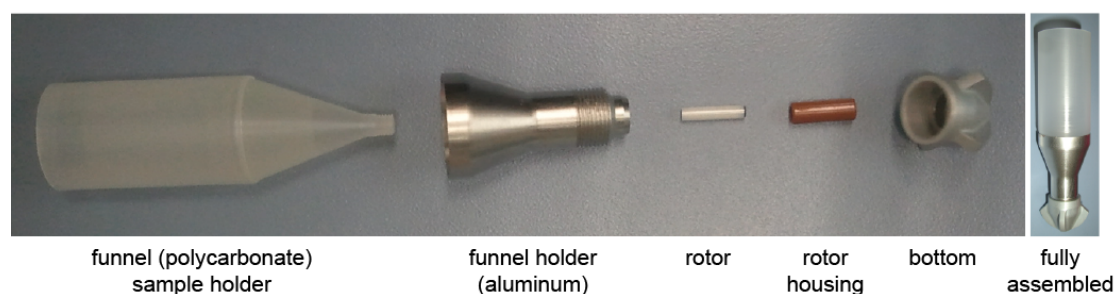


Figure 2.1: MAS rotor filling tool for ultracentrifuges. The tools were kindly provided by David Osen (Bruker BioSpin).

2.2.5.4.2 Sulindac sulfide incubated A β ₁₋₄₀ fibrils

50 μ M A β ₁₋₄₀ fibrils were incubated with a 5-fold molar excess of sulindac sulfide (250 μ M) and 1% DMSO-d₆ for 1 h at RT in a glass vial under quiescent conditions. A reference fibril sample was incubated with 1% DMSO-d₆ under the same conditions. After the incubation, the sulindac sulfide incubated fibrils were packed into a 3.2 mm rotor, and the reference fibrils were packed into a 4.0 mm rotor.

2.2.5.4.3 Sulindac sulfide induced A β ₁₋₄₀ aggregates

Monomeric A β ₁₋₄₀ was dissolved to a concentration of 100 μ M and incubated in the presence of a 5-fold (500 μ M) and a 10-fold (1 mM) molar excess of sulindac sulfide and 1% DMSO-d₆ in a glass vial. The presence of sulindac sulfide causes the A β ₁₋₄₀ peptide to precipitate out of solution. The concentration of monomeric A β ₁₋₄₀ was monitored by centrifuging a 200 μ l sample for 10 min at 21100 g and measuring the UV absorbance at 280 nm of the supernatant. After 24 h only negligible amounts of A β ₁₋₄₀ were present as soluble peptide, and the aggregated samples were packed into a 4.0 mm rotor (5-fold molar excess of sulindac sulfide) and a 3.2 mm rotor (10-fold molar excess of sulindac sulfide). As a reference sample, 100 μ M monomeric A β ₁₋₄₀ was incubated with 1% DMSO-d₆ under the same conditions. The incubation time was extended to 8 days, as DMSO-d₆ is less efficient in precipitating A β ₁₋₄₀. The sample was packed into a 4.0 mm rotor. Crystalline sulindac sulfide was packed into a 3.2 mm rotor as a reference.

2.2.5.4.4 K3L3K3-GI induced A β ₁₋₄₀ aggregates

A β ₁₋₄₀ at a concentration of 20 μ M was incubated with a 1.23-X molar excess of K3L3K3-GI (10 mg). All steps were carried out on ice and in glass vials. Monomeric A β ₁₋₄₀ was prepared as described in Section 2.2.4.2, however using a stronger buffer (200 mM Na-P, 10 mM NaCl, pH 7.4) supplemented with 1% HFIP. The peptide inhibitor K3L3K3-GI was dissolved in 13 ml of 1 mM HCl (10% final concentration), added to A β ₁₋₄₀ and incubated at 4 °C for 14 days. The sample was then sedimented into a 3.2 mm rotor.

2.2.5.5 MAS Solid-state NMR measurements

The magic angle of MAS solid-state NMR spectrometers was adjusted using KBr. ¹³C and ¹⁵N chemical shift scales were referenced to external standards. The ¹³C CS scale was calibrated by referencing the stronger low field signal of adamantane to

38.48 ppm^[400]. The ¹⁵N CS scale was calibrated by referencing the low field methionine signal of the MLF peptide to 125.5 ppm^[401].

Conventional 2D ¹³C-¹³C PDSO and ¹³C-¹⁵N TEDOR experiments, as well as assignment spectra of sulindac sulfide incubated fibrils were measured on an Avance wide bore spectrometer with a ¹H Larmor frequency of 700 MHz. Measurements were performed using a 3.2 mm and a 4.0 mm triple resonance probe (¹H/¹³C/¹⁵N). Spectra of A β ₁₋₄₀ aggregates induced by sulindac sulfide at a 5-X molar excess and of reference aggregates were recorded on a spectrometer at a ¹H Larmor frequency of 600 MHz using a 4.0 mm triple resonance MAS probe (¹H/¹³C/¹⁵N). MAS solid-state NMR experiments involving ¹⁹F nuclei were recorded on an Avance III wide bore spectrometer operating at a ¹H Larmor frequency of 600 MHz equipped with a 3.2 mm triple resonance (¹H/¹³C/¹⁹F) CP MAS probe under the guidance of Dr. Gerhard Althoff-Ospelt (Bruker BioSpin). Measurements for other samples and other experiments including the ¹³C-¹⁵N TEDOR detecting the D23-K28 A β ₁₋₄₀ salt bridge were performed on an Avance III standard-bore spectrometer operating at a ¹H Larmor frequency of 750 MHz equipped with an E^{free} 3.2 mm triple resonance (¹H/¹³C/¹⁵N) probe (Bruker BioSpin). MAS rotation frequencies and temperatures during measurements are indicated in figure legends of spectra.

2.2.5.5.1 Conventional 2D and 3D assignment spectra

For conventional 2D ¹³C-¹³C and ¹³C-¹⁵N correlations, the initial magnetization transfer from ¹H to ¹³C was achieved by ramped (70-100%) CP on the ¹H channel^[402]. In 2D experiments, homonuclear ¹³C-¹³C mixing was facilitated by PDSO^[40] with mixing times of 50 ms or 200 ms and ¹³C-¹⁵N magnetization transfer was achieved by TEDOR. The 3D assignment spectra NCACX and NCOCX^[403] were recorded in two different ways. In the first version, magnetization was transferred from ¹H to ¹³C by ramped (70-100%) CP, followed by a TEDOR from ¹³C to ¹⁵N, CS evolution (t_1), and a selective TEDOR back to ¹³C, followed again by CS evolution (t_2). In the second version, magnetization was initially transferred from ¹H to ¹⁵N by ramped (70-100%) CP (t_1) followed by a second specific ramped (100%-90%) CP to ¹³C (t_2). In both cases, the magnetization from ¹⁵N to ¹³C was specifically transferred to C α of residue *i* in NCACX spectra and to CO of residue *i*-1 in NCOCX spectra. This was followed by a homonuclear DARR recoupling scheme^[41] (t_3) with mixing times of 20 ms or 50 ms.

2.2.5.5.2 Detecting the A β salt bridge

3D TEDOR experiments (Appendix 5.3) based on the pulse sequence published by Jaroniec *et al.*^[39] were carried out to detect the D23-K28 salt bridge of A β ^[404]. Magnetization was initially transferred from ^1H to ^{13}C by ramped (70-100%) CP on the ^1H channel. The two REDOR blocks reintroduce dipolar couplings between ^{13}C and ^{15}N spins by rotor-synchronized π -pulses. The first REDOR step transfers magnetization from ^{13}C to ^{15}N , followed by t_1 and the second REDOR, which transfers magnetization back to ^{13}C for detection. This yielded a 2D ^{13}C - ^{15}N correlation spectrum. Experiments were recorded with TEDOR mixing times of 7.72 ms and 15.72 ms.

2.2.5.5.3 Detecting ^{13}C - ^{19}F dipolar couplings in A β aggregated by sulindac sulfide

In order to detect ^{13}C atoms of A β in vicinity of sulindac sulfide ^{19}F atom in A β aggregates induced by sulindac sulfide, 3D TEDOR experiments similar as described for the detection of the D23-K28 salt bridge were carried out (Appendix 5.3). Magnetization was initially transferred from ^1H to ^{13}C by ramped (90-100%) CP on the ^1H channel. Magnetization was then transferred to the ^{19}F channel, instead of the ^{15}N channel, to reintroduce ^{13}C - ^{19}F dipolar couplings. Experiments were recorded in 1D mode, hence, no ^{19}F evolution time was used. TEDOR mixing times of 0.65, 1.29, 2.58, 5.16 and 7.74 ms were employed. As the spectra do not exclude intramolecular natural abundance ^{13}C - ^{19}F dipolar couplings of sulindac sulfide, reference experiments were recorded for crystalline sulindac sulfide. Reference spectra were subtracted from the spectra of A β aggregated by sulindac sulfide with a factor 0.5. This factor was determined by estimating the S/N in both samples. Signals at 104.9 ppm and 110.8 ppm were used for referencing, as they do not overlap with A β and must thus arise due to intramolecular ^{13}C - ^{19}F dipolar couplings.

2.2.5.5.4 Detecting ^{13}C - ^{19}F dipolar couplings in A β fibrils

REDOR experiments were recorded to detect ^{13}C atoms of A β in vicinity to sulindac sulfide ^{19}F atom in A β fibrils^[404] (Appendix 5.3). Magnetization was initially transferred from ^1H to ^{13}C by ramped (90-100%) CP on the ^1H channel. This was followed by a REDOR block reintroducing ^{13}C - ^{19}F dipolar couplings, an evolution time on ^{13}C (t_1) and a PSDS mixing scheme. ^{13}C atoms will be dephased due to dipolar coupling to ^{19}F . Reference experiments were recorded without dipolar recoupling and REDOR spectra were subtracted from reference spectra to visualize dephased signals. This

yielded a 2D ^{13}C - ^{13}C correlation spectrum containing only diagonal peaks for aliphatic resonances. Hence, spectra are displayed as 1D projections. REDOR mixing times of 1.1, 2.2 and 4.4 ms were used.

2.2.6 Structure calculation

The solution-state NMR structure of R3-GI was determined using ARIA2^[381]. The N-methylations of G17 and I19 were not taken into account for the structure calculations. Peaks and chemical shifts from the homonuclear 2D ^1H - ^1H NOESY experiments were used as restraints for calculation of the dimeric and pentameric structures. In addition, ambiguous distance restraints and torsion angles as generated by CcpNmr were used for the calculation of the monomeric structures. Symmetric homodimers were calculated with symmetry type C2. All structure calculations were run for 8 iterations, generating 20 lowest energy structures each. Structures from the last iteration were water refined, generating 10 lowest energy structures. An ensemble of these 10 structures represents the final NMR structure.

3. Results

3.1 Expression, purification and characterization of monomeric A β ₁₋₄₀

The A β ₁₋₄₀ peptide was recombinantly expressed and purified via RP-HPLC (Figure 3.1a). The purification protocol produced a yield of around 10-12 mg per 4 L of ¹⁵N, ¹³C labeled cultures.

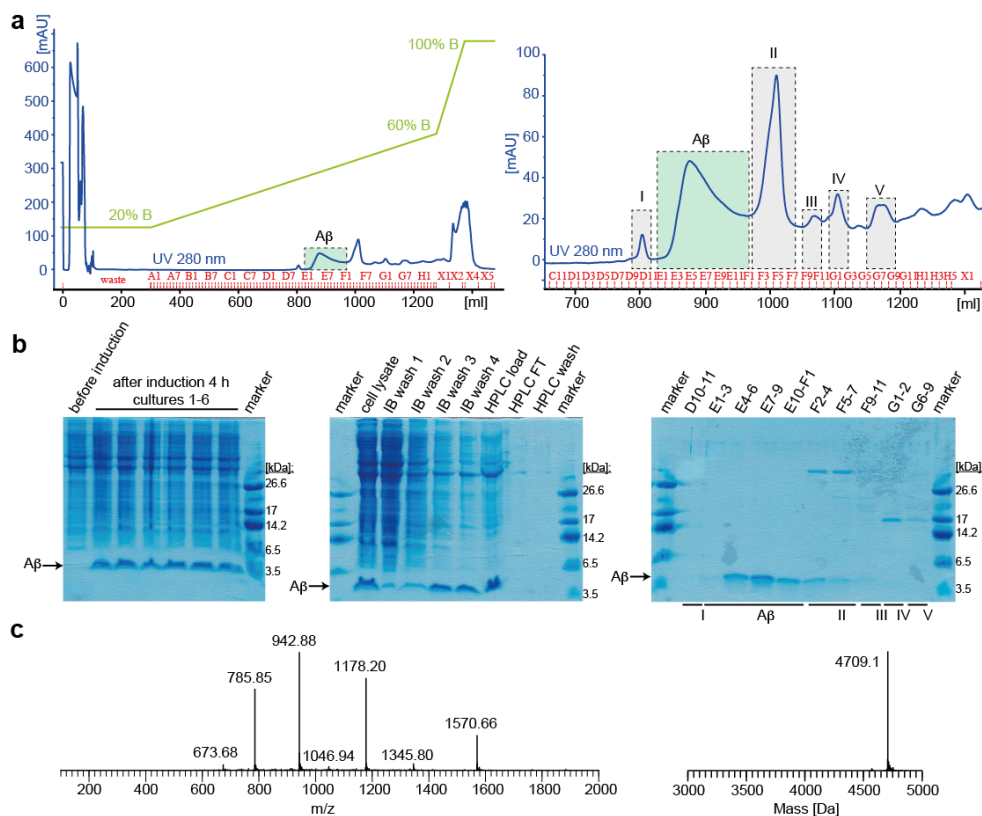


Figure 3.1: Expression and purification of A β ₁₋₄₀. (a) Typical RP-HPLC run for the purification of U-¹⁵N, ¹³C labeled A β ₁₋₄₀. The chromatogram at UV 280 nm is shown in blue and the gradient of %B is shown in light green. The chromatogram is shown enlarged (right) to illustrate elution of A β ₁₋₄₀. (b) Representative gels of A β ₁₋₄₀ expression (left), supernatant after washing and centrifuging of IB (center) and the fractions collected from the RP-HPLC run (center and right). (c) Mass spectrometric analysis of purified A β ₁₋₄₀ yields a mass of 4709.1 Da after spectral convolution, which is close to the theoretical mass of 4714.0 Da of U-¹⁵N, ¹³C labeled A β ₁₋₄₀.

The expression and purity of the recombinantly produced peptide was controlled by tricine SDS-PAGE (Figure 3.1b). Elution fractions showing high purity on the SDS-PAGE gels were pooled, lyophilized and analyzed by mass spectrometry (Figure 3.1c). A single peak was obtained in the mass spectrometric analysis at a peptide mass of 4709.1 Da for U- ^{15}N , ^{13}C labeled $\text{A}\beta_{1-40}$ (theoretical mass = 4714.0 Da). (Figure 3.1c)

The monomeric entity of $\text{A}\beta_{1-40}$ gives rise to well defined solution-state NMR spectra of a typical random coil peptide as shown for the ^1H - ^{15}N HMQC (Figure 3.2a) and ^1H - ^{13}C HSQC (Figure 3.3). The lack of dispersion in the ^1H dimension of the ^1H - ^{15}N HMQC demonstrates the unstructured character of $\text{A}\beta_{1-40}$. Backbone and side chain resonances of the peptide were assigned, although no backbone assignments were found for D01, H06 and H14, and some of the assignments in the side chains are ambiguous. All assigned $\text{A}\beta_{1-40}$ resonances are listed in Appendix 5.2.1 and published by Mainz *et al*.^[405]. Sequential assignment was achieved by analysis of the 3D assignment spectra HNCA, HNCACB, HNCOC and HNCANNH for backbone resonances, and HNHA and HCCH-TOCSY for side chain resonances.

It is well known that the monomeric $\text{A}\beta_{1-40}$ peptide adopts a random coil conformation in solution^[239]. The obtained chemical shifts were subject to secondary structure analysis (Figure 3.2b). Analysis by TALOS+ demonstrates that the major part of the peptide mostly exists in random coil conformation. This is further supported by secondary chemical shifts $\Delta\delta\text{C}\alpha$ (ppm) and $\Delta\delta\text{C}\alpha$ - $\Delta\delta\text{C}\beta$ (ppm). Several residues (Q15-F19) show a tendency for the formation of β -strands. These findings may indicate the presence of transient intermediates, as these residues are part of the hydrophobic core^[238].

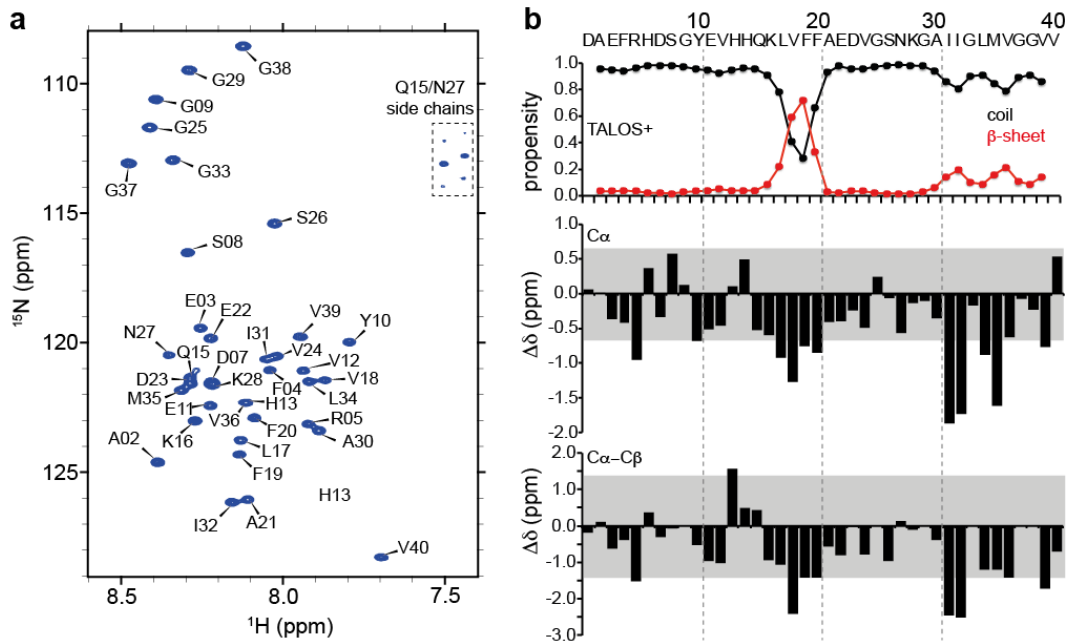


Figure 3.2: Solution-state NMR analysis of monomeric $\text{A}\beta_{1-40}$. (a) ^1H - ^{15}N HMQC of $\text{A}\beta_{1-40}$ at a concentration of 50 μM , recorded at 277 K and 600 MHz. (b) Secondary structural elements as predicted by TALOS+ (top panel), and secondary chemical shifts $\Delta\delta_{\text{C}\alpha}$ (ppm) and $\Delta\delta_{\text{C}\alpha} - \Delta\delta_{\text{C}\beta}$ (ppm) (lower panels). The propensities for the formation of random coil (black) and β -sheet (red) elements are shown for TALOS+. No significant propensities for α -helical elements are observed throughout the sequence. The gray bar indicates a range of ± 0.7 ppm ($\Delta\delta_{\text{C}\alpha}$) and ± 1.4 ppm ($\Delta\delta_{\text{C}\alpha} - \Delta\delta_{\text{C}\beta}$), as this is the range of random coil CS specified by Wishart *et al.*^[390]. Values within this range are considered insignificant.

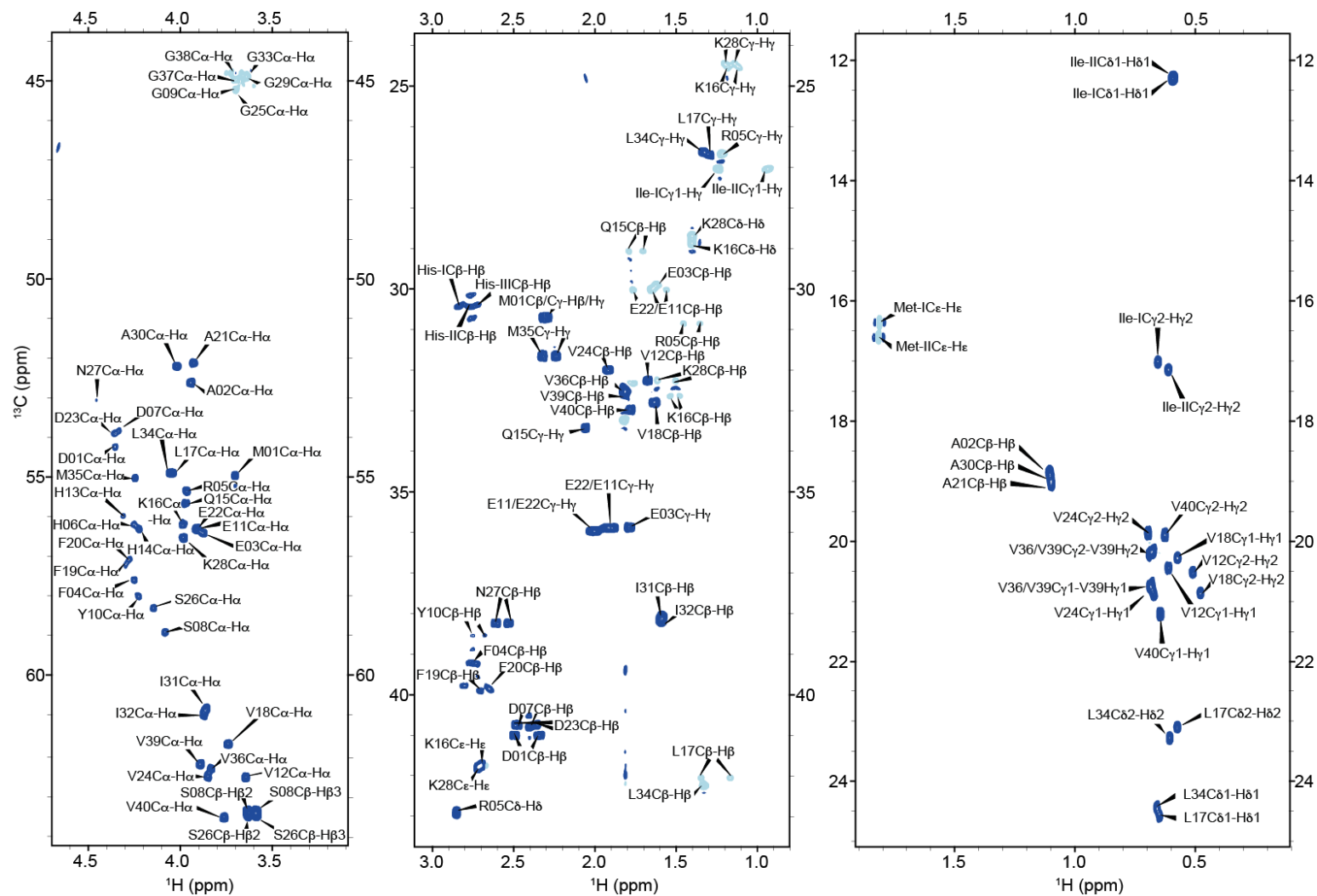


Figure 3.3: Solution-state NMR ^1H - ^{13}C HSQC of monomeric $\text{A}\beta_{1-40}$. The sample concentration of 50 μM was used, and spectra were recorded at 277 K and 600 MHz. Positive contours are displayed in dark blue and negative contours are displayed in light blue.

3.2 The effect of sulindac sulfide on aggregation and biochemical properties of monomeric A β ₁₋₄₀

The γ -secretase inhibitor (GSM) sulindac sulfide has been demonstrated to influence A β properties in various aggregation states^[322,333,334]. We use solution-state NMR spectroscopy to determine the impact of sulindac sulfide on monomeric A β ₁₋₄₀. A monomeric solution, free of aggregation seeds, was titrated with sulindac sulfide and peptide resonances were monitored in 1D-¹H and 2D ¹H-¹⁵N HMQC spectra. In the presence of sulindac sulfide, A β ₁₋₄₀ aggregates rapidly out of solution in a concentration dependent manner (Figure 3.4a). The fraction of aggregated peptide is dependent on the absolute concentration of sulindac sulfide, not the molar excess or A β ₁₋₄₀ starting concentration. For instance, at 100 μ M sulindac sulfide, 60.8% (30.4 μ M), 61.7% (61.7 μ M) and 69% (138 μ M) of A β ₁₋₄₀ remained soluble at starting concentrations of 50 μ M, 100 μ M and 200 μ M, respectively.

By contrast, when titrating A β ₁₋₄₀ with the oxidized derivative sulindac sulfone in the same conditions, no peptide aggregation is observed (Figure 3.4b). Even at a 20-X molar excess, 97% (48.5 μ M) of A β ₁₋₄₀ remains soluble, compared to 2% of sulindac sulfide (1.01 μ M) at the same concentration. The differences in aggregation behavior caused by the two NSAIDs are further demonstrated in 1D-¹H spectra shown above ¹H-¹⁵N HMQCs of monomeric A β incubated with NSAIDs (Figure 3.4c).

A β ₁₋₄₀ precipitation is uniform throughout the peptide sequence, as all residues aggregate at similar rates, as observed for backbone (Figure 3.4d) and side chain signals (Figure 3.4e). However, no CSPs are observed in the presence of the NSAIDs for backbone (Figure 3.4c, f) and side chain resonances (data not shown). At 5-X molar excesses of the NSAIDs, CSPs for all residues are negligible (<0.007 ppm).

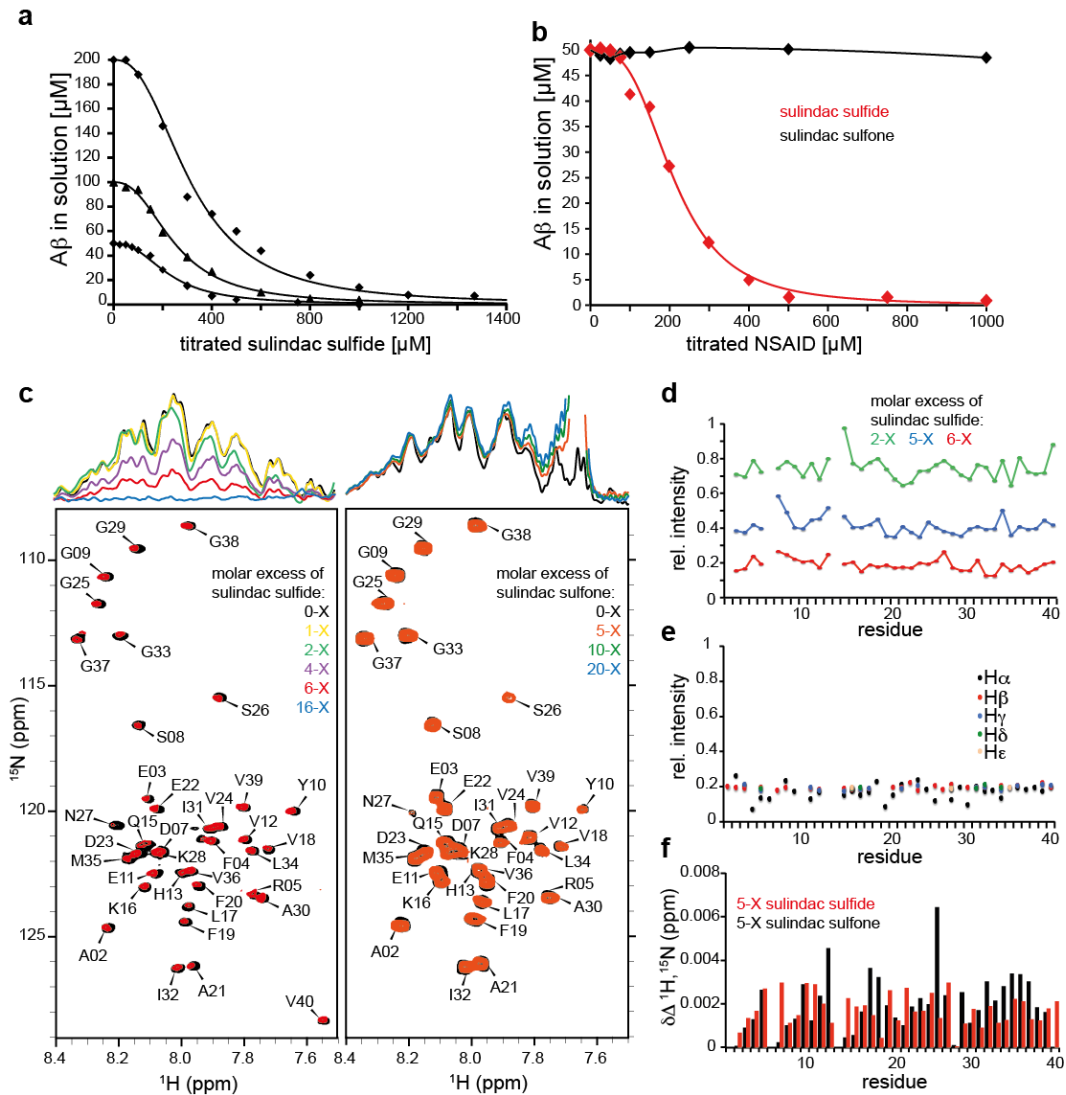


Figure 3.4: The effect of NSAIDs on monomeric Aβ by solution-state NMR. (a) Solubility of Aβ₁₋₄₀ as a function of the amount of sulindac sulfide in the sample. (b) Solubility of Aβ₁₋₄₀ as a function of the amount of sulindac sulfide and sulindac sulfone in the sample. (c) ¹H-¹⁵N HMQC of 50 μM Aβ₁₋₄₀ in the presence of a 6-fold molar excess of sulindac sulfide (left) and a 5-fold molar excess of sulindac sulfone (right). Corresponding 1D-¹H spectra are shown above the 2Ds at increasing concentrations of the NSAIDs to illustrate the enhanced signal loss in the presence of sulindac sulfide compared to sulindac sulfone. (d-e) Relative residue specific signal intensities extracted from peaks in the ¹H-¹⁵N HMQC (d) and ¹H-¹³C HSQC (e) of 50 μM Aβ₁₋₄₀ in the presence of increasing concentrations of sulindac sulfide. (f) Residue specific CSPs Δδ (ppm) for ¹H and ¹⁵N as observed for 50 μM Aβ₁₋₄₀ in the presence of a 5-fold molar excess of sulindac sulfide and sulindac sulfone. All experiments were recorded at 277 K and 750 MHz.

As the NSAIDs were titrated from a DMSO- d_6 stock, residual DMSO- d_6 was found in nearly all NMR samples (usually $\leq 1\%$). Titrations of DMSO- d_6 to $A\beta_{1-40}$ were carried out to exclude effects of DMSO- d_6 on the peptide (Figure 3.5a-b). 1H - ^{15}N HMQCs demonstrate that DMSO- d_6 concentrations up to 2% do not affect $A\beta_{1-40}$ CS, although CSPs are observed at higher concentrations of 8% mainly for S08-V12, several residues between V18-N27 and the C-terminal V40 (Figure 3.5a). Similarly, the influence of DMSO- d_6 on $A\beta_{1-40}$ solubility is negligible up to a concentration of 4% (Figure 3.5b). As these critical DMSO- d_6 concentrations are higher than the actual concentration used in the experiments, side effects of DMSO- d_6 were not taken into account in further experimental setups.

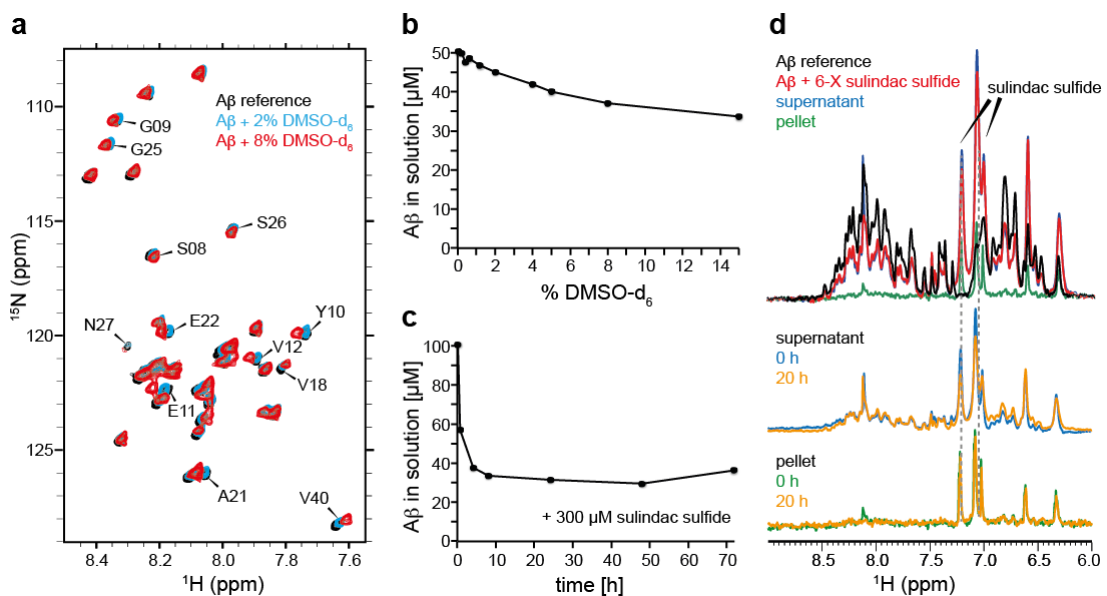


Figure 3.5: Properties of monomeric $A\beta$ in the presence of sulindac sulfide and DMSO- d_6 . (a) 1H - ^{15}N HMQC of 50 μ M $A\beta_{1-40}$ in the presence of increasing concentrations of DMSO- d_6 . (b) Solubility of $A\beta_{1-40}$ as a function of DMSO- d_6 . (c) Solubility of $A\beta_{1-40}$ in the presence of a 3-X molar excess of sulindac sulfide as a function of time. (d) 1D- 1H spectra of 50 μ M $A\beta_{1-40}$ in the absence and presence of a 6-X molar excess of sulindac sulfide, and after separation (and resuspension) of the aggregated (pellet) and soluble (supernatant) fraction measured immediately and after 20 h. All experiments were recorded at 277 K and 750 MHz.

A time-follow experiment shows that upon the addition of sulindac sulfide, the aggregation reaction of $A\beta_{1-40}$ occurs rapidly and continues at a slower rate for 4 h (Figure 3.5c). 300 μM of sulindac sulfide reduces $A\beta_{1-40}$ solubility to 56.5% immediately, and to a stable state of 37.1% after 4 h. After 72 h, $A\beta_{1-40}$ solubility remained at 35.9%. Hence, sulindac sulfide induced $A\beta_{1-40}$ aggregation is slightly time dependent but will reach equilibrium eventually. The resulting aggregates are persistent and irreversible (Figure 3.5d). Sulindac sulfide induced $A\beta_{1-40}$ aggregates were separated from the soluble fractions and redissolved in buffer. No peptide was resolubilized, even after 20 h incubation. Similarly, the fraction containing soluble peptide did not produce further aggregates, even after 20 h incubation. However, both fractions contain sulindac sulfide, as can be seen from the presence of two characteristic signals.

Small phenolic molecules such as sulindac sulfide form colloidal aggregates in aqueous solutions^[338]. To assess the solubility of the NSAIDs, we monitored their characteristic signals in 1D-¹H spectra (Figure 3.6a-b). At increasing concentrations, sulindac sulfide signal are attenuated and broadened (Figure 3.6a), indicating the formation of larger assemblies and chemical exchange. By contrast, sulindac sulfone signals increase according to the concentration present in the sample (Figure 3.6b). The solubility of sulindac sulfide is impaired at concentrations above 300 μM in buffer (Figure 3.6c). The presence of $A\beta_{1-40}$ hampers sulindac sulfide solubility even further, and the NSAID precipitates at concentrations above 100 μM . Therefore, $A\beta_{1-40}$ and sulindac sulfide must aggregate into complexes. In accordance with the report that sulindac sulfone is not prone to aggregating into colloids^[335], its 1D-¹H NMR spectrum demonstrates that it is soluble even at high concentration. The monitored signal intensities correlate with the amount titrated into the sample (Figure 3.6d). The presence of $A\beta_{1-40}$ has no effect on sulindac sulfone signals when compared to the buffer control.

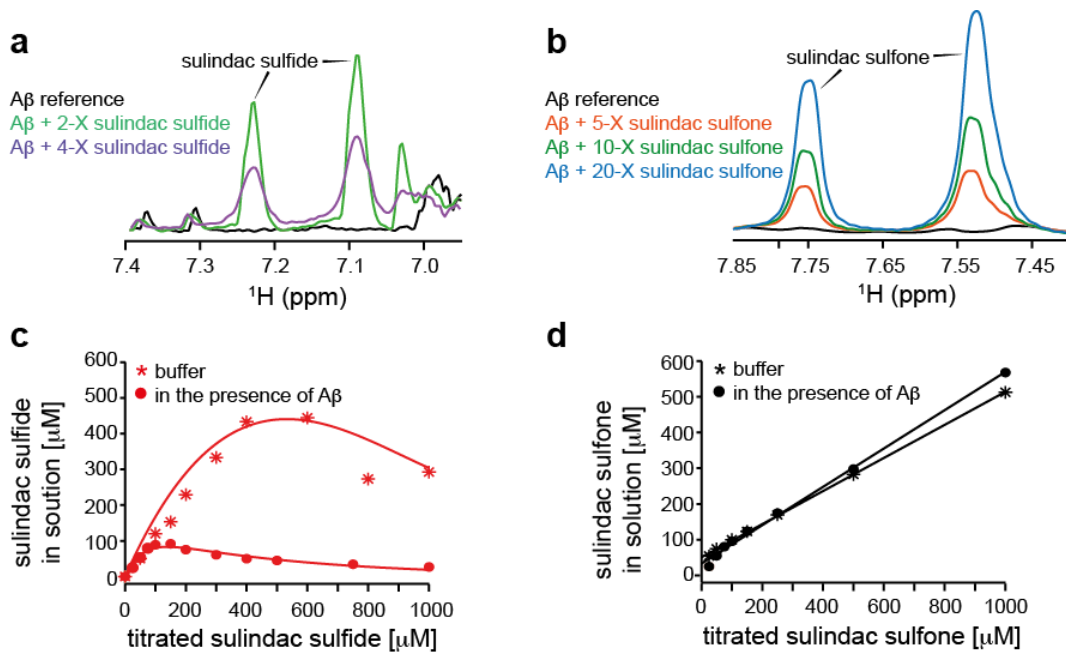


Figure 3.6: Solubility of NSAIDs analyzed by solution-state NMR. Solution-state NMR spectra of characteristic sulindac sulfide (a) and sulindac sulfone (b) signals at increasing concentrations of the NSAIDs. The spectra were recorded in the presence 50 μM Aβ₁₋₄₀. Signals at 7.22 and 7.08 ppm for sulindac sulfide (c) and signals at 7.75 and 7.52 ppm for sulindac sulfone (d) were integrated in the presence (*) and absence (•) of 50 μM Aβ₁₋₄₀ to determine solubilities and plotted as a function of NSAID titrated into the sample. All experiments were recorded at 277 K and 750 MHz.

Morphological and biochemical characteristics of sulindac sulfide induced Aβ₁₋₄₂ aggregates were analyzed by TEM, SEC and MTT assays by Dr. Cristian Barucker in the group of Prof. Dr. Gerd Multhaup (McGill University, Department of Pharmacology and Therapeutics, Montreal, Canada). As demonstrated by TEM and MPL measurements, Aβ aggregated in the presence of sulindac sulfide seems to form oligomeric complexes, which are ca. 20 nm larger in size than their counterparts aggregated by DMSO (Figure 3.7a). Specifically, sulindac sulfide shifts the population of 4-6mers to higher n oligomers consisting of 16-20 subunits as revealed by size exclusion chromatography (SEC) (Figure 3.7b). This effect is more pronounced after 8 h. There is strong evidence that small oligomers constitute the neurotoxic Aβ species^[205,209]. Indeed, the larger oligomers formed in the presence of sulindac sulfide exert a decreased toxicity on neuron cells compared to the smaller aggregates formed by DMSO (Figure 3.7c). This protective effect is even more pronounced after 8 h. Therefore, the reduction in neurotoxicity correlates with the increased population of high-n oligomers after a longer incubation time, as shown by SEC.

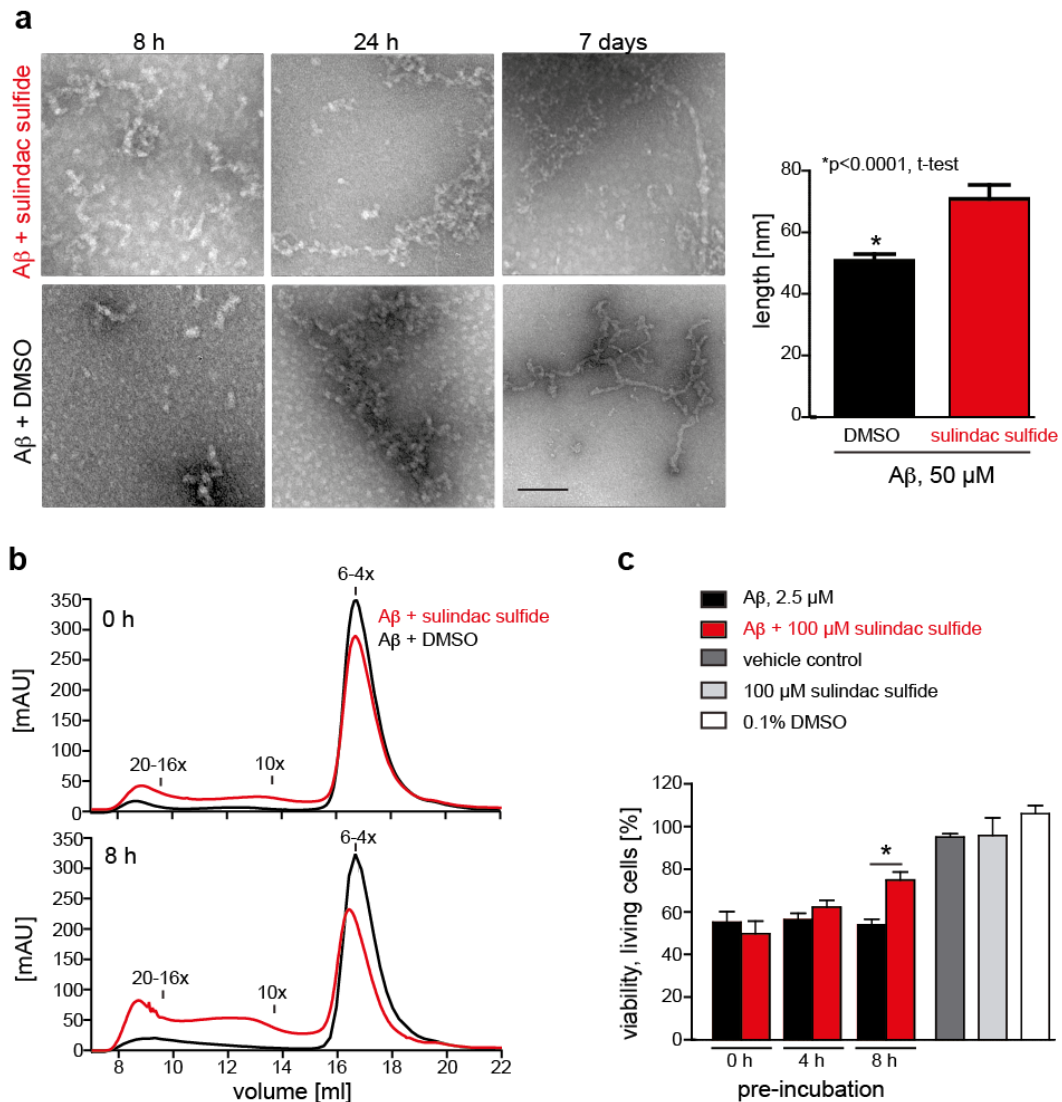


Figure 3.7: The effect of sulindac sulfide on morphological and neurotoxic properties of A β . All experiments were performed in the lab of Prof. Dr. Gerd Multhaup by Dr. Christian Barucker (McGill University). (a) TEM images and mass-per-length measurements of A β ₁₋₄₀ in the presence of sulindac sulfide or DMSO after 8 h, 24 h and 7 days. * $p < 0.01$; black scale bar = 100 nm. (b) SEC of A β ₁₋₄₂ aggregates induced by sulindac sulfide (red) or DMSO (black) after 0 h and 8 h incubation. (c) MTT assay of neuron cells in the presence of A β ₁₋₄₂ incubated in the presence of sulindac sulfide (red) or DMSO (black) for 0 h, 4 h and 8 h.

3.3 Solid-state NMR investigations of A β ₁₋₄₀ aggregates induced by sulindac sulfide

A β ₁₋₄₀ aggregates induced by sulindac sulfide are too large to be observable by solution-state NMR. In order to investigate structural characteristics of the aggregates, we carried out MAS solid-state NMR measurements of A β ₁₋₄₀ aggregated by a 5-X and 10-X molar excess of sulindac sulfide, as well as a reference sample (1% DMSO-d₆) (Figures 3.8 and 3.9).

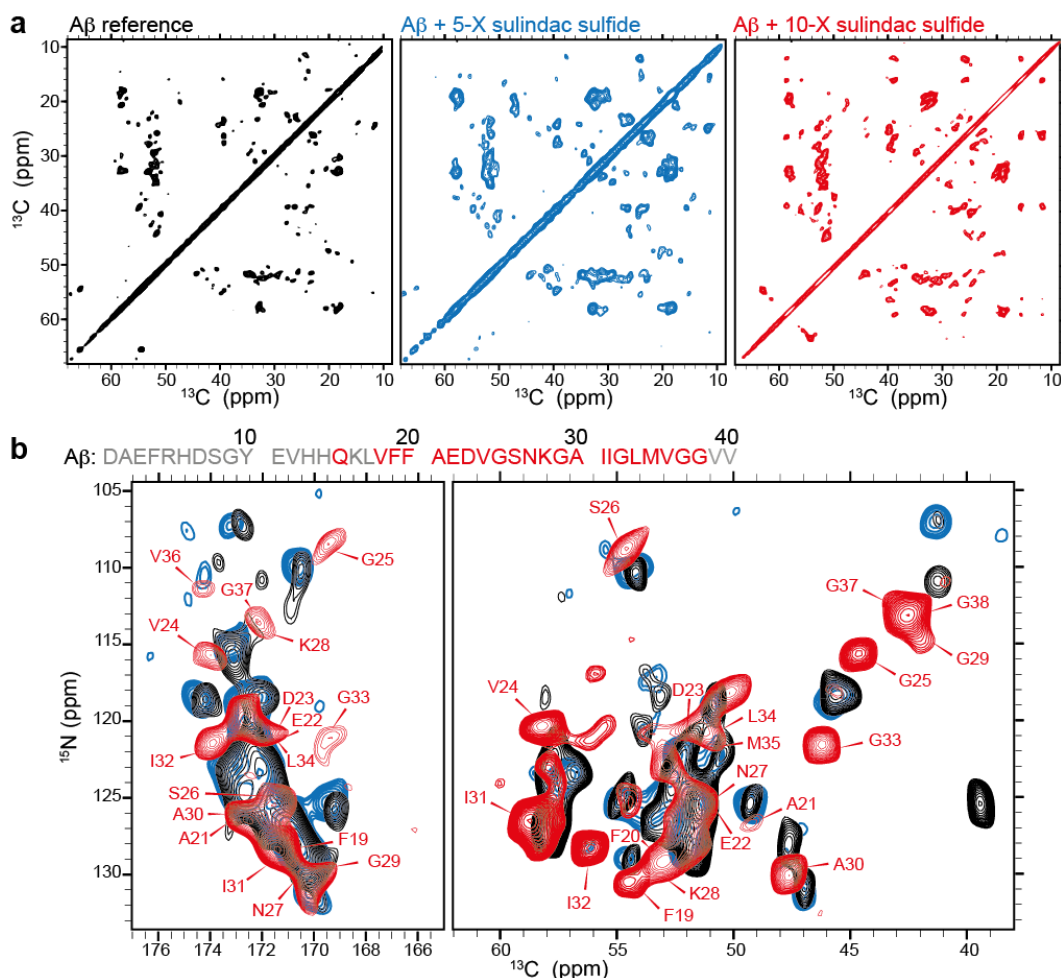


Figure 3.8: MAS solid-state NMR spectra of sulindac sulfide induced A β aggregates. 100 μ M A β ₁₋₄₀ was aggregated by a 5-X (blue), a 10-X (red) molar excess of sulindac sulfide and 1% DMSO-d₆ (black). (a) 2D ¹³C-¹³C PDS correlation spectra and (b) 2D ¹³C-¹⁵N TEDOR spectra. Overlays of the 2D PDS spectra including assignments are shown in Figure 3.9. Residues marked in red in the A β ₁₋₄₀ sequence are assigned for the 10-X sample. (b) Residue *i* is marked in N-C α correlation (right) and residue *i*-1 is marked in the N-CO correlation (left). The 2D spectra of the 5-X, as well as the reference sample were recorded at a MAS rotation frequency of 13 kHz, 275 K and 600 MHz. The displayed 2D and corresponding 3D assignment spectra for the 10-X sample were recorded at a MAS rotation frequency of 15 kHz, 270 K and 750 MHz. A PDSs mixing time of 50 ms was used.

The overlays demonstrate that A β_{1-40} peptide aggregated in the presence of 5-X sulindac sulfide and the DMSO reference produce highly comparable spectra. This effect is most apparent in the ^{13}C - ^{15}N TEDOR (Figure 3.8b), but also in the ^{13}C - ^{13}C PDSO spectra (Figure 3.9). It seems that a 10-X excess of sulindac sulfide is necessary to evoke spectral changes and CSPs. Therefore we recorded 3D NCACX and NCOCX experiments for A β_{1-40} aggregated by 10-X sulindac sulfide. Analysis of these spectra allowed sequential assignments of individual backbone ^{13}C and ^{15}N shifts and side chain ^{13}C shifts for residues V18-G38. The characteristic C β -C γ cross peak of Q15 could also be assigned, as there is only one glutamine present in the A β_{1-40} sequence. All assigned chemical shifts are listed in Appendix 5.2.2.

A 10-X molar excess of sulindac sulfide causes two obvious changes in the spectra. The first one is the appearance of additional and more intense cross peaks, particularly in the ^{13}C - ^{13}C correlation (Figure 3.9). These cross peaks mainly originate from the isoleucine side chains of I31 and I32. The presence of such cross peaks indicates a high degree of stability of these side chains. Additionally, a 10-X sulindac sulfide excess results in pronounced CSPs observed in the spectra. CSPs are seen for individual resonances of almost all residues from F19-G33, but are most severe for S26, A30, I31, I32 and several glycines. For some residues such as E22 and N27, CSPs are also observed in A β_{1-40} aggregated by 5-X sulindac sulfide, although to a lesser extent (Figure 3.9). For S26, spectra of A β_{1-40} aggregated by 5-X sulindac sulfide contain cross peaks at the original and the new position, indicating the presence of both conformations in the aggregates (Figure 3.9).

A β_{1-40} aggregates induced by a 10-X molar excess of sulindac sulfide were analyzed for their secondary structural elements by TALOS+ calculations, as well as secondary chemical shifts (Figure 3.10a). There is a clear tendency for the formation of β -sheet elements. The β -strand starts around V18 (the first assigned residue) and is interrupted by some residues surrounding V24-N27 (depending on the atoms analyzed) and G33.

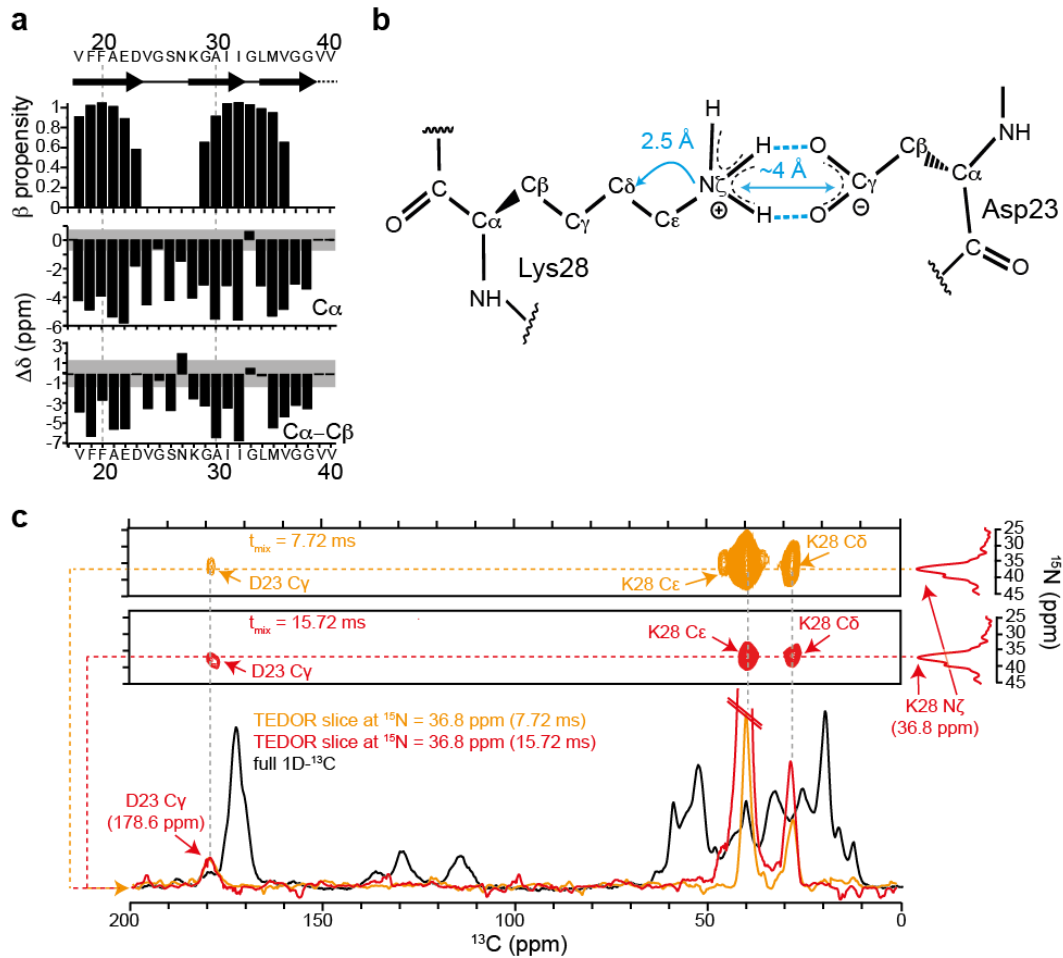


Figure 3.10: Structural elements of A β aggregated by 10-X sulindac sulfide determined by solid-state NMR. (a) Secondary structural elements predicted by TALOS+ (upper panel) and secondary chemical shifts $\Delta\delta C\alpha$ (ppm) and $\Delta\delta C\alpha-\Delta\delta C\beta$ (ppm) (lower panels). β -sheet propensities above 0.5 are shown, as predicted by TALOS+. Values within the gray range of ± 0.7 ppm ($\Delta\delta C\alpha$) and ± 1.4 ppm ($\Delta\delta C\alpha-\Delta\delta C\beta$) are considered insignificant, as this is the range of random coil CS specified by Wishart *et al.*^[390]. (b) Schematic model of the salt bridge formed by side chains of D23 and K28. (c) ^{13}C - ^{15}N TEDOR experiments detecting the salt bridge between D23 C γ (178.6 ppm) and N28 N ζ (36.8 ppm) at TEDOR mixing times of 7.72 (orange) and 15.72 ms (red). Slices extracted from the TEDOR spectra are superimposed with a full 1D- ^{13}C spectrum of the same sample (black). Experiments were recorded at a MAS rotation frequency of 11 kHz, 270 K and 750 MHz.

Further structural information about A β_{1-40} aggregates induced by a 10-X molar excess of sulindac sulfide is provided by 3D ^{13}C - ^{15}N TEDOR spectra. These experiments detect heteronuclear dipolar couplings and have been employed to detect the characteristic salt bridge (Figure 3.10b) found in various A β_{1-40} species^[266]. We observe intermolecular cross peaks of similar intensity between D23-C γ (178.6 ppm) and of K28-N ζ (36.8 ppm) at mixing times of 7.72 ms and 15.72 ms.

(Figure 3.10c). Our data are in agreement with experiments performed by Jaroniec *et al.*^[39], who report the maximum transfer efficiency for a 4 Å distance using TEDOR mixing times on the order of ~ 7-15 ms. This distance corresponds to the distance expected for the atoms forming the salt bridge in A β ₁₋₄₀ aggregates.

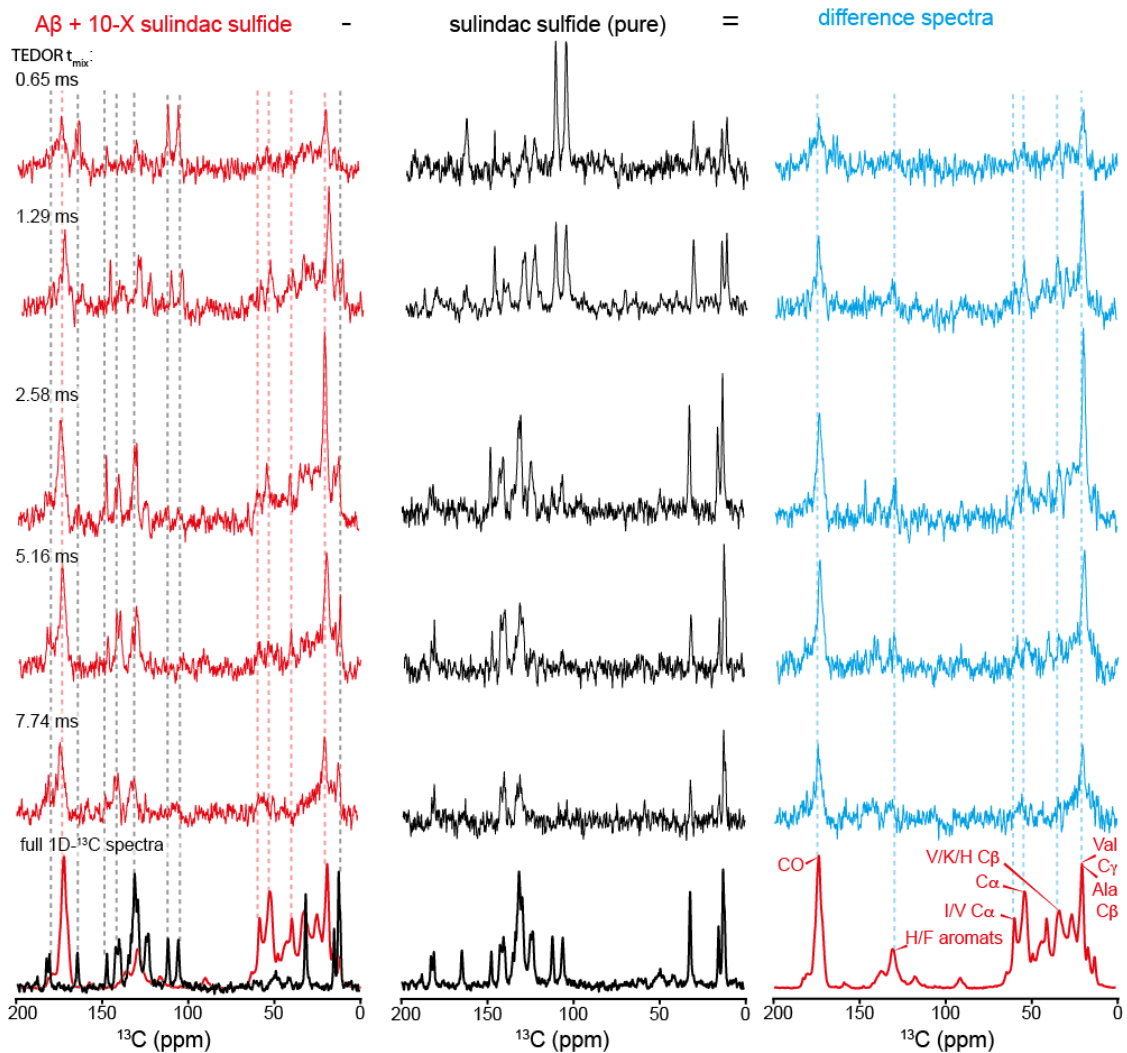


Figure 3.11: ^{13}C - ^{19}F TEDOR spectra of A β aggregated by 10-X sulindac sulfide. TEDOR experiments were recorded for A β ₁₋₄₀ aggregated by 10-X sulindac sulfide (red) and pure crystalline sulindac sulfide (black) at the indicated TEDOR mixing times. The crystalline sulindac sulfide spectra were subtracted from A β ₁₋₄₀ spectra with a factor 0.5, resulting in difference spectra (blue). The lower panel shows full 1D- ^{13}C spectra of the same samples for references. The full spectra, as well as the TEDOR spectrum at 2.58 ms mixing time is shown enlarged in Figure 3.12. Experiments were recorded with assistance of Dr. Gerhard Althoff-Ospelt (Bruker BioSpin) at a MAS rotation frequency of 12.4 kHz, 270 K and 600 MHz.

The solution-state NMR studies suggest that sulindac sulfide and A β ₁₋₄₀ aggregate into complexes when incubated together (Figure 3.6). To understand the molecular mechanism in which sulindac sulfide interacts with A β ₁₋₄₀ in the aggregated state, we detected dipolar couplings between ¹³C of A β ₁₋₄₀ and the NMR active ¹⁹F atom of sulindac sulfide. This was achieved by recording ¹³C-¹⁹F TEDOR experiments on A β ₁₋₄₀ aggregated by a 10-X molar excess of sulindac sulfide (Figure 3.11).

The ¹³C-¹⁹F TEDOR experiment detects ¹³C atoms in proximity to ¹⁹F, and therefore provides information of the binding mode and site of sulindac sulfide to A β ₁₋₄₀. However, the measured sample contains 1 mM unlabeled sulindac sulfide with a natural abundance of around 1% ¹³C, which is equivalent to around 10 μ M ¹³C labeled sulindac sulfide. To take this matter into account, we recorded the same set of TEDOR experiments on pure crystalline sulindac sulfide. These spectra were then subtracted from the sample with the complexes to extinguish TEDOR signals arising from dipolar couplings between intramolecular ¹³C-¹⁹F dipolar couplings of sulindac sulfide. The resulting difference spectra should contain solely intermolecular A β ₁₋₄₀ ¹³C to sulindac sulfide ¹⁹F contacts.

The lower panel of Figure 3.11 contains full 1D-¹³C spectra for reference signals. For clarity, the full 1D-¹³C spectra including assignments of A β ₁₋₄₀ aggregated by a 10-X sulindac sulfide (a) and pure crystalline sulindac sulfide (b), as well as an exemplary ¹³C-¹⁹F TEDOR difference spectrum ($t_{\text{mix}} = 2.58$ ms) (c) are shown in Figure 3.12. Superimposition of the TEDOR difference spectrum with the full 1D-¹³C of A β ₁₋₄₀-sulindac sulfide complexes demonstrates that a broad range of signals from backbone C α , CO and side chains are observed in the TEDOR experiments. These signals arise due to their spatial proximity to sulindac sulfide in the aggregates. These findings further support the formation of complexes. The lack of specific signals indicates a promiscuous binding mode.

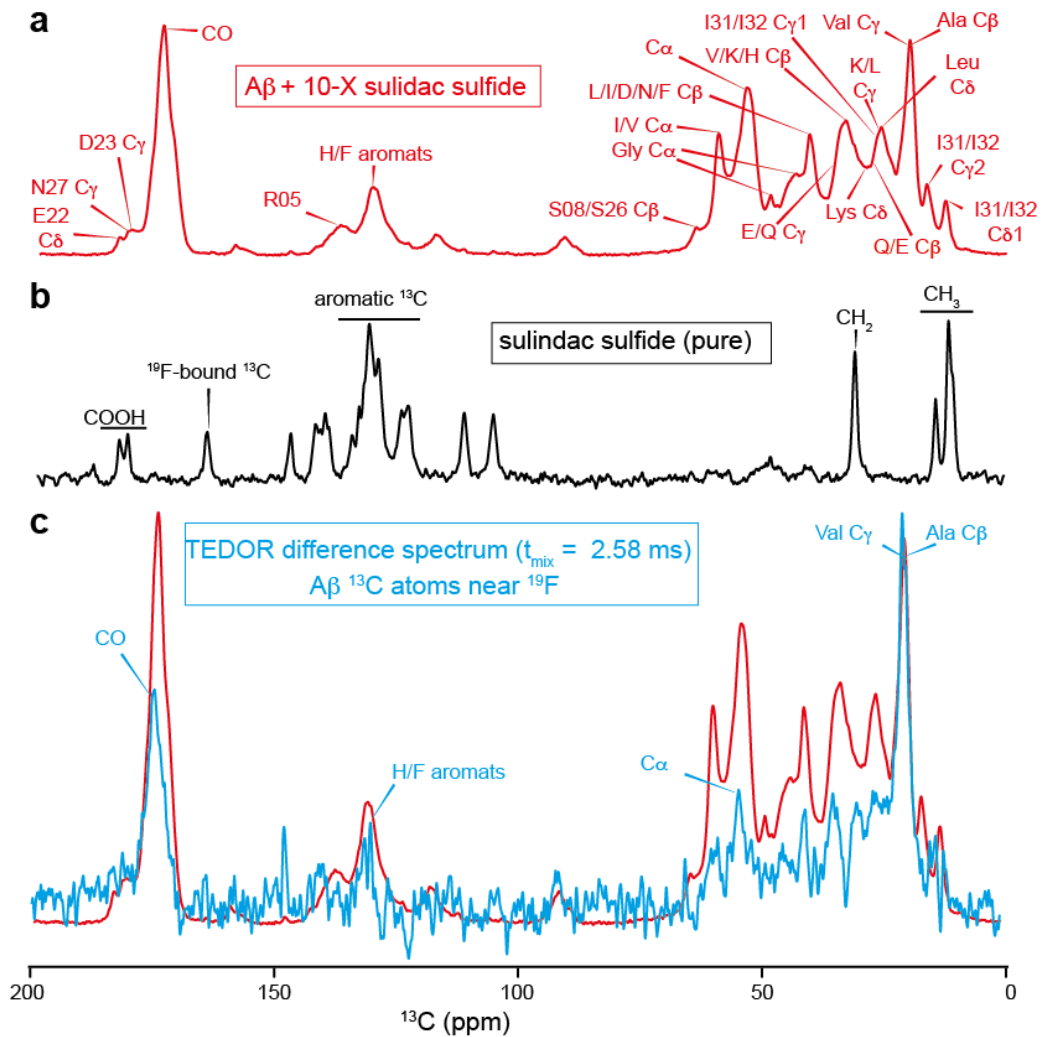


Figure 3.12: $A\beta$ ^{13}C atoms interacting with sulindac sulfide. (a) Full 1D- ^{13}C spectrum of $A\beta_{1-40}$ aggregates induced by 10-X sulindac sulfide including assignments. (b) Full 1D- ^{13}C spectrum of pure crystalline sulindac sulfide including assignments. (c) ^{13}C - ^{19}F TEDOR spectrum at a mixing time of 2.58 ms of $A\beta_{1-40}$ aggregated by 10-X sulindac sulfide including assignments (blue) overlaid with the full 1D- ^{13}C of the same sample (red).

3.4 Interactions of sulindac sulfide with fibrillar A β_{1-40}

To elucidate the interaction of sulindac sulfide with mature A β_{1-40} fibrils, we recorded solid-state NMR experiments on seeded fibrils incubated with a 5-X molar excess of the NSAID and DMSO- d_6 as a reference (Figures 3.13 and 3.14). The resulting 2D ^{13}C - ^{13}C PDS correlation (Figure 3.13a and 3.14) and ^{13}C - ^{15}N TEDOR (Figure 3.13b) spectra are amenable for further analysis. Results of this study have been published by Prade *et al*^[404].

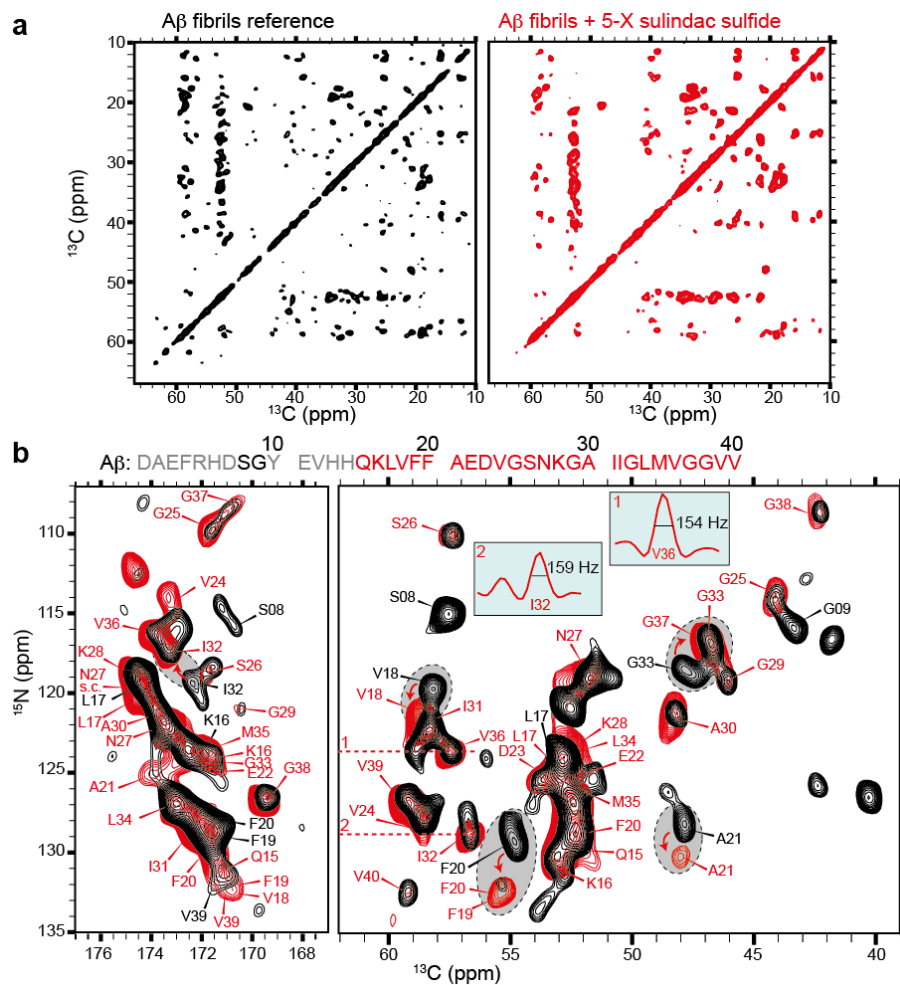


Figure 3.13: MAS solid-state NMR spectra of sulindac sulfide incubated A β fibrils. Seeded A β_{1-40} fibrils at a concentration of 50 μM were incubated with a 5-X molar excess of sulindac sulfide (red) and 1% DMSO- d_6 as a reference (black). (a) 2D ^{13}C - ^{13}C PDS correlation spectra and (b) 2D ^{13}C - ^{15}N TEDOR spectra. Overlays of the 2D PDS spectra including assignments are shown in Figure 3.14. Residues marked in the A β_{1-40} sequence are assigned. Line widths of resolved peaks are shown in blue panels. (b) Residue i is marked in N-C α correlation (right) and residue $i-1$ is marked in the N-CO correlation (left). The displayed 2D and corresponding 3D assignment spectra were recorded at 285 K and 700 MHz, and a MAS rotation frequency of 17 kHz and 13 kHz for sulindac sulfide incubated and reference fibrils, respectively. A PDSs mixing time of 200 ms was used.

The spectra feature well resolved peaks and line widths of directly detected ^{13}C signals between 120-165 Hz, indicating homogeneously structured fibrils. Incubation with sulindac sulfide does not alter the overall fibrillar architecture, as both samples yield similar spectra. However, it does cause defined CSPs for specific residues. CSPs are highlighted by gray areas in the ^{13}C - ^{15}N TEDOR (Figure 3.13b) and ^{13}C - ^{13}C PDS spectra (Figure 3.14). For clarification, areas of interest in the ^{13}C - ^{13}C correlations are magnified in Figure 3.14b. We do not observe peak splitting or line broadening, indicating quantitative binding.

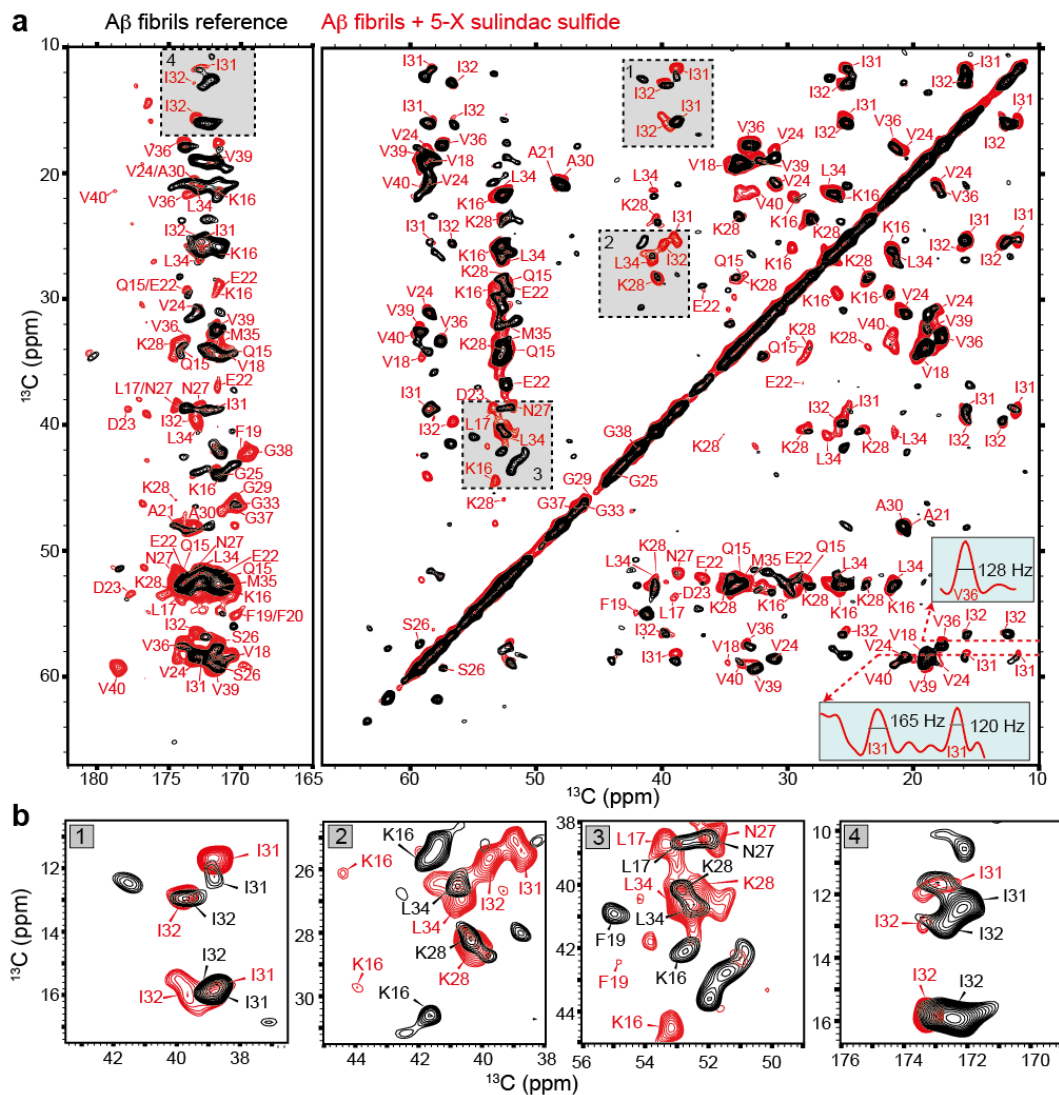


Figure 3.14: Overlay of 2D ^{13}C - ^{13}C PDS correlation spectra of sulindac sulfide incubated A β fibrils. Seeded A β_{1-40} at a concentration of 50 μM were incubated with a 5-X molar excess of sulindac sulfide (red) and 1% DMSO- d_6 as a reference (black). Line widths of resolved cross peaks are shown in blue panels. The lower panel shows magnifications of the squares marked in the full 2D ^{13}C - ^{13}C PDS correlation spectrum.

Resonances of residues Q15-V40 were assigned for A β ₁₋₄₀ fibrils in the presence and absence of sulindac sulfide. In addition, residues S08 and G09 of the reference fibrils were assigned (Figure 3.13b). No cross peaks in the spectra of A β ₁₋₄₀ fibrils incubated with the NSAIDs remain unassigned. Sequential assignment was obtained from analysis of 3D NCACX and NCOCX spectra. Representative strip plots of the 3D experiments of A β ₁₋₄₀ fibrils incubated with a 5-X molar excess of sulindac sulfide are shown for residues A30-G33 in Figure 3.15. All assigned chemical shifts are listed in Appendix 5.2.3. We observe only one set of signals for all residues, indicating the existence of only one set of conformation. The chemical shifts we observe are mostly identical to conformer I described by Lopez del Amo *et al*, who report the formation of an asymmetric dimer as the basic subunit of A β ₁₋₄₀ fibrils^[264]. However, residues V24-S26 seem to correspond to conformer II.

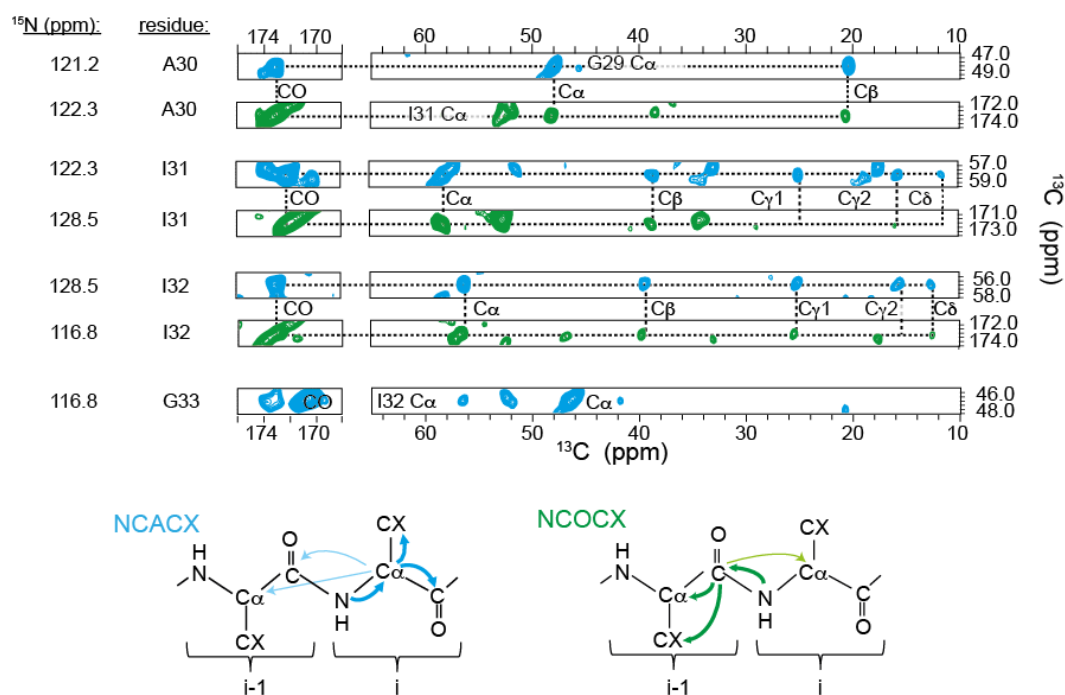


Figure 3.15: Strip plot of sulindac sulfide incubated A β fibrils. Representative strips from NCACX (blue) and NCOCX (green) spectra showing connectivities for A30-G33. Schematic representations of magnetization transfers are shown below. Lighter arrows indicate weaker magnetization transfers, which were occasionally observed in the spectra.

Electron microscopy images reveal that the fibrillar character of A β ₁₋₄₀ fibrils is maintained upon incubation with sulindac sulfide (Figure 3.16a). Black deposits in the upper image may be caused by sulindac sulfide aggregates. Based on chemical shifts of the assigned resonances, secondary structural elements were predicted by TALOS+ and secondary chemical shifts (Figure 3.16b). Both calculations demonstrate the formation of the two typical β -sheets for both samples, interrupted by several residues around G25-K28 (depending on the type of analysis). This pattern is commonly observed for A β ₁₋₄₀ aggregates, and the presence of sulindac sulfide does not seem to influence the β -arch formation.

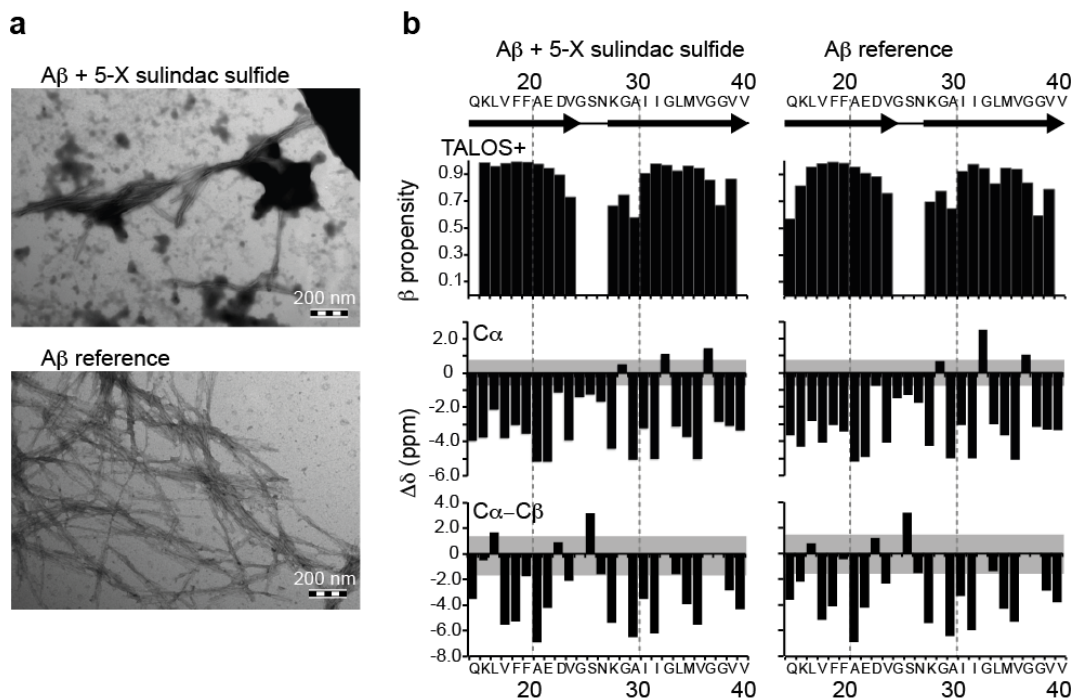


Figure 3.16: Structural details of sulindac sulfide incubated A β fibrils. (a) TEM images A β ₁₋₄₀ incubated with a 5-X molar excess of sulindac sulfide or DMSO-d₆. Scale bar = 200 nm. (b) Secondary structural elements predicted by TALOS+ (upper panel) and secondary chemical shifts $\Delta\delta$ C α (ppm) and $\Delta\delta$ C α - $\Delta\delta$ C β (ppm) (lower panels). β -sheet propensities above 0.5 are shown as predicted by TALOS+. Values within the gray range of ± 0.7 ppm ($\Delta\delta$ C α) and ± 1.4 ppm ($\Delta\delta$ C α - $\Delta\delta$ C β) are considered insignificant, as this is the range of random coil CS specified by Wishart *et al.*^[390].

The β -loop- β motif is stabilized by a salt bridge connecting the side chains of D23 and K28 (Figure 3.10b), which can be detected employing dipolar couplings. Peaks connecting D23-C γ and K28-N ζ are observed in ^{13}C - ^{15}N TEDOR experiments (Figure 3.17) for A β ₁₋₄₀ fibrils incubated with sulindac sulfide and reference fibrils. Hence, sulindac sulfide does not destroy the formation of the salt bridge. EM images, prediction of secondary structures and ^{13}C - ^{15}N TEDOR experiments demonstrate that sulindac sulfide does not cause drastic changes to the fibrillar structures of A β ₁₋₄₀, and thereby further support the observation made by solid-state NMR.

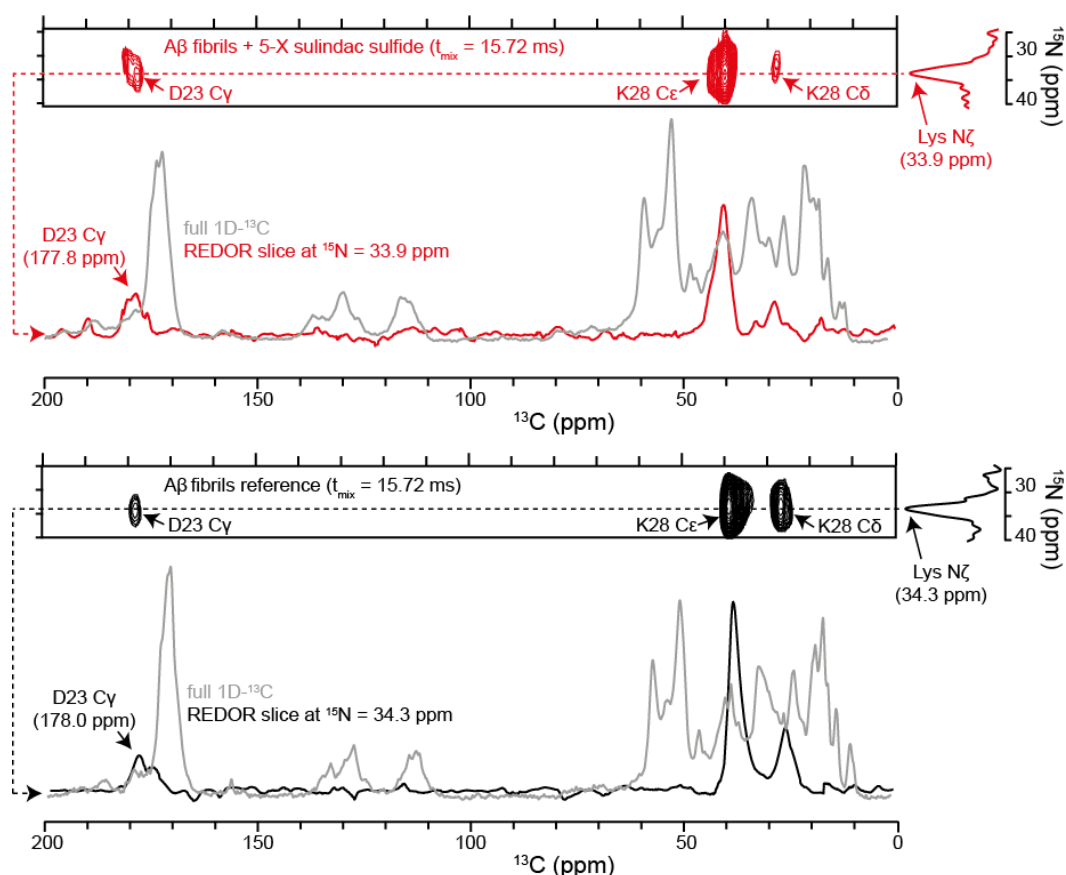


Figure 3.17: The effect of sulindac sulfide on the salt bridge in A β fibrils. ^{13}C - ^{15}N TEDOR experiments detecting the salt bridge between D23 C γ and N28 N ζ at a TEDOR mixing time of 15.72 ms. TEDOR spectra recorded for sulindac sulfide incubated fibrils (red) contain a peak at $^{13}\text{C} = 177.8$ ppm and $^{15}\text{N} = 33.9$ ppm, and reference fibrils (black) contain a peak at $^{13}\text{C} = 178.0$ ppm and $^{15}\text{N} = 34.3$ ppm, the positions of D23-C γ and K28-N ζ , respectively. Slices extracted from the TEDOR spectra are superimposed with a full $1\text{D-}^{13}\text{C}$ spectrum of the same sample (gray). Experiments were recorded at a MAS rotation frequency of 11 kHz, 270 K and 750 MHz.

Next, we analyzed the CSPs introduced by sulindac sulfide to the spectra in order to investigate which residues are involved in binding of the NSAID (Figure 3.18a). Residues most severely affected by sulindac sulfide include K16, F19, F20 and G33. In particular, the backbone resonances of these residues undergo chemical shift changes. These changes are apparent in the ^{13}C - ^{15}N correlations (Figure 3.13b). In addition, we observe defined CSPs for side chains of V18 C β , F19-20 C β , N27 C γ , M35 C β and several resonances K16, which are reflected in the ^{13}C - ^{13}C correlations (Figure 3.14).

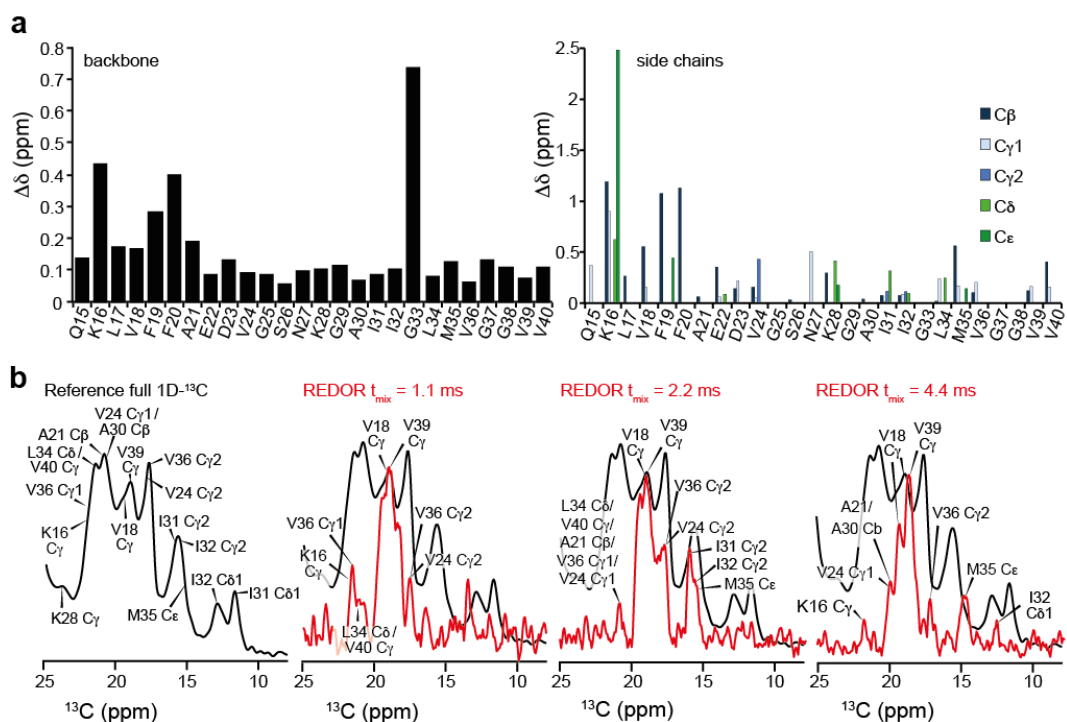


Figure 3.18: Solid-state NMR restraints collected for sulindac sulfide incubated A β fibrils. (a) Residue specific CSPs for backbone (left) and side chain resonances (right) of A β ₁₋₄₀ fibrils as induced by sulindac sulfide. (b) ^{13}C - ^{19}F REDOR experiments recorded on sulindac sulfide incubated A β ₁₋₄₀ fibrils. Proximity to ^{19}F causes dephasing of ^{13}C atoms in A β ₁₋₄₀. REDOR spectra were subtracted from reference spectra without a REDOR recoupling pulse to yield the difference spectra (red). The experiments were recorded as 2D ^{13}C - ^{13}C PDS correlations. As only diagonal and no cross peaks were observed, the REDOR experiments are displayed as 1D projections of the 2D spectra. REDOR mixing times of 1.1 ms, 2.2 ms and 4.4 ms were used. All REDOR spectra (red) are superimposed with the full 1D- ^{13}C of the same sample (black), which is shown containing full assignment on the left. Experiments were recorded with assistance of Dr. Gerhard Althoff-Ospelt (Bruker BioSpin) at a MAS rotation frequency of 14.6 kHz, 270 K and 600 MHz.

To elucidate the nature of sulindac sulfide binding to A β ₁₋₄₀ fibrils, we recorded ¹³C-¹⁹F REDOR experiments on fibrils incubated with the NSAID (Figure 3.18b). In the experiment, magnetization was transferred between ¹³C of the A β ₁₋₄₀ peptide and ¹⁹F of sulindac sulfide via dipolar couplings. This leads to signal attenuation of A β ₁₋₄₀ atoms in vicinity of the NSAID. REDOR spectra were subtracted from reference experiments without a REDOR recoupling pulse. Signals appearing in the REDOR spectra originate from A β ₁₋₄₀ atoms nearby ¹⁹F of sulindac sulfide. The experiment gives rise to only aliphatic resonances. For clarity, a full 1D-¹³C spectrum of the same sample including assignments is shown on the left, and is overlaid with REDOR spectra at all mixing times. The strongest REDOR signals are observed for V18 and/or V39 C γ . Further resonances affected by signal attenuations are K16 C γ , V24 and/or V36 C γ 1/2, A21 and/or A30 C β , L34 C δ , V40 C γ , as well as I31 C γ 2, I32 C γ 2 and C δ 1, and M35 C ϵ at longer mixing times. Analysis of the spectra is hindered by signal overlap. A list of all observed ¹³C-¹⁹F REDOR signals, including their intensities and assignments (\pm 0.5 ppm) is shown in Table 3.1.

Peak position (ppm)	Rel. intensity	Assignment	Mixing time
18.9	1.00	V39 C γ / V18 C γ	4.4 ms
19.6	0.80	V18 C γ	4.4 ms
19.2	0.58	V18 C γ / V39 C γ	2.2 ms
20.3	0.55	A30 C β / V24 C γ 1 / A21 C β	4.4 ms
15.1	0.49	M35 C ϵ	4.4 ms
17.5	0.48	V36 C γ 2	4.4 ms
19.2	0.43	V18 C γ / V39 C γ	1.1 ms
18.1	0.41	V24 C γ 2 / V36 C γ 2	2.2 ms
16.2	0.40	I31 C γ 2 / I32 C γ 2	2.2 ms
18.5	0.34	V24 C γ 2 / V36 C γ 2	1.1 ms
15.8	0.33	I32 C γ 2 / I31 C γ 2 / M35 C ϵ	2.2 ms
21.7	0.27	V36 C γ 1 / K16 C γ / V40 C γ / L34 C δ	1.1 ms
21.1	0.27	L34 C δ / V40 C γ / A21 C β / V36 C γ 1 / V24 C γ 1	2.2 ms
21.2	0.22	L34 C δ / V40 C γ / V36 C γ 1 / A21 C β	1.1 ms
12.9	0.20	I32 C δ 1	4.4 ms
22.1	0.13	K16 C γ	4.4 ms

Table 3.1: ¹³C-¹⁹F REDOR restraints of fibrillar A β . Restraints are sorted by their intensities. Signals were assigned to resonances \pm 0.5 ppm.

Experiments based on ^{13}C - ^{19}F dipolar couplings provide information on the binding mode of sulindac sulfide to $\text{A}\beta_{1-40}$. The ^{13}C - ^{19}F REDOR spectra obtained for fibrillar $\text{A}\beta_{1-40}$ incubated with sulindac sulfide differ significantly from ^{13}C - ^{19}F TEDOR spectra of monomeric $\text{A}\beta_{1-40}$ aggregated with sulindac sulfide (Section 3.3) (Figure 3.19). Signals throughout the peptide sequence originating from CO, C α , C β , methyl and aromatic atoms are seen in spectra of the aggregated monomer, indicating nonspecific interactions with sulindac sulfide. However, in the fibrillar spectra, we observe defined signals, which can be assigned to individual residues. Sulindac sulfide must therefore interact specifically with individual atoms in the fibril, but promiscuously in induced aggregates.

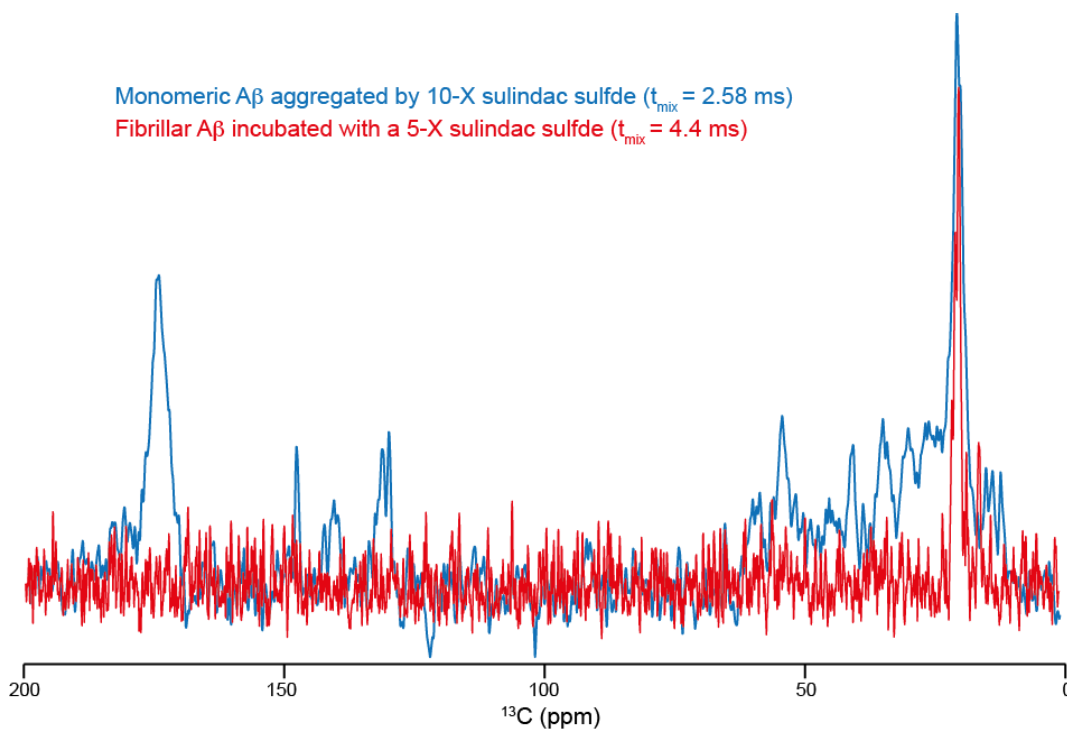


Figure 3.19: Dipolar coupling based ^{19}F - ^{13}C spectra of different $\text{A}\beta$ samples. Superimposition of the ^{13}C - ^{19}F TEDOR spectrum recorded for $\text{A}\beta_{1-40}$ monomers aggregated by 10-X excess of sulindac sulfide at a mixing time of 2.58 ms (blue) as shown in Figure 3.11 indicative of nonspecific NSAID binding, and the ^{13}C - ^{19}F REDOR spectrum of sulindac sulfide incubated $\text{A}\beta_{1-40}$ fibrils at a mixing time of 4.4 ms (red) as shown in Figure 3.18b, indicative of specific NSAID binding.

The solid-state NMR part of this study focused on the collection of structural information about A β ₁₋₄₀ fibrils incubated with sulindac sulfide. The NSAID has an impact on chemical shifts of the peptide and can be detected in close proximity of the fibrils. The CSPs are ¹³C-¹⁹F REDOR contacts were employed as restraints for docking sulindac sulfide for A β ₁₋₄₀ fibrils. Currently, three wild type solid-state NMR A β ₁₋₄₀ fibril structures are available^[232,257,260]. We compared our chemical shifts to the structures, as well as to all models of A β ₁₋₄₀ fibrils, for which CS information is available^[264-267]. For this purpose, we calculated the correlation coefficient (\bar{r}) and $\overline{\Delta\delta}$, both based on C α , C β and CO shifts, for all CS information in the literature to sulindac sulfide incubated and reference fibrils (Table 3.2). All correlation plots and residue specific $\overline{\Delta\delta}$ analyses are shown in Appendix 5.4. Both CS analyses demonstrate that A β ₁₋₄₀ fibrils featuring a 3-fold symmetric subunit are the most similar to our current fibrils, followed by A β ₁₋₄₀ fibrils featuring a 2-fold symmetric subunit. Our fibril preparation is similar to the one reported for the 2-fold symmetric model, therefore, we employed both the 3-fold (PDB: 2LMN)^[257] and the 2-fold symmetric (PDB: 2LMP)^[260] structures for docking experiments.

	Author, year	PDB	\bar{r}		$\overline{\Delta\delta}$ (σ)	
			Sulindac sulfide	Ref	Sulindac sulfide	Ref
Structures	Paravastu <i>et al.</i> 2008 3-fold symmetry	2LMP/ 2LMQ	0.939	0.934	0.16 (1.59)	0.08 (1.49)
	Petkova <i>et al.</i> 2006 2-fold symmetry	2LMN/ 2KMO	0.920	0.904	0.25 (1.62)	0.16 (1.54)
	Lu <i>et al.</i> 2013 brain tissue derived	2M4J	0.857	0.873	1.84 (2.16)	1.80 (2.07)
Models and CS	Lopez del Amo <i>et al.</i> 2012 Conf I	-	0.936	0.940	0.16 (1.59)	0.13 (1.58)
	A β aggregates by sulindac sulfide (current)	-	0.850	0.867	-0.52 (1.53)	0.64 (1.56)
	Lopez del Amo <i>et al.</i> 2012 Conf II	-	0.835	0.845	-0.23 (2.06)	-0.25 (2.14)
	Petkova <i>et al.</i> 2002	-	0.809	0.812	0.21 (1.90)	0.19 (1.78)
	Niu <i>et al.</i> 2014	-	0.771	0.742	1.61 (2.29)	1.58 (2.29)
	Bertini <i>et al.</i> 2011	-	0.760	0.756	0.56 (2.30)	0.52 (2.26)

Table 3.2: Comparison of sulindac sulfide incubated A β fibrils to literature. CS of current sulindac sulfide incubated A β ₁₋₄₀ fibrils (red) and reference fibrils (black) were compared to CS of a 3-fold symmetric structure^[257], a 2-fold symmetric structure^[225,260], and a brain tissue derived structure^[232], as well as models of an asymmetric dimer^[264], a model of synthetic fibrils^[266], a reference to fibrils binding phospholipids^[267], a model of recombinant fibrils^[265] and A β ₁₋₄₀ monomers incubated with sulindac sulfide Section 3.3. The correlation coefficient \bar{r} and the deviation of chemical shifts $\overline{\Delta\delta}$ were calculated as average values of C α , C β and CO values. The standard deviation (σ) is indicated for $\overline{\Delta\delta}$ values. Individual plots are shown in Appendix 5.4.

The NMR restraints collected by solid-state NMR are plotted onto both the 2-fold and 3-fold symmetric A β ₁₋₄₀ fibril structures (Figure 3.20a). Atoms experiencing CSPs are marked in different colors, according to the strength of the CSP. In addition, ¹³C-¹⁹F REDOR contacts are marked in green. The REDOR restraints are considered more valuable, as they arise due to direct contact with sulindac sulfide, whereas CSPs may be caused by conformational changes. Figure 3.20a illustrates that sulindac sulfide affects atoms between the two β -strands, as well as atoms on the fibril surface.

In the following, sulindac sulfide was docked onto A β ₁₋₄₀ fibril structures. All molecular modeling experiments were performed by Heiko Bittner and Prof. Dr. Peter Hildebrand (Charité-Universitätsmedizin, Molecular Modeling, Institute of Medical Physics and Biophysics, Berlin, Germany). Briefly, the structures were analyzed for cavities in a packing analysis using the Voronoi cell method^[406,407], ProtOr^[408] and a Delaunay triangulation. Five clusters of cavities were found (Figure 3.20b), out of which two surrounding I32 (Cluster 1) and V36 (Cluster 2) were employed for further induced fit approaches, due to their polarity as assessed by DOWSER^[409]. They are large and hydrophobic enough to potentially harbor a sulindac sulfide molecule. Induced fit docking^[410,411] of sulindac sulfide to cluster 1 and cluster 2 of the 2-fold and 3-fold symmetric A β structures reveals that sulindac sulfide can bind A β in various poses (Figure 3.20c). These binding scenarios include parallel (pose 1 in cluster 1) and perpendicular (pose 2 in cluster 2) alignment of the aromatic rings with respect to the fibril axis. A combination of all poses shown in Figure 3.20 fulfills the experimental NMR restraints.

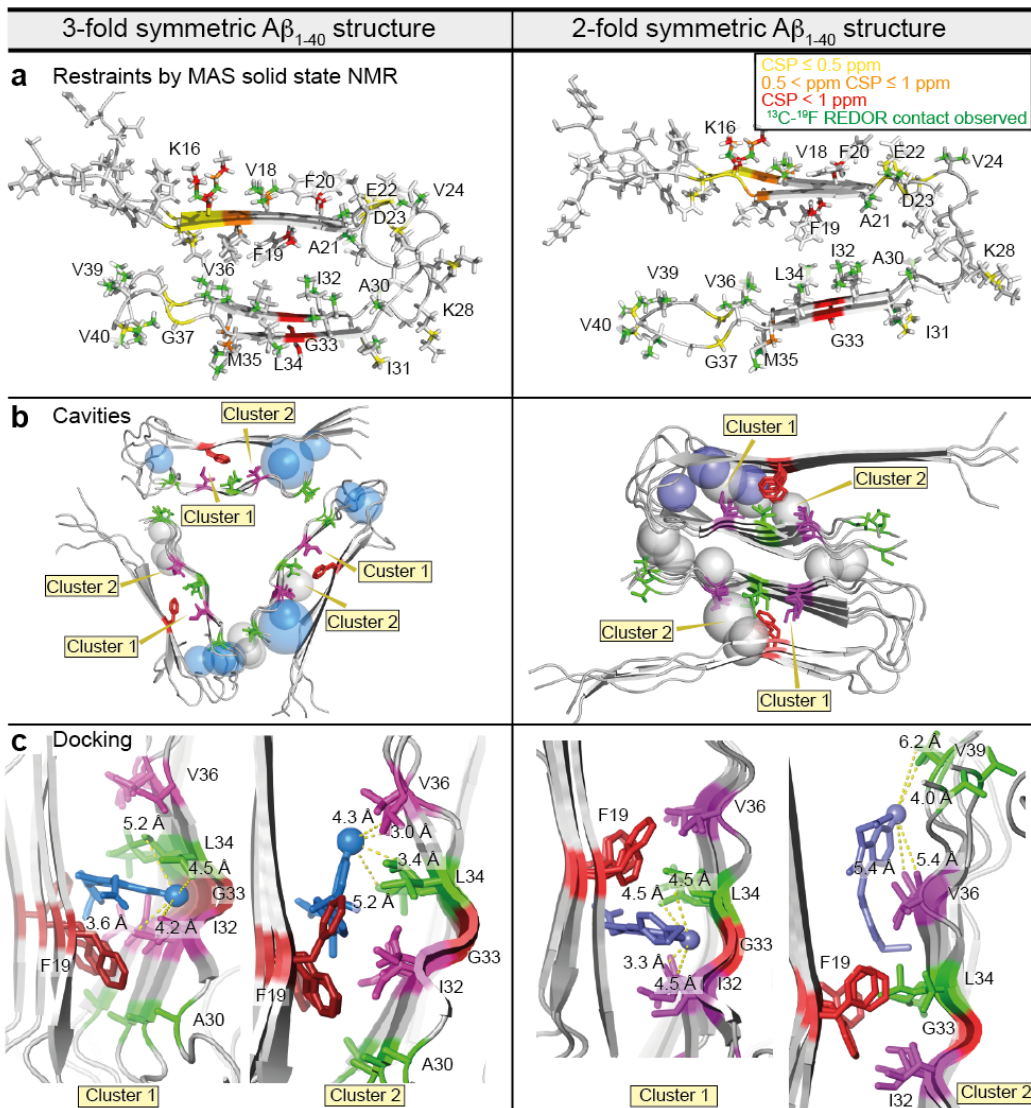


Figure 3.20: Docking of sulindac sulfide to A β fibrils. A 3-fold symmetric structure (PDB: 2LMP)^[257] and a 2-fold symmetric structure (PDB: 2LMN)^[260] were employed. (a) NMR restraints based on CSPs and ¹³C-¹⁹F REDOR contacts plotted onto A β_{1-40} fibrillar structures. (b) Packing analysis of the fibrillar structures screening for cavities. Relevant cavities cluster around I32 (Cluster 1) and V36 (Cluster 2). Hydrophilic cavities are colored blue, hydrophobic cavities are colored gray. (b) Induced fitting of sulindac sulfide to A β_{1-40} fibrils. The sulindac sulfide molecule is shown in blue. Distances of the ¹⁹F atom to nearby methyl groups are shown as yellow lines. Heiko Bittner and Prof. Dr. Peter Hildebrand (Charité-Universitätsmedizin) performed the packing analysis and molecular modeling and provided Figures 3.20b and 3.20c.

3.5 Oxidation of A β ₁₋₄₀

Oxidation of M35 alters toxicity and aggregation properties of A β ^[184-187]. The model of sulindac sulfide docking to A β ₁₋₄₀ fibrils suggests that the NSAID binds to a hydrophobic pocket near M35, and may be involved in redox regulation of A β . To test this hypothesis, we recorded solution-state NMR spectra of monomeric and fibrillar A β ₁₋₄₀ in oxidized and reduced states.

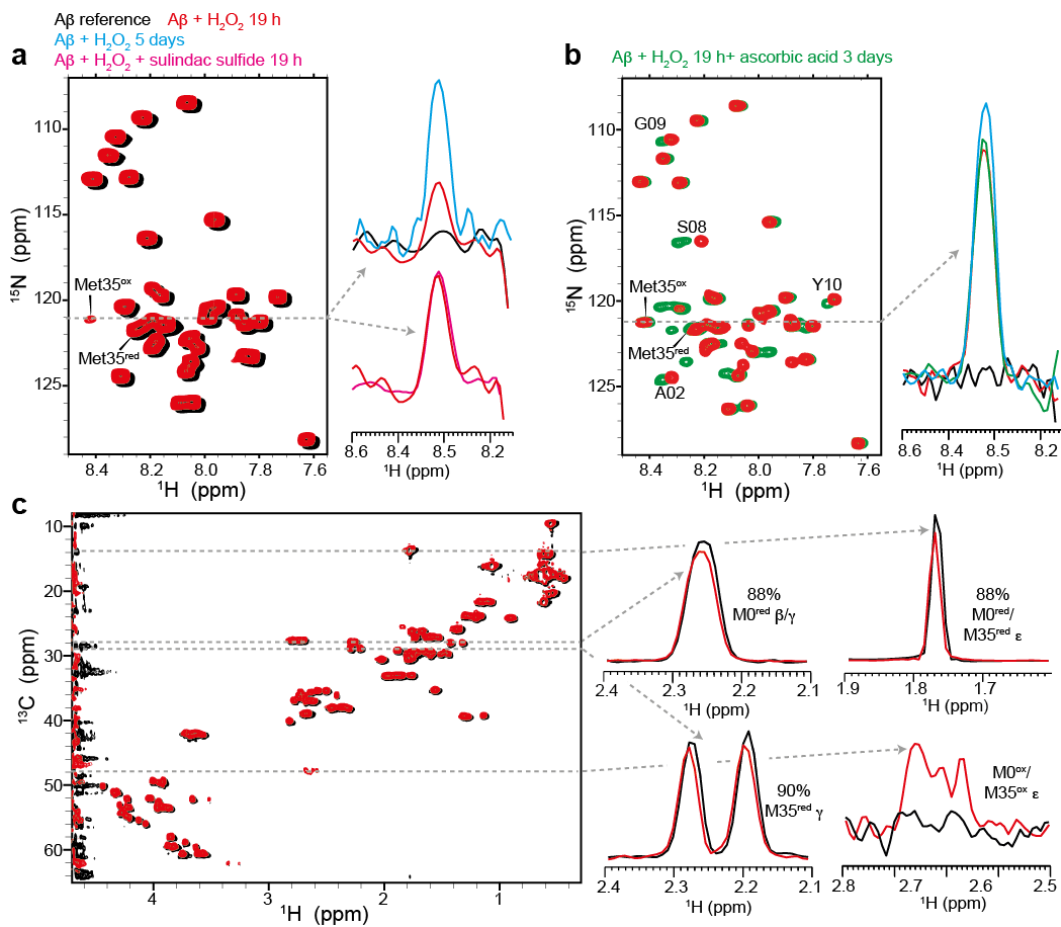


Figure 3.21: Oxidation of monomeric A β . (a) 2D ¹H-¹⁵N HMQCs of 50 μ M A β ₁₋₄₀ incubated with a 10-X molar excess of H₂O₂ (500 μ M) for 19 h (red) and 5 days (blue) and a reference sample treated with the same conditions (black). The experiment was repeated in the presence of 100 μ M sulindac sulfide (pink). (b) 2D ¹H-¹⁵N HMQCs of 50 μ M A β ₁₋₄₀ incubated with a 10-X molar excess of H₂O₂ (500 μ M, red) for 19 h and a reference (black). After 19 h, 25 mM ascorbic acid was added to the sample (green) and the appropriate amount of water was added to the reference (blue) and incubated for 3 days. Slices are extracted at ¹⁵N = 121.2 ppm, the position of the M35^{ox} HN signal. (c) 2D ¹H-¹³C HSQCs of 50 μ M A β ₁₋₄₀ incubated with a 10-X molar excess of H₂O₂ (500 μ M) for 19 h (red) and a reference sample treated with the same conditions (black). Slices are extracted at ¹³C shifts of M0^{red} β/γ, M35^{red} γ, M0/35^{red} ε and M0/35^{ox} ε. 1% DMSO-d₆ was present in all samples. All experiments were recorded at 277 K and 500 MHz.

In order to determine conditions for further experiments, monomeric A β_{1-40} was oxidized by a 10-X molar excess of H₂O₂. The resulting 2D ¹H-¹⁵N and ¹H-¹³C HSQCs show that an oxidized peak of M35 appears for the backbone HN signals (Figure 3.21a-b) as described by Hou *et al*^[186]. However, oxidation by H₂O₂ does not seem to have a significant impact on the side chain resonances (Figure 3.21c). Signal intensities of H ϵ -C ϵ , H β -C β and H γ -C γ are reduced only by 10-12%. However, a new signal appears at ¹H = 2.64 ppm and ¹³C = 48.2 ppm. Wang *et al* observed a similar shift of methionine methyl groups upon the oxidation of the light-harvesting complex of *Rhodospirillum rubrum*^[412]. In the case of A β_{1-40} , M0 and M35 methyl groups overlap, and the newly arising signal may originate from oxidation of M0 instead of M35.

The oxidation reaction of A β_{1-40} continued up to 5 days in solution (Figure 3.21a). Co-incubation of monomeric A β_{1-40} with sulindac sulfide and H₂O₂ does not decrease M35 oxidation. This is not surprising, as we expect sulindac sulfide to bind to a pocket formed only by mature fibrils. In order to analyze the oxidation state of fibrils, A β_{1-40} fibrils were oxidized, centrifuged, dissolved in DMSO-d₆, 0.2% TFA, 25 mM ascorbic acid and recorded by solution-state NMR spectroscopy. Ascorbic acid was added to the mixture to ensure only mature fibrils are oxidized, and the oxidizing reaction is quenched when fibrils are dissolved. Ascorbic acid inhibits further oxidation and does not reduce methionine sulfoxide back to methionine (Figure 3.21b).

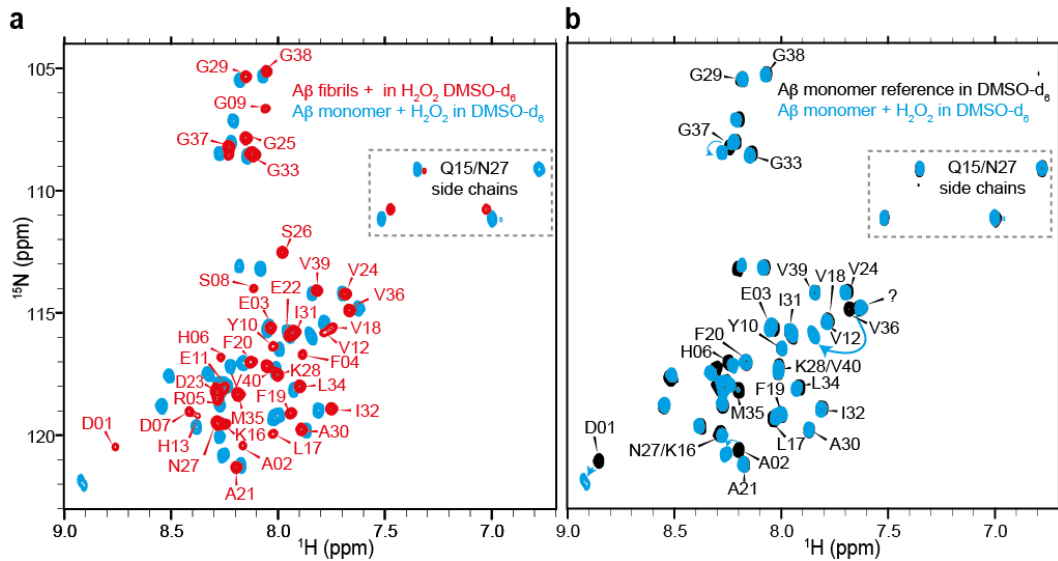


Figure 3.22: Comparison of oxidized monomeric and fibrillar $\text{A}\beta$. (a) 2D ^1H - ^{15}N HMQCs of 50 μM monomeric $\text{A}\beta_{1-40}$ incubated with a 100-X molar excess of H_2O_2 (5 mM) for 19 h (blue) and 50 μM seeded $\text{A}\beta_{1-40}$ fibrils incubated with a 100-X molar excess of H_2O_2 (5 mM) for 19 h (red). (b) 2D ^1H - ^{15}N HMQCs of oxidized and monomeric $\text{A}\beta_{1-40}$ (blue) and a reference treated with the same conditions (black). Monomeric samples were lyophilized and dissolved in DMSO-d_6 , 0.2% TFA, 25 mM ascorbic acid. Fibrils were sedimented and dissolved in DMSO-d_6 , 0.2% TFA, 25 mM ascorbic acid. Assignments were obtained from Dasari *et al.*^[383]. All experiments were recorded at 298 K and 600 MHz.

Figure 3.22a shows the resonance assignment of $\text{A}\beta_{1-40}$ fibrils dissolved in DMSO-d_6 (red). Incubation with H_2O_2 and addition of ascorbic acid does not alter the spectra, except for some peak splitting, presumably a result of M0 oxidation (Figure 3.23a). From the spectra it remains unclear if fibrillar M35 is oxidized by H_2O_2 . In aqueous conditions M35 oxidation is clearly observed upon incubation with H_2O_2 . Hence, in order to determine the spectrum of $\text{A}\beta$ containing M35^{ox} , ^1H - ^{15}N HMQCs were recorded of Met35 oxidized, monomeric $\text{A}\beta_{1-40}$, which was lyophilized and dissolved in DMSO-d_6 and reduced $\text{A}\beta_{1-40}$ treated with the same conditions (Figure 3.22b). In the resulting spectra, the HN peak of M35^{red} disappears, although it is unclear where it is shifting. Residues surrounding M0 and M35 are also shifted upon oxidation. The spectrum of oxidized $\text{A}\beta_{1-40}$ does not overlap well with mature $\text{A}\beta_{1-40}$ fibrils in their oxidized form (Figure 3.22a). Therefore the ^1H - ^{15}N HMQC of M35^{ox} $\text{A}\beta_{1-40}$ fibrils cannot be derived from M35^{ox} $\text{A}\beta_{1-40}$ monomers. In order to induce significant and observable M35 oxidation in fibrils, a variety of oxidation agents were tested (Figure 3.23).

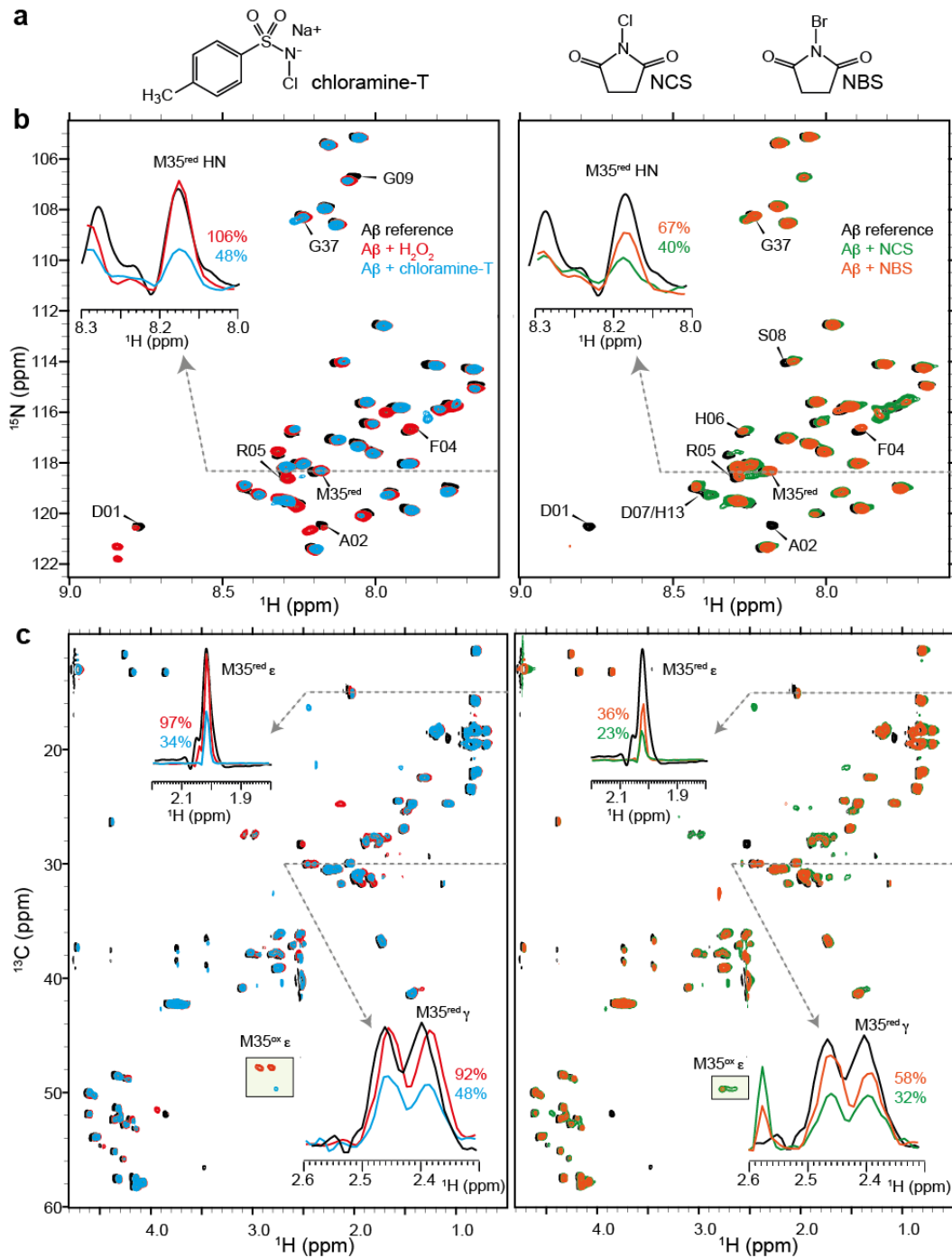


Figure 3.23: Oxidation of fibrillar A β by a variety of oxidizing agents. (a) Chemical structures of the oxidizing agents chloramine-T, NCS and NBS. (b) 2D ^1H - ^{15}N HMQCs and (b) of 2D ^1H - ^{13}C HSQCs of 50 μM seeded A β_{1-40} fibrils incubated with a 400-X molar excess of H_2O_2 (20 mM) (red), and 200-X molar excesses of T-chloramine (blue), NCS (green) and NBS (orange) (10 mM) for 2 days, as well as a reference sample treated with the same conditions. The samples were sedimented and dissolved in DMSO- d_6 , 0.2% TFA, 25 mM ascorbic acid. (a) Slices are extracted at the HN peak of M35 $^{\text{red}}$ at $^{15}\text{N} = 118.3$ ppm. (b) Slices are extracted at $^{13}\text{C} = 15$ ppm (M35 $^{\text{red}}$ ϵ) and 30 ppm (M35 $^{\text{red}}$ γ). The signal at $^1\text{H} = 2.58$ ppm and $^{13}\text{C} = 30$ ppm originates from incomplete deuteration of DMSO- d_6 . All experiments were recorded at 298 K and 500 MHz.

Mature A β_{1-40} fibrils were treated with various oxidizing agent, including H₂O₂, chloramine-T, N-chlorosuccinimide (NCS) and N-bromosuccinimide (NBS) (Figure 3.23a) before being dissolved and measured in DMSO-d₆. The presence of all oxidizing agents causes CSPs in the 2D spectra (Figure 3.23b-c). In particular, residues in the N-terminus are most severely affected, as can be seen in the ¹H-¹⁵N HMQCs (Figure 3.23b). This may be due to the accessibility of the N-terminus, or because of the chemical environment introduced through M0 oxidation, or direct binding of the oxidizing agents. Chloramine-T, NCS and NBS reduce the population of M35^{red}, as demonstrated by slices extracted at peaks of M35 HN (Figure 3.23b), and side chain γ and ϵ (Figure 3.23c). NCS has the strongest effect on oxidizing M35, followed by chloramine-T and NBS. H₂O₂ seems to only oxidize M0. No new peaks corresponding to M35^{ox} population appear in the ¹H-¹⁵N HMQC. However, the signal originating from the oxidized Met ϵ atom appears in the ¹H-¹³C HSQC (Figure 3.23c). The loss of M35^{red} population is most apparent for the H ϵ -C ϵ peak, as it is the closest to the thioether group. The H γ -C γ peak is also strongly affected. The HN peak of the backbone shows the weakest impact.

It should be noted, that there is currently no CS assignment for the ¹H-¹³C HSQC of A β_{1-40} in DMSO-d₆. The H β -C β and H γ -C γ assignments were adapted from A β_{1-40} in aqueous buffer (Figure 3.3), as the position of the peaks overlap. The H ϵ -C ϵ were assigned due to their unique CS. We assume that the sharper signal (Figure 3.24b, line 1) originates from M0, as it is more flexible, and the broader signal (Figure 3.24b, line 2) corresponds to M35.

When mature fibrils are co-incubated with sulindac sulfide during the oxidizing reaction with NCS, the loss of M35^{red} population is less severe (Figure 3.24). This is demonstrated by slices extracted at peaks of M35^{red} from a ¹H-¹⁵N (Figure 3.24a) and ¹H-¹³C HSQC (Figure 3.24b). Hence, sulindac sulfide reduces M35 oxidation by NCS. Signals from S26 and V39 (Figure 3.24a) were plotted for as references to ensure that all samples contain comparable amount of material.

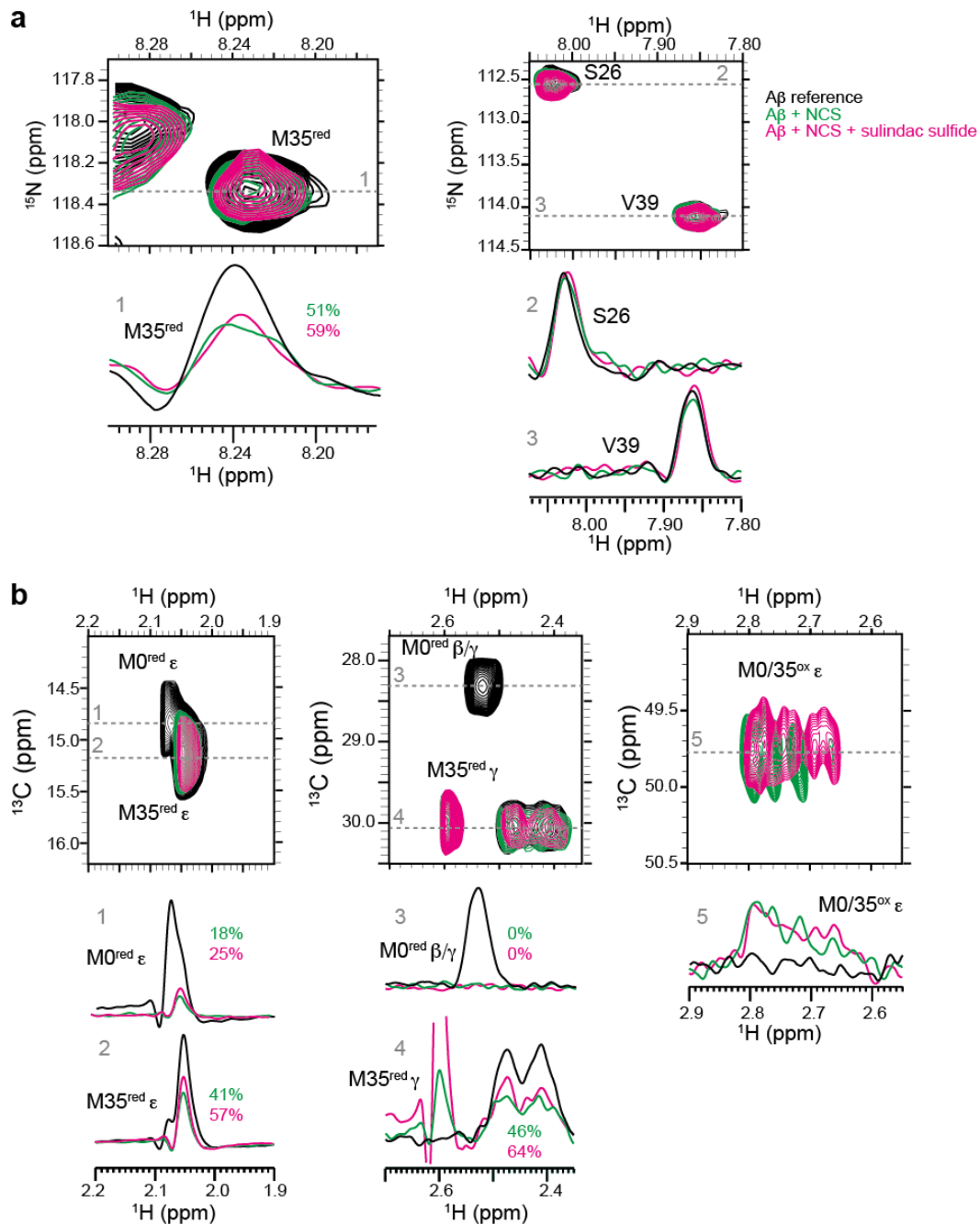


Figure 3.24: Oxidation of fibrillar A β in the presence of sulindac sulfide. 50 μM seeded A β_{1-40} fibrils were incubated with a 375-X molar excess of NCS (18.75 mM) (green) and a 375-X molar excess of NCS and a 10-X molar excess of sulindac sulfide (500 μM) (pink) for 4 days. A reference sample (black) was treated with the same conditions. 1% DMSO- d_6 was present in all samples. (a) ^1H - ^{15}N HMQC spectra of M35^{red} (left) and S26 and V39 (right) as references. (b) ^1H - ^{13}C HSQC spectra of M0^{red} and M35^{red} of H ϵ -C ϵ (left), H β / γ -C β / γ (center) and M0^{ox} or M35^{ox} H ϵ -C ϵ (right). Slices were extracted from the 2D correlations and are shown in the lower panels. Experiments were recorded at 298 K and 500 MHz. (b) 1D- ^1H spectra of 50 μM sulindac sulfide (black), sulindac sulfide incubated with a 40-X molar excess of H $_2$ O $_2$ for 20 h (red) and sulindac sulfone (blue). Experiments were recorded at 277 K and 500 MHz.

As sulindac sulfide seems to attenuate methionine oxidation in A β , the question arises whether this effect is due to the NSAID binding to a pocket formed in fibrils, thereby blocking access for oxidizing agents, or whether it may function as an anti-oxidant. For this purpose, we performed experiments to oxidize pure sulindac sulfide in buffer. In principle, a 1-time oxidation of sulindac sulfide will yield sulindac, and a 2-time oxidation will yield sulindac sulfone. 1D- ^1H spectra of the three NSAIDs are shown in Figure 3.25. Sulindac sulfide was incubated with H_2O_2 , NCS and chloramine-T. All three oxidizing agents produced sulindac Figure 3.25, as can be determined by the presence of the characteristic sulindac signal at 2.87 ppm (green 2), although to different extents. NCS was the most efficient oxidizing agent, as no remainders of sulindac sulfide (blue 2, blue 6) were left after 1.5 h incubation. In the presence of H_2O_2 , smaller signals of sulindac sulfide remained even after 8 h incubation. A second oxidation step to sulindac sulfone was not seen in all three samples after 8 days (data not shown), as demonstrated by the absence of the characteristic sulindac sulfone signal at 7.94 ppm. Hence, NCS, the agent used for oxidation of fibrils, is able to convert sulindac sulfide to sulindac.

To test in which oxidized state the NSAID is present in the fibril sample oxidized with NCS, we subtracted the 1D- ^1H spectrum of A β fibrils incubated with NCS from A β fibrils incubated with NCS and sulindac sulfide. The resulting spectrum (Figure 3.26) should in principle contain NSAID signals only. Several small signals in the amide region can be observed, most likely originating from CS differences between the two spectra. In addition three distinctive signals between 7.0 and 7.3 ppm may correspond to NSAID signals. 1D- ^1H spectra of sulindac sulfone, sulindac and sulindac sulfide recorded in DMSO-d_6 are displayed in the lower part of Figure 3.26 and serve as references for the difference spectrum, which was also recorded in DMSO-d_6 . The signals do not correspond perfectly to any of the three NSAIDs. The signals most upstream, at 7.05 and 7.15 ppm may originate both from sulindac or sulindac sulfone, suggesting an oxidized state of the NSAID in the fibril bound state, but analysis of the difference spectrum is difficult. The large signal difference at ca. 2.5 ppm originates from incomplete deuteration of different DMSO-d_6 batches used.

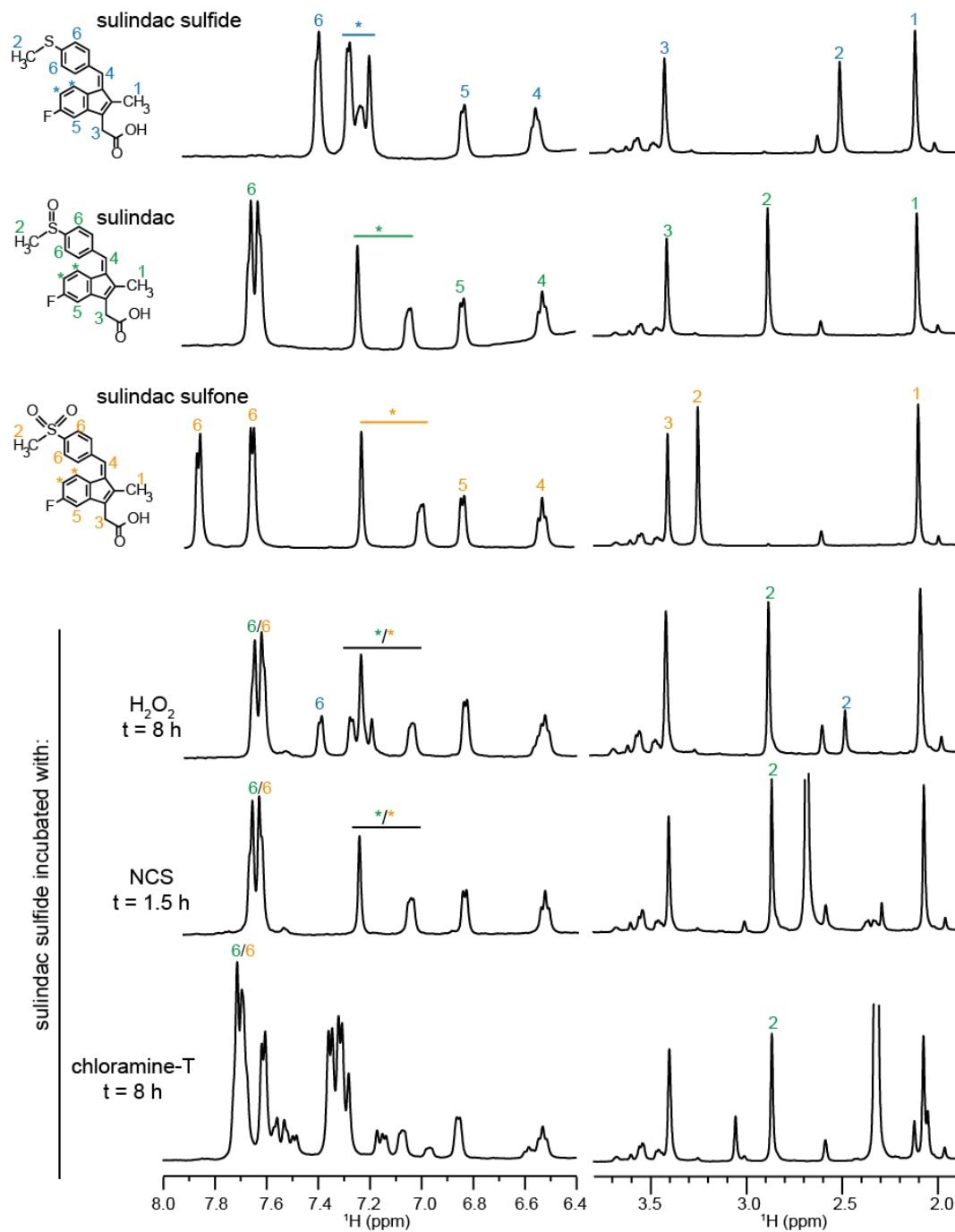


Figure 3.25: Oxidation of NSAIDs. The NSAIDs sulindac sulfide, sulindac and sulindac sulfone were dissolved in aqueous buffer to 200 μ M containing 0.4% DMSO- d_6 . Reference 1D-¹H spectra are shown in the top part. Assignments are indicated in blue, green and yellow, respectively. Sulindac sulfide was incubated with 20 mM H₂O₂, 1 mM NCS and 1 mM T-chloramine for 1.5 h, 8 h and 8 days. Representative time points are shown for each oxidizing reagent. Experiments were recorded at 298 K and 600 MHz.

A β incubated with NCS and sulindac sulfide - A β incubated with NCS

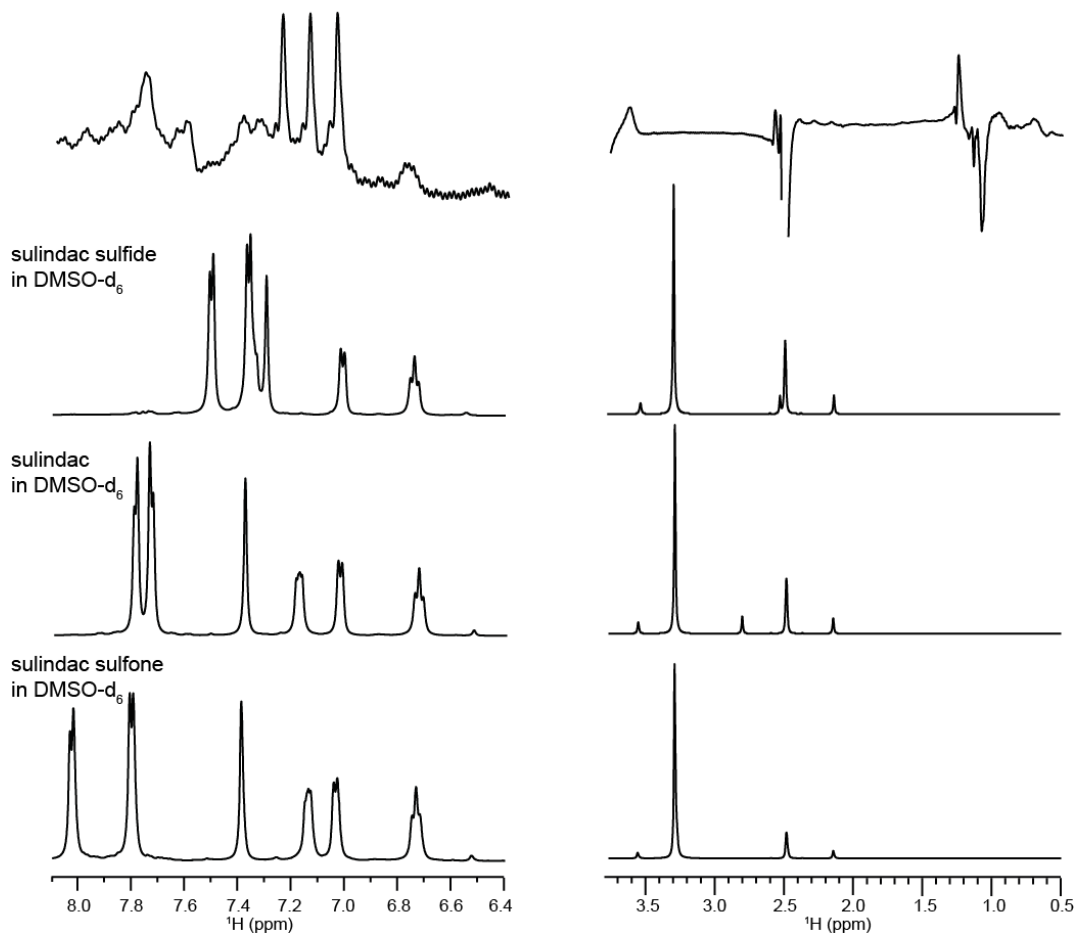


Figure 3.26: The oxidized state of fibril bound NSAIDs. The $1\text{D-}^1\text{H}$ spectrum of A β fibrils incubated with NCS was subtracted from the $1\text{D-}^1\text{H}$ spectrum of A β fibrils incubated with NCS and sulindac sulfide. Samples were prepared as described for Figure 3.24. The resulting difference spectrum containing NSAID signals only is shown in the top panel. The three lower spectra represent $1\text{D-}^1\text{H}$ spectra of sulindac sulfide, sulindac and sulindac sulfone dissolved at concentrations of 1 mM in DMSO-d_6 . Experiments were recorded at 298 K and 600 MHz.

3.6 Interaction of ISMs with A β ₁₋₄₀

The IAPP cross-amyloid interaction surface mimic (ISM) L3-GI inhibits and reverses A β aggregation and reduces its neurotoxicity^[378]. To understand the molecular interaction on a molecular level, we carried out solution-state NMR experiments to probe L3-GI binding to A β ₁₋₄₀. For this purpose, L3-GI was added to 20 μ M A β ₁₋₄₀ in a 1-X and a 10-X molar excess (Figure 3.27).

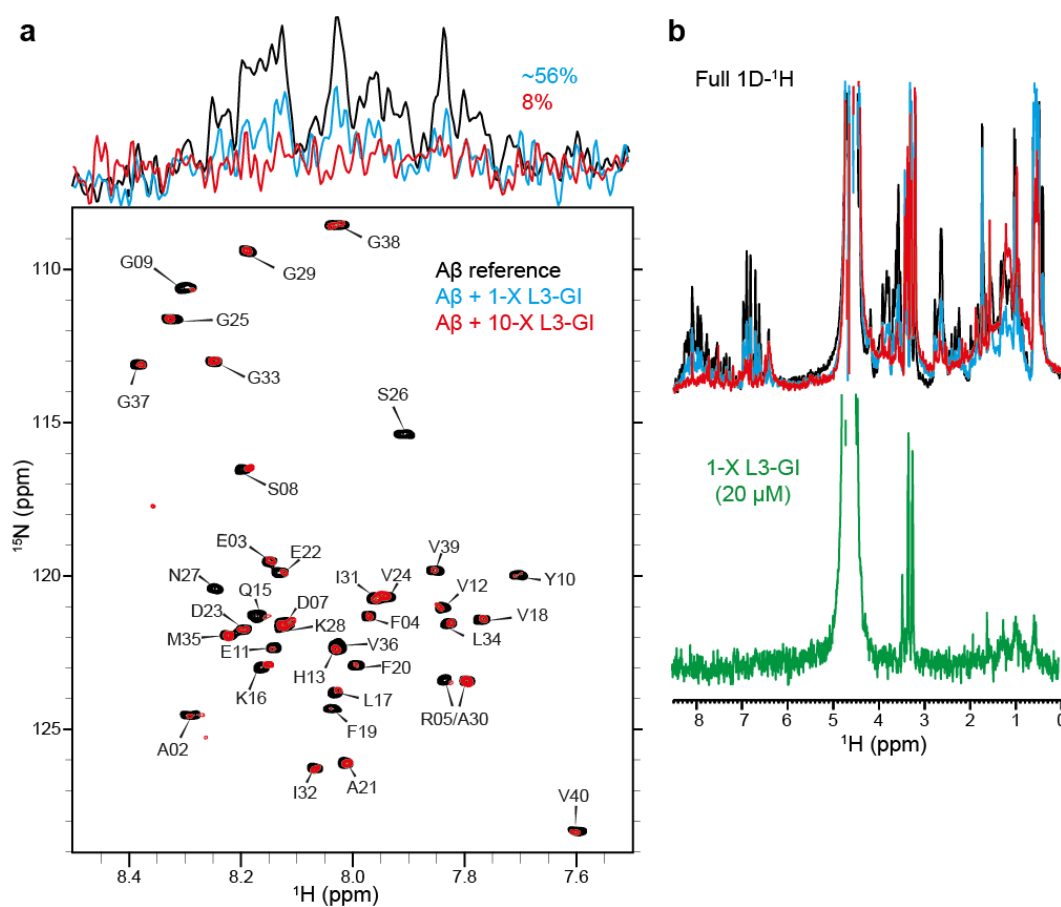


Figure 3.27: Interactions of L3-GI with A β . (a) 2D ^1H - ^{15}N HMQCs of 20 μM A β ₁₋₄₀ incubated with a 1-X (blue) and a 10-X molar excess of L3-GI. Corresponding 1D- ^1H spectra are shown above the 2D to illustrate A β ₁₋₄₀ aggregation. The peptides were incubated in HFIP before being dissolved in buffer. (b) Full 1D- ^1H spectra of 20 μM A β ₁₋₄₀ incubated with a 1-X (blue) and a 10-X (red) molar excess of L3-GI and 20 μM L3-GI (green). Experiments were recorded at 277 K and 750 MHz.

At a 10-X molar excess of the ISM, only 8% of A β ₁₋₄₀ remains soluble. The peptide inhibitor does not affect A β ₁₋₄₀ CS, although some very minor changes can be observed for R05, S08-G09, E11-V12, Q15-L17 and E22. The peptides were allowed

to react in a film of the organic solvent HFIP. In the presence of L3-GI, $A\beta_{1-40}$ aggregates out of solution in a concentration dependent manner (Figure 3.27a). The $1D-^1H$ spectrum reveals that like $A\beta_{1-40}$, L3-GI is not soluble upon incubation with $A\beta_{1-40}$, as no signals of the unlabeled inhibitor peptide are observable at a 10-X molar excess (Figure 3.27b). A $1D-^1H$ spectrum of pure L3-GI demonstrates that the ISM is insoluble at 20 μM .

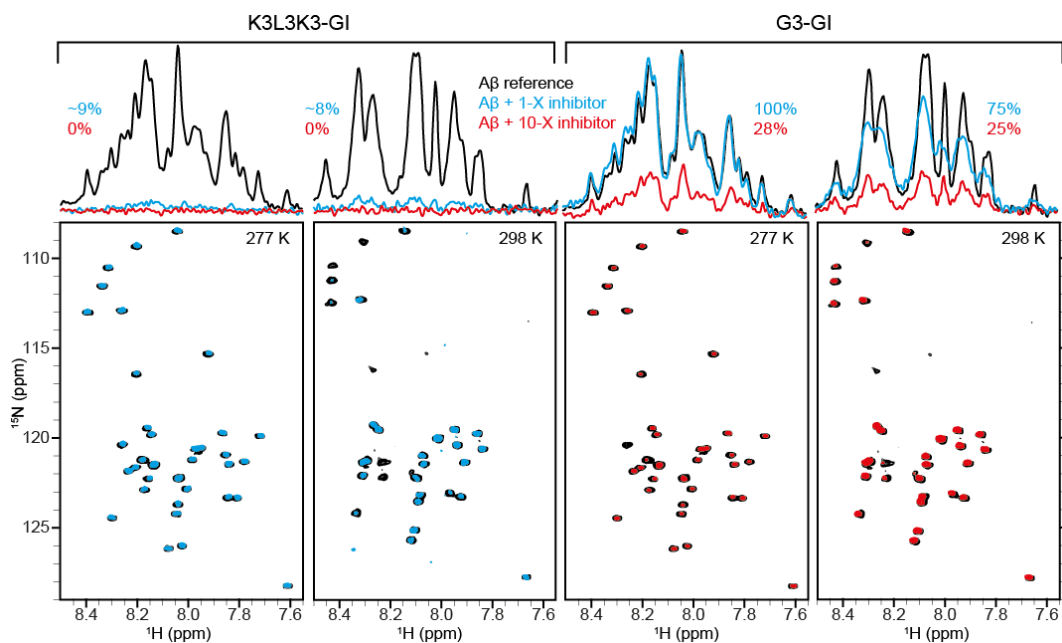


Figure 3.28: Interactions of K3L3K3-GI with $A\beta$ in an HFIP film. $2D\ ^1H-^{15}N$ HMQCs of 20 μM $A\beta_{1-40}$ incubated with a 1-X (blue) and a 10-X molar excess of K3L3K3-GI (left) and G3-GI (right). Corresponding $1D-^1H$ spectra are shown above the 2D to illustrate $A\beta_{1-40}$ aggregation. The peptides were incubated in HFIP before being dissolved in buffer. Experiments were recorded at 277 K and 298 K and 600 MHz.

In order to enhance solubility and to find a suitable system that can be studied by NMR, L3-GI was resynthesized with three lysine tags on each terminus (K3L3K3-GI). $A\beta_{1-40}$ was incubated with K3L3K3-GI at a 1-X and a 10-X molar excess in the same conditions as previously (Figure 3.28). K3L3K3-GI efficiently reduces the amount of soluble $A\beta_{1-40}$, even at a 1-X molar excess, and does not cause $A\beta_{1-40}$ CSPs. Recording the NMR experiments at a higher temperature of 298 K does not alter the effect of K3L3K3-GI on $A\beta_{1-40}$. Thus, K3L3K3-GI can be employed in further analysis. The ISM G3-GI fails to inhibit $A\beta$ or IAPP fibrillation, and can therefore be used as a negative control. Indeed, when incubated with G3-GI, $A\beta_{1-40}$ remains soluble compared to incubation with K3L3K3-GI. A 1-X molar excess of G3-GI has no impact

on $A\beta_{1-40}$ solubility. A 10-X molar excess reduces the $A\beta_{1-40}$ population to 28%, however 0% is left in solution when incubated with K3L3K3-GI. Likewise, G3-GI does not influence $A\beta_{1-40}$ CS.

The aim of this study is to understand the $A\beta$ -ISM interaction at an atomic level. However, since $A\beta_{1-40}$ aggregates in the presence of the inhibitor, it becomes invisible to solution-state NMR. In principle, the aggregated peptides can be investigated by solid-state NMR. The peptides are incubated in HFIP, which is evaporated during sample preparation. Upon addition of the buffer, no macromolecular aggregates can be observed in solution by eye. Most likely, $A\beta$ peptides stay within the HFIP film. As the peptides must be accessible to be packed into a rotor, the protocol cannot be used for the preparation of solid-state NMR samples. The interaction study of $A\beta_{1-40}$ and K3L3K3-GI was therefore repeated under different conditions to optimize the protocol for the preparation of a solid-state NMR sample. For this purpose, both peptides were dissolved and incubated in solution. It was found that the presence of HFIP is crucial for the inhibitory effect of the ISMs.

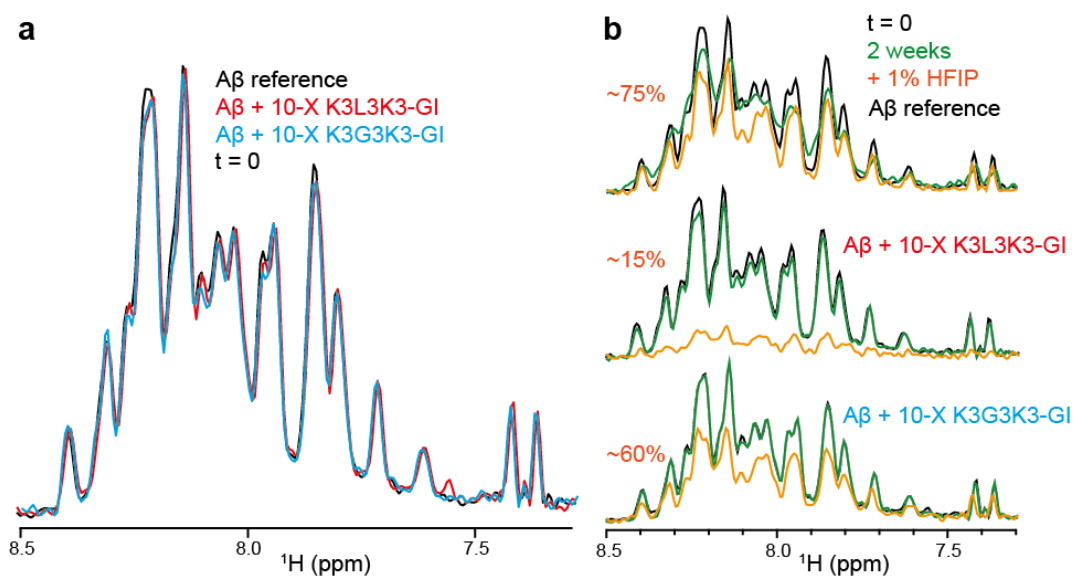


Figure 3.29: Interactions of K3L3K3-GI with $A\beta$ in the absence of HFIP. (a) 1D- 1H spectra extracted from 2D 1H - ^{15}N HMQCs of 20 μM $A\beta_{1-40}$ incubated with 10-X molar excesses of K3L3K3-GI (red) and K3G3K3-GI (blue). (b) 1D- 1H spectra extracted from 2D 1H - ^{15}N HMQCs of 20 μM $A\beta_{1-40}$ incubated with 10-X molar excesses of K3L3K3-GI (red) and K3G3K3-GI (blue) measured after two weeks before (green) and after (orange) the addition of 1% HFIP.

More specifically, a solution of monomeric $A\beta_{1-40}$ dissolved in 10 mM NaOH and 50 mM Na-Phosphate, 50 mM NaCl, pH 7.4 as described in Section 2.2.4.6 was prepared and incubated with the peptide inhibitor, which was dissolved in 1 mM HCl (Figure 3.29). The ^{15}N -edited 1D- ^1H spectra demonstrate that K3L3K3-GI, like the reference K3G3K3-GI, does no longer affect $A\beta_{1-40}$ solubility (Figure 3.29a). The samples were stable for 2 weeks (Figure 3.29b). Upon the addition of 1% HFIP after 2 weeks, $A\beta_{1-40}$ incubated with K3L3K3-GI aggregated immediately to ca. 15%, whereas 60% of $A\beta_{1-40}$ incubated with K3G3K3-GI remained soluble. Therefore, the presence of HFIP is necessary for the interaction of $A\beta$ with the ISM. This effect can be observed when the experiments are repeated with a fresh solution of monomeric $A\beta_{1-40}$ and immediate addition of 1% HFIP (Figure 3.30). Under these conditions, K3L3K3-GI causes 50% aggregation at a 1-X molar excess, and complete aggregation at a 10-X molar excess. This seems to be a time-dependent process, as the soluble $A\beta_{1-40}$ population is decreased to 33% at 1-X K3L3K3-GI after 6 days. This is a specific effect, as the negative control G3-GI does not cause $A\beta_{1-40}$ aggregation. As in experiments observed before, the presence of ISMs does not affect $A\beta_{1-40}$ CS. Differences in solubilities of the two peptide inhibitors is demonstrated full 1D- ^1H spectra in Figure 3.30b. Whereas the intensities of G3-GI signals increases according to its concentration, K3L3K3-GI seems to aggregate along with $A\beta_{1-40}$ into co-aggregates.

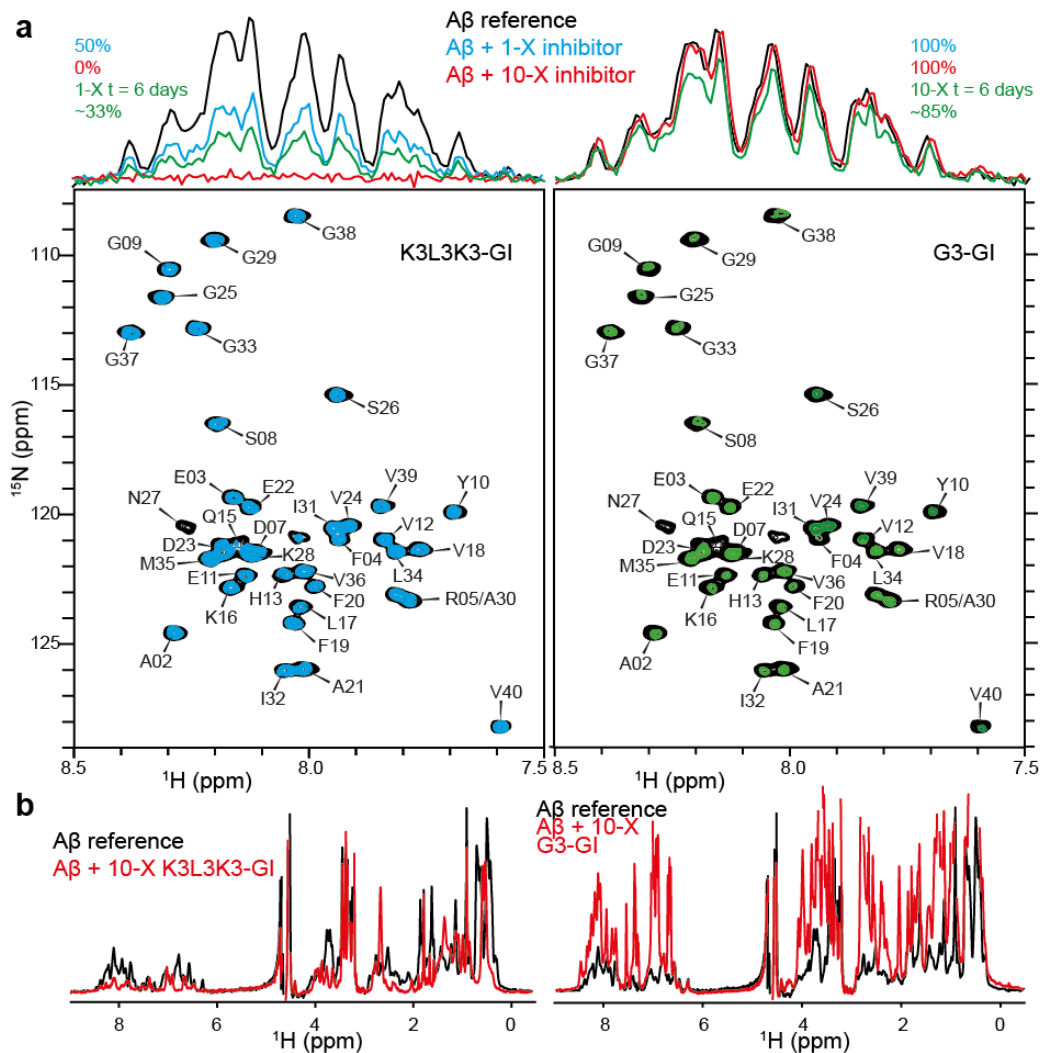


Figure 3.30: Interactions of K3L3K3-GI with A β in the presence of HFIP. (a) 2D ^1H - ^{15}N HMQCs of 20 μM A β_{1-40} incubated with K3L3K3-GI (left) and G3-GI (right). The peptides were incubated at a 1-X (blue) and a 10-X (red) molar excess, and useful samples were measured again after 6 days (green). Corresponding 1D- ^1H spectra are shown above the 2D to illustrate A β_{1-40} aggregation. (b) Full 1D- ^1H spectra of 20 μM A β_{1-40} incubated with a 10-X molar excess (red) of K3L3K3-GI and G3-GI. Experiments were recorded at 277 K and 600 MHz.

Solution-state NMR serves as a tool to determine the conditions to be used for the preparation of a solid-state NMR sample. Insoluble particles are observed in experiments reported in Figure 3.30, where a monomeric A β_{1-40} solution containing 1% HFIP was incubated with K3L3K3-GI. Therefore similar conditions were applied for the preparation of A β_{1-40} -K3L3K3-GI co-aggregates at a larger scale. A 1-X molar excess of the peptide inhibitor was used, as it is actively aggregating A β_{1-40} at this concentration. The mixture was incubated for 14 days in order to deplete the soluble fraction further. The aggregates were measured by MAS solid-state NMR spectroscopy (Figures 3.31 and 3.32).

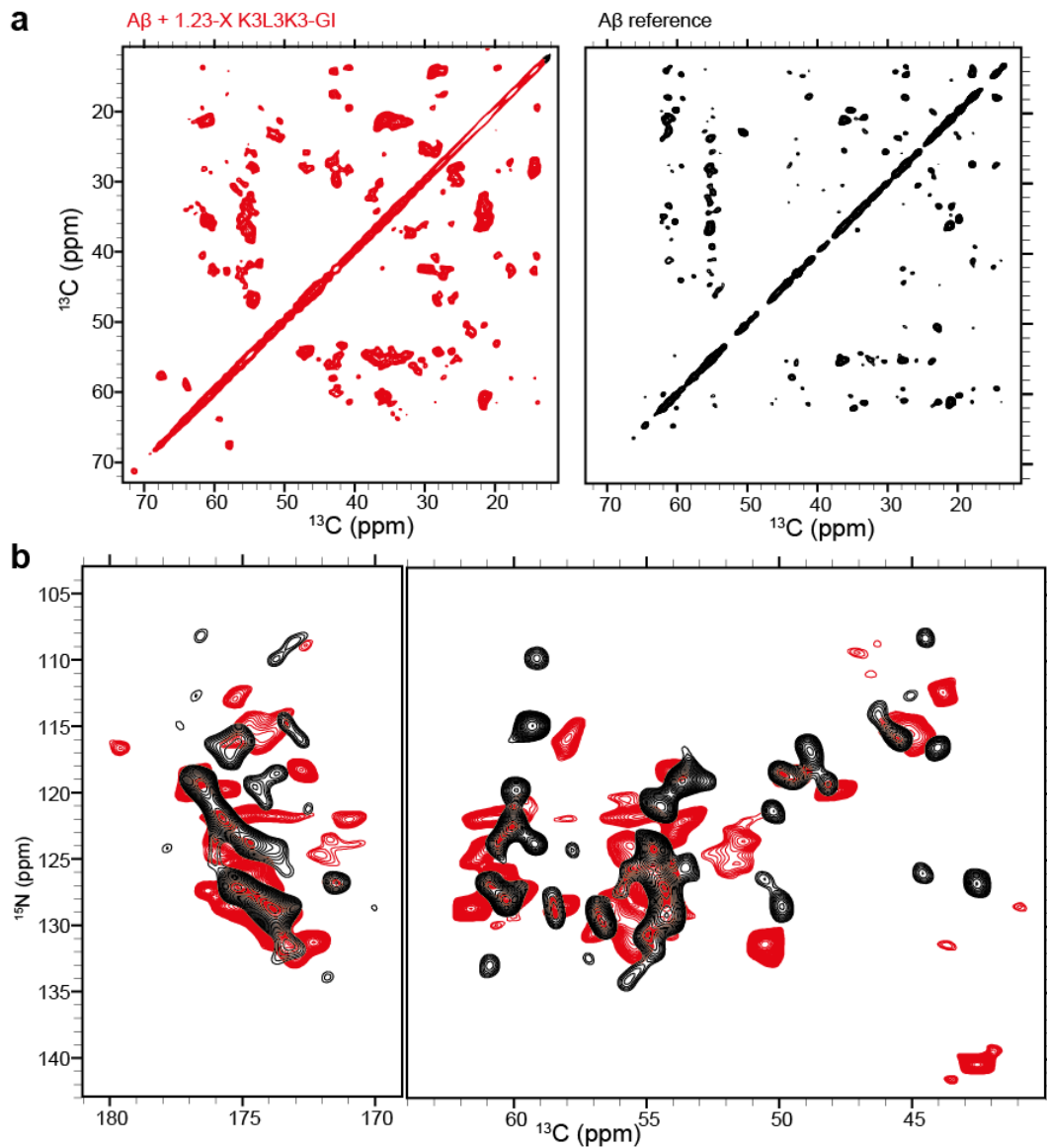


Figure 3.31: MAS solid-state NMR spectra of K3L3K3-GI induced A β aggregates. Monomeric A β_{1-40} at a concentration of 20 μ M was incubated with a 1.23-X molar excess of K3L3K3-GI (red) and seeded A β_{1-40} fibrils incubated with 1% DMSO- d_6 . (a) 2D ^{13}C - ^{13}C PDSD correlation spectra and (b) 2D ^{13}C - ^{15}N TEDOR spectra. Experiments were recorded at a MAS rotation frequency of 15.5 kHz, 270 K and 750 MHz. A PDSDs mixing time of 50 ms was employed.

Only A β_{1-40} appears in the spectra, as it is uniformly ^{13}C and ^{15}N labeled, whereas K3L3K3-GI is unlabeled. The resulting 2D ^{13}C - ^{13}C PDSD (Figure 3.31a and 3.32a) and ^{13}C - ^{15}N TEDOR (Figure 3.31b) correlations reveal well resolved A β_{1-40} signals indicating structural homogeneity within the co-aggregates. The spectra are superimposed with seeded A β_{1-40} fibrils (in the presence of 1% DMSO- d_6). The spectra display clear differences between seeded fibrils and the ISM induced

aggregates. However, the overall folds are similar, pointing to β -sheet formation. Judging from TEM images, $A\beta_{1-40}$ forms short fibrillar structures when aggregated in the presence of K3L3K3-GI (Figure 3.32b).

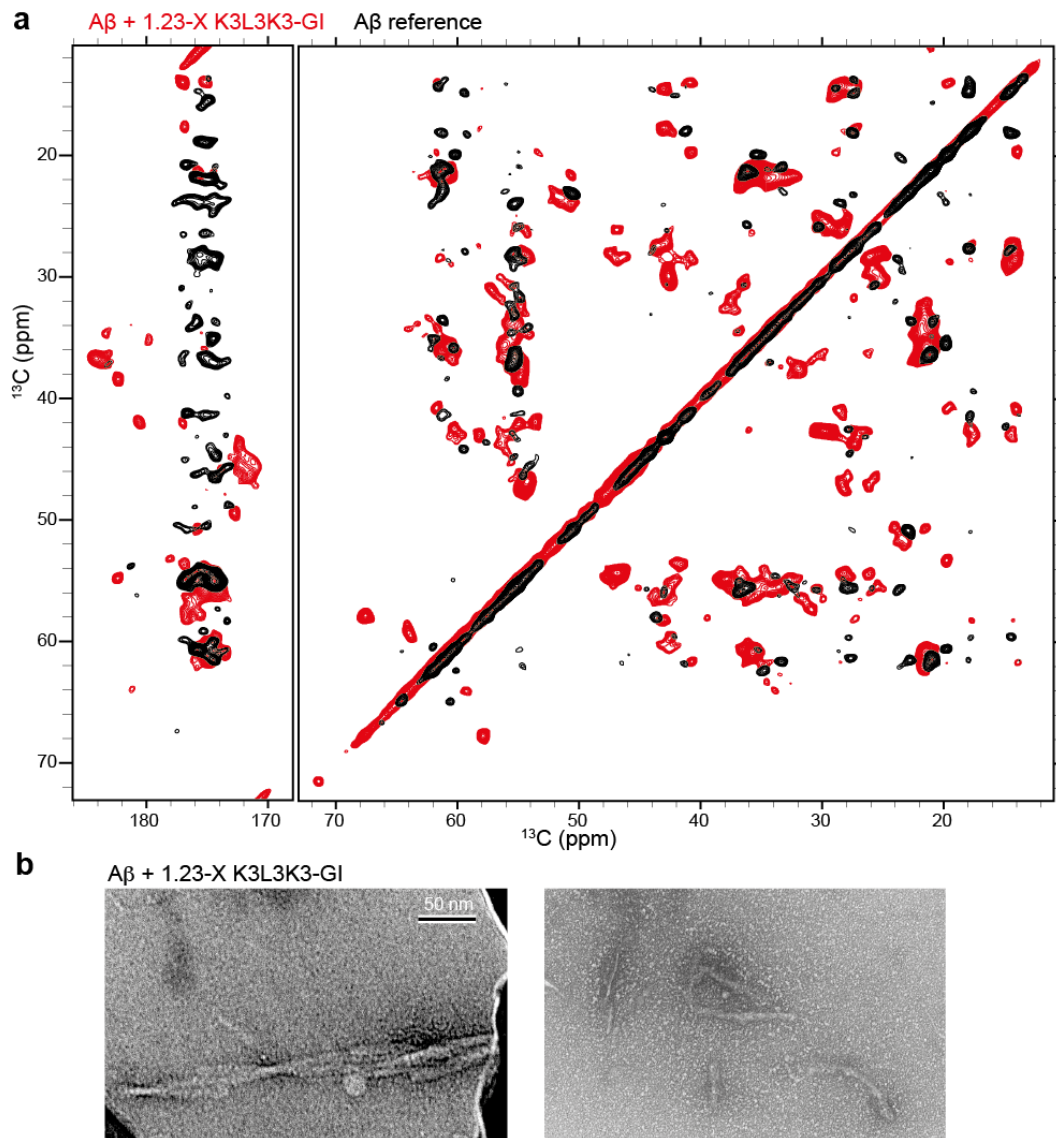


Figure 3.32: $A\beta$ incubated with K3L3K3-GI. (a) Superimposition of 2D ^{13}C - ^{13}C PDSD correlation of monomeric $A\beta_{1-40}$ at a concentration of $20\ \mu\text{M}$ was incubated with a 1.23-X molar excess of K3L3K3-GI (red) and seeded $A\beta_{1-40}$ fibrils incubated with 1% DMSO-d_6 . (b) TEM images $A\beta_{1-40}$ incubated with a 1.23-X molar excess of K3L3K3-GI. Scale bar = 50 nm.

3.7 Solution-state NMR structure of R3-GI

Although it is well known that ISMs interfere with amyloid aggregation, it is not understood how the inhibitors act on a molecular level. It has been suggested that such peptides mimic the IAPP cross-amyloid interaction surface and thereby exert inhibitory effects^[378]. To elucidate structural details, we investigated the solution-state NMR structure of ISMs. Part of the reported work has been published by Andreetto *et al.*^[378]. For this purpose, we employed the ISM containing an arginine linker (R3-GI). Although this peptide contains the least amount of β -sheet elements in all inhibitory ISMs, it has proven to be the most applicable peptide for solution-state NMR spectroscopic analysis.

The peptide yields a well resolved homonuclear 2D ^1H - ^1H NOESY spectrum (Figure 3.33). Individual spins systems could be identified in the NOESY and sequential assignment was possible due to $\text{HN}_{(i)}\text{-HN}_{(i\pm 1)}$ and $\text{HN}_{(i)}\text{-H}\alpha_{(i-1)}$ contacts. Two sets of peaks are observed for residues N15-L20, indicating the presence of two conformations in this region, which may arise due to cis-trans isomerizations induced by G17 and I19 N-methylations. Additionally, a third set of signals for I19 is found. Sequential contacts for both conformers are presented in Figure 3.33a. ^{13}C chemical shifts were obtained from a 2D ^1H - ^{13}C spectrum involving ^{13}C natural abundance. Individual ^{15}N chemical shifts were collected from selectively labeled R3-GI sample containing U- ^{13}C , ^{15}N labeling at residues A06, V10, L20 and S21. 2D ^1H - ^{15}N as well as ^1H - ^{13}C HSQCs of the partially labeled R3-GI are shown in Figure 3.33a-b. All assigned R3-GI chemical shifts are listed in Appendix 5.2.4.

After obtaining the full CS assignment, it was possible to further analyze the spectrum for structurally relevant long distance NOEs. Indeed, several NOEs between distant residues in the primary sequence are observed, which could potentially support the formation of a loop. Representative long distance NOEs are presented in Figure 3.34, and a full list is shown in Table 3.5.

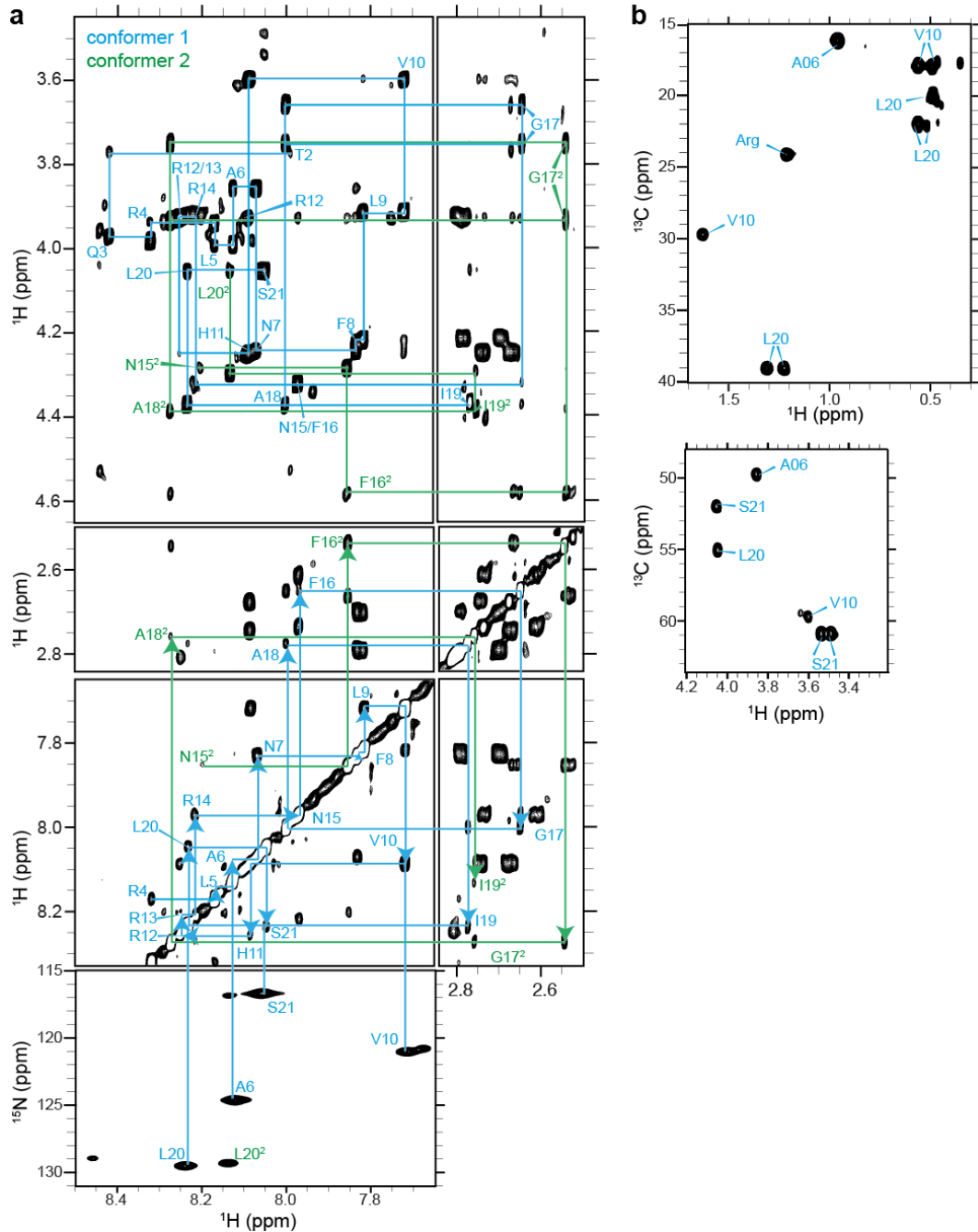


Figure 3.33: 2D ^1H - ^1H NOESY of R3-GI including assignments. (a) 2D ^1H - ^1H NOESY of 500 μM R3-GI including assignment of residues A01-S21. A second conformer is observed for residues N15-L20. Sequential assignments are represented for HN-H α and HN-HN regions for conformer 1 (blue) and conformer 2 (green, superscript "2"). The lowest panel shows the ^1H - ^{15}N HMQC of 500 μM R3-GI uniformly ^{13}C and ^{15}N labeled at residues A06, V10, L20 and S21. Extracts of the 2D ^1H - ^{13}C HSQC recorded for the partially labeled R3-GI sample are shown in (b). Experiments were recorded at 277 K and 900 MHz and a NOESY mixing time of 300 ms. The figure is adapted from Andreetto *et al* [378].

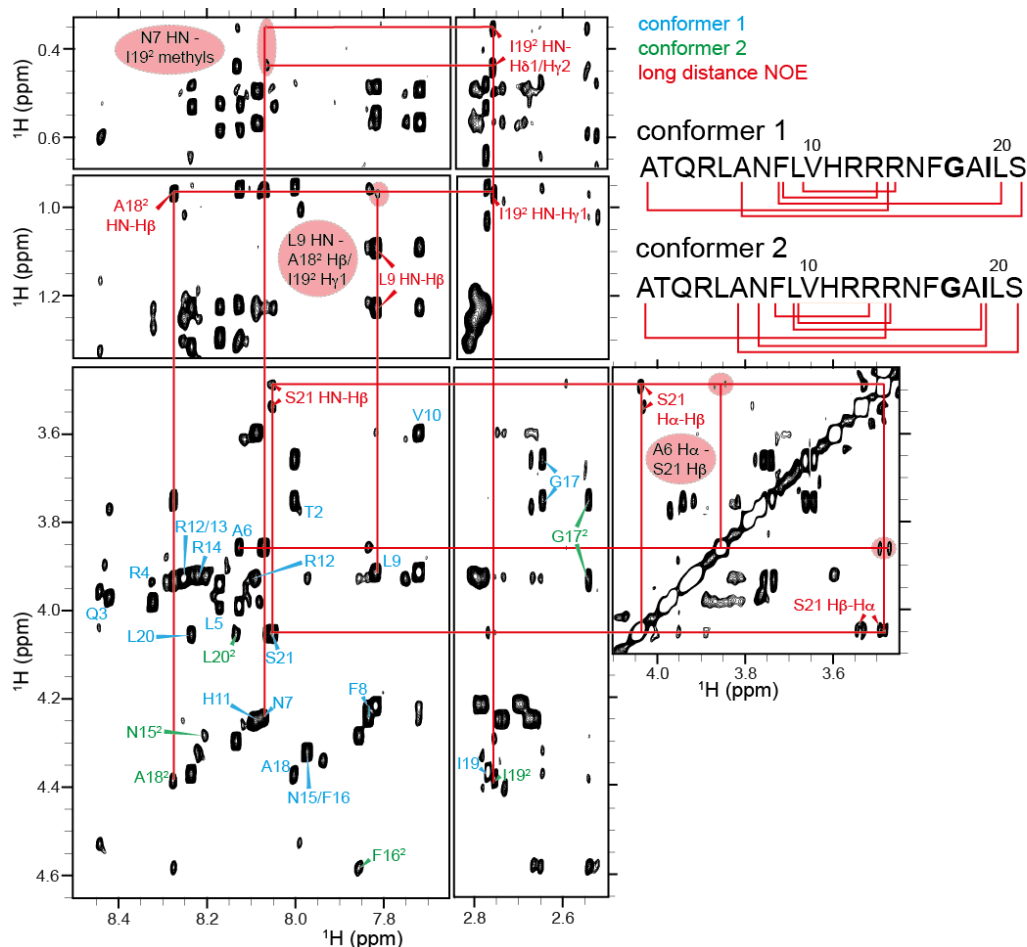


Figure 3.34: Long range NOEs observed for R3-GI. 2D ^1H - ^1H NOESY of 500 μM R3-GI, including assignments of conformer 1 (blue) and conformer 2 (green). Long range NOEs are indicated in red and plotted onto the peptide sequence for both conformers (N-methylated G17 and I19 are marked in bold). A list of all observed long range NOEs and measured distances is listed in Table 3.4. The experiment was recorded at 277 K and 900 MHz and a NOESY mixing time of 300 ms. The figure is adapted from Andreetto *et al* [378].

Residue interaction maps of both conformers illustrate all NOE contacts observed in the interresidual NOESY spectrum (Figure 3.35a). The shading intensity correlates to the amount of NOEs observed for the residues. The majority of contacts are observed between residues i and $i+1$ and $i+2$, indicative of helical content. Several structurally relevant long distance NOEs are observed in both conformers, as mentioned before. Some long-distance NOEs are observed for both conformers, and some are unique for conformers 1 or 2. CD spectroscopy suggests a high β -sheet content for inhibitory ISMs and a mixture of β -sheet and random coil content for R3-GI [378]. Analysis of the obtained CS by TALOS+ and secondary chemical shift predicts a mainly random coil character for R3-GI (Figure 3.35b).

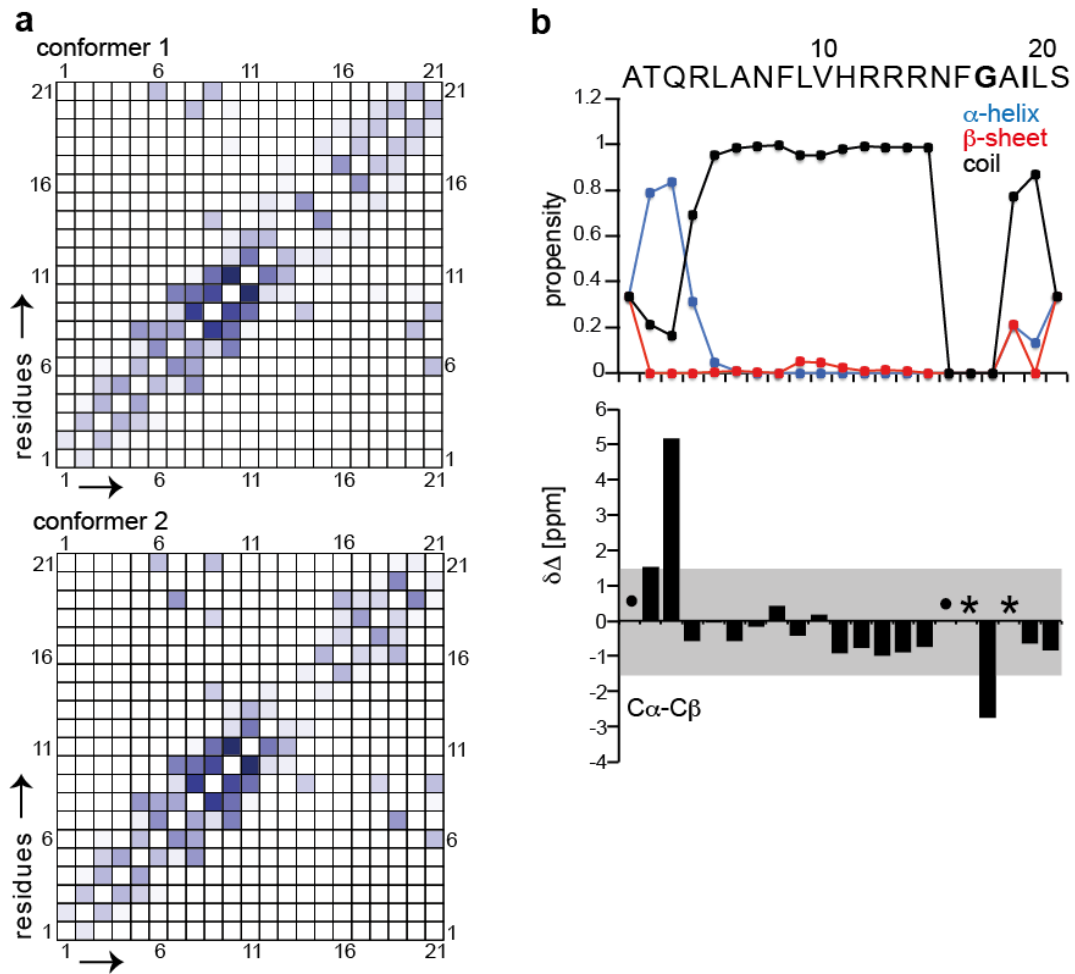


Figure 3.35: Residue interaction map and secondary structure of R3-GI. (a) Residue interaction map of NOEs observed in the 2D ^1H - ^1H NOESY spectrum of R3-GI. Both axes represent the peptide sequence. Filled squares indicate an NOE observed between the two residues. The shading of the colored filling represents the number of NOEs observed, where a stronger intensity represents a higher number of NOEs. The NOE patterns are indicative for secondary structural content. The images were generated by CcpNmr^[389]. (b) Secondary structural elements as predicted by TALOS+ (top panel), and secondary chemical shifts $\Delta\delta_{C\alpha}-\Delta\delta_{C\beta}$ (ppm) (lower panel). The propensities for the formation of random coil (black) and β -sheet (red) and α -helical (blue) elements are shown for TALOS+. The gray bar indicates a range of ± 1.4 ppm ($\Delta\delta_{C\alpha}-\Delta\delta_{C\beta}$), as this is the range of random coil CS specified by Wishart *et al.*^[390]. Values within this range are considered insignificant. • no CS assignment. * No random coil CS values were found for N-methylated G17 and I19.

It has been suggested that inhibitory ISMs form β -hairpin like structures^[378]. To determine the molecular structure of R3-GI, the collected NMR data was subject to structure calculation by ARIA. We calculated preliminary monomeric structures for both conformers (Figures 3.39 and 3.40). It remains unclear whether R3-GI exists as a monomer, dimer or oligomer at above 500 μ M, the concentration used for NMR experiments. Investigations of R3-GI by DLS have predicted a molecular weight of around 4-5 kDa (peak 1), suggesting the formation of monomers or low-n oligomers (Figure 3.36, Table 3.3) However, the DLS results are calculated for globular proteins, and should be treated with caution. Yet, it tentatively excludes the presence of large oligomers. The large particle observed by DLS (peak 2) does not contain mass and thus does not originate from the peptide.

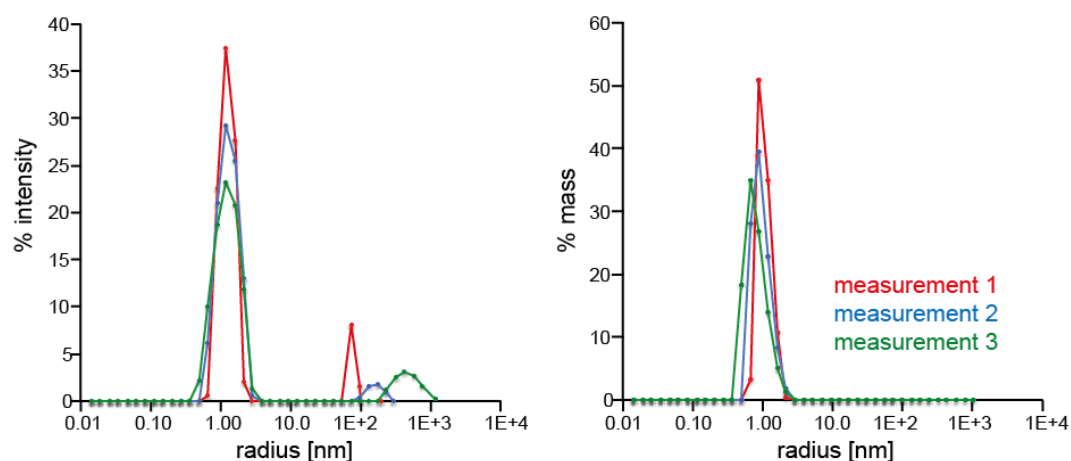


Figure 3.36: DLS of 1mM R3-GI. The % intensity (left) and % mass (right) are plotted as a function of the radius (nm).

	Peak	Radius (nm)	MW (kDa)	Intensity (%)	Mass (%)
Measurement 1	peak 1	1.258	5	90.4	100.0
	peak 2	77.332	88220	9.6	0.0
Measurement 2	peak 1	1.339	5	95.4	100.0
	peak 2	166.689	532104	4.6	0.0
Measurement 3	peak 1	1.301	4	88.2	100.0
	peak 2	498.055	6890780	11.8	0.0

Table 3.3 DLS of 1 mM R3-GI. The molecular mass of the monomeric R3-GI peptide is 2.49 kDa.

Based on the ^1H NMR line widths of around 12-14 Hz in the directly acquired dimension, the peptide presumably exists in a monomeric or low-n oligomeric state, supporting the DLS findings. To avoid bias, we calculated preliminary structures of R3-GI for a symmetric homodimer (Figures 3.41 and 3.42) and pentamer for both conformers. The pentamers contain no major structured regions, and the r.m.s.d. values (\AA) are 9.46 (± 1.18) for backbone atoms and 9.87 (± 1.14) for heavy atoms of conformer 1 and 9.70 (± 1.61) for backbone atoms and 10.26 (± 1.50) for heavy atoms of conformer 2. Due to the high r.m.s.d. values, the pentameric structures were excluded from further analysis. The r.m.s.d. values for monomeric and dimeric structures are listed in Table 3.4. All four determined structures differ significantly, based on the r.m.s.d. values. The monomeric chains within the dimeric structures are different to monomers alone. Residue specific r.m.s.d. demonstrates that the structures are more consistent at around A06-R13 and are more flexible towards the termini (Figure 3.37). Details for structure calculations and output analysis by ARIA can be found in Table 3.10.

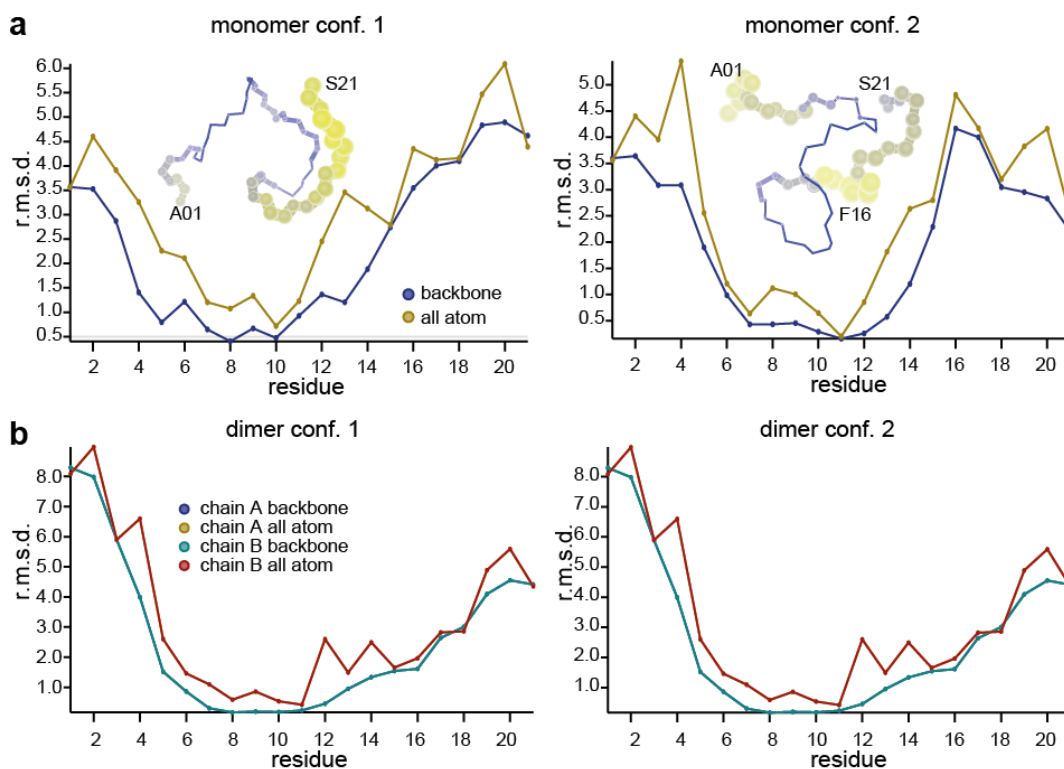


Figure 3.37: Residue specific r.m.s.d. values for preliminary monomeric and dimer R3-GI structures. (a) Residue specific r.m.s.d. values for 10 lowest energy, water refined monomeric structures of R3-GI conformer 1 (left) and conformer 2 (right). r.m.s.d. values are plotted as spheres onto the peptide structure. (b) Residue specific r.m.s.d. values for 10 lowest energy, water refined for chains A and B of dimeric R3-GI structures for conformer 1 (left) and conformer 2 (right). The images were generated by CcpNmr^[389].

r.m.s.d.	Monomer conf. 1	Monomer conf. 2	Dimer conf .1	Dimer conf .2
Monomer conf. 1	0.61	-	-	-
Monomer conf. 2	4.05	0.38	-	-
Dimer conf. 1	5.46	5.90	0.36	-
Dimer conf. 2	5.77	6.03	7.13	1.55

Table 3.4: r.m.s.d. values of preliminary monomeric and dimeric R3-GI structures . r.m.s.d values (Å) for 10 lowest energy, water refined structures are calculated for major structured regions by CcpNmr^[389].

All calculated ARIA structures of R3-GI contain a large amount of random coil structure. A common motif is the presence of two loops in the monomeric and dimeric structures. In the monomers, the first loop comprises A06-F08, followed by a kink at V10-R12 and a loop comprising R12-R14 in conformer 2 (Figure 3.40a) and R14-G17 in conformer 1 (Figure 3.39a). Both monomeric structures adopt a S-like motif. In the dimeric structure of conformer 1, two loops are formed between Q03-A06 and R13-F16 (Figure 3.41a). The dimeric structures of conformer 2 do not yield a well defined bundle and result in a relatively high r.m.s.d. (Table 3.4), hence, no loops can be defined (Figure 3.42a). No significant amounts of secondary structural elements can be detected in any of the obtained structures, consistent with the TALOS+ and secondary chemical shift calculations. The arginine side chains of the R3 linker are not oriented in the same way. Instead, in conformer 1, R12 and R14 are oriented towards the N-terminus and R13 is oriented into the space formed by the second loop (Figure 3.39b). In conformer 2, R13 also points towards the N-terminus, whereas R12 and R14 are oriented towards the surface of the structure (Figure 3.40b). The formation of the S-shaped motifs is supported by hydrogen bonds (Figures 3.39c and 3.40c). For instance, a hydrogen bond connecting R04 and N15 stabilizes the first loop and a hydrogen bond connecting R14 to S21 stabilizes the second loop of the monomeric conformer 1 (Figure 3.39c, Table 3.6). Intermolecular hydrogen bonds are found to stabilize the dimeric structures (Tables 3.8 and 3.9). A table listing all hydrogen bonds detected in one model of each structure is shown below the individual structures.

All observed long distance NOEs were measured in the individual monomeric and dimeric structures. A summary of all long distance NOEs including violations is shown in Table 3.5. All confirmed NOEs are schematically plotted onto the calculated structures (Figure 3.38). For both conformers, most long distance NOEs observed in the NOESY spectrum are confirmed in the monomeric R3-GI structures of both

conformers. Only the NOE observed between L09 H and S21 H β^* is a violation in every structure. In dimeric structures, the NOE may potentially arise from intra- and intermolecular contacts between the two chains A and B. Therefore, both scenarios were taken into account and intra-, as well as intermolecular distances were measured in the dimeric structures. In general, more NOE violations are observed in dimeric structures. Only two long distance NOEs could be confirmed for conformer 1, assuming they both arise from intermolecular contacts. For conformer 2, five long distance NOEs are confirmed, assuming four of the NOEs are caused by intermolecular contacts and one is based on intramolecular contacts. However, given the low r.m.s.d. value and the lack of structural elements in the dimeric structure of conformer 2, the distance measurements are unreliable. The measured distances in the individual structures are depicted in yellow for the monomeric structures in Figures 3.39d and 3.40d-e, as well as in yellow for intramolecular contacts and in blue for intermolecular contacts between chains in the dimeric structures in Figures 3.41c-d and 3.42c-d.

NOE	Monomer conf. 1	Monomer conf. 2	Dimer conf. 1 inter	Dimer conf. 1 intra	Dimer conf. 2 inter	Dimer conf. 2 intra
A06 H α – S21 H β	3.3	2.3	4.0	11.9	3.1	12.7
L09 H δ^* – R14 H δ^*	3.8	4.1	4.5	13.4	12.5	3.1
■A01 H β^* – R14 H α	3.6	5.3	8.0	7.9	3.4	12.5
■F08 H ζ – R13/14 H γ^*	2.6 (R14)	3.0 (R13)	9.9 (R14)	14.3 (R14)	10.9 (R13)	7.6 (R13)
F08 H ϵ – L20 ¹ H	4.4	-	11.9	8.4	-	-
L09 H – A18 ² H β^*	-	3.7	-	-	7.1	7.5
N07 H – I19 ² H γ^*	-	3.8	-	-	4.1	12.2
N07 H – I19 ² H δ^*	-	3.9	-	-	5.1	12.1
L09 H – S21 H β^*	7.7	11.3	8.0	7.7	6.9	9.0

Table 3.5: R3-GI long range NOEs observed in 2D ¹H-¹H NOESY. Lowest distances (Å) as measured between atoms in calculated monomeric and dimeric R3-GI structures. Inter- and intramolecular distances are shown for the dimeric structures. Violations are indicated in red. ■NOE was determined by ARIA. NOEs found in only one conformer are labeled with a superscript number of the respective conformer.

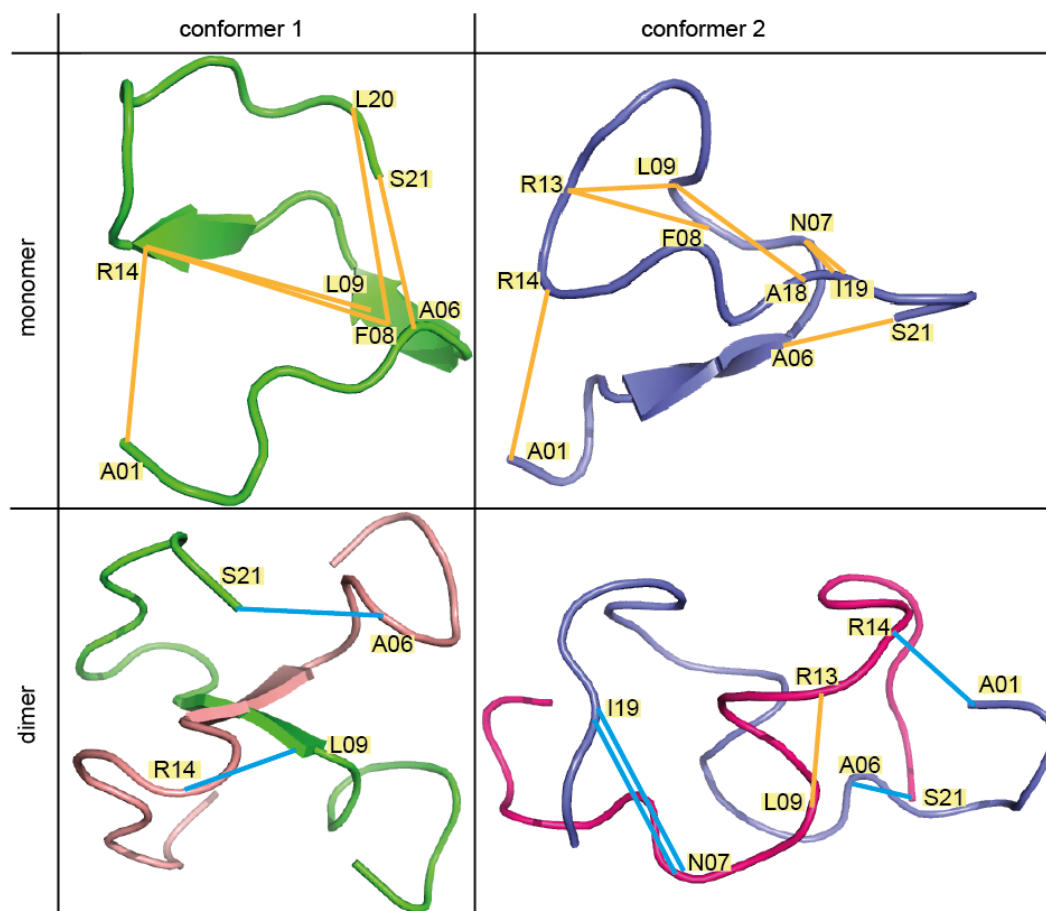


Figure 3.38: R3-GI confirmed long distance NOEs. All confirmed long distance NOEs were plotted onto the structures of conformer 1 and 2 monomeric and dimer structures. Intramolecular contacts are shown in yellow and intermolecular contacts between the two chains of dimers are shown in blue.

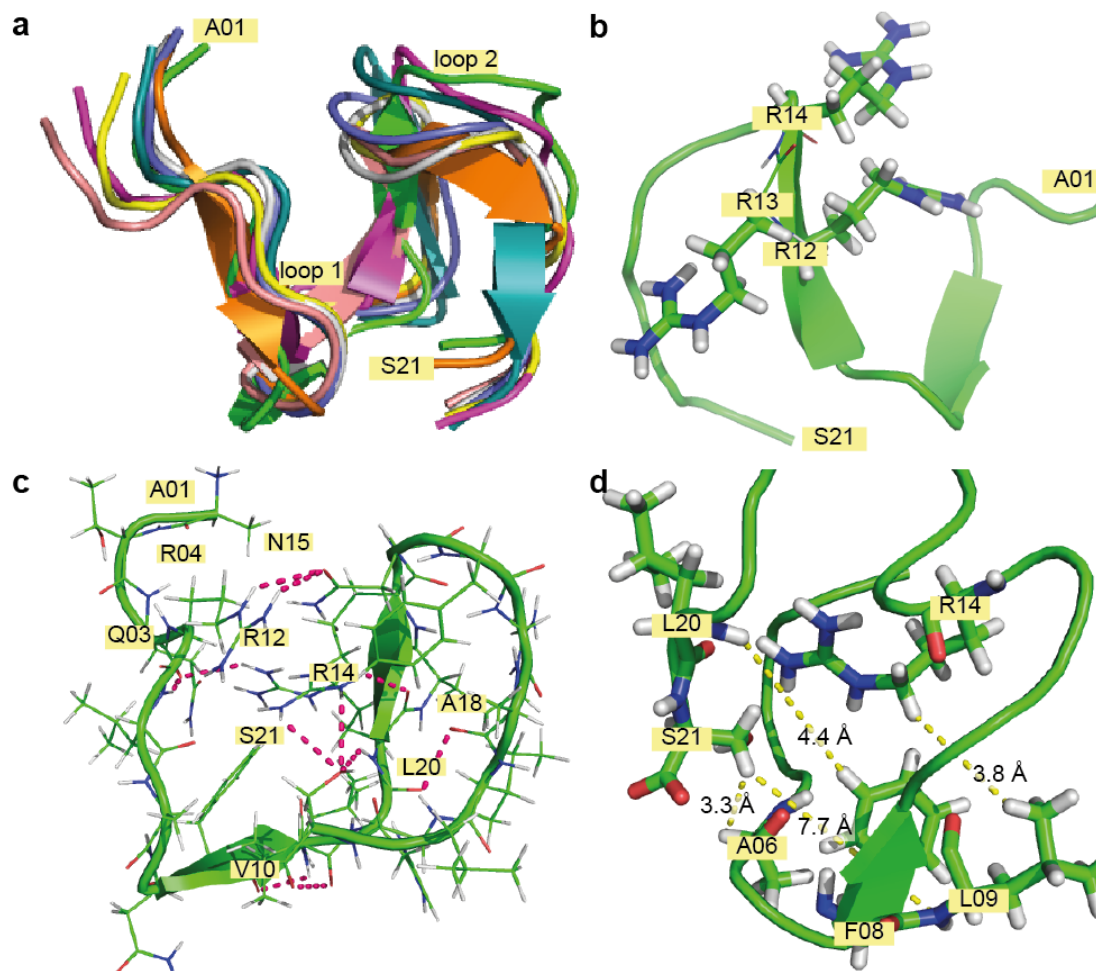


Figure 3.39: Preliminary solution-state NMR structure of monomeric R3-GI conformer 1. (a) Bundle of models for conformer 1 of R3-GI as a monomer. (b) Orientation of arginine side chains in the R3 linker. (c) Hydrogen bonds stabilizing the turns in R3-GI (pink) (Table 3.6). (d) Distances of long range NOEs observed in the 2D ^1H - ^1H NOESY spectrum (yellow).

Donor	Acceptor	Distance (Å)
R04 H ϵ	N15 O δ 1	2.5
R04 H η 21	N15 O δ 1	2.4
R14 H η 12	S21 O γ	2.6
R14 H η 22	S21 O γ	2.9
R12 H	S21 O γ	2.2
R14 H η 11	R12 O	2.3
L05 H	Q03 O	1.5
R12 H η 12	Q03 O	2.5
S21 Term COOH	V10 O	3.1
V10 H	F08 O	2.3
L20 H	A18 O	2.6

Table 3.6: Hydrogen bonds in preliminary monomeric R3-GI structure of conformer 1.

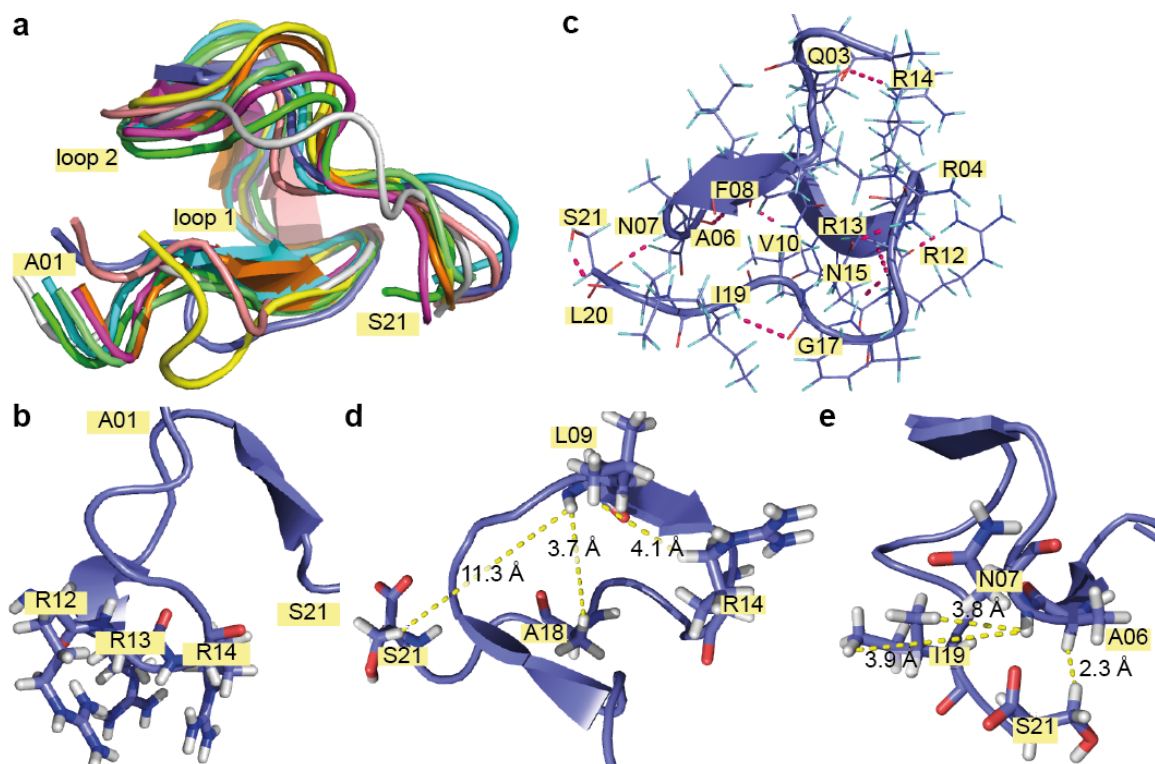


Figure 3.40: Preliminary solution-state NMR structure of monomeric R3-GI conformer 2. (a) Bundle of models for conformer 2 of R3-GI as a monomer. (b) Orientation of arginine side chains in the R3 linker. (c) Hydrogen bonds stabilizing the turns in R3-GI (pink) (Table 3.7). (d-e) Distances of long range NOEs observed in the 2D ^1H - ^1H NOESY spectrum (yellow).

Donor	Acceptor	Distance (Å)
S21 H γ	L20 O	1.9
N07 H	S21 Term COOH	1.9
I19 H	G17 O	2.6
F08 H	A06 O	2.3
R13 H	N15 O	2.7
G17 H	N15 O	1.9
R12 H η 11	R12 O	1.7
R14 H ϵ	Q03 O ϵ 1	2.6
R04 H η 11	N15 O δ 1	1.7
V10 H	F08 O	1.9

Table 3.7: Hydrogen bonds in preliminary monomeric R3-GI structure of conformer 2.

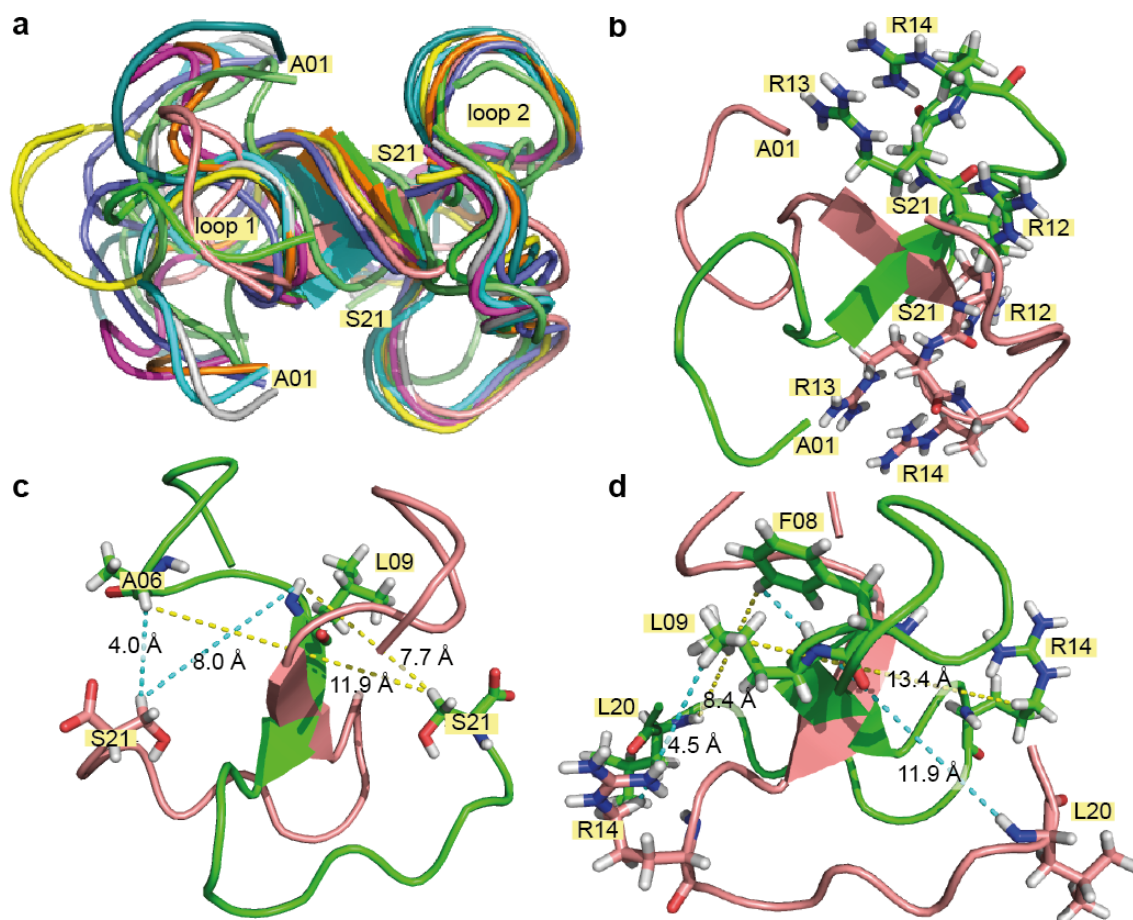


Figure 3.41: Preliminary solution-state NMR structure of dimeric R3-GI conformer 1. (a) Bundle of models for conformer 1 of R3-GI as a dimer. (b) Orientation of arginine side chains in the R3 linker. (c-d) Distances of long range NOEs observed in the 2D ^1H - ^1H NOESY spectrum within the same chain (yellow) or intermolecular contacts between the two chains (blue).

Donor	Acceptor	Distance (Å)
(B) S21 H γ	(A) A06 O	2.7
(A) R13 H η 21	(B) S21 O γ	2.0
(A) R13 H ϵ	(B) S21 O γ	1.9
(B) V10 H	(A) R12 O	1.8

Table 3.8: Intermolecular hydrogen bonds in preliminary dimeric R3-GI structure of conformer 1. The chain is indicated in parantheses.

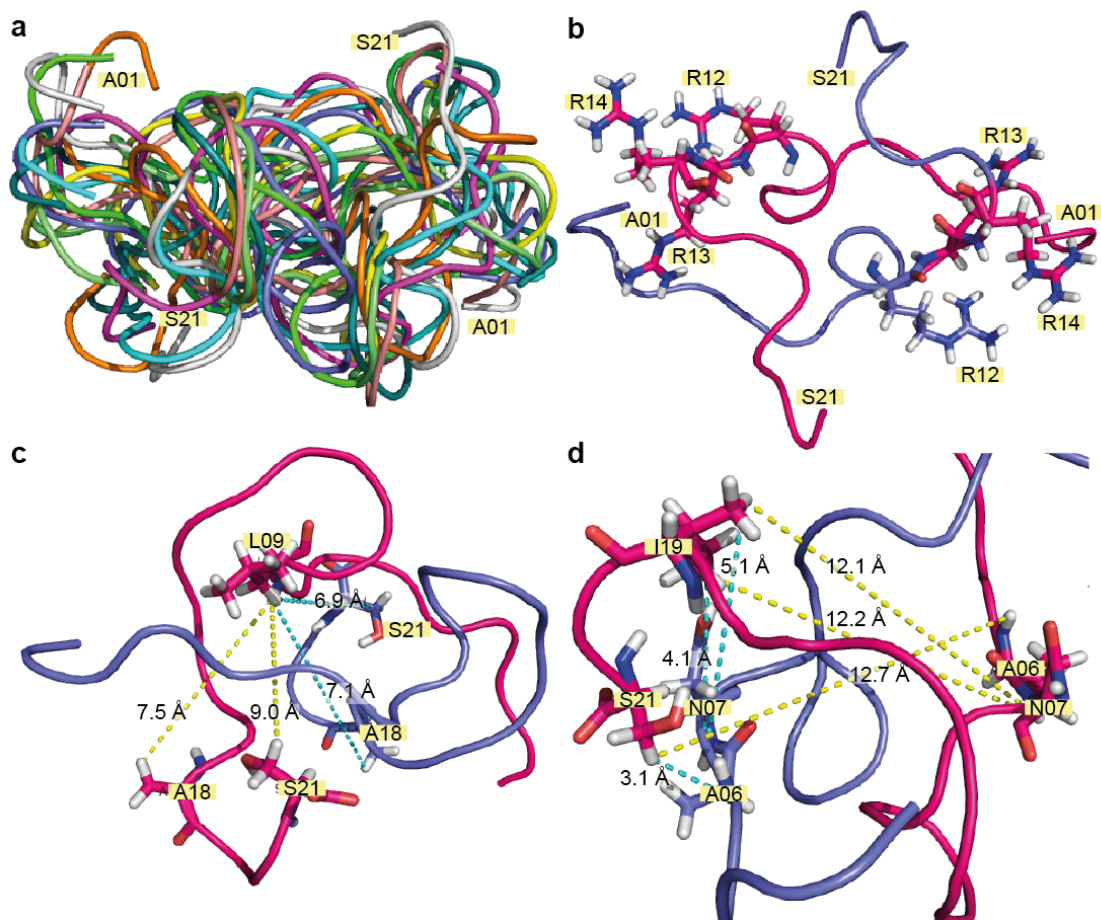


Figure 3.42: Preliminary solution-state NMR structure of dimeric R3-GI conformer 2. (a) Bundle of models for conformer 2 of R3-GI as a dimer. (b) Orientation of arginine side chains in the R3 linker. (c-d) Distances of long range NOEs observed in the 2D ^1H - ^1H NOESY spectrum within the same chain (yellow) or intermolecular contacts between the two chains (blue).

Donor	Acceptor	Distance (Å)
(A) R14 H η 21	(B) A01 O	2.1
(A) R14 H η 12	(B) Q03 O	2.3

Table 3.9: Intermolecular hydrogen bonds in preliminary dimeric R3-GI structure of conformer 2. The chain is indicated in parantheses.

	monomer		dimer	
	conformer 1	conformer 2	conformer 1	conformer 2
NMR restraints				
NOE distance restraints	458	455	468	529
dihedral angles ($\phi+\psi$)	30	28	-	-
Structure statistics				
Violations				
Distance violations (> 0.5 Å)	98.9 ± 3.14	77.2 ± 4.42	9.2 ± 4.31	19.3 ± 8.67
Dihedral angle violations (> 5°)	14.4 ± 2.24	9.6 ± 1.35	-	-
Average r.m.s.d. (Å)				
Backbone	2.09 ± 1.46	1.89 ± 1.30	3.30 ± 0.87	3.62 ± 0.50
Heavy	2.78 ± 1.59	2.62 ± 1.21	3.6s ± 0.84	4.12 ± 0.44
Major structured regions ^[389]	0.61	0.38	0.36	1.55
Deviations from idealized geometry				
Bonds (Å)	2.52 ± 0.00	2.73 ± 0.00	1.09 ± 0.00	1.33 ± 0.00
Angles (°)	2.06 ± 0.15	1.97 ± 0.11	1.15 ± 0.07	1.42 ± 0.15
Ramachandran plot analysis				
Residues in most favored regions	16.7%	31.1%	18.3%	25.8%
Residues in allowed regions	72.8%	55.5%	55.6%	50.0%
Residues in generously allowed regions	7.8%	10.6%	15.0%	16.1%
Residues in disallowed regions	2.8%	2.8%	11.1%	8.1%

Table 3.10: NMR restraints and statistics of preliminary R3-GI structures calculated by ARIA.

r.m.s.d. values are calculated for the 10 lowest energy, water refined structures.

4. Discussion

4.1 A β interactions with sulindac sulfide

Molecular interactions of A β with sulindac sulfide

It is commonly agreed upon that the NSAID and 1st generation GSM sulindac sulfide influences properties of the AD peptide A β . For instance, sulindac sulfide is able to alter production levels of A β ^[305], and interfere with its aggregation properties^[336]. Furthermore, sulindac sulfide has been reported to bind directly to A β species^[322,333,334]. The details of the impact that sulindac sulfide exerts on amyloids are still a matter of debate^[335]. In this study we investigate the molecular interaction of sulindac sulfide with A β at an atomic level by NMR spectroscopy. In particular, we characterized the mechanism of interaction of sulindac sulfide with induced A β aggregates and seeded mature A β fibrils by MAS solid-state NMR. This technique has been successfully applied in the past to solve structures of large insoluble protein complexes^[48,49,51,52] as well as to characterize amyloids in conjunction with small molecules^[288,296-298,300].

Colloidal sulindac sulfide nonspecifically induces A β aggregation.

In the presence of sulindac sulfide, soluble monomeric A β aggregates rapidly out of solution in a concentration dependent manner, as demonstrated by solution-state NMR spectroscopy (Figure 3.4). Above a critical concentration, sulindac sulfide forms colloidal self-assemblies^[335]. This phenomenon is commonly observed for phenolic compounds^[338] and is known to cause nonspecific protein aggregation^[341]. Several experimental observations support the assumption that A β aggregation by sulindac sulfide is based on a nonspecific mechanism and driven by colloids. Firstly, no chemical shift perturbations are caused by the presence of the sulindac sulfide. Secondly, A β aggregation is uniform throughout the peptide sequence and no regions are more severely affected by sulindac sulfide than others. Thirdly, the total concentration of sulindac sulfide and not the molar ratio to A β is decisive for the amount of aggregated A β , and colloid formation is a concentration dependent

process. Fourthly, A β solubility is unaffected by sulindac sulfone. Unlike sulindac sulfide, sulindac sulfone is highly soluble in aqueous solutions^[335], which we also confirmed by solution-state NMR (Figure 3.6). The lack of colloid formation of sulindac sulfone may be responsible for the persistence of A β solubility and its inefficacy to interfere with A β biogenesis^[322].

The CMC for sulindac sulfide colloid formation has been reported to be around 50 μ M, although this value is dependent on the DMSO concentration^[344]. In our experiments, we observe aggregation of sulindac sulfide at concentrations of ~200-300 μ M (Figure 3.6). Line broadening and signal attenuation of the compound imply large complex formation and chemical exchange. At this NSAID concentration, ~50% of the A β population is aggregated as a consequence of nonspecific interactions. Although sulindac sulfide precipitates by itself in buffer, the aggregation is enhanced in the presence of A β . This suggests that sulindac sulfide and A β aggregate together into complexes. The nonspecific induction of A β aggregation by sulindac sulfide, as well as the formation of co-aggregates is further supported by MAS solid-state NMR experiments.

Sulindac sulfide induces structured A β co-aggregates with reduced neurotoxicity.

Even though monomeric interacts with sulindac sulfide in a nonspecific manner, the resulting aggregates are not amorphous, but well structured. MAS solid-state NMR spectra of the aggregates yield well resolved spectra (Figures 3.8 and 3.9), supporting homogenous structure formation induced by sulindac sulfide. The concentration of sulindac sulfide plays a crucial role for A β aggregation, further indicating the involvement of colloids in the interaction. Spectra of the sample aggregated by a 5-fold molar excess of sulindac sulfide display highly similar patterns to reference aggregates. It seems that a 10-X molar excess is necessary to induce structural changes in the spectra. At this concentration, CSPs are observed especially for several residues including glycines and alanines. Furthermore, new cross peaks originating from isoleucine side chains appear at an increased sulindac sulfide concentration. The presence of such cross peaks indicates a high degree of stability of these side chains and their involvement in NSAID interaction. The A β sample prepared at a 10-X molar excess of sulindac sulfide contains the highest S/N and all further analyses were carried out on this sample.

Resonances of residues V18-G38 are detected in the spectra, suggesting that the C-terminus forms a well structured amyloid core of the NSAID induced aggregates. The lack of signals from the N-terminus is a consequence of broad lines resulting from signal averaging due to flexibility and heterogeneity. Typically, the C-terminus is responsible for A β aggregation^[168]. Analysis of the obtained chemical shifts demonstrates the presence of β -sheet elements (Figure 3.10a). Furthermore, the typical salt bridge connecting D23 and K28 side chains is detectable by TEDOR experiments (Figure 3.10b). Hence, sulindac sulfide does not interfere with the formation of typical A β structural elements. The aggregates appear as short prefibrillar structures in TEM images (Figure 3.7a). SEC analysis demonstrates that A β forms larger oligomers in the presence of sulindac sulfide compared to controls. It is well known that small A β oligomers constitute the toxic amyloid species^[205,209-211]. Indeed, MTT assays demonstrate a reduced neurotoxicity exerted by the relatively smaller sulindac sulfide induced A β aggregates compared to larger A β complexes aggregated by DMSO.

In order to detect sulindac sulfide in the aggregates, we employed the NMR active properties of its ¹⁹F atom. ¹³C-¹⁹F TEDOR experiments allow the detection of ¹³C atoms in proximity of ¹⁹F via dipolar couplings. The resulting spectrum features signals from the entire protein sequence, including backbone, aromatic and side chain resonances (Figure 3.12c). Hence, sulindac sulfide aggregates together with A β , as previously indicated by solution-state NMR. No specific binding site can be defined. Rather, sulindac sulfide binds nonspecifically to A β and aggregates as an amyloid bound colloid.

Sulindac sulfide does not alter A β fibrils

In a second part of this work, we investigated the mechanism of interaction of sulindac sulfide with seeded mature A β fibrils. For this purpose, seeded fibrils were prepared as described by Lopez del Amo *et al*^[264] and incubated with sulindac sulfide or DMSO as a reference. Although the protocols for fibrillation are identical, we observe one set of signals in our study instead of two conformations as described by Lopez del Amo *et al*^[264]. The current polymorph resembles mostly conformer I, although V24-S26 and various individual resonances show a high correlation to conformer II, whereas several resonances do not resemble either of the conformers. Overall, comparison of CS demonstrates the differences between the asymmetric dimer^[264] and the current fibrils (Table 3.2, Appendix 5.4). The presence of DMSO may be responsible for the change in polymorphism. By functioning as a hydrogen

bond acceptor, DMSO disturbs the hydrogen bond network surrounding protein surfaces^[413], which may alter self-assembly of A β ^[414]. Furthermore, slight variations of experimental conditions strongly affect A β aggregation kinetics^[415,416] and may account for the different polymorphs.

Mature seeded fibrils in the presence of absence of the NSAID reveal highly similar patterns solid-state NMR spectra (Figures 3.13 and 3.14) and TEM images (Figure 3.16a). The fibrillar character of A β is maintained in the presence of sulindac sulfide. The resulting spectra were amenable for further analysis, and residues Q15-V40 were assigned in both samples. CS analysis (Figure 3.16b) and TEDOR experiments (Figure 3.17) detect the presence of β -sheet elements and the D23-K28 salt bridge. When incubated with sulindac sulfide, defined CSPs in A β fibrils are observed for specific resonances, including K16, G33 and hydrophobic residues between V18-A21 (Figure 3.18a). It is important to note that the observed CSPs are quantitative, and we do not observe peak splitting or line broadening. Hence, sulindac sulfide exerts the same effect on each A β molecule within the fibril structure. Similarly, in ¹³C-¹⁹F TEDOR spectra, individual ¹³C signals in ¹⁹F vicinity are detected which are assignable to specific resonances, namely to Cys of V18, V24, V36 and V39 C β s of A21 and A30, the side chain of K16 and methyl groups of I31, I32, L34 and M35, although some signals remain ambiguous due to spectral overlap (Figure 3.18b, Table 3.1).

Sulindac sulfide intercalates between the two β -strands formed by A β fibrils.

Signals from ¹³C-¹⁹F TEDOR spectra and the observed CSPs are strong indicators for the binding site of sulindac sulfide to A β fibrils. TEDOR restraints are more valuable restraints, as they arise from direct binding to the NSAID, whereas CSPs may be caused by conformational changes. We used both sets of restraints in an induced fit study to dock sulindac sulfide to A β fibrils. Similar approaches in the past include a solid-state NMR supported docking of Cu²⁺^[300] and a blind docking of sulindac sulfide^[333], both to A β fibrils. For our molecular docking, we employed two out of three wild type A β ₁₋₄₀ fibril structures currently available. These include a 3-fold symmetric structure (PDB: 2LMP)^[257], which shows the highest correlation to our obtained CS (Table 3.2, Appendix 5.4), and a 2-fold symmetric structure (PDB: 2LMN)^[260], which resembles best our protocol for fibril preparation. Further available structures include fibrils obtained from brain tissue seeded material^[232], as well as several familial mutants^[261-263]. These structures were neglected as they show a high degree of variance in CS patterns and in the peptide sequence to our current

analysis. A packing analysis of the analyzed structures demonstrates a high degree of similarity in cavity size and polarity found in the fibrillar structures. Although the employed structures do most likely differ from our current polymorph, we conclude that docking sulindac sulfide to the published structures is a valid approach for various reasons. First, we use two structures which best resembles our polymorph to avoid bias. Second, a packing analysis serves as a base for the induced fit, and the packing density is consistent throughout various amyloid fibril structures. Third, the docking is based on experimentally observed NMR restraints, and the results are discussed critically.

The packing analysis revealed that cavities cluster to five different regions, although the presence of cavities depends on the rotameric state of F19. The position of the cavities (Figure 3.20b) reflects residues affected by sulindac sulfide based on NMR restraints (Figure 3.20a). The clusters are approximately consistent in both structures, although the 3-fold symmetric structure is more tightly packed. To assess polarity, the probability of each cavity to harbor water molecules was predicted. Two clusters provide the necessary size and hydrophobicity to accommodate a sulindac sulfide molecule, marked “cluster 1” surrounding I32 and “cluster 2” surrounding V36 (Figure 3.20b). An induced fitting approach to both cavities reveals that sulindac sulfide can dock to both fibril structures, in a manner consistent with the NMR restraints (Figure 3.20c). In both structures, sulindac sulfide can bind parallel to the fibril axis in groove formed by G33 (pose 1) in cluster 1, or with its aromatic ring system parallel to the β -sheets and perpendicular to the fibril axis (pose 2) in cluster 2. In pose 2 of the 2-fold symmetric structure, sulindac sulfide interacts with the fibril towards the C-terminus. In addition, sulindac sulfide can bind in cluster 2 of the 2-fold symmetric structure in a third pose with its ^{19}F atom facing F19 (not shown). The combination of all poses fulfills important ^{13}C - ^{19}F REDOR restraints, as the ^{19}F atom is located less than 6 Å from the methyl groups of I32, L34, V36 and V39. In the solid-state, ^{13}C - ^{19}F distances can be measured reliably up to a distance of 12 Å, as demonstrated by REDOR measurements in complexes of the *Staphylococcus aureus* cell wall and various glycopeptides^[417]. Furthermore, the binding modes account for the large CSP observed for G33, as this residue is involved in forming a groove to accommodate the NSAID. Yesuvadian *et al* found a weak interaction of sulindac sulfide with K16 and V18 on the fibril surface^[333]. As docking to the surface was not taken into account in our current study, the previous report complements our results and attributes for the observed CSPs of K16 and the large ^{13}C - ^{19}F REDOR signal of V18. Sulindac sulfide must bind to all clusters in order

to fulfill the experimental restraints, although their availability is determined by the rotameric state of F19. Hence, we assume not a simultaneous, but a dynamic binding of the NSAID. We hope to confirm this assumption by relaxation dispersion experiments in the future.

Sulindac sulfide protects A β from M35 oxidation

M35 in the A β sequence is a mediator of oxidative stress^[181], which contributes significantly to AD progression^[174]. Oxidation of M35 is commonly observed in A β peptides^[182], and interferes with its aggregation properties^[175]. In addition, due to its proximity to M35, G33 assists in stabilization of ROS^[418,419] and thereby contributes to A β oxidation^[420,421]. In our docking model, all poses suggest binding of sulindac sulfide near M35 and near G33 in pose 1. This residue is essential for A β toxicity and responsible for its aggregation into oligomers^[422]. The localization of the NSAID near G33 may alter these abilities and have beneficial influences on A β toxicity. More importantly, sulindac sulfide binding may protect from A β M35 oxidation^[404].

In order to develop a system for testing fibrillar A β oxidation, fibrils were incubated under oxidizing conditions and dissolved in DMSO-d₆ in the presence of ascorbic acid to quench further oxidation. We were able to efficiently oxidize M35 of A β fibrils with the oxidizing agents NCS and NBS, but not H₂O₂ (Figure 3.23). In addition to M35, M0 seems to undergo oxidation in the presence of all oxidizing agents tested, as residues in the N-terminal region near M0 are subject to CSPs and peak splitting (H₂O₂) or signal loss (NCS, NBS). These processes may arise due to exchange between two states. Peak splitting indicates slow exchange, whereas intermediate exchange will result in line broadening and signal loss. The oxidizing agents were added in high molar excesses, hence, we assume that the A β peptide becomes fully oxidized. It is possible that the oxidizing reagents bind the N-terminal part of A β and thereby induce conformational exchange of the N-terminus between a ligand bound and unbound state. Mass spectrometric analysis should be carried out in the future to support the hypothesis of the binding event between A β and the oxidizing reagents.

Attenuated M35 oxidation in A β fibrils by the oxidizing agent NCS when co-incubated with sulindac sulfide was observed (Figure 3.24). Sulindac sulfide itself undergoes oxidation to sulindac (Figure 3.25), suggesting a role as an anti-oxidant for the NSAID. Anti-oxidants exert highly beneficial effects on AD progression^[423,424], and this is the first time that sulindac sulfide is reported as an anti-oxidant. Sulindac sulfide may thus protect M35 oxidation in two mechanisms. The first mechanism

assumes oxidation of the NSAID instead of A β . However, no anti-oxidizing effect of sulindac sulfide is found for monomeric A β when oxidized with H₂O₂ (Figure 3.21a). It should be taken into account that H₂O₂ is less efficient in oxidizing sulindac sulfide to sulindac (Figure 3.25), and the effect of sulindac sulfide on monomeric A β M35 oxidation in the presence of NCS should be investigated in the future. The second mechanism suggests a competitive inhibitory role for sulindac sulfide. By binding to a cluster of hydrophobic cavities present in A β fibrils surrounding G33 and M35, sulindac sulfide prohibits access of NCS, thereby shielding M35 from NCS oxidation. We assume that sulindac sulfide has a higher preference for binding to the pocket due to its relative high hydrophobicity in comparison to NCS, and its ring system, which will most likely interact with aromatic rings of side chains present in the binding pocket, for instance, F19. The absence of this pocket in monomeric A β may in addition explain the inefficiency of sulindac sulfide to prevent monomeric A β M35 oxidation (Figure 3.21a). In all experiments, NCS was added in high molar excess in respect to A β or sulindac sulfide, ensuring that the anti-oxidizing effect of the NSAID was negligible. We assume that sulindac sulfide binding to A β fibrils occurs rapidly, hence, the NSAID may be protected from oxidation once bound to the fibrillar hydrophobic pocket. However, it could not be determined with certainty in which oxidized version the NSAID interacts with fibrils. The concept of sulindac sulfide acting as a competitive inhibitor strongly supports the accuracy of the binding site as predicted by the induced fit study, and moreover demonstrates a biological relevance of NSAID binding to A β fibrils.

Comparison of A β interactions with NSAID to other studies

Solid-state NMR studies in the past have revealed that small molecules may induce a variety of changes to amyloid structures^[288,296-298,300]. Curcumin^[297] and Zn²⁺^[299] exert severe changes to the fibrillar character and disrupt the D23-K28 salt bridge. Similarly, EGCG drives A β into nonfibrillar oligomers, although typical features such as the salt bridge and β -sheets are preserved^[288]. In contrast, CR^[296], ThT^[425] and Cu²⁺^[300] solely bind to fibrils without introducing structural changes. Similarly, sulindac sulfide is unable to prevent the formation of, or disrupt characteristic structural A β elements. However, unlike CR^[296] and Cu²⁺^[300], which bind to a superficial groove along the fibril axis or at the termini, respectively, our NMR data based docking approach revealed that the NSAID intercalates between the β -strands of fibrils. This is a novel binding site for small molecules, as all previously described sites of interactions for inhibitory molecules on amyloid structures are superficial. This model for the interaction of sulindac sulfide with fibrillar A β may also assist in

understanding the influence of the NSAID on monomeric A β . In 2D ^{13}C - ^{13}C correlation spectra of NSAID induced aggregates, we observe an increased intensity for I31 and I32 side chain cross peaks upon the addition of a 10-X molar excess of sulindac sulfide (Figure 3.9a). This suggests that the side chains are no longer flexible or averaged out due to conformational flexibility, but more rigid and stabilized by sulindac sulfide. Indeed, a large cluster of hydrophobic cavities around I32 side chain is one of the primary binding sites of sulindac sulfide in fibrils (Figure 3.20c). Analysis of CS reveals the presence of β -sheets (Figure 3.10a) in the pre-fibrillar aggregates induced by sulindac sulfide. Hence, it is likely to assume the presence of similar cavities in the induced structures, and sulindac sulfide binding to these cavities. However, based on the relatively large differences in chemical shift (Table 3.2, Appendix 5.4), we assume that monomeric A β in the presence of sulindac sulfide folds into a polymorph structurally different to mature fibrils incubated with sulindac sulfide. Thus, although sulindac sulfide may bind to a common binding site, which is integrated in characteristic A β structural elements, overall differences exist between the two structures and interaction modes with sulindac sulfide.

Evidence for discrepancies in the nature of the NSAID-A β interaction in the two systems can be found in the NMR data. Unlike for the NSAID induced A β aggregates, sulindac sulfide causes defined CSPs in A β fibrils for specific resonances (Figure 3.18a). Further differences in the interaction in the two species are visualized when comparing the ^{13}C nuclei detected in proximity to the sulindac sulfide ^{19}F atom in ^{13}C - ^{19}F REDOR and TEDOR experiments (Figure 3.19). Superimposition of the individual spectra featuring all ^{19}F dipolar coupled ^{13}C atoms of fibrils and NSAID induced aggregates reveals the different patterns in the spectra. In principle, the spectrum of induced aggregates contains signals of a full protein spectrum. In the case of mature fibrils, individual ^{13}C signals originating from specific resonances are detected. Unlike the NSAID induced A β aggregates, we assume specific NSAID binding to fibrils, accounting for the defined CSPs and ^{13}C - ^{19}F TEDOR signals.

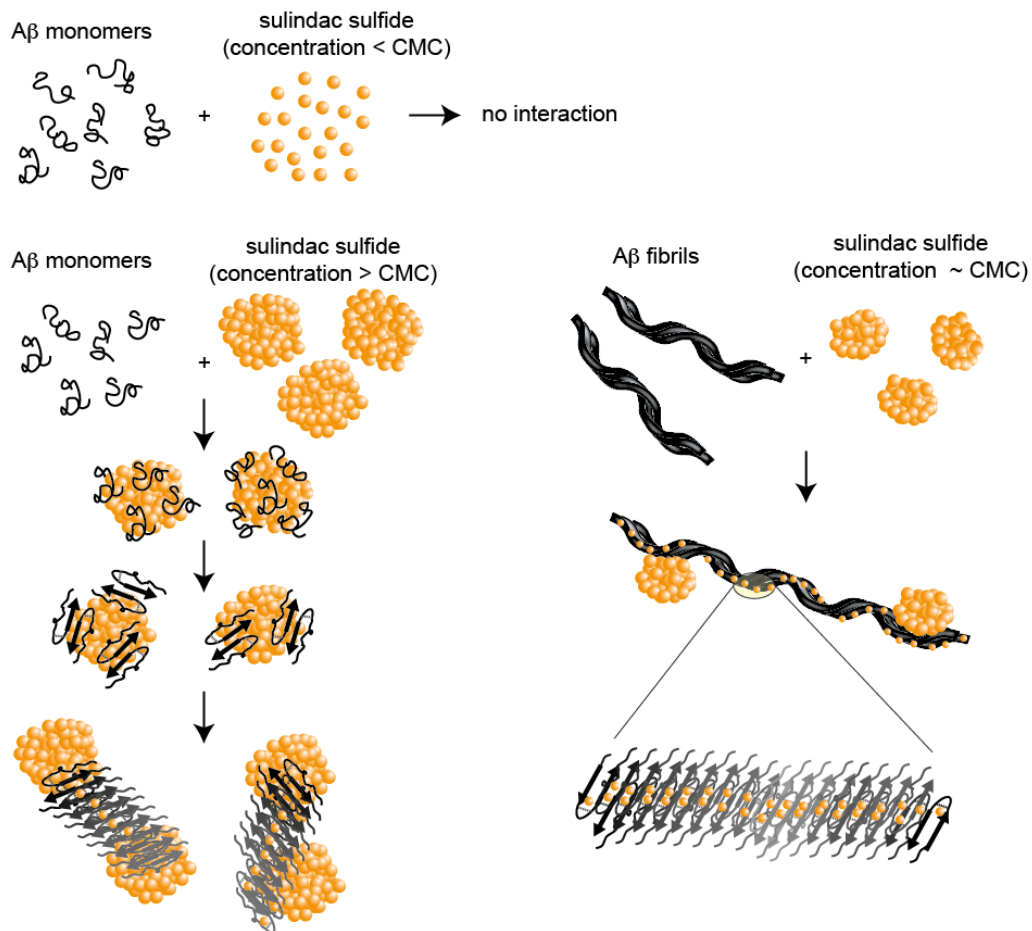


Figure 4.1: Schematic representation of mechanism of interaction between sulindac sulfide and A β monomers and fibrils.

Based on experimental observations, we are able to derive a mechanism of interaction between the NSAID sulindac sulfide and A β species (Figure 4.1). When incubated with monomeric A β at concentrations above its CMC, sulindac sulfide will nonspecifically induce A β aggregation. Due to its colloidal character, sulindac sulfide will promiscuously bind individual A β molecules. As these self-assemblies can reach submicrometer sizes^[338], presumably several A β monomers are recruited to the surface of each colloid, leading to an A β accumulation. Hence, by bringing A β monomer close together, the sulindac sulfide surface acts as a nucleation seeds promoting structure formation and amyloid elongation into large off-pathway oligomeric or pre-fibrillar aggregates with reduced toxicity, which are structurally diverse from seeded fibrils. Upon addition of sulindac sulfide to seeded mature fibrils, we observe a specific mechanism of interaction. At 250 μ M sulindac sulfide is likely

start forming colloids. Yet, we assume that individual sulindac sulfide molecules dissociate from the larger complexes to specifically intercalate in hydrophobic cavities formed between the two β -strands of the A β fibrils. By occupying these cavities, sulindac sulfide may protect A β from M35 oxidation. This may be a general binding mechanism of sulindac sulfide. As we assume the existence of similar cavities in the sulindac sulfide induced A β aggregates, it is likely that individual NSAID molecules bind to the same site.

4.2 Interactions of A β with ISMs

K3L3K3-GI induces structured A β aggregates

IAPP cross-amyloid interaction surface mimics (ISMs) are potent inhibitors of IAPP and A β fibrillation and toxicity^[378]. The structure of ISMs seems crucial for its inhibitory activities, as ISMs containing large amounts of β -sheet elements are the most effective to block amyloidogenic processes, although the exact mechanism of action is unknown. As reported before^[378], we find by solution-state NMR that A β interacts strongly with ISMs containing a leucine linker, L3-GI and K3L3K3-GI (Figures 3.27 and Figures 3.28-3.30, respectively), but not with ISMs containing a glycine linker, G3-GI (Figure 3.28 and and 3.30). This is expected, as L3-GI contains a high degree of β -sheet elements, whereas G3-GI is mostly unstructured and of random coil character. The presence of HFIP is crucial for the interaction to occur. The organic solvent may provide an interface for interaction of the two peptides. Analogous to experiments with sulindac sulfide, K3L3K3-GI aggregates A β without affecting A β CS, indicating a nonspecific type of interaction. On a nM scales, L3-GI and A β form nonfibrillar hetero-oligomeric assemblies featuring a β -sheet/ β -turn structure^[378]. The experimental conditions had to be adjusted to μ M ranges for the NMR experiments. Yet, the solution-state NMR experiments provide evidence that hetero-oligomers may exist at the higher concentrations, as K3L3K3-GI aggregates together with A β (Figure 3.30b). Solid-state NMR spectra revealed that the resulting aggregates exhibit a high degree of secondary structure. (Figures 3.31 ad 3.32a). Judging from the patterns in the spectra, it is highly likely that A β forms into β -sheet containing structures. Overall, the spectra are well dispersed and feature resolved peaks. For instance, individual signals are detected in the carboxylic region, indicating structured and stabilized side chains. Two serine signals are found. In the future, sequential assignments of the complex will reveal if these originate from the two serines in the A β sequence, or from two conformers of the same serine. TEM

images of the aggregates show fibrillar structures, in contrast to previous reports^[378]. The discrepancies may arise due to the higher concentrations of both binding partners. Furthermore, it should be considered that K3L3K3-GI and A β primarily from hetero-oligomers, which are too large to be observable by solution-state NMR and difficult to see by TEM. The prefibrillar species may be an alternative structure formed by A β alone due to the experimental conditions. So far we can conclude that K3L3K3-GI drives A β into structured and not amorphous aggregates, observed by solid-state NMR. Experiments including various labeling schemes of the two binding partners will be carried out in the future to answer further questions. For instance, 2D ^{15}N - ^{13}C correlation spectra of ^{15}N labeled K3L3K3-GI incubated with ^{13}C labeled A β will reveal the presence of the ISM in the complex, and provide information about the binding site. Uniformly ^{15}N and ^{13}C labeled K3L3K3-GI will be measured to study structural details of the inhibitor in the complex.

R3-GI forms loop-like structures

Although the inhibitory effects of ISMs have been proven in numerous experiments, the detailed mechanism of its molecular interaction with amyloid peptides remains elusive and lacks experimental evidence. It has been suggested that ISMs form β -hairpin like structures, thereby mimicking the amyloidogenic binding interface. Upon binding to an amyloid species, the N-methylations at G24 and I26 will prevent further self-assembly^[372]. To gather insight into the mechanism of interaction, we analyzed the ISM structure by solution-state NMR. Approaches involving K3L3K3-GI have failed in the past due to its low S/N in solution-state NMR spectra. Studies were further hindered by the unavailability of uniformly isotope ^{13}C and ^{15}N labeled peptide. The ISM R3-GI is the most suitable for structural characterization due to its relative high solubility. In 2D ^1H - ^1H NOESY spectra, residues N15-L20 of R3-GI are present as two conformers, and I19 as three conformers, although conformer 1 is the most populated. The two conformations are observed for residues surrounding G17 and I19 and most presumably arise due to cis-trans isomerization brought about by the N-methylations of the two residues. In total we observe 5 confirmed long range NOEs for conformer 1, and 7 confirmed long range NOEs for conformer 2 (Table 3.5). It remains unclear, whether R3-GI is present as a monomer or oligomer at the concentration above 500 μM used in the NMR experiments, although DLS suggests the lack of large oligomeric species (Figure 3.36 and Table 3.3). Four preliminary structures for R3-GI were calculated, including monomeric and dimeric structures for each conformer. It should be noted that there are several violations of NMR restraints (Table 3.10), and N-methylations of G17 and I19 were not taken into

account for the structure calculation. Hence, the presented structures should be treated with caution and be considered preliminary structures only. Overall, the monomeric structures yield better r.m.s.d. values, and seem to fulfill the NOEs to a greater extent than dimeric structures, even when considering the possibility of intra- and intermolecular origins for the NOEs in dimers (Table 3.5). Although all four structures differ, they all consistently lack secondary structural elements and contain various loops (Figures 3.39-3.42). The arginine linker is solvent exposed and the central arginines points away from the other two arginines in the linker. The termini are flexible (Figure 3.37). The loops seem to be supported by hydrogen bond networks (Tables 3.6-3.9). Indeed compared to L3-GI, R3-GI contains a much higher amount of random coil character, however some β -sheet content is expected^[378].

The lack of structural elements makes it challenging to explain how the ISM can interact with A β species. For further investigations, it is crucial to identify the primary and active R3-GI species present under the current conditions. The signals we observe in the NOESY spectrum are relatively narrow (~14 Hz) and most likely originate from a monomeric species. However, the monomer may solely constitute the NMR visible species and account for only part of the total peptide. Although DLS measurements exclude the presence of higher-n species, further experiments such as SAXS need be carried out to confirm this result. In the meantime, it should be taken into account that the NOEs may originate from transferred NOEs caused by exchange between a monomeric and a higher-n state. Due to the relatively long NOESY mixing time (300 ms), such processes may be observed. In addition, the long mixing time may capture two dynamic states, for instance the formation of two loops, which are actually not co-existent, but exist two transient states, which are in dynamic equilibrium. Therefore, the experiments should be repeated with shorter NOESY mixing times.

The inhibitory mechanism described for ISMs so far relies on ISMs adopting structures to mimic the amyloid interaction surface^[372]. The NOE patterns observed for R3-GI strongly indicate loop formation, which is an essential observation in order to explain the mechanism of interaction with amyloids. The dynamics of these loops need to be elucidated in the future.

4.3 Conclusions

In this study we have focused on elucidating molecular interactions between the AD peptide A β and inhibitory molecules by MAS solid-state NMR spectroscopy. This method is a powerful tool, which allows the structural analysis of insoluble protein assemblies, which are elusive to other standard biophysical methods. Based on experimental data, we have suggested two distinct binding mechanisms of sulindac sulfide to various A β species and described the binding site of sulindac sulfide to fibrillar A β . Based on structural details, we derived conclusions how the interaction of sulindac sulfide with A β may hinder on-pathway amyloidogenesis and block neurotoxicity. Similarly, ISM peptide inhibitors sequester A β peptides from on-pathway amyloidogenesis by adopting structures to mimic amyloidogenic binding interfaces. The approaches shown here are applicable to various disease causing amyloid forming peptides and unlabeled ligands. To date, AD remains an untreatable disease. This study highlights the importance of structure-based drug discovery in the development of potential drug targets targeting A β and further amyloidogenic peptides on the way to curing amyloid based diseases.

5.1.2 Cross-Amyloid Interaction Surface Mimics (ISMs)^[378]

- R3-GI*

1 11 21
ATQRLANFLV HRRRN**F**GAIL S

Molecular weight (unlabeled): 2468.8 Da

Molecular weight (A06, V10, L20, S21 U-¹³C, ¹⁵N labeled): 2489.8 Da

Theoretical pI: 12.48

Extinction coefficient (M⁻¹ cm⁻¹ at 280 nm): 0

- L3-GI*

1 11 21
ATQRLANFLV HLLL**N**F**G**AIL S

Molecular weight (unlabeled): 2339.7 Da

Theoretical pI: 9.80

Extinction coefficient (M⁻¹ cm⁻¹ at 280 nm): 0

- K3L3K3-GI*

1 11 21
KKKATQRLAN FLVHLLL**N**F**G** AILSKKK

Molecular weight (unlabeled): 3108.8 Da

Theoretical pI: 11.43

Extinction coefficient (M⁻¹ cm⁻¹ at 280 nm): 0

- G3-GI*

1 11 21
ATQRLANFLV HGG**N**F**G**AIL S

Molecular weight (unlabeled): 2171.4 Da

Theoretical pI: 9.80

Extinction coefficient (M⁻¹ cm⁻¹ at 280 nm): 0

- K3G3K3-GI*

1 11 21
KKKATQRLAN FLVHGG**N**F**G** AILSKKK

Molecular weight (unlabeled): 2940.4 Da

Theoretical pI: 11.43

Extinction coefficient (M⁻¹ cm⁻¹ at 280 nm): 0

* The glycine and isoleucine residue marked bold are N-methylated.

5.2 Chemical shifts

5.2.1 Chemical shifts of monomeric A β_{1-40} in solution

aa	H	N	CO	C α	C β	C γ	C δ	C ϵ	H α	^1H side chain
M0	-	-	-	54.89	30.69*	30.69*	-	16.34*	3.71	2.30 H β^* , 2.30 H γ^* , 1.81 H ϵ^*
D01	-	-	175.63	54.16	41.05	-	-	-	4.36	2.34 H β a, 2.49 H β b
A02	8.38	124.59	177.48	52.51	18.91	-	-	-	3.95	1.10 H β
E03	8.24	119.43	175.05	56.33	29.95	35.87	-	-	3.88	1.61 H β , 1.75 H γ
F04	8.04	121.12	175.12	57.48	39.26	-	-	-	4.26	2.75 H β b
R05	7.89	123.39	-	55.35	30.86	26.70	42.95	-	3.97	1.34 H β a, 1.44 H β b, 2.85 H δ , 1.21 H γ
H06	-	-	174.98	56.16	30.46*	-	-	-	4.25	2.83 H β^*
D07	8.19	121.51	176.15	53.77	40.78	-	-	-	4.34	2.40 H β a, 2.48 H β b
S08	8.28	116.50	175.00	58.87	63.34	-	-	-	4.09	3.59 H β a, 3.63 H β b
G09	8.38	110.58	173.79	45.12	-	-	-	-	3.70	
Y10	7.77	119.91	175.56	57.92	38.55	-	-	-	4.24	2.67 H β a, 2.75 H β b
E11	8.21	122.41	175.96	56.18	30.14*	35.98*	-	-	3.92	1.64 H β a*, 1.76 H β b*, 1.99 H γ^*
V12	7.94	121.21	175.95	62.54	32.26	20.56, 20.51	-	-	3.65	1.66 H β , 0.50 H γ a, 0.60 H γ b
H13	8.12	122.48	-	55.91	30.53	-	-	-	4.32	2.71 H β^*
H14	-	-	175.03	56.29	30.48*	-	-	-	4.22	2.77 H β^*
Q15	8.25	121.31	175.50	55.67	29.14	33.49	-	-	3.98	1.69 H β a, 1.79 H β b, 2.05 H γ
K16	8.26	123.01	176.08	56.10	32.64	24.52	29.12	41.74	4.00	1.47 H β a, 1.53 H β b, 1.11 H γ a, 1.19 H γ b, 1.40 H δ , 2.70 H ϵ
L17	8.12	123.73	176.61	54.77	42.03	26.76	25.12	-	4.04	1.16 H β a, 1.34 H β b, 1.29 H γ
V18	7.86	121.51	174.97	61.73	32.84	20.97, 20.30	-	-	3.75	1.62 H β , 0.47 H γ a, 0.57 H γ b
F19	8.13	124.41	174.59	57.15	39.96	-	-	-	4.31	2.70 H β
F20	8.08	123.00	174.52	57.05	39.87	-	-	-	4.29	2.65 H β
A21	8.10	126.10	177.08	52.09	19.16	-	-	-	3.94	1.09 H β
E22	8.21	119.89	175.93	56.30	30.11*	35.85*	-	-	3.91	1.55 H β a*, 1.64 H β b*, 1.90 H γ^*
D23	8.28	121.66	176.37	53.86	40.77	-	-	-	4.37	2.35 H β a, 2.49 H β b
V24	8.02	120.61	176.87	62.51	32.00	20.89, 19.97	-	-	3.86	1.91 H β , 0.69 H γ
G25	8.41	111.71	174.28	45.24	-	-	-	-	3.70	
S26	8.01	115.39	174.29	58.24	63.60	-	-	-	4.15	3.60 H β a, 3.63 H β b
N27	8.35	120.48	175.29	53.04	38.30	-	-	-	4.46	2.53 H β a, 2.60 H β b
K28	8.21	121.60	177.00	56.57	32.28	24.48	28.63	41.80	3.99	1.50 H β a, 1.61 H β b, 1.14 H γ a, 1.20 H γ b, 1.40 H δ , 2.71 H ϵ
G29	8.28	109.45	173.54	44.89	-	-	-	-	3.64	
A30	7.88	123.40	177.45	52.14	19.02	-	-	-	4.02	1.09 H β
I31	8.05	120.75	176.27	60.73	38.09	17.03*, 27.02*	12.32*	-	3.87	1.58 H β^* , 1.24 H γ aa*, 0.94 H γ ab*, 0.63 H γ b*, 0.58 H δ a*
I32	8.16	126.30	176.46	60.87	38.29	17.16*, 27.02*	12.28*	-	3.87	1.58 H β^* , 1.24 H γ aa*, 0.94 H γ ab*, 0.63 H γ b*,

										0.58 Hδa*
G33	8.34	113.01	173.50	44.83	-	-	-	-	3.63	
L34	7.92	121.50	177.15	54.82	42.22	26.58	24.42	-	4.06	1.32 Hβ, 1.33 Hγ, 0.65 Hδa, 0.60 Hδb
M35	8.31	121.90	175.97	54.99	32.40	31.60	-	16.64*	4.25	2.24 Hβ, 2.23 Hγa, 2.31 Hγb, 1.76 Hε*
V36	8.12	122.48	176.54	62.37	32.48	20.23, 20.80	-	-	3.84	1.81 Hβ, 0.68 Hγ
G37	8.48	113.11	174.29	44.92	-	-	-	-	3.7	3.65 Hab
G38	8.12	108.52	173.52	44.77	-	-	-	-	3.72	
V39	7.94	119.80	175.41	62.23	32.64	-	-	-	3.90	1.81 Hβ, 0.67 Hγ
V40	7.69	128.31	-	63.54	32.94	21.26, 20.07	-	-	3.77	1.78 Hβ, 0.63 Hγ

Table 5.1: Solution-state NMR chemical shifts of monomeric Aβ₁₋₄₀ at 277 K. Aβ₁₋₄₀ was dissolved in NaOH and measured in 50 mM Na-phosphate, 50mM NaCl, pH 7.4. All values are given in ppm. * indicates ambiguous assignment. CS assignment is published by Mainz *et al.*^[405].

5.2.2 Chemical shifts of sulindac sulfide induced A β ₁₋₄₀ aggregates

aa	N	CO	C α	C β	C γ	C δ	C ϵ	N ζ
Q15	-	-	-	30.93	33.90	-	-	
V18	-	171.83	58.27	32.25	18.73	-	-	
F19	131.00	170.35	53.19	41.23	136.22	129.62	128.84	
F20	128.77	169.74	54.16	38.62	135.20	129.96	128.25	
A21	127.50	173.07	47.75	19.12	-	-	-	
E22	126.69	171.44	51.49	29.63	34.51	181.30	-	
D23	121.89	171.38	52.84	39.06	178.56	-	-	
V24	120.97	174.46	57.97	31.62	18.29	-	-	
G25	115.63	169.25	44.75	-	-	-	-	
S26	108.56	171.97	54.47	63.10	-	-	-	
N27	125.26	170.33	52.03	35.14	179.51	-	-	
K28	131.22	171.59	52.85	31.18	24.94	27.84	39.32	36.8
G29	115.15	169.36	42.21	-	-	-	-	
A30	130.05	173.15	47.60	19.82	-	-		
I31	127.18	171.42	58.40	38.77	15.43 26.08	11.76		-
I32	129.06	174.46	55.99	39.61	15.52 25.34	11.74		-
G33	121.73	169.49	45.97	-	-	-		
L34	120.88	171.84	50.72	43.91	25.15	23.05 22.46		-
M35	122.16	172.32	50.79	-	31.26	-	18.47	
V36	-	174.88	57.66	32.13	18.16	-	-	
G37	111.25	171.63	42.28	-	-	-	-	
G38	112.67	169.52	41.94	-	-	-	-	

Table 5.2: Solid-state NMR chemical shifts of A β ₁₋₄₀ aggregates induced by a 10-X molar excess of sulindac sulfide. Measurements were carried out at 270 K. All values are given in ppm.

5.2.3 Chemical shifts of sulindac sulfide incubated and reference A β ₁₋₄₀ fibrils

aa	N	CO	C α	C β	C γ	C δ	C ϵ	¹⁵ N side chain
S08	115.02	173.17	57.82	61.81				
G09	115.59	170.67	43.17					
Q15	129.55 129.51	170.50 170.58	52.60 52.99	28.73 -	33.99 34.36	38.82		
K16	130.40 130.05	171.58 171.34	53.14 52.67	29.56 30.76	21.85 20.95	26.09 25.46	44.40 41.91	
L17	123.64 123.59	173.95 173.73	53.46 52.87	38.48 38.74				
V18	120.59 119.87	170.56 171.04	58.71 58.52	34.47 33.92	19.17 19.01			
F19	131.98 131.92	170.60 171.39	55.03 55.09	42.16 41.08		130.72	129.71 129.26	
F20	131.35 129.24	170.64 171.35	54.54 54.71	38.16 37.03			129.59	
A21	129.64 127.77	174.62 174.51	47.97 48.03	20.73 20.80				
E22	125.60 125.51	171.47 171.53	52.12 52.46	29.02 29.38	36.69 36.75	173.77 173.68		
D23	124.87 124.96	175.46	53.50 53.95	38.84 38.98	177.78 178.01			
V24	127.88 127.52	173.22 173.01	58.56 58.51	30.89 31.05	20.60, 18.22 20.65, 18.65			
G25	113.51 113.81	171.73 171.50	43.95 43.93					
S26	109.80 109.97	171.84 171.63	57.41 57.45	59.26 59.29				
N27	118.46 118.56	172.75 172.45	51.83 51.84	38.54 38.55	174.31 173.80			120.36 N δ 2 120.54 N δ 2
K28	122.99 122.89	174.55 174.16	52.47 52.70	33.71 34.00	23.67 23.672	28.65 28.23	40.38 40.56	33.9 N ζ 34.3 N ζ
G29	118.66 119.19	170.49 170.36	45.83 46.06					
A30	121.21 121.08	173.17 173.40	48.09 48.22	20.49 20.35				
I31	121.41 122.33	172.30 172.25	58.33 58.60	38.82 38.89	25.31, 15.83 25.32, 15.95	11.75 12.07		
I32	128.46 127.95	173.27 172.63	56.56 56.68	39.74 39.67	25.40, 15.79 25.48, 15.83	12.90 12.81		
G33	116.82 118.98	170.72 172.16	46.43 48.86					
L34	124.02 124.08	172.82 173.05	52.47 52.69	40.70 40.72	26.61 26.37	21.36 21.61		
M35	126.02 125.80	171.70 172.10	52.38 52.51	33.13 33.69	32.52 32.34		15.46 15.61	
V36	123.84 123.16	173.81 173.93	57.47 57.53	33.20 33.09	21.56, 17.72 21.35, 17.72			
G37	116.47 116.35	170.85 170.66	46.76 46.42					
G38	108.34 108.57	169.57 169.40	42.50 42.25					
V39	126.53 126.20	171.26 171.51	59.41 59.26	32.50 32.37	18.93 18.76			
V40	132.24 132.42	178.80 178.51	59.16 59.24	33.67 33.27	21.44 21.60			

Table 5.3: Solid-state NMR chemical shifts of A β ₁₋₄₀ fibrils incubated with a 5-X molar excess of sulindac sulfide. CS of fibrils in the presence of sulindac sulfide are red, CS of reference fibrils are black. Measurements were carried out at 285 K. All values are given in ppm. CS assignment is published by Prade *et al*^[404].

5.2.4 Chemical shift assignment of R3-GI

aa	H	N	H α	H β	H γ	H δ	additional ^1H	C α	C β	C γ	C δ
A01	-	-	3.96	1.01	-	-	-	-	16.27	-	-
T02	7.99	-	3.77	3.78	0.87	-	-	66.87	72.74	18.66	-
Q03	8.42	-	3.97	1.63, 1.72	2.02	-	6.65, 7.32	59.20	26.57	30.70	-
R04	8.32	-	3.93	1.39, 1.45	1.23, 1.27	2.80	-	53.19	27.8	24.00	40.34
L05	8.17	-	3.99	1.22, 1.30	-	0.58, 0.52	-	52.84	39.24	-	20.32
A06	8.13	124.63	3.86	0.96	-	-	-	49.74	16.10	-	-
N07	8.07	-	4.24	2.38, 2.36	-	7.35, 6.62	-	50.30	35.65	-	-
F08	7.83	-	4.22	2.70, 2.79	-	-	6.88	55.07	36.43	-	-
L09	7.82	-	3.91	1.23, 1.09	-	0.49, 0.54	-	52.31	39.34	-	20.50, 21.98
V10	7.72	121.03	3.6	1.63	0.49, 0.57	-	6.99	59.75	29.70	17.86, 17.91	-
H11	8.09	-	4.25	2.68, 2.74	-	6.66	7.52	53.37	28.04	-	-
R12	8.25	-	3.93	1.45, 1.37	1.30	2.81	6.93	53.08	27.81	24.09	40.33
R13	8.25	-	3.92	1.49, 1.42	1.22, 1.25	2.81	6.91	53.01	27.79	24.03	40.29
R14	8.22	-	3.92	1.48, 1.36	1.19, 1.19	2.80	6.91	52.92	27.73	24.04	40.29
N15	7.97 8.20	-	4.32 4.28	2.39, 2.34 2.31, 2.37	-	6.64, 7.34 6.63, 6.67	-	49.96	35.81 35.89	-	-
F16	7.98 7.85	-	4.32 4.58	2.61, 2.73 2.54, 2.66	-	7.36	6.91 6.86, 6.99	-	36.60	-	-
G17	2.65 2.54	-	3.75, 3.66 3.75, 3.93	-	-	-	-	50.69 (C ^{met} 36.37) (C ^{met} 34.88)	-	-	-
A18	8.00 8.27	-	4.37 4.38	0.96 0.97	-	-	-	46.43	14.98 19.77	-	-
I19	2.77 2.75 2.53	-	4.37 4.30	1.71 1.65 1.69	0.53, 0.64 0.59, 0.44 0.60, 0.67	0.90 0.97 1.02	-	60.72 (C ^{met} 30.16)	31.33	23.81, 14.24 14.17 14.61	9.31 9.28
L20	8.23 8.13	129.5 129.3	4.05 4.30	1.23, 1.32 1.32	-	0.49, 0.53 0.50, 0.57	-	51.94	39.07	-	19.97, 21.80
S21	8.05	116.7	4.05	3.53, 3.49	-	-	-	55.02	60.88	-	-

Table 5.4: Solution-state NMR chemical shifts of R3-GI at 277 K. R3-GI was dissolved in 10 mM sodium phosphate and 1% HFIP. All values are given in ppm. Chemical shifts of the second conformation observed for N15-L20 is marked in red. A third set of chemical shifts is observed for I19 and marked in green. The ^{13}C chemical shift of the methyl group of N-methylated G17 and I19 is labeled as C^{met}.

5.3 Pulse sequences

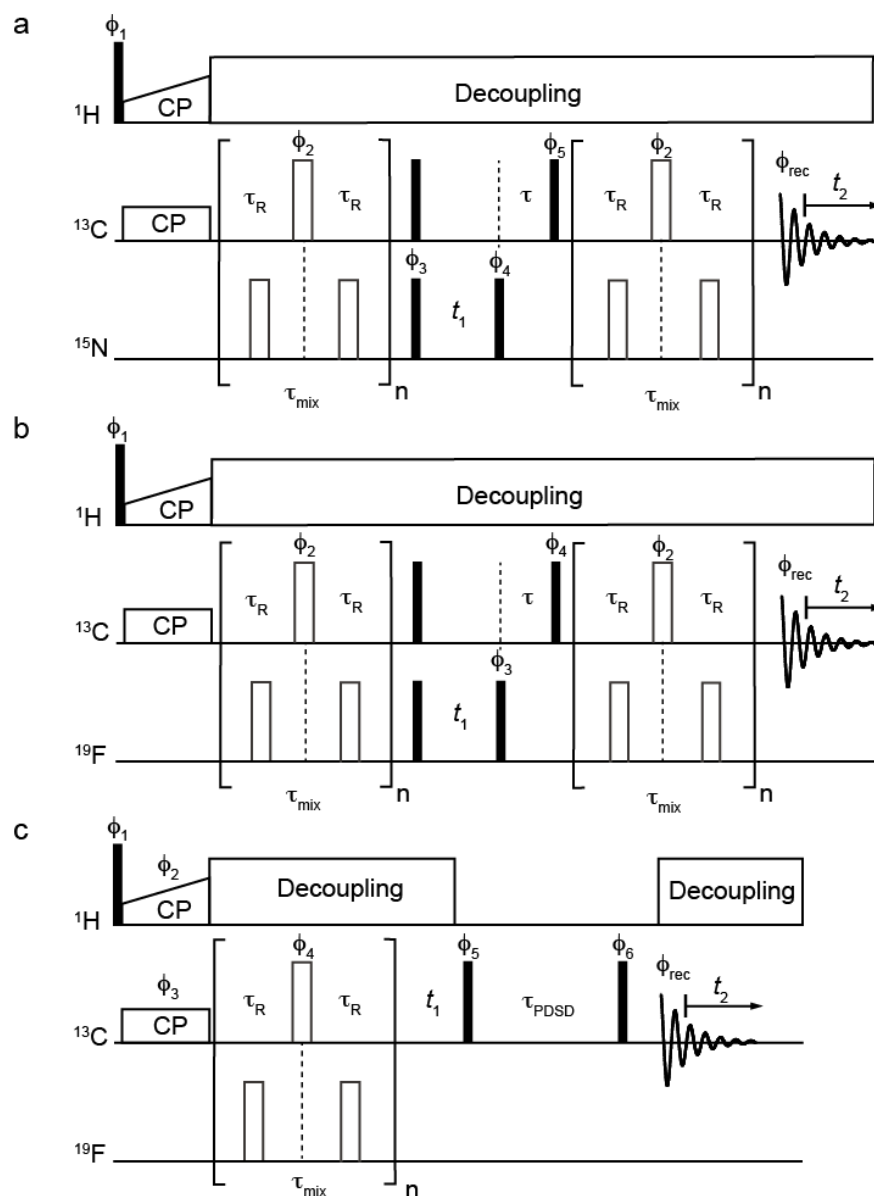


Figure 5.1: Solid-state NMR pulse sequences. (a) ^{13}C - ^{15}N TEDOR pulse sequence employed for the detection of the D23 C γ – DK28 N ζ salt bridge. (b) ^{13}C - ^{19}F TEDOR pulse sequence employed to detect A β -NSAIDs dipolar couplings of sulindac sulfide induced A β aggregates. (c) ^{13}C - ^{19}F REDOR pulse sequence used to detect A β -NSAIDs dipolar couplings of fibrillar A β . All pulse sequences are based on the 3D TEDOR experiments described by Jaroniec *et al.*^[39] and have been reported previously^[40]. White rectangles represent π -pulses and black rectangles represent $\pi/2$ -pulses. In all experiments, magnetization is transferred from ^1H to ^{13}C via ramped CP. During the REDOR blocks, a train of π -pulses reintroduces dipolar couplings between ^{13}C and $^{15}\text{N}/^{19}\text{F}$. In the TEDOR pulse sequences (a, b) this is used to transfer magnetization from ^{13}C to $^{15}\text{N}/^{19}\text{F}$ and back to ^{13}C , interrupted by CS evolution (t_1). In the REDOR pulse sequence (c), this causes dephasing of ^{13}C atoms are dipolar coupled to ^{19}F , and is followed by PDSD mixing (t_1). Reference experiments must be recorded without dipolar recoupling. The following phase-cycling was used: (a) $\phi_1 = y, -y$; $\phi_2 = y$; $\phi_3 = x, x, -x, -x$; $\phi_4 = -x$; $\phi_5 = y, y, y, -y, -y, -y, -y$; $\phi_{\text{rec}} = x, -x, -x, x, -x, x, x, -x$; the REDOR π -pulses on ^{15}N are phase-cycled according to the xy-16 scheme^[42]. (b) $\phi_1 = y, -y$; $\phi_2 = y$; $\phi_3 = x, x, -x, -x$; $\phi_4 = (x)^4, (y)^4, (-x)^4, (-y)^4$; $\phi_{\text{rec}} = -x, x, x, -x, y, -y, -y, y, x, -x, -x, x, -y, y, y, -y$. The REDOR π -pulses on the S-spins are phase-cycled according to the xy-16 scheme (c) $\phi_1 = y, -y$; $\phi_2 = x$; $\phi_3 = y$; $\phi_4 = y$; $\phi_5 = (x)^8, (-x)^8$; $\phi_6 = x, x, -x, -x, y, y, -y, -y$; $\phi_{\text{rec}} = x, -x, -x, x, y, -y, -y, y, -x, x, x, -x, -y, y, y, -y$; the REDOR π -pulses on ^{19}F are phase-cycled according to the xy-4 scheme^[42]. All other pulses were along x.

5.4 Comparison of A β ₁₋₄₀ chemical shifts to sulindac sulfide incubated and reference A β ₁₋₄₀ fibrils

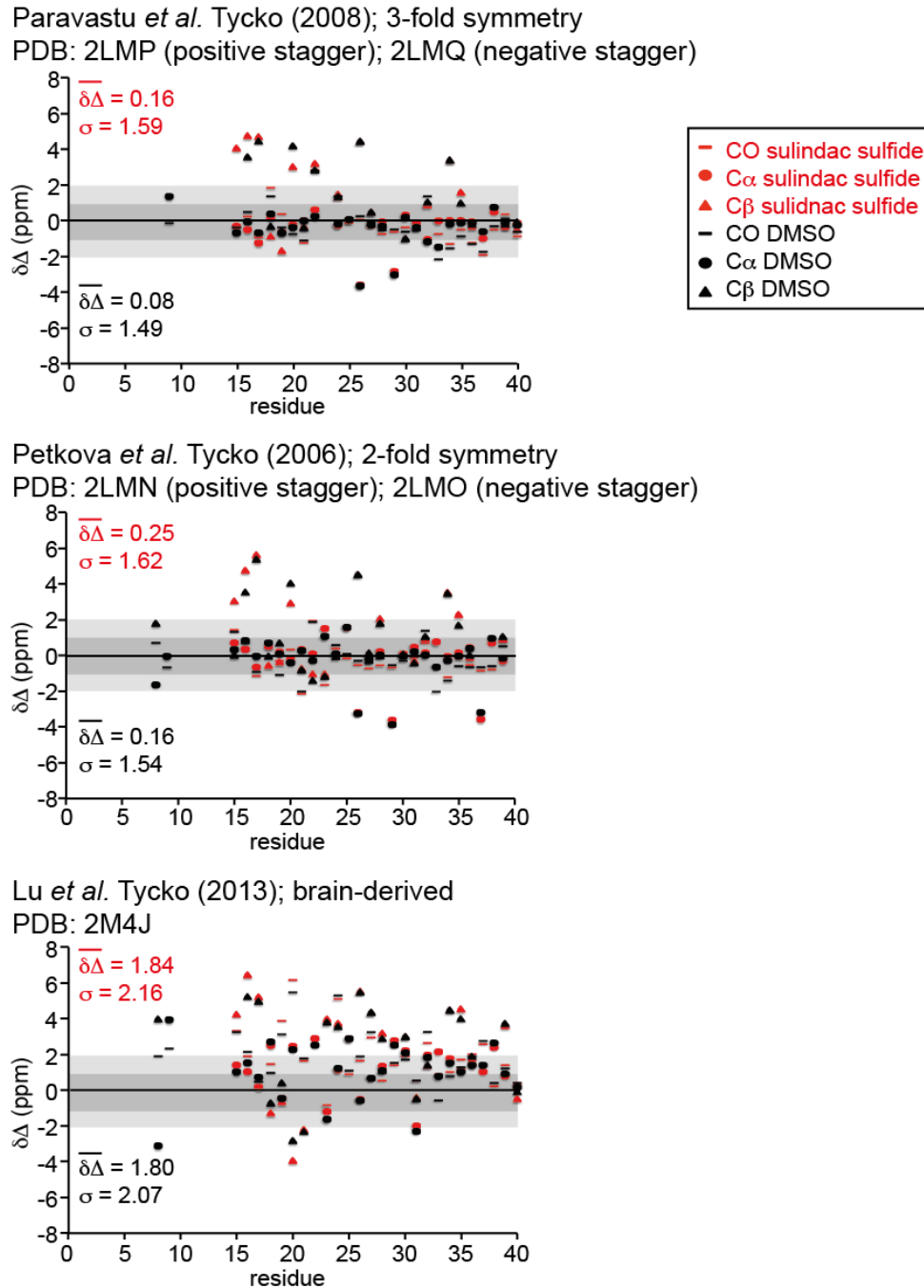


Figure 5.2: Residue specific CS differences; structures. $\Delta\delta$ of A β ₁₋₄₀ fibrils incubated with sulindac sulfide (red) and reference fibrils (black) to previously published A β ₁₋₄₀ structures. The mean chemical shift deviation ($\overline{\Delta\delta}$) and standard deviation (σ) are shown for each comparison. The figure is reproduced from Prade *et al.*^[404]. CS differences were compared to a 3-fold^[257] and a 2-fold^[260] symmetric A β ₁₋₄₀ fibrillar structure, as well as to A β ₁₋₄₀ fibrils derived from brain tissue^[232].

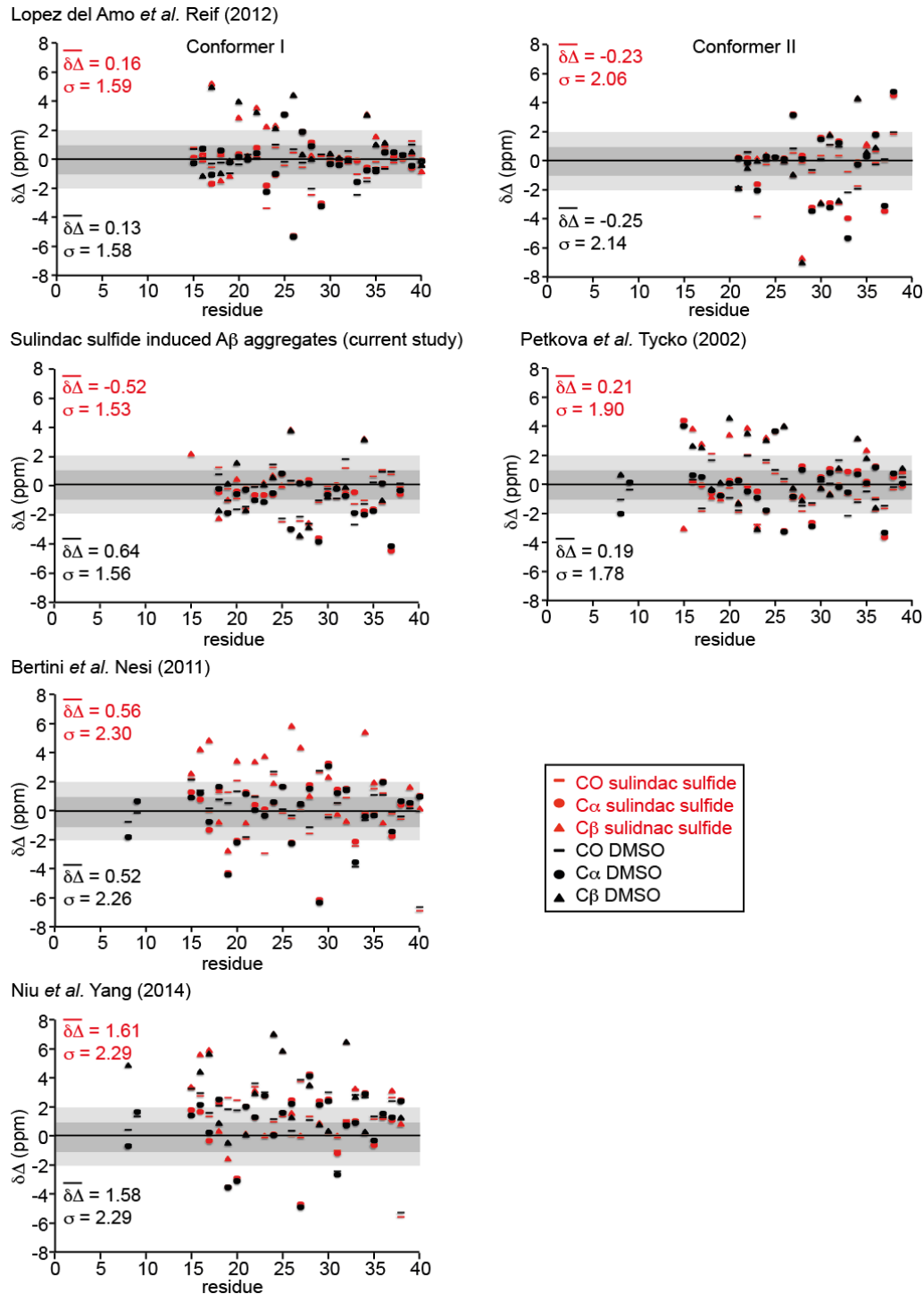


Figure 5.3: Residue specific CS differences; models. $\Delta\delta$ of $A\beta_{1-40}$ fibrils incubated with sulindac sulfide (red) and reference fibrils (black) to $A\beta_{1-40}$ models and chemical shifts published previously, and to $A\beta_{1-40}$ aggregates induced by sulindac sulfide presented in this study. The mean chemical shift deviation ($\overline{\Delta\delta}$) and standard deviation (σ) are shown for each comparison. The figure is reproduced from Prade *et al.*^[404]. CS differences were compared to two conformers of an asymmetric dimer structure^[264], $A\beta_{1-40}$ fibrils^[266], reference $A\beta_{1-40}$ fibrils incubated with phospholipid vesicles^[267] and $A\beta_{1-40}$ fibrils grown under agitated conditions^[265].

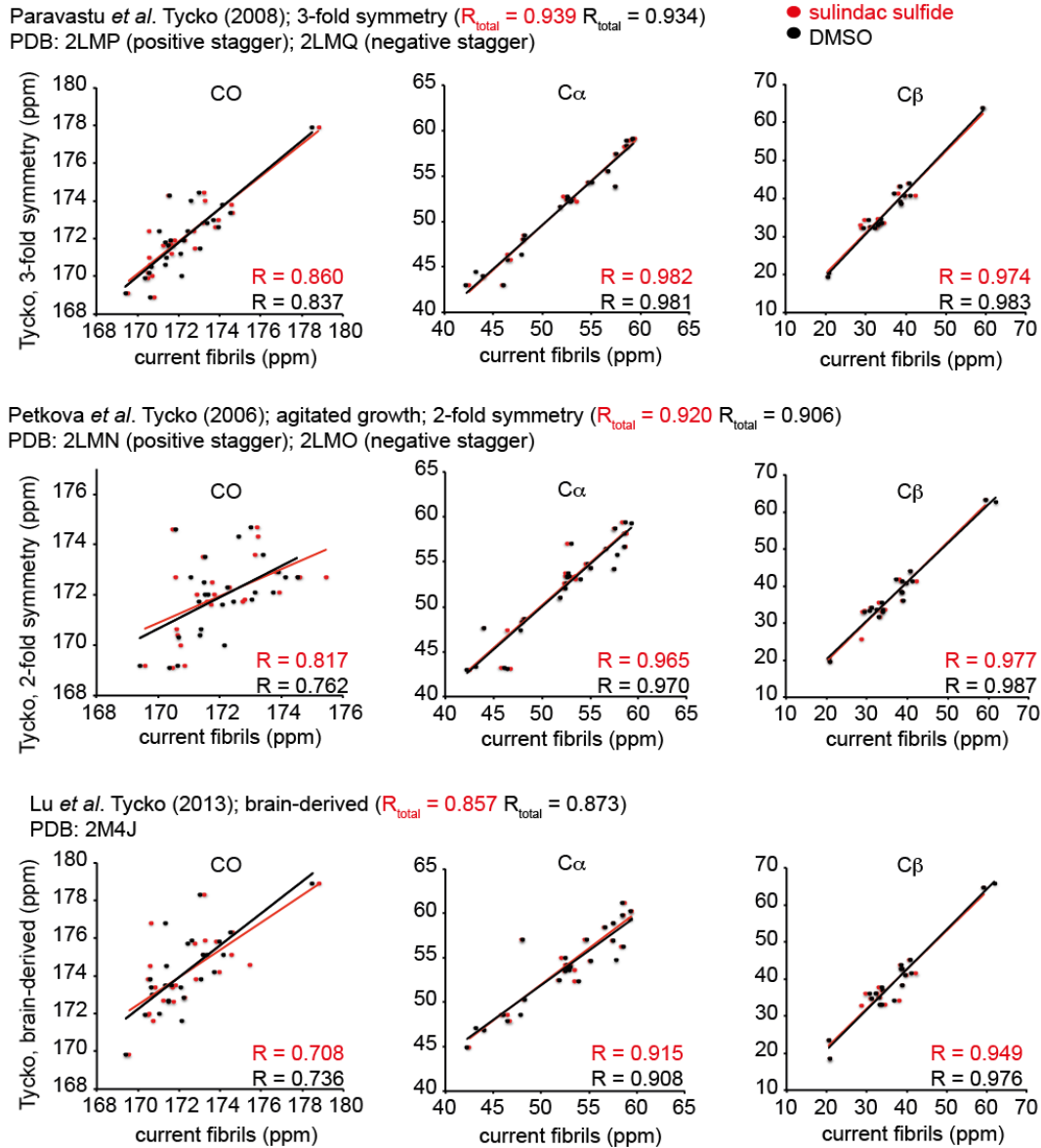


Figure 5.4: CS correlations; structures. CS correlations for C_{α} , C_{β} and CO atoms of $A\beta_{1-40}$ fibrils incubated with sulindac sulfide (red) and reference fibrils (black) to previously published $A\beta_{1-40}$ structures. The correlation coefficient R is shown for each correlation. CS were compared to a 3-fold^[257] and a 2-fold^[260] symmetric $A\beta_{1-40}$ fibrillar structure, as well as to $A\beta_{1-40}$ fibrils derived from brain tissue^[232].

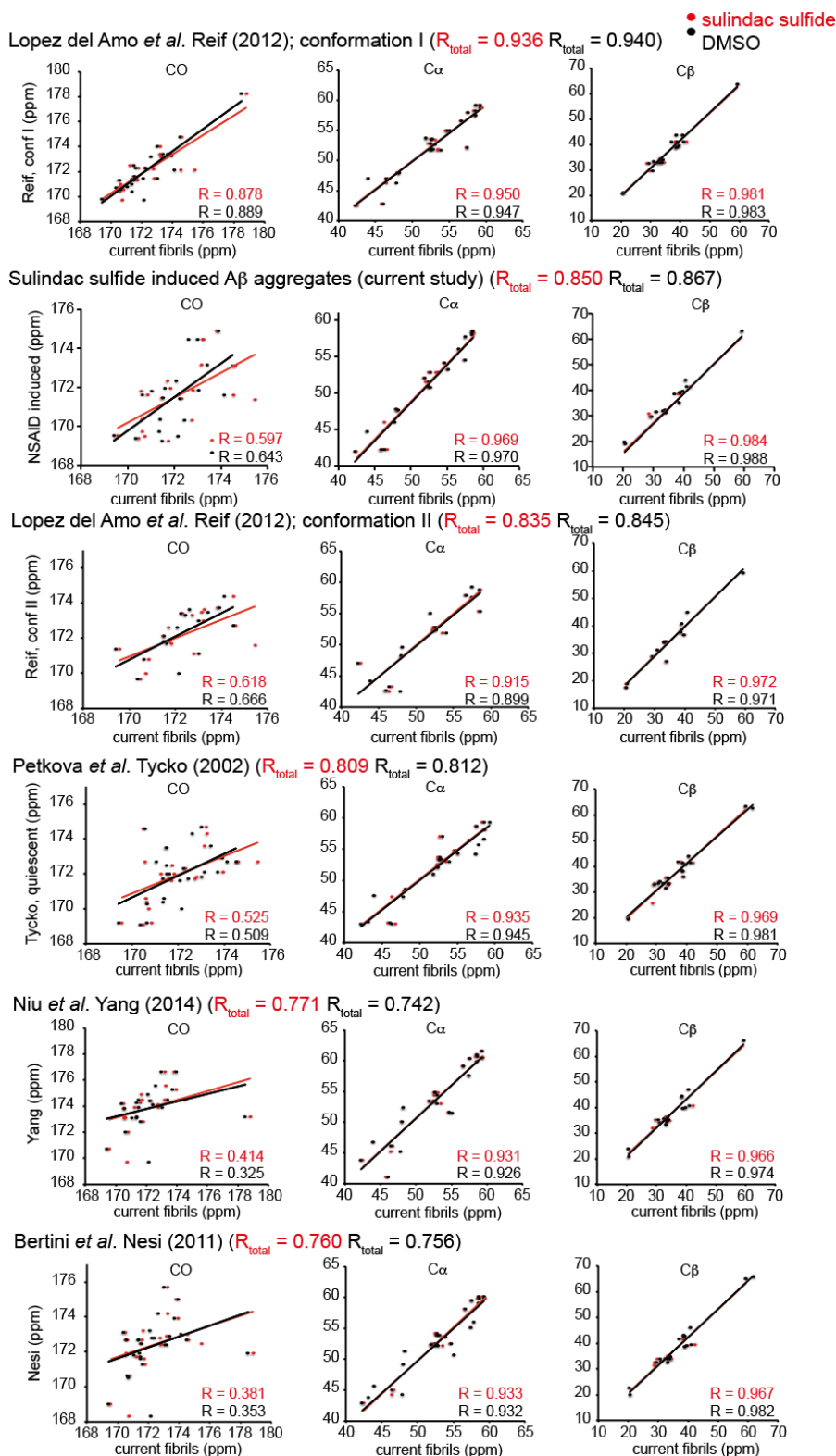


Figure 5.5: CS correlations; models. CS correlations for C α , C β and CO atoms of A β ₁₋₄₀ fibrils incubated with sulindac sulfide (red) and reference fibrils (black) to previously published A β ₁₋₄₀ models and chemical shifts published previously, and to A β ₁₋₄₀ aggregates induced by sulindac sulfide presented in this study. The correlation coefficient R is shown for each correlation. CS were compared to two conformers of an asymmetric dimer structure^[264], A β ₁₋₄₀ fibrils^[266], reference A β ₁₋₄₀ fibrils incubated with phospholipid vesicles^[267] and A β ₁₋₄₀ fibrils grown under agitated conditions^[265].

6. Abbreviations

aa	amino acid
A β	Amyloid- β
AD	Alzheimer's disease
APP(-TMS)	amyloid precursor protein (transmembrane sequence)
ARIA	ambiguous restraints for iterative assignment
α S	α -synuclein
CD	circular dichroism spectroscopy
CMC	critical micelle concentration
CP	cross polarization
CPMG	Carr-Purcell-Meiboom-Gill
CR	Congo Red
CS	chemical shift
CSA	chemical shift anisotropy
CSP	chemical shift perturbation
CV	column volume
Da	Dalton
DARR	dipolar-assisted rotational resonance
DEST	dark state exchange saturation transfer
DLS	dynamic light scattering
<i>E. coli</i>	<i>Escherichia coli</i>
EM	electron microscopy
EOAD	early-onset Alzheimer's disease
FAD	Familial Alzheimer's disease
FID	free induction decay
FT	flow-through
g	gravitational acceleration
GSM	γ -secretase-modulator
HFIP	hexafluoroisopropanol
HPLC	high performance liquid chromatography
HMQC	heteronuclear multiple quantum coherence
HSQC	heteronuclear single quantum coherence
IAPP	islet amyloid polypeptide
IB	inclusion bodies
ISM	IAPP cross-amyloid interaction surface mimic
LB	lysogeny broth
LOAD	late-onset Alzheimer's disease
mA	milliampere
mAU	milli absorbance units
MAS	magic angle spinning
MD	molecular dynamics
MPL	mass-per-length
MTT	3-(4,5-dimethylthiazol-2-yl)-2,5-diphenyl-tetrazolium bromide
NBS	N-bromosuccinimide

XXIV | **ABBREVIATIONS**

NCS	N-chlorosuccinimide
NOE(SY)	nuclear Overhauser effect (spectroscopy)
NMR	nuclear magnetic resonance
NSAID	non steroidal anti-inflammatory drug
o/n	over night
OD ₆₀₀	optical density at 600 nm
PDS	proton-driven spin diffusion
PIB	Pittsburgh compound B
ppm	parts per million
PRE	paramagnetic relaxation enhancement
PSEN 1 and 2	Presenilin 1 and 2
p-tau	hyperphosphorylated tau
r	correlation coefficient
RDC	residual dipolar couplings
r.m.s.d.	root mean square deviation
REDOR	rotational echo double resonance
RF	radiofrequency
ROS	reactive oxygen species
RP-HPLC	reversed-phase high performance liquid chromatography
RPM	rotations per minute
RT	room temperature
SDS-PAGE	sodium dodecyl sulfate polyacrylamide gel electrophoresis
SEC	size exclusion chromatography
S/N	signal to noise
T	tesla
T1D	type 1 diabetes
T2D	type 2 diabetes
TALOS+	torsion angle likeliness obtained from shift and sequence similarity
TEDOR	transferred echo double resonance
TEM	transmission electron microscopy
TFA	trifluoroacetic acid
ThT	Thioflavin T
TROSY	transverse relaxation-optimized spectroscopy
UV	ultraviolet
UV/VIS	ultraviolet/visible
V	Volt

References

1. Keeler, J. *Understanding NMR Spectroscopy, 2nd Edition*, (John Wiley & Sons, 2010).
2. Cavanagh, J., Fairbrother, W.J., Palmer, A.G., Skelton, N.J. & Rance, M. *Protein NMR Spectroscopy. Principles and Practice*, (Elsevier, 2006).
3. Duer, M.J. *Solid State NMR Spectroscopy: Principles and Applications*, (Wiley-Blackwell, 2001).
4. Croasmun, W.R. & Carlson, R.M.K. *Two-Dimensional NMR Spectroscopy, Applications for Chemists and Biochemists*, (John Wiley and Sons, 1994).
5. Lu, K., Miyazaki, Y. & Summers, M.F. Isotope labeling strategies for NMR studies of RNA. *J. Biomol. NMR* **46**, 113-25 (2010).
6. Wüthrich, K. *NMR of Proteins and Nucleic Acids*, (John Wiley & Sons, 1986).
7. Boehr, D.D., McElheny, D., Dyson, H.J. & Wright, P.E. The dynamic energy landscape of dihydrofolate reductase catalysis. *Science* **313**, 1638-42 (2006).
8. Mittermaier, A.K. & Kay, L.E. Observing biological dynamics at atomic resolution using NMR. *Trends Biochem. Sci.* **34**, 601-11 (2009).
9. Loria, J.P., Berlow, R.B. & Watt, E.D. Characterization of enzyme motions by solution NMR relaxation dispersion. *Acc. Chem. Res.* **41**, 214-21 (2008).
10. Neudecker, P., Lundstrom, P. & Kay, L.E. Relaxation dispersion NMR spectroscopy as a tool for detailed studies of protein folding. *Biophys. J.* **96**, 2045-54 (2009).
11. Krushelnitsky, A., Reichert, D. & Saalwachter, K. Solid-state NMR approaches to internal dynamics of proteins: from picoseconds to microseconds and seconds. *Acc. Chem. Res.* **46**, 2028-36 (2013).
12. Siemer, A.B. et al. Observation of highly flexible residues in amyloid fibrils of the HET-s prion. *J. Am. Chem. Soc.* **128**, 13224-8 (2006).
13. Krushelnitsky, A. et al. Direct observation of millisecond to second motions in proteins by dipolar CODEX NMR spectroscopy. *J. Am. Chem. Soc.* **131**, 12097-9 (2009).
14. Lewandowski, J.R., Sass, H.J., Grzesiek, S., Blackledge, M. & Emsley, L. Site-specific measurement of slow motions in proteins. *J. Am. Chem. Soc.* **133**, 16762-5 (2011).
15. Lewandowski, J.R. Advances in solid-state relaxation methodology for probing site-specific protein dynamics. *Acc. Chem. Res.* **46**, 2018-27 (2013).
16. Tollinger, M., Sivertsen, A.C., Meier, B.H., Ernst, M. & Schanda, P. Site-resolved measurement of microsecond-to-millisecond conformational-exchange processes in proteins by solid-state NMR spectroscopy. *J. Am. Chem. Soc.* **134**, 14800-7 (2012).
17. Schanda, P., Huber, M., Boisbouvier, J., Meier, B.H. & Ernst, M. Solid-state NMR measurements of asymmetric dipolar couplings provide insight into protein side-chain motion. *Angew. Chem. Int. Ed. Engl.* **50**, 11005-9 (2011).
18. Reif, B. et al. Protein side-chain dynamics observed by solution- and solid-state NMR: comparative analysis of methyl ²H relaxation data. *J. Am. Chem. Soc.* **128**, 12354-5 (2006).
19. Chevelkov, V., Diehl, A. & Reif, B. Quantitative measurement of differential ¹⁵N-H(alpha/beta)T₂ relaxation rates in a perdeuterated protein by MAS solid-state NMR spectroscopy. *Magn. Reson. Chem.* **45 Suppl 1**, S156-60 (2007).
20. Chevelkov, V., Diehl, A. & Reif, B. Measurement of ¹⁵N-T₁ relaxation rates in a perdeuterated protein by magic angle spinning solid-state nuclear magnetic resonance spectroscopy. *J. Chem. Phys.* **128**, 052316 (2008).
21. Hologne, M., Faelber, K., Diehl, A. & Reif, B. Characterization of dynamics of perdeuterated proteins by MAS solid-state NMR. *J. Am. Chem. Soc.* **127**, 11208-9 (2005).
22. Wishart, D.S., Sykes, B.D. & Richards, F.M. The chemical shift index: a fast and simple method for the assignment of protein secondary structure through NMR spectroscopy. *Biochemistry* **31**, 1647-51 (1992).

23. Cornilescu, G., Delaglio, F. & Bax, A. Protein backbone angle restraints from searching a database for chemical shift and sequence homology. *J. Biomol. NMR* **13**, 289-302 (1999).
24. Shen, Y., Delaglio, F., Cornilescu, G. & Bax, A. TALOS+: a hybrid method for predicting protein backbone torsion angles from NMR chemical shifts. *J. Biomol. NMR* **44**, 213-23 (2009).
25. Shen, Y. et al. Consistent blind protein structure generation from NMR chemical shift data. *Proc. Natl. Acad. Sci. U. S. A.* **105**, 4685-90 (2008).
26. Marion, D. An introduction to biological NMR spectroscopy. *Mol. Cell. Proteomics* **12**, 3006-25 (2013).
27. Tjandra, N. & Bax, A. Direct measurement of distances and angles in biomolecules by NMR in a dilute liquid crystalline medium. *Science* **278**, 1111-4 (1997).
28. Barbet-Massin, E. & Pintacuda, G. Biomolecular Solid-State NMR/Basics. in *NMR of Biomolecules* 345-364 (Wiley-VCH Verlag GmbH & Co. KGaA, 2012). Reproduced with permission.
29. Maricq, M.M. & Waugh, J.S. NMR in rotating solids. *J. Chem. Phys.* **70**, 3300-3316 (1979).
30. Oas, T.G., Griffin, R.G. & Levitt, M.H. Rotary resonance recoupling of dipolar interactions in solid-state nuclear magnetic resonance spectroscopy. *J. Chem. Phys.* **89**, 692-695 (1988).
31. Pines, A., Gibby, M.G. & Waugh, J.S. Proton-Enhanced Nuclear Induction Spectroscopy. A Method for High Resolution NMR of Dilute Spins in Solids. *J. Chem. Phys.* **56**, 1776-1777 (1972).
32. Schaefer, J. & Stejskal, E.O. Carbon-13 nuclear magnetic resonance of polymers spinning at the magic angle. *J. Am. Chem. Soc.* **98**, 1031-1032 (1976).
33. Gullion, T. & Schaefer, J. Rotational-echo double-resonance NMR. *J. Magn. Reson.* **81**, 196-200 (1989).
34. Bennett, A.E., Griffin, R.G., Ok, J.H. & Vega, S. Chemical shift correlation spectroscopy in rotating solids: Radio frequency-driven dipolar recoupling and longitudinal exchange. *J. Chem. Phys.* **96**, 8624-8627 (1992).
35. Hartmann, S.R. & Hahn, E.L. Nuclear Double Resonance in the Rotating Frame. *Phys. Rev.* **128**, 2042-2053 (1962).
36. Gullion, T. Rotational-Echo, Double-Resonance NMR. in *Modern Magnetic Resonance* (ed. Webb, G.) 713-718 (Springer Netherlands, 2006).
37. Hing, A.W., Vega, S. & Schaefer, J. Transferred-echo double-resonance NMR. *J. Magn. Reson.* **96**, 205-209 (1992).
38. Hing, A.W., Vega, S. & Schaefer, J. Measurement of Heteronuclear Dipolar Coupling by Transferred-Echo Double-Resonance NMR. *J. Magn. Reson.* **103**, 151-162 (1993).
39. Jaroniec, C.P., Filip, C. & Griffin, R.G. 3D TEDOR NMR experiments for the simultaneous measurement of multiple carbon-nitrogen distances in uniformly (¹³C,¹⁵N)-labeled solids. *J. Am. Chem. Soc.* **124**, 10728-42 (2002).
40. Szeverenyi, N.M., Sullivan, M.J. & Maciel, G.E. Observation of spin exchange by two-dimensional fourier transform ¹³C cross polarization-magic-angle spinning. *J. Magn. Reson.* **47**, 462-475 (1982).
41. Takegoshi, K., Nakamura, S. & Terao, T. ¹³C-¹H dipolar-assisted rotational resonance in magic-angle spinning NMR. *Chem. Phys. Lett.* **344**, 631-637 (2001).
42. Scholz, I., Meier, B.H. & Ernst, M. Operator-based triple-mode Floquet theory in solid-state NMR. *J. Chem. Phys.* **127**, 204504 (2007).
43. Weingarh, M., Demco, D.E., Bodenhausen, G. & Tekely, P. Improved magnetization transfer in solid-state NMR with fast magic angle spinning. *Chem. Phys. Lett.* **469**, 342-348 (2009).
44. Scholz, I., Huber, M., Manolikas, T., Meier, B.H. & Ernst, M. MIRROR recoupling and its application to spin diffusion under fast magic-angle spinning. *Chem. Phys. Lett.* **460**, 278-283 (2008).
45. Lewandowski, J.R., De Paepe, G. & Griffin, R.G. Proton assisted insensitive nuclei cross polarization. *J. Am. Chem. Soc.* **129**, 728-9 (2007).
46. LeMaster, D.M. & Kushlan, D.M. Dynamical Mapping of E. coli Thioredoxin via ¹³C NMR Relaxation Analysis. *J. Am. Chem. Soc.* **118**, 9255-9264 (1996).

47. Hong, M. & Jakes, K. Selective and extensive ¹³C labeling of a membrane protein for solid-state NMR investigations. *J. Biomol. NMR* **14**, 71-4 (1999).
48. Castellani, F. et al. Structure of a protein determined by solid-state magic-angle-spinning NMR spectroscopy. *Nature* **420**, 98-102 (2002).
49. Wasmer, C. et al. Amyloid fibrils of the HET-s(218-289) prion form a beta solenoid with a triangular hydrophobic core. *Science* **319**, 1523-6 (2008).
50. Van Melckebeke, H. et al. Atomic-resolution three-dimensional structure of HET-s(218-289) amyloid fibrils by solid-state NMR spectroscopy. *J. Am. Chem. Soc.* **132**, 13765-75 (2010).
51. Jehle, S. et al. Solid-state NMR and SAXS studies provide a structural basis for the activation of alphaB-crystallin oligomers. *Nat. Struct. Mol. Biol.* **17**, 1037-42 (2010).
52. Loquet, A. et al. Atomic model of the type III secretion system needle. *Nature* **486**, 276-9 (2012).
53. Clore, G.M. Exploring sparsely populated states of macromolecules by diamagnetic and paramagnetic NMR relaxation. *Protein Sci.* **20**, 229-46 (2011).
54. Clore, G.M. Seeing the invisible by paramagnetic and diamagnetic NMR. *Biochem. Soc. Trans.* **41**, 1343-54 (2013).
55. Clore, G.M. Interplay between conformational selection and induced fit in multidomain protein-ligand binding probed by paramagnetic relaxation enhancement. *Biophys. Chem.* **186**, 3-12 (2014).
56. Anthis, N.J. & Clore, G.M. Visualizing transient dark states by NMR spectroscopy. *Q. Rev. Biophys.* **48**, 35-116 (2015).
57. Tang, C., Schwieters, C.D. & Clore, G.M. Open-to-closed transition in apo maltose-binding protein observed by paramagnetic NMR. *Nature* **449**, 1078-82 (2007).
58. Anthis, N.J., Doucleff, M. & Clore, G.M. Transient, sparsely populated compact states of apo and calcium-loaded calmodulin probed by paramagnetic relaxation enhancement: interplay of conformational selection and induced fit. *J. Am. Chem. Soc.* **133**, 18966-74 (2011).
59. Iwahara, J. & Clore, G.M. Detecting transient intermediates in macromolecular binding by paramagnetic NMR. *Nature* **440**, 1227-30 (2006).
60. Libich, D.S., Fawzi, N.L., Ying, J. & Clore, G.M. Probing the transient dark state of substrate binding to GroEL by relaxation-based solution NMR. *Proc. Natl. Acad. Sci. U. S. A.* **110**, 11361-6 (2013).
61. Fawzi, N.L., Ying, J., Torchia, D.A. & Clore, G.M. Kinetics of amyloid beta monomer-to-oligomer exchange by NMR relaxation. *J. Am. Chem. Soc.* **132**, 9948-51 (2010).
62. Fawzi, N.L., Ying, J., Torchia, D.A. & Clore, G.M. Probing exchange kinetics and atomic resolution dynamics in high-molecular-weight complexes using dark-state exchange saturation transfer NMR spectroscopy. *Nat. Protoc.* **7**, 1523-33 (2012).
63. Bayburt, T.H. & Sligar, S.G. Membrane protein assembly into Nanodiscs. *FEBS Lett.* **584**, 1721-7 (2010).
64. Inagaki, S., Ghirlando, R. & Grisshammer, R. Biophysical characterization of membrane proteins in nanodiscs. *Methods* **59**, 287-300 (2013).
65. Schuler, M.A., Denisov, I.G. & Sligar, S.G. Nanodiscs as a new tool to examine lipid-protein interactions. *Methods Mol. Biol.* **974**, 415-33 (2013).
66. Baas, B.J., Denisov, I.G. & Sligar, S.G. Homotropic cooperativity of monomeric cytochrome P450 3A4 in a nanoscale native bilayer environment. *Arch. Biochem. Biophys.* **430**, 218-28 (2004).
67. Denisov, I.G., Baas, B.J., Grinkova, Y.V. & Sligar, S.G. Cooperativity in cytochrome P450 3A4: linkages in substrate binding, spin state, uncoupling, and product formation. *J. Biol. Chem.* **282**, 7066-76 (2007).
68. Inagaki, S. et al. Modulation of the interaction between neurotensin receptor NTS1 and Gq protein by lipid. *J. Mol. Biol.* **417**, 95-111 (2012).
69. Maldonado, A.Y., Burz, D.S. & Shekhtman, A. In-cell NMR spectroscopy. *Prog. Nucl. Magn. Reson. Spectrosc.* **59**, 197-212 (2011).
70. Li, C. & Liu, M. Protein dynamics in living cells studied by in-cell NMR spectroscopy. *FEBS Lett.* **587**, 1008-11 (2013).
71. Selenko, P. et al. In situ observation of protein phosphorylation by high-resolution NMR spectroscopy. *Nat. Struct. Mol. Biol.* **15**, 321-9 (2008).
72. Giriati, I. & Muir, T.W. Protein semi-synthesis in living cells. *J. Am. Chem. Soc.* **125**, 7180-1 (2003).

73. Burz, D.S. & Shekhtman, A. The STINT-NMR method for studying in-cell protein-protein interactions. *Curr. Protoc. Protein Sci.* **Chapter 17**, Unit 17.11 (2010).
74. Xie, J., Thapa, R., Reverdatto, S., Burz, D.S. & Shekhtman, A. Screening of small molecule interactor library by using in-cell NMR spectroscopy (SMILI-NMR). *J. Med. Chem.* **52**, 3516-22 (2009).
75. Venters, R.A., Farmer, B.T., 2nd, Fierke, C.A. & Spicer, L.D. Characterizing the use of perdeuteration in NMR studies of large proteins: ¹³C, ¹⁵N and ¹H assignments of human carbonic anhydrase II. *J. Mol. Biol.* **264**, 1101-16 (1996).
76. Pervushin, K., Riek, R., Wider, G. & Wuthrich, K. Attenuated T2 relaxation by mutual cancellation of dipole-dipole coupling and chemical shift anisotropy indicates an avenue to NMR structures of very large biological macromolecules in solution. *Proc. Natl. Acad. Sci. U. S. A.* **94**, 12366-71 (1997).
77. Fiaux, J., Bertelsen, E.B., Horwich, A.L. & Wuthrich, K. NMR analysis of a 900K GroEL GroES complex. *Nature* **418**, 207-11 (2002).
78. Riek, R., Fiaux, J., Bertelsen, E.B., Horwich, A.L. & Wuthrich, K. Solution NMR techniques for large molecular and supramolecular structures. *J. Am. Chem. Soc.* **124**, 12144-53 (2002).
79. Tugarinov, V., Ollerenshaw, J.E. & Kay, L.E. Probing side-chain dynamics in high molecular weight proteins by deuterium NMR spin relaxation: an application to an 82-kDa enzyme. *J. Am. Chem. Soc.* **127**, 8214-25 (2005).
80. Tugarinov, V. & Kay, L.E. Methyl groups as probes of structure and dynamics in NMR studies of high-molecular-weight proteins. *Chembiochem* **6**, 1567-77 (2005).
81. Wiesner, S. & Sprangers, R. Methyl groups as NMR probes for biomolecular interactions. *Curr. Opin. Struct. Biol.* **35**, 60-67 (2015).
82. Lichtenecker, R.J., Coudeville, N., Konrat, R. & Schmid, W. Selective isotope labelling of leucine residues by using alpha-ketoacid precursor compounds. *Chembiochem* **14**, 818-21 (2013).
83. Tugarinov, V. & Kay, L.E. Ile, Leu, and Val methyl assignments of the 723-residue malate synthase G using a new labeling strategy and novel NMR methods. *J. Am. Chem. Soc.* **125**, 13868-78 (2003).
84. Miyanoiri, Y. et al. Differential isotope-labeling for Leu and Val residues in a protein by E. coli cellular expression using stereo-specifically methyl labeled amino acids. *J. Biomol. NMR* **57**, 237-49 (2013).
85. Linser, R., Fink, U. & Reif, B. Assignment of dynamic regions in biological solids enabled by spin-state selective NMR experiments. *J. Am. Chem. Soc.* **132**, 8891-3 (2010).
86. Reif, B., Jaroniec, C.P., Rienstra, C.M., Hohwy, M. & Griffin, R.G. 1H-1H MAS correlation spectroscopy and distance measurements in a deuterated peptide. *J. Magn. Reson.* **151**, 320-7 (2001).
87. Linser, R., Bardiaux, B., Higman, V., Fink, U. & Reif, B. Structure calculation from unambiguous long-range amide and methyl 1H-1H distance restraints for a microcrystalline protein with MAS solid-state NMR spectroscopy. *J. Am. Chem. Soc.* **133**, 5905-12 (2011).
88. Linser, R., Fink, U. & Reif, B. Proton-detected scalar coupling based assignment strategies in MAS solid-state NMR spectroscopy applied to perdeuterated proteins. *J. Magn. Reson.* **193**, 89-93 (2008).
89. Akbey, U. et al. Optimum levels of exchangeable protons in perdeuterated proteins for proton detection in MAS solid-state NMR spectroscopy. *J. Biomol. NMR* **46**, 67-73 (2010).
90. Asami, S., Schmieder, P. & Reif, B. High resolution 1H-detected solid-state NMR spectroscopy of protein aliphatic resonances: access to tertiary structure information. *J. Am. Chem. Soc.* **132**, 15133-5 (2010).
91. Samoson, A., Tuhern, T. & Gan, Z. High-field high-speed MAS resolution enhancement in 1H NMR spectroscopy of solids. *Solid State Nucl. Magn. Reson.* **20**, 130-6 (2001).
92. Knight, M.J. et al. Fast resonance assignment and fold determination of human superoxide dismutase by high-resolution proton-detected solid-state MAS NMR spectroscopy. *Angew. Chem. Int. Ed. Engl.* **50**, 11697-701 (2011).
93. Zhou, D.H. et al. Proton-detected solid-state NMR spectroscopy of fully protonated proteins at 40 kHz magic-angle spinning. *J. Am. Chem. Soc.* **129**, 11791-801 (2007).

94. Marchetti, A. et al. Backbone assignment of fully protonated solid proteins by ^1H detection and ultrafast magic-angle-spinning NMR spectroscopy. *Angew. Chem. Int. Ed. Engl.* **51**, 10756-9 (2012).
95. Barbet-Massin, E. et al. Rapid proton-detected NMR assignment for proteins with fast magic angle spinning. *J. Am. Chem. Soc.* **136**, 12489-97 (2014).
96. Barbet-Massin, E. et al. Insights into the structure and dynamics of measles virus nucleocapsids by ^1H -detected solid-state NMR. *Biophys. J.* **107**, 941-6 (2014).
97. Barna, J.C.J., Laue, E.D., Mayger, M.R., Skilling, J. & Worrall, S.J.P. Exponential sampling, an alternative method for sampling in two-dimensional NMR experiments. *J. Magn. Reson.* **73**, 69-77 (1987).
98. Coggins, B.E., Venters, R.A. & Zhou, P. Radial sampling for fast NMR: Concepts and practices over three decades. *Prog. Nucl. Magn. Reson. Spectrosc.* **57**, 381-419 (2010).
99. Hyberts, S.G., Arthanari, H. & Wagner, G. Applications of non-uniform sampling and processing. *Top. Curr. Chem.* **316**, 125-48 (2012).
100. Huber, M. et al. A proton-detected 4D solid-state NMR experiment for protein structure determination. *Chemphyschem* **12**, 915-8 (2011).
101. Su, Y., Andreas, L. & Griffin, R.G. Magic angle spinning NMR of proteins: high-frequency dynamic nuclear polarization and (^1H) detection. *Annu. Rev. Biochem.* **84**, 465-97 (2015).
102. Lee, D., Hediger, S. & De Paepe, G. Is solid-state NMR enhanced by dynamic nuclear polarization? *Solid State Nucl. Magn. Reson.* **66-67**, 6-20 (2015).
103. Overhauser, A.W. Polarization of Nuclei in Metals. *Phys. Rev.* **92**, 411-415 (1953).
104. Carver, T.R. & Slichter, C.P. Experimental Verification of the Overhauser Nuclear Polarization Effect. *Phys. Rev.* **102**, 975-980 (1956).
105. Cheng, C.Y. & Han, S. Dynamic nuclear polarization methods in solids and solutions to explore membrane proteins and membrane systems. *Annu. Rev. Phys. Chem.* **64**, 507-32 (2013).
106. Bajaj, V.S., Mak-Jurkauskas, M.L., Belenky, M., Herzfeld, J. & Griffin, R.G. Functional and shunt states of bacteriorhodopsin resolved by 250 GHz dynamic nuclear polarization-enhanced solid-state NMR. *Proc. Natl. Acad. Sci. U. S. A.* **106**, 9244-9 (2009).
107. Bajaj, V.S., Mak-Jurkauskas, M.L., Belenky, M., Herzfeld, J. & Griffin, R.G. DNP enhanced frequency-selective TEDOR experiments in bacteriorhodopsin. *J. Magn. Reson.* **202**, 9-13 (2010).
108. Debelouchina, G.T. et al. Higher order amyloid fibril structure by MAS NMR and DNP spectroscopy. *J. Am. Chem. Soc.* **135**, 19237-47 (2013).
109. Lopez del Amo, J.M., Schneider, D., Loquet, A., Lange, A. & Reif, B. Cryogenic solid state NMR studies of fibrils of the Alzheimer's disease amyloid-beta peptide: perspectives for DNP. *J. Biomol. NMR* **56**, 359-63 (2013).
110. Potapov, A., Yau, W.M., Ghirlando, R., Thurber, K.R. & Tycko, R. Successive Stages of Amyloid-beta Self-Assembly Characterized by Solid-State Nuclear Magnetic Resonance with Dynamic Nuclear Polarization. *J. Am. Chem. Soc.* **137**, 8294-307 (2015).
111. Agarwal, V. et al. De novo 3D structure determination from sub-milligram protein samples by solid-state 100 kHz MAS NMR spectroscopy. *Angew. Chem. Int. Ed. Engl.* **53**, 12253-6 (2014).
112. Prince, M. et al. The global prevalence of dementia: a systematic review and metaanalysis. *Alzheimers Dement* **9**, 63-75 e2 (2013).
113. 2015 Alzheimer's disease facts and figures. *Alzheimers Dement* **11**, 332-84 (2015).
114. Hippus, H. & Neundörfer, G. The discovery of Alzheimer's disease. *Dialogues Clin. Neurosci.* **5**, 101-108 (2003).
115. Reitz, C. & Mayeux, R. Alzheimer disease: epidemiology, diagnostic criteria, risk factors and biomarkers. *Biochem. Pharmacol.* **88**, 640-51 (2014).
116. Lloret, A., Fuchsberger, T., Giraldo, E. & Vina, J. Molecular mechanisms linking amyloid beta toxicity and Tau hyperphosphorylation in Alzheimers disease. *Free Radic. Biol. Med.* **83**, 186-191 (2015).
117. Imtiaz, B., Tolppanen, A.M., Kivipelto, M. & Soininen, H. Future directions in Alzheimer's disease from risk factors to prevention. *Biochem. Pharmacol.* **88**, 661-70 (2014).

118. Blennow, K., de Leon, M.J. & Zetterberg, H. Alzheimer's disease. *Lancet* **368**, 387-403 (2006).
119. Bekris, L.M., Yu, C.E., Bird, T.D. & Tsuang, D.W. Genetics of Alzheimer disease. *J. Geriatr. Psychiatry Neurol.* **23**, 213-27 (2010).
120. Ringman, J.M. et al. Genetic heterogeneity in Alzheimer disease and implications for treatment strategies. *Curr. Neurol. Neurosci. Rep.* **14**, 499 (2014).
121. St George-Hyslop, P.H. et al. Genetic linkage studies suggest that Alzheimer's disease is not a single homogeneous disorder. *Nature* **347**, 194-7 (1990).
122. Liu, C.C., Kanekiyo, T., Xu, H. & Bu, G. Apolipoprotein E and Alzheimer disease: risk, mechanisms and therapy. *Nat. Rev. Neurol.* **9**, 106-18 (2013).
123. Ringman, J.M. & Coppola, G. New genes and new insights from old genes: update on Alzheimer disease. *Continuum (Minneapolis)* **19**, 358-71 (2013).
124. Teller, J.K. et al. Presence of soluble amyloid beta-peptide precedes amyloid plaque formation in Down's syndrome. *Nat. Med.* **2**, 93-5 (1996).
125. Kuusisto, J. et al. Association of apolipoprotein E phenotypes with late onset Alzheimer's disease: population based study. *BMJ* **309**, 636-8 (1994).
126. Blennow, K., Mattsson, N., Scholl, M., Hansson, O. & Zetterberg, H. Amyloid biomarkers in Alzheimer's disease. *Trends Pharmacol. Sci.* **36**, 297-309 (2015).
127. Blennow, K., Hampel, H. & Zetterberg, H. Biomarkers in amyloid-beta immunotherapy trials in Alzheimer's disease. *Neuropsychopharmacology* **39**, 189-201 (2014).
128. Hampel, H. et al. Core biological marker candidates of Alzheimer's disease - perspectives for diagnosis, prediction of outcome and reflection of biological activity. *J. Neural. Transm.* **111**, 247-72 (2004).
129. Bateman, R. Alzheimer's disease and other dementias: advances in 2014. *Lancet. Neurol.* **14**, 4-6 (2015).
130. Lobello, K., Ryan, J.M., Liu, E., Rippon, G. & Black, R. Targeting Beta amyloid: a clinical review of immunotherapeutic approaches in Alzheimer's disease. *Int. J. Alzheimers Dis.* **2012**, 628070 (2012).
131. Folch, J. et al. Review of the advances in treatment for Alzheimer disease: Strategies for combating beta-amyloid protein. *Neurologia* (2015).
132. Morrone, C.D., Liu, M., Black, S.E. & McLaurin, J. Interaction between therapeutic interventions for Alzheimer's disease and physiological Abeta clearance mechanisms. *Front. Aging Neurosci.* **7**, 64 (2015).
133. Toyn, J. What lessons can be learned from failed Alzheimer's disease trials? *Expert Rev. Clin. Pharmacol.* **8**, 267-9 (2015).
134. Zhang, B. et al. Integrated systems approach identifies genetic nodes and networks in late-onset Alzheimer's disease. *Cell* **153**, 707-20 (2013).
135. Akiyama, H. et al. Inflammation and Alzheimer's disease. *Neurobiol. Aging* **21**, 383-421 (2000).
136. De Felice, F.G. Alzheimer's disease and insulin resistance: translating basic science into clinical applications. *J. Clin. Invest.* **123**, 531-9 (2013).
137. Heneka, M.T. et al. Neuroinflammation in Alzheimer's disease. *Lancet. Neurol.* **14**, 388-405 (2015).
138. McGeer, P.L. & McGeer, E.G. The inflammatory response system of brain: implications for therapy of Alzheimer and other neurodegenerative diseases. *Brain Res. Brain Res. Rev.* **21**, 195-218 (1995).
139. Agostinho, P., Cunha, R.A. & Oliveira, C. Neuroinflammation, oxidative stress and the pathogenesis of Alzheimer's disease. *Curr. Pharm. Des.* **16**, 2766-78 (2010).
140. Broussard, G.J., Mytar, J., Li, R.C. & Klapstein, G.J. The role of inflammatory processes in Alzheimer's disease. *Inflammopharmacology* **20**, 109-26 (2012).
141. Ferreira, S.T., Clarke, J.R., Bomfim, T.R. & De Felice, F.G. Inflammation, defective insulin signaling, and neuronal dysfunction in Alzheimer's disease. *Alzheimers Dement* **10**, S76-83 (2014).
142. Kukar, T. & Golde, T.E. Possible mechanisms of action of NSAIDs and related compounds that modulate gamma-secretase cleavage. *Curr. Top. Med. Chem.* **8**, 47-53 (2008).
143. Etminan, M., Gill, S. & Samii, A. Effect of non-steroidal anti-inflammatory drugs on risk of Alzheimer's disease: systematic review and meta-analysis of observational studies. *BMJ* **327**, 128 (2003).

144. Hayden, K.M. et al. Does NSAID use modify cognitive trajectories in the elderly? The Cache County study. *Neurology* **69**, 275-82 (2007).
145. Wang, J. et al. Anti-inflammatory drugs and risk of Alzheimer's disease: an updated systematic review and meta-analysis. *J. Alzheimers Dis.* **44**, 385-96 (2015).
146. Kelly, J.W. The alternative conformations of amyloidogenic proteins and their multi-step assembly pathways. *Curr. Opin. Struct. Biol.* **8**, 101-6 (1998).
147. Dobson, C.M. The structural basis of protein folding and its links with human disease. *Philos. Trans. R. Soc. Lond. B. Biol. Sci.* **356**, 133-45 (2001).
148. Bucciantini, M. et al. Inherent toxicity of aggregates implies a common mechanism for protein misfolding diseases. *Nature* **416**, 507-11 (2002).
149. Kelly, J.W. Towards an understanding of amyloidogenesis. *Nat. Struct. Biol.* **9**, 323-5 (2002).
150. Cornwell, G.G., 3rd et al. Identification and characterization of different amyloid fibril proteins in tissue sections. *Scand. J. Immunol.* **6**, 1071-80 (1977).
151. Trojanowski, J.Q. & Lee, V.M. Aggregation of neurofilament and alpha-synuclein proteins in Lewy bodies: implications for the pathogenesis of Parkinson disease and Lewy body dementia. *Arch. Neurol.* **55**, 151-2 (1998).
152. Mukherjee, A., Morales-Scheihing, D., Butler, P.C. & Soto, C. Type 2 diabetes as a protein misfolding disease. *Trends Mol. Med.* (2015).
153. Masters, C.L. et al. Amyloid plaque core protein in Alzheimer disease and Down syndrome. *Proc. Natl. Acad. Sci. U. S. A.* **82**, 4245-9 (1985).
154. Kang, J. et al. The precursor of Alzheimer's disease amyloid A4 protein resembles a cell-surface receptor. *Nature* **325**, 733-6 (1987).
155. Selkoe, D.J. Alzheimer's disease: genes, proteins, and therapy. *Physiol. Rev.* **81**, 741-66 (2001).
156. Haass, C. & Selkoe, D.J. Cellular processing of beta-amyloid precursor protein and the genesis of amyloid beta-peptide. *Cell* **75**, 1039-42 (1993).
157. Muresan, V. & Ladescu Muresan, Z. Amyloid-beta precursor protein: Multiple fragments, numerous transport routes and mechanisms. *Exp. Cell Res.* **334**, 45-53 (2015).
158. Selkoe, D.J. Translating cell biology into therapeutic advances in Alzheimer's disease. *Nature* **399**, A23-31 (1999).
159. Haass, C. et al. Amyloid beta-peptide is produced by cultured cells during normal metabolism. *Nature* **359**, 322-5 (1992).
160. Vassar, R. et al. Beta-secretase cleavage of Alzheimer's amyloid precursor protein by the transmembrane aspartic protease BACE. *Science* **286**, 735-41 (1999).
161. Haass, C. Take five--BACE and the gamma-secretase quartet conduct Alzheimer's amyloid beta-peptide generation. *EMBO J.* **23**, 483-8 (2004).
162. Vassar, R. & Citron, M. Abeta-generating enzymes: recent advances in beta- and gamma-secretase research. *Neuron* **27**, 419-22 (2000).
163. Steiner, H. & Haass, C. Intramembrane proteolysis by presenilins. *Nat. Rev. Mol. Cell Biol.* **1**, 217-24 (2000).
164. Olsson, F. et al. Characterization of intermediate steps in amyloid beta (Abeta) production under near-native conditions. *J. Biol. Chem.* **289**, 1540-50 (2014).
165. Vigo-Pelfrey, C., Lee, D., Keim, P., Lieberburg, I. & Schenk, D.B. Characterization of beta-amyloid peptide from human cerebrospinal fluid. *J. Neurochem.* **61**, 1965-8 (1993).
166. Dovey, H.F., Suomensaari-Chrysler, S., Lieberburg, I., Sinha, S. & Keim, P.S. Cells with a familial Alzheimer's disease mutation produce authentic beta-peptide. *Neuroreport* **4**, 1039-42 (1993).
167. Kim, J. et al. Abeta40 inhibits amyloid deposition in vivo. *J. Neurosci.* **27**, 627-33 (2007).
168. Jarrett, J.T., Berger, E.P. & Lansbury, P.T., Jr. The carboxy terminus of the beta amyloid protein is critical for the seeding of amyloid formation: implications for the pathogenesis of Alzheimer's disease. *Biochemistry* **32**, 4693-7 (1993).
169. Roher, A.E. et al. beta-Amyloid-(1-42) is a major component of cerebrovascular amyloid deposits: implications for the pathology of Alzheimer disease. *Proc. Natl. Acad. Sci. U. S. A.* **90**, 10836-40 (1993).
170. Lansbury, P.T., Jr. Structural neurology: are seeds at the root of neuronal degeneration? *Neuron* **19**, 1151-4 (1997).

171. Teplow, D.B. Structural and kinetic features of amyloid beta-protein fibrillogenesis. *Amyloid* **5**, 121-42 (1998).
172. Duering, M., Grimm, M.O., Grimm, H.S., Schroder, J. & Hartmann, T. Mean age of onset in familial Alzheimer's disease is determined by amyloid beta 42. *Neurobiol. Aging* **26**, 785-8 (2005).
173. Kumar-Singh, S. et al. Mean age-of-onset of familial Alzheimer disease caused by presenilin mutations correlates with both increased Abeta42 and decreased Abeta40. *Hum. Mutat.* **27**, 686-95 (2006).
174. Butterfield, D.A. Amyloid beta-peptide (1-42)-induced oxidative stress and neurotoxicity: implications for neurodegeneration in Alzheimer's disease brain. A review. *Free Radic. Res.* **36**, 1307-13 (2002).
175. Butterfield, D.A., Reed, T., Newman, S.F. & Sultana, R. Roles of amyloid beta-peptide-associated oxidative stress and brain protein modifications in the pathogenesis of Alzheimer's disease and mild cognitive impairment. *Free Radic. Biol. Med.* **43**, 658-77 (2007).
176. Butterfield, D.A. & Stadtman, E.R. Chapter 7 Protein Oxidation Processes in Aging Brain. in *Advances in Cell Aging and Gerontology*, Vol. Volume 2 (eds. Paula, S.T. & Bittar, E.E.) 161-191 (Elsevier, 1997).
177. Levine, R.L., Mosoni, L., Berlett, B.S. & Stadtman, E.R. Methionine residues as endogenous antioxidants in proteins. *Proc. Natl. Acad. Sci. U. S. A.* **93**, 15036-40 (1996).
178. Moskowitz, J., Berlett, B.S., Poston, J.M. & Stadtman, E.R. Methionine sulfoxide reductase in antioxidant defense. *Methods Enzymol.* **300**, 239-44 (1999).
179. Markesbery, W.R. Oxidative stress hypothesis in Alzheimer's disease. *Free Radic. Biol. Med.* **23**, 134-47 (1997).
180. Varadarajan, S., Yatin, S., Aksenova, M. & Butterfield, D.A. Review: Alzheimer's amyloid beta-peptide-associated free radical oxidative stress and neurotoxicity. *J. Struct. Biol.* **130**, 184-208 (2000).
181. Butterfield, D.A. & Boyd-Kimball, D. The critical role of methionine 35 in Alzheimer's amyloid beta-peptide (1-42)-induced oxidative stress and neurotoxicity. *Biochim. Biophys. Acta* **1703**, 149-56 (2005).
182. Kuo, Y.M. et al. Comparative analysis of amyloid-beta chemical structure and amyloid plaque morphology of transgenic mouse and Alzheimer's disease brains. *J. Biol. Chem.* **276**, 12991-8 (2001).
183. Huang, X. et al. Cu(II) potentiation of Alzheimer abeta neurotoxicity. Correlation with cell-free hydrogen peroxide production and metal reduction. *J. Biol. Chem.* **274**, 37111-6 (1999).
184. Watson, A.A., Fairlie, D.P. & Craik, D.J. Solution structure of methionine-oxidized amyloid beta-peptide (1-40). Does oxidation affect conformational switching? *Biochemistry* **37**, 12700-6 (1998).
185. Hou, L., Kang, I., Marchant, R.E. & Zagorski, M.G. Methionine 35 oxidation reduces fibril assembly of the amyloid abeta-(1-42) peptide of Alzheimer's disease. *J. Biol. Chem.* **277**, 40173-6 (2002).
186. Hou, L. et al. Solution NMR studies of the A beta(1-40) and A beta(1-42) peptides establish that the Met35 oxidation state affects the mechanism of amyloid formation. *J. Am. Chem. Soc.* **126**, 1992-2005 (2004).
187. Palmblad, M., Westlind-Danielsson, A. & Bergquist, J. Oxidation of methionine 35 attenuates formation of amyloid beta -peptide 1-40 oligomers. *J. Biol. Chem.* **277**, 19506-10 (2002).
188. Seilheimer, B. et al. The toxicity of the Alzheimer's beta-amyloid peptide correlates with a distinct fiber morphology. *J. Struct. Biol.* **119**, 59-71 (1997).
189. Khurana, R. et al. Mechanism of thioflavin T binding to amyloid fibrils. *J. Struct. Biol.* **151**, 229-38 (2005).
190. Naiki, H. & Gejyo, F. Kinetic analysis of amyloid fibril formation. *Methods Enzymol.* **309**, 305-18 (1999).
191. Wood, S.J. et al. alpha-synuclein fibrillogenesis is nucleation-dependent. Implications for the pathogenesis of Parkinson's disease. *J. Biol. Chem.* **274**, 19509-12 (1999).
192. Bhak, G., Choe, Y.J. & Paik, S.R. Mechanism of amyloidogenesis: nucleation-dependent fibrillation versus double-concerted fibrillation. *BMB Rep.* **42**, 541-51 (2009).

193. Ghosh, P., Kumar, A., Datta, B. & Rangachari, V. Dynamics of protofibril elongation and association involved in Abeta42 peptide aggregation in Alzheimer's disease. *BMC Bioinformatics* **11 Suppl 6**, S24 (2010).
194. Naiki, H., Higuchi, K., Nakakuki, K. & Takeda, T. Kinetic analysis of amyloid fibril polymerization in vitro. *Lab. Invest.* **65**, 104-10 (1991).
195. Naiki, H. & Nakakuki, K. First-order kinetic model of Alzheimer's beta-amyloid fibril extension in vitro. *Lab. Invest.* **74**, 374-83 (1996).
196. Jarrett, J.T. & Lansbury, P.T., Jr. Seeding "one-dimensional crystallization" of amyloid: a pathogenic mechanism in Alzheimer's disease and scrapie? *Cell* **73**, 1055-8 (1993).
197. Yoshimura, Y. et al. Distinguishing crystal-like amyloid fibrils and glass-like amorphous aggregates from their kinetics of formation. *Proc. Natl. Acad. Sci. U. S. A.* **109**, 14446-51 (2012).
198. Vekilov, P.G. Phase diagrams and kinetics of phase transitions in protein solutions. *J. Phys. Condens Matter* **24**, 193101 (2012).
199. Cabriolu, R., Kashchiev, D. & Auer, S. Atomistic theory of amyloid fibril nucleation. *J. Chem. Phys.* **133**, 225101 (2010).
200. Stathopoulos, P.B. et al. Sonication of proteins causes formation of aggregates that resemble amyloid. *Protein Sci.* **13**, 3017-27 (2004).
201. Ohhashi, Y., Kihara, M., Naiki, H. & Goto, Y. Ultrasonication-induced amyloid fibril formation of beta2-microglobulin. *J. Biol. Chem.* **280**, 32843-8 (2005).
202. So, M. et al. Ultrasonication-dependent acceleration of amyloid fibril formation. *J. Mol. Biol.* **412**, 568-77 (2011).
203. Selkoe, D.J. The molecular pathology of Alzheimer's disease. *Neuron* **6**, 487-98 (1991).
204. Hardy, J.A. & Higgins, G.A. Alzheimer's disease: the amyloid cascade hypothesis. *Science* **256**, 184-5 (1992).
205. Hardy, J. & Selkoe, D.J. The amyloid hypothesis of Alzheimer's disease: progress and problems on the road to therapeutics. *Science* **297**, 353-6 (2002).
206. Ferreira, S.T. & Klein, W.L. The Abeta oligomer hypothesis for synapse failure and memory loss in Alzheimer's disease. *Neurobiol. Learn. Mem.* **96**, 529-43 (2011).
207. Morris, G.P., Clark, I.A. & Vissel, B. Inconsistencies and controversies surrounding the amyloid hypothesis of Alzheimer's disease. *Acta Neuropathol. Commun.* **2**, 135 (2014).
208. The amyloid cascade hypothesis has misled the pharmaceutical industry. *Biochem. Soc. Trans.* **39**, 920-3 (2011).
209. Haass, C. & Selkoe, D.J. Soluble protein oligomers in neurodegeneration: lessons from the Alzheimer's amyloid beta-peptide. *Nat. Rev. Mol. Cell Biol.* **8**, 101-12 (2007).
210. Ono, K. & Yamada, M. Low-n oligomers as therapeutic targets of Alzheimer's disease. *J. Neurochem.* **117**, 19-28 (2011).
211. Ferreira, S.T., Lourenco, M.V., Oliveira, M.M. & De Felice, F.G. Soluble amyloid-beta oligomers as synaptotoxins leading to cognitive impairment in Alzheimer's disease. *Front. Cell Neurosci.* **9**, 191 (2015).
212. Lambert, M.P. et al. Diffusible, nonfibrillar ligands derived from Abeta1-42 are potent central nervous system neurotoxins. *Proc. Natl. Acad. Sci. U. S. A.* **95**, 6448-53 (1998).
213. Dahlgren, K.N. et al. Oligomeric and fibrillar species of amyloid-beta peptides differentially affect neuronal viability. *J. Biol. Chem.* **277**, 32046-53 (2002).
214. De Felice, F.G. et al. Alzheimer's disease-type neuronal tau hyperphosphorylation induced by A beta oligomers. *Neurobiol. Aging* **29**, 1334-47 (2008).
215. Walsh, D.M. et al. Naturally secreted oligomers of amyloid beta protein potently inhibit hippocampal long-term potentiation in vivo. *Nature* **416**, 535-9 (2002).
216. Shankar, G.M. et al. Natural oligomers of the Alzheimer amyloid-beta protein induce reversible synapse loss by modulating an NMDA-type glutamate receptor-dependent signaling pathway. *J. Neurosci.* **27**, 2866-75 (2007).
217. Figueiredo, C.P. et al. Memantine rescues transient cognitive impairment caused by high-molecular-weight abeta oligomers but not the persistent impairment induced by low-molecular-weight oligomers. *J. Neurosci.* **33**, 9626-34 (2013).
218. Lesne, S.E. et al. Brain amyloid-beta oligomers in ageing and Alzheimer's disease. *Brain* **136**, 1383-98 (2013).

219. O'Malley, T.T. et al. Abeta dimers differ from monomers in structural propensity, aggregation paths and population of synaptotoxic assemblies. *Biochem. J.* **461**, 413-26 (2014).
220. Hung, L.W. et al. Amyloid-beta peptide (Abeta) neurotoxicity is modulated by the rate of peptide aggregation: Abeta dimers and trimers correlate with neurotoxicity. *J. Neurosci.* **28**, 11950-8 (2008).
221. O'Nuallain, B. et al. Amyloid beta-protein dimers rapidly form stable synaptotoxic protofibrils. *J. Neurosci.* **30**, 14411-9 (2010).
222. Tycko, R. Amyloid Polymorphism: Structural Basis and Neurobiological Relevance. *Neuron* **86**, 632-645 (2015).
223. Qiang, W., Kelley, K. & Tycko, R. Polymorph-specific kinetics and thermodynamics of beta-amyloid fibril growth. *J. Am. Chem. Soc.* **135**, 6860-71 (2013).
224. Kodali, R., Williams, A.D., Chemuru, S. & Wetzel, R. Abeta(1-40) forms five distinct amyloid structures whose beta-sheet contents and fibril stabilities are correlated. *J. Mol. Biol.* **401**, 503-17 (2010).
225. Petkova, A.T. et al. Self-propagating, molecular-level polymorphism in Alzheimer's beta-amyloid fibrils. *Science* **307**, 262-5 (2005).
226. Giasson, B.I. et al. Initiation and synergistic fibrillization of tau and alpha-synuclein. *Science* **300**, 636-40 (2003).
227. O'Nuallain, B., Williams, A.D., Westermarck, P. & Wetzel, R. Seeding specificity in amyloid growth induced by heterologous fibrils. *J. Biol. Chem.* **279**, 17490-9 (2004).
228. Snyder, S.W. et al. Amyloid-beta aggregation: selective inhibition of aggregation in mixtures of amyloid with different chain lengths. *Biophys. J.* **67**, 1216-28 (1994).
229. Jan, A., Gokce, O., Luthi-Carter, R. & Lashuel, H.A. The ratio of monomeric to aggregated forms of Abeta40 and Abeta42 is an important determinant of amyloid-beta aggregation, fibrillogenesis, and toxicity. *J. Biol. Chem.* **283**, 28176-89 (2008).
230. Hasegawa, K., Yamaguchi, I., Omata, S., Gejyo, F. & Naiki, H. Interaction between A beta(1-42) and A beta(1-40) in Alzheimer's beta-amyloid fibril formation in vitro. *Biochemistry* **38**, 15514-21 (1999).
231. Pauwels, K. et al. Structural basis for increased toxicity of pathological abeta42:abeta40 ratios in Alzheimer disease. *J. Biol. Chem.* **287**, 5650-60 (2012).
232. Lu, J.X. et al. Molecular structure of beta-amyloid fibrils in Alzheimer's disease brain tissue. *Cell* **154**, 1257-68 (2013).
233. Xiao, Y. et al. Abeta(1-42) fibril structure illuminates self-recognition and replication of amyloid in Alzheimer's disease. *Nat. Struct. Mol. Biol.* **22**, 499-505 (2015).
234. Tycko, R. Solid-state NMR studies of amyloid fibril structure. *Annu. Rev. Phys. Chem.* **62**, 279-99 (2011).
235. Habenstein, B. & Loquet, A. Solid-state NMR: An emerging technique in structural biology of self-assemblies. *Biophys. Chem.* (2015).
236. Abelein, A. et al. The hairpin conformation of the amyloid beta peptide is an important structural motif along the aggregation pathway. *J. Biol. Inorg. Chem.* **19**, 623-34 (2014).
237. Benilova, I., Karran, E. & De Strooper, B. The toxic Abeta oligomer and Alzheimer's disease: an emperor in need of clothes. *Nat. Neurosci.* **15**, 349-57 (2012).
238. Zhang, S. et al. The Alzheimer's peptide a beta adopts a collapsed coil structure in water. *J. Struct. Biol.* **130**, 130-41 (2000).
239. Riek, R., Guntert, P., Dobeili, H., Wipf, B. & Wuthrich, K. NMR studies in aqueous solution fail to identify significant conformational differences between the monomeric forms of two Alzheimer peptides with widely different plaque-competence, A beta(1-40)(ox) and A beta(1-42)(ox). *Eur. J. Biochem.* **268**, 5930-6 (2001).
240. Dyson, H.J. & Wright, P.E. Intrinsically unstructured proteins and their functions. *Nat. Rev. Mol. Cell Biol.* **6**, 197-208 (2005).
241. Vivekanandan, S., Brender, J.R., Lee, S.Y. & Ramamoorthy, A. A partially folded structure of amyloid-beta(1-40) in an aqueous environment. *Biochem. Biophys. Res. Commun.* **411**, 312-6 (2011).
242. Breydo, L. & Uversky, V.N. Structural, morphological, and functional diversity of amyloid oligomers. *FEBS Lett.* (2015).
243. Rahimi, F., Shanmugam, A. & Bitan, G. Structure-function relationships of pre-fibrillar protein assemblies in Alzheimer's disease and related disorders. *Curr. Alzheimer Res.* **5**, 319-41 (2008).

244. Chimon, S. & Ishii, Y. Capturing intermediate structures of Alzheimer's beta-amyloid, Abeta(1-40), by solid-state NMR spectroscopy. *J. Am. Chem. Soc.* **127**, 13472-3 (2005).
245. Bitan, G., Lomakin, A. & Teplow, D.B. Amyloid beta-protein oligomerization: prenucleation interactions revealed by photo-induced cross-linking of unmodified proteins. *J. Biol. Chem.* **276**, 35176-84 (2001).
246. Rahimi, F., Maiti, P. & Bitan, G. Photo-induced cross-linking of unmodified proteins (PICUP) applied to amyloidogenic peptides. *J. Vis. Exp.* (2009).
247. Barghorn, S. et al. Globular amyloid beta-peptide oligomer - a homogenous and stable neuropathological protein in Alzheimer's disease. *J. Neurochem.* **95**, 834-47 (2005).
248. Shinoda, K., Sohma, Y. & Kanai, M. Synthesis of chemically-tethered amyloid-beta segment trimer possessing amyloidogenic properties. *Bioorg. Med. Chem. Lett.* **25**, 2976-9 (2015).
249. Rangachari, V. et al. Amyloid-beta(1-42) rapidly forms protofibrils and oligomers by distinct pathways in low concentrations of sodium dodecylsulfate. *Biochemistry* **46**, 12451-62 (2007).
250. Sandberg, A. et al. Stabilization of neurotoxic Alzheimer amyloid-beta oligomers by protein engineering. *Proc. Natl. Acad. Sci. U. S. A.* **107**, 15595-600 (2010).
251. Ahmed, M. et al. Structural conversion of neurotoxic amyloid-beta(1-42) oligomers to fibrils. *Nat. Struct. Mol. Biol.* **17**, 561-7 (2010).
252. Nichols, M.R. et al. Growth of beta-amyloid(1-40) protofibrils by monomer elongation and lateral association. Characterization of distinct products by light scattering and atomic force microscopy. *Biochemistry* **41**, 6115-27 (2002).
253. Kaye, R. et al. Annular protofibrils are a structurally and functionally distinct type of amyloid oligomer. *J. Biol. Chem.* **284**, 4230-7 (2009).
254. Scheidt, H.A., Morgado, I. & Huster, D. Solid-state NMR reveals a close structural relationship between amyloid-beta protofibrils and oligomers. *J. Biol. Chem.* **287**, 22822-6 (2012).
255. Ono, K., Condron, M.M. & Teplow, D.B. Structure-neurotoxicity relationships of amyloid beta-protein oligomers. *Proc. Natl. Acad. Sci. U. S. A.* **106**, 14745-50 (2009).
256. Fawzi, N.L., Ying, J., Ghirlando, R., Torchia, D.A. & Clore, G.M. Atomic-resolution dynamics on the surface of amyloid-beta protofibrils probed by solution NMR. *Nature* **480**, 268-72 (2011).
257. Paravastu, A.K., Leapman, R.D., Yau, W.M. & Tycko, R. Molecular structural basis for polymorphism in Alzheimer's beta-amyloid fibrils. *Proc. Natl. Acad. Sci. U. S. A.* **105**, 18349-54 (2008).
258. Tycko, R. Physical and structural basis for polymorphism in amyloid fibrils. *Protein Sci.* **23**, 1528-39 (2014).
259. Sunde, M. & Blake, C.C. From the globular to the fibrous state: protein structure and structural conversion in amyloid formation. *Q. Rev. Biophys.* **31**, 1-39 (1998).
260. Petkova, A.T., Yau, W.M. & Tycko, R. Experimental constraints on quaternary structure in Alzheimer's beta-amyloid fibrils. *Biochemistry* **45**, 498-512 (2006).
261. Sgourakis, N.G., Yau, W.M. & Qiang, W. Modeling an in-register, parallel "iowa" abeta fibril structure using solid-state NMR data from labeled samples with rosetta. *Structure* **23**, 216-27 (2015).
262. Schutz, A.K. et al. Atomic-resolution three-dimensional structure of amyloid beta fibrils bearing the Osaka mutation. *Angew. Chem. Int. Ed. Engl.* **54**, 331-5 (2015).
263. Qiang, W., Yau, W.M., Luo, Y., Mattson, M.P. & Tycko, R. Antiparallel beta-sheet architecture in Iowa-mutant beta-amyloid fibrils. *Proc. Natl. Acad. Sci. U. S. A.* **109**, 4443-8 (2012).
264. Lopez del Amo, J.M. et al. An asymmetric dimer as the basic subunit in Alzheimer's disease amyloid beta fibrils. *Angew. Chem. Int. Ed. Engl.* **51**, 6136-9 (2012).
265. Bertini, I., Gonnelli, L., Luchinat, C., Mao, J. & Nesi, A. A new structural model of Abeta40 fibrils. *J. Am. Chem. Soc.* **133**, 16013-22 (2011).
266. Petkova, A.T. et al. A structural model for Alzheimer's beta -amyloid fibrils based on experimental constraints from solid state NMR. *Proc. Natl. Acad. Sci. U. S. A.* **99**, 16742-7 (2002).
267. Niu, Z. et al. The molecular structure of Alzheimer beta-amyloid fibrils formed in the presence of phospholipid vesicles. *Angew. Chem. Int. Ed. Engl.* **53**, 9294-7 (2014).

268. Tycko, R. & Wickner, R.B. Molecular structures of amyloid and prion fibrils: consensus versus controversy. *Acc. Chem. Res.* **46**, 1487-96 (2013).
269. Luhrs, T. et al. 3D structure of Alzheimer's amyloid-beta(1-42) fibrils. *Proc. Natl. Acad. Sci. U. S. A.* **102**, 17342-7 (2005).
270. Olofsson, A., Sauer-Eriksson, A.E. & Ohman, A. The solvent protection of alzheimer amyloid-beta-(1-42) fibrils as determined by solution NMR spectroscopy. *J. Biol. Chem.* **281**, 477-83 (2006).
271. Ma, B. & Nussinov, R. Polymorphic triple beta-sheet structures contribute to amide hydrogen/deuterium (H/D) exchange protection in the Alzheimer amyloid beta42 peptide. *J. Biol. Chem.* **286**, 34244-53 (2011).
272. Schmidt, M. et al. Comparison of Alzheimer Abeta(1-40) and Abeta(1-42) amyloid fibrils reveals similar protofilament structures. *Proc. Natl. Acad. Sci. U. S. A.* **106**, 19813-8 (2009).
273. Colvin, M.T. et al. High Resolution Structural Characterization of Abeta Amyloid Fibrils by Magic Angle Spinning NMR. *J. Am. Chem. Soc.* (2015).
274. Rowe, C.C. et al. Imaging of amyloid beta in Alzheimer's disease with 18F-BAY94-9172, a novel PET tracer: proof of mechanism. *Lancet. Neurol.* **7**, 129-35 (2008).
275. Prade, E., Lopez del Amo, J.M. & Reif, B. CHAPTER 27:NMR Studies of Small Molecules Interacting with Amyloidogenic Proteins. in *Advances in Biological Solid-State NMR : Proteins and Membrane-Active Peptides* (eds. Separovic, F. & Naito, A.) 533-555 (Royal Society of Chemistry, 2014).
276. Clarkson, J. & Campbell, I.D. Studies of protein-ligand interactions by NMR. *Biochem. Soc. Trans.* **31**, 1006-9 (2003).
277. Carlomagno, T. Ligand-target interactions: what can we learn from NMR? *Annu. Rev. Biophys. Biomol. Struct.* **34**, 245-66 (2005).
278. Pedersen, M.O. et al. NMR reveals two-step association of Congo Red to amyloid beta in low-molecular-weight aggregates. *J. Phys. Chem. B.* **114**, 16003-10 (2010).
279. Abelein, A., Lang, L., Lendel, C., Graslund, A. & Danielsson, J. Transient small molecule interactions kinetically modulate amyloid beta peptide self-assembly. *FEBS Lett.* **586**, 3991-5 (2012).
280. Abelein, A., Bolognesi, B., Dobson, C.M., Graslund, A. & Lendel, C. Hydrophobicity and conformational change as mechanistic determinants for nonspecific modulators of amyloid beta self-assembly. *Biochemistry* **51**, 126-37 (2012).
281. Bieschke, J. et al. Small-molecule conversion of toxic oligomers to nontoxic beta-sheet-rich amyloid fibrils. *Nat. Chem. Biol.* **8**, 93-101 (2012).
282. Chen, Z., Krause, G. & Reif, B. Structure and orientation of peptide inhibitors bound to beta-amyloid fibrils. *J. Mol. Biol.* **354**, 760-76 (2005).
283. Rezaei-Ghaleh, N., Andreetto, E., Yan, L.M., Kapurniotu, A. & Zweckstetter, M. Interaction between amyloid beta peptide and an aggregation blocker peptide mimicking islet amyloid polypeptide. *PLoS One* **6**, e20289 (2011).
284. Yoo, S.I. et al. Inhibition of amyloid peptide fibrillation by inorganic nanoparticles: functional similarities with proteins. *Angew. Chem. Int. Ed. Engl.* **50**, 5110-5 (2011).
285. Danielsson, J., Pierattelli, R., Banci, L. & Graslund, A. High-resolution NMR studies of the zinc-binding site of the Alzheimer's amyloid beta-peptide. *FEBS J.* **274**, 46-59 (2007).
286. Nair, N.G., Perry, G., Smith, M.A. & Reddy, V.P. NMR studies of zinc, copper, and iron binding to histidine, the principal metal ion complexing site of amyloid-beta peptide. *J. Alzheimers Dis.* **20**, 57-66 (2010).
287. Zirah, S. et al. Structural changes of region 1-16 of the Alzheimer disease amyloid beta-peptide upon zinc binding and in vitro aging. *J. Biol. Chem.* **281**, 2151-61 (2006).
288. Lopez del Amo, J.M. et al. Structural properties of EGCG-induced, nontoxic Alzheimer's disease Abeta oligomers. *J. Mol. Biol.* **421**, 517-24 (2012).
289. Ge, J.F., Qiao, J.P., Qi, C.C., Wang, C.W. & Zhou, J.N. The binding of resveratrol to monomer and fibril amyloid beta. *Neurochem. Int.* **61**, 1192-201 (2012).
290. Ono, K. et al. Phenolic compounds prevent amyloid beta-protein oligomerization and synaptic dysfunction by site-specific binding. *J. Biol. Chem.* **287**, 14631-43 (2012).
291. Ishima, R. CPMG relaxation dispersion. *Methods Mol. Biol.* **1084**, 29-49 (2014).
292. Maltsev, A.S., Grishaev, A. & Bax, A. Monomeric alpha-synuclein binds Congo Red micelles in a disordered manner. *Biochemistry* **51**, 631-42 (2012).

293. Salvatella, X. & Giralt, E. NMR-based methods and strategies for drug discovery. *Chem. Soc. Rev.* **32**, 365-72 (2003).
294. Robbins, K.J., Liu, G., Selmani, V. & Lazo, N.D. Conformational analysis of thioflavin T bound to the surface of amyloid fibrils. *Langmuir* **28**, 16490-5 (2012).
295. Franks, W.T., Linden, A.H., Kunert, B., van Rossum, B.J. & Oschkinat, H. Solid-state magic-angle spinning NMR of membrane proteins and protein-ligand interactions. *Eur. J. Cell Biol.* **91**, 340-8 (2012).
296. Schutz, A.K. et al. The amyloid-Congo red interface at atomic resolution. *Angew. Chem. Int. Ed. Engl.* **50**, 5956-60 (2011).
297. Masuda, Y. et al. Solid-state NMR analysis of interaction sites of curcumin and 42-residue amyloid beta-protein fibrils. *Bioorg. Med. Chem.* **19**, 5967-74 (2011).
298. Mithu, V.S. et al. Curcumin alters the salt bridge-containing turn region in amyloid beta(1-42) aggregates. *J. Biol. Chem.* **289**, 11122-31 (2014).
299. Mithu, V.S. et al. Zn(++) binding disrupts the Asp(23)-Lys(28) salt bridge without altering the hairpin-shaped cross-beta Structure of Abeta(42) amyloid aggregates. *Biophys. J.* **101**, 2825-32 (2011).
300. Parthasarathy, S. et al. Molecular-level examination of Cu²⁺ binding structure for amyloid fibrils of 40-residue Alzheimer's beta by solid-state NMR spectroscopy. *J. Am. Chem. Soc.* **133**, 3390-400 (2011).
301. Suzuki, N. et al. An increased percentage of long amyloid beta protein secreted by familial amyloid beta protein precursor (beta APP717) mutants. *Science* **264**, 1336-40 (1994).
302. Shoji, M. et al. Production of the Alzheimer amyloid beta protein by normal proteolytic processing. *Science* **258**, 126-9 (1992).
303. Andersson, E.R., Sandberg, R. & Lendahl, U. Notch signaling: simplicity in design, versatility in function. *Development* **138**, 3593-612 (2011).
304. Golde, T.E., Koo, E.H., Felsenstein, K.M., Osborne, B.A. & Miele, L. gamma-Secretase inhibitors and modulators. *Biochim. Biophys. Acta* **1828**, 2898-907 (2013).
305. Weggen, S. et al. A subset of NSAIDs lower amyloidogenic Abeta42 independently of cyclooxygenase activity. *Nature* **414**, 212-6 (2001).
306. Etienne, F., Resnick, L., Sagher, D., Brot, N. & Weissbach, H. Reduction of Sulindac to its active metabolite, sulindac sulfide: assay and role of the methionine sulfoxide reductase system. *Biochem. Biophys. Res. Commun.* **312**, 1005-10 (2003).
307. Brunell, D., Sagher, D., Kesaraju, S., Brot, N. & Weissbach, H. Studies on the metabolism and biological activity of the epimers of sulindac. *Drug Metab. Dispos.* **39**, 1014-21 (2011).
308. Duggan, D.E., Hooke, K.F., Risley, E.A., Shen, T.Y. & Arman, C.G. Identification of the biologically active form of sulindac. *J. Pharmacol. Exp. Ther.* **201**, 8-13 (1977).
309. Wick, M. et al. Peroxisome proliferator-activated receptor-gamma is a target of nonsteroidal anti-inflammatory drugs mediating cyclooxygenase-independent inhibition of lung cancer cell growth. *Mol. Pharmacol.* **62**, 1207-14 (2002).
310. Tinsley, H.N. et al. Sulindac sulfide selectively inhibits growth and induces apoptosis of human breast tumor cells by phosphodiesterase 5 inhibition, elevation of cyclic GMP, and activation of protein kinase G. *Mol. Cancer Ther.* **8**, 3331-40 (2009).
311. Williams, C.S., Goldman, A.P., Sheng, H., Morrow, J.D. & DuBois, R.N. Sulindac sulfide, but not sulindac sulfone, inhibits colorectal cancer growth. *Neoplasia* **1**, 170-6 (1999).
312. Li, X. et al. Sulindac inhibits tumor cell invasion by suppressing NF-kappaB-mediated transcription of microRNAs. *Oncogene* **31**, 4979-86 (2012).
313. Morihara, T., Chu, T., Ubeda, O., Beech, W. & Cole, G.M. Selective inhibition of Abeta42 production by NSAID R-enantiomers. *J. Neurochem.* **83**, 1009-12 (2002).
314. Eriksen, J.L. et al. NSAIDs and enantiomers of flurbiprofen target gamma-secretase and lower Abeta 42 in vivo. *J. Clin. Invest.* **112**, 440-9 (2003).
315. Kukar, T. et al. Diverse compounds mimic Alzheimer disease-causing mutations by augmenting Abeta42 production. *Nat. Med.* **11**, 545-50 (2005).
316. Crump, C.J., Johnson, D.S. & Li, Y.M. Development and mechanism of gamma-secretase modulators for Alzheimer's disease. *Biochemistry* **52**, 3197-216 (2013).
317. Takahashi, Y. et al. Sulindac sulfide is a noncompetitive gamma-secretase inhibitor that preferentially reduces Abeta 42 generation. *J. Biol. Chem.* **278**, 18664-70 (2003).

318. Beher, D. et al. Selected non-steroidal anti-inflammatory drugs and their derivatives target gamma-secretase at a novel site. Evidence for an allosteric mechanism. *J. Biol. Chem.* **279**, 43419-26 (2004).
319. Clarke, E.E. et al. Intra- or intercomplex binding to the gamma-secretase enzyme. A model to differentiate inhibitor classes. *J. Biol. Chem.* **281**, 31279-89 (2006).
320. Kukar, T.L. et al. Substrate-targeting gamma-secretase modulators. *Nature* **453**, 925-9 (2008).
321. Munter, L.M. et al. Aberrant amyloid precursor protein (APP) processing in hereditary forms of Alzheimer disease caused by APP familial Alzheimer disease mutations can be rescued by mutations in the APP GxxxG motif. *J. Biol. Chem.* **285**, 21636-43 (2010).
322. Richter, L. et al. Amyloid beta 42 peptide (Abeta42)-lowering compounds directly bind to Abeta and interfere with amyloid precursor protein (APP) transmembrane dimerization. *Proc. Natl. Acad. Sci. U. S. A.* **107**, 14597-602 (2010).
323. Scheuermann, S. et al. Homodimerization of amyloid precursor protein and its implication in the amyloidogenic pathway of Alzheimer's disease. *J. Biol. Chem.* **276**, 33923-9 (2001).
324. Munter, L.M. et al. GxxxG motifs within the amyloid precursor protein transmembrane sequence are critical for the etiology of Abeta42. *EMBO J.* **26**, 1702-12 (2007).
325. Botev, A. et al. The amyloid precursor protein C-terminal fragment C100 occurs in monomeric and dimeric stable conformations and binds gamma-secretase modulators. *Biochemistry* **50**, 828-35 (2011).
326. Green, R.C. et al. Effect of tarenflurbil on cognitive decline and activities of daily living in patients with mild Alzheimer disease: a randomized controlled trial. *JAMA* **302**, 2557-64 (2009).
327. Barrett, P.J. et al. The amyloid precursor protein has a flexible transmembrane domain and binds cholesterol. *Science* **336**, 1168-71 (2012).
328. Manrique-Moreno, M., Garidel, P., Suwalsky, M., Howe, J. & Brandenburg, K. The membrane-activity of Ibuprofen, Diclofenac, and Naproxen: a physico-chemical study with lecithin phospholipids. *Biochim. Biophys. Acta* **1788**, 1296-303 (2009).
329. Husch, J. et al. Structural properties of so-called NSAID-phospholipid-complexes. *Eur. J. Pharm. Sci.* **44**, 103-16 (2011).
330. Lichtenberger, L.M. et al. Insight into NSAID-induced membrane alterations, pathogenesis and therapeutics: characterization of interaction of NSAIDs with phosphatidylcholine. *Biochim. Biophys. Acta* **1821**, 994-1002 (2012).
331. Nadezhdin, K.D., Bocharova, O.V., Bocharov, E.V. & Arseniev, A.S. Dimeric structure of transmembrane domain of amyloid precursor protein in micellar environment. *FEBS Lett.* **586**, 1687-92 (2012).
332. Chen, W. et al. Familial Alzheimer's mutations within APPTM increase Abeta42 production by enhancing accessibility of epsilon-cleavage site. *Nat. Commun.* **5**, 3037 (2014).
333. Yesuvadian, R., Krishnamoorthy, J., Ramamoorthy, A. & Bhunia, A. Potent gamma-secretase inhibitors/modulators interact with amyloid-beta fibrils but do not inhibit fibrillation: a high-resolution NMR study. *Biochem. Biophys. Res. Commun.* **447**, 590-5 (2014).
334. Fu, Z. et al. Capping of abeta42 oligomers by small molecule inhibitors. *Biochemistry* **53**, 7893-903 (2014).
335. Barrett, P.J., Sanders, C.R., Kaufman, S.A., Michelsen, K. & Jordan, J.B. NSAID-based gamma-secretase modulators do not bind to the amyloid-beta polypeptide. *Biochemistry* **50**, 10328-42 (2011).
336. Hirohata, M., Ono, K., Naiki, H. & Yamada, M. Non-steroidal anti-inflammatory drugs have anti-amyloidogenic effects for Alzheimer's beta-amyloid fibrils in vitro. *Neuropharmacology* **49**, 1088-99 (2005).
337. Hirohata, M., Ono, K., Morinaga, A. & Yamada, M. Non-steroidal anti-inflammatory drugs have potent anti-fibrillogenic and fibril-destabilizing effects for alpha-synuclein fibrils in vitro. *Neuropharmacology* **54**, 620-7 (2008).
338. McGovern, S.L., Caselli, E., Grigorieff, N. & Shoichet, B.K. A common mechanism underlying promiscuous inhibitors from virtual and high-throughput screening. *J. Med. Chem.* **45**, 1712-22 (2002).

339. Hagerman, A.E. & Butler, L.G. The specificity of proanthocyanidin-protein interactions. *J. Biol. Chem.* **256**, 4494-7 (1981).
340. Haslam, E. Vegetable tannins - lessons of a phytochemical lifetime. *Phytochemistry* **68**, 2713-21 (2007).
341. McGovern, S.L., Helfand, B.T., Feng, B. & Shoichet, B.K. A specific mechanism of nonspecific inhibition. *J. Med. Chem.* **46**, 4265-72 (2003).
342. Skowronek, M. et al. Self-assembly of Congo Red—A theoretical and experimental approach to identify its supramolecular organization in water and salt solutions. *Biopolymers* **46**, 267-281 (1998).
343. Feng, B.Y. et al. Small-molecule aggregates inhibit amyloid polymerization. *Nat. Chem. Biol.* **4**, 197-9 (2008).
344. Beel, A.J. et al. Nonspecificity of binding of gamma-secretase modulators to the amyloid precursor protein. *Biochemistry* **48**, 11837-9 (2009).
345. Sonksen, P. & Sonksen, J. Insulin: understanding its action in health and disease. *Br. J. Anaesth.* **85**, 69-79 (2000).
346. Battaglia, M. Experiments by nature: lessons on type 1 diabetes. *Tissue Antigens* **83**, 1-9 (2014).
347. Palermo, A., Maggi, D., Maurizi, A.R., Pozzilli, P. & Buzzetti, R. Prevention of type 2 diabetes mellitus: is it feasible? *Diabetes Metab. Res. Rev.* **30 Suppl 1**, 4-12 (2014).
348. Mathers, C.D. & Loncar, D. Projections of global mortality and burden of disease from 2002 to 2030. *PLoS Med.* **3**, e442 (2006).
349. Wild, S., Roglic, G., Green, A., Sicree, R. & King, H. Global prevalence of diabetes: estimates for the year 2000 and projections for 2030. *Diabetes Care* **27**, 1047-53 (2004).
350. Hull, R.L., Westermark, G.T., Westermark, P. & Kahn, S.E. Islet amyloid: a critical entity in the pathogenesis of type 2 diabetes. *J. Clin. Endocrinol. Metab.* **89**, 3629-43 (2004).
351. Westermark, P. et al. Amyloid fibrils in human insulinoma and islets of Langerhans of the diabetic cat are derived from a neuropeptide-like protein also present in normal islet cells. *Proc. Natl. Acad. Sci. U. S. A.* **84**, 3881-5 (1987).
352. Westermark, P., Wernstedt, C., Wilander, E. & Sletten, K. A novel peptide in the calcitonin gene related peptide family as an amyloid fibril protein in the endocrine pancreas. *Biochem. Biophys. Res. Commun.* **140**, 827-31 (1986).
353. Cooper, G.J. et al. Purification and characterization of a peptide from amyloid-rich pancreases of type 2 diabetic patients. *Proc. Natl. Acad. Sci. U. S. A.* **84**, 8628-32 (1987).
354. Kahn, S.E. et al. Evidence of cosecretion of islet amyloid polypeptide and insulin by beta-cells. *Diabetes* **39**, 634-8 (1990).
355. Westermark, P., Andersson, A. & Westermark, G.T. Islet amyloid polypeptide, islet amyloid, and diabetes mellitus. *Physiol. Rev.* **91**, 795-826 (2011).
356. Montane, J., Klimek-Abercrombie, A., Potter, K.J., Westwell-Roper, C. & Bruce Verchere, C. Metabolic stress, IAPP and islet amyloid. *Diabetes Obes. Metab.* **14 Suppl 3**, 68-77 (2012).
357. Kaye, R. et al. Common structure of soluble amyloid oligomers implies common mechanism of pathogenesis. *Science* **300**, 486-9 (2003).
358. Porat, Y., Kolusheva, S., Jelinek, R. & Gazit, E. The human islet amyloid polypeptide forms transient membrane-active prefibrillar assemblies. *Biochemistry* **42**, 10971-7 (2003).
359. Janson, J. et al. Increased risk of type 2 diabetes in Alzheimer disease. *Diabetes* **53**, 474-81 (2004).
360. Nicolls, M.R. The clinical and biological relationship between Type II diabetes mellitus and Alzheimer's disease. *Curr. Alzheimer Res.* **1**, 47-54 (2004).
361. Li, L. & Holscher, C. Common pathological processes in Alzheimer disease and type 2 diabetes: a review. *Brain Res. Rev.* **56**, 384-402 (2007).
362. Akter, K. et al. Diabetes mellitus and Alzheimer's disease: shared pathology and treatment? *Br. J. Clin. Pharmacol.* **71**, 365-76 (2011).
363. Marszalek, M. [Diabetes type 2 and Alzheimer disease - one or two diseases? Mechanisms of association]. *Postepy Hig. Med. Dosw. (Online)* **67**, 653-71 (2013).

364. Funakoshi, S. et al. Analysis of factors influencing pancreatic beta-cell function in Japanese patients with type 2 diabetes: association with body mass index and duration of diabetic exposure. *Diabetes Res. Clin. Pract.* **82**, 353-8 (2008).
365. Brands, A.M., Kessels, R.P., de Haan, E.H., Kappelle, L.J. & Biessels, G.J. Cerebral dysfunction in type 1 diabetes: effects of insulin, vascular risk factors and blood-glucose levels. *Eur. J. Pharmacol.* **490**, 159-68 (2004).
366. de la Monte, S.M. & Wands, J.R. Molecular indices of oxidative stress and mitochondrial dysfunction occur early and often progress with severity of Alzheimer's disease. *J. Alzheimers Dis.* **9**, 167-81 (2006).
367. Haan, M.N. Therapy Insight: type 2 diabetes mellitus and the risk of late-onset Alzheimer's disease. *Nat. Clin. Pract. Neurol.* **2**, 159-66 (2006).
368. Peila, R., Rodriguez, B.L. & Launer, L.J. Type 2 diabetes, APOE gene, and the risk for dementia and related pathologies: The Honolulu-Asia Aging Study. *Diabetes* **51**, 1256-62 (2002).
369. Qiu, W.Q. & Folstein, M.F. Insulin, insulin-degrading enzyme and amyloid-beta peptide in Alzheimer's disease: review and hypothesis. *Neurobiol. Aging* **27**, 190-8 (2006).
370. Freude, S. et al. Peripheral hyperinsulinemia promotes tau phosphorylation in vivo. *Diabetes* **54**, 3343-8 (2005).
371. Yan, L.M., Velkova, A., Tatarek-Nossol, M., Andreetto, E. & Kapurniotu, A. IAPP mimic blocks Abeta cytotoxic self-assembly: cross-suppression of amyloid toxicity of Abeta and IAPP suggests a molecular link between Alzheimer's disease and type II diabetes. *Angew. Chem. Int. Ed. Engl.* **46**, 1246-52 (2007).
372. Yan, L.M., Tatarek-Nossol, M., Velkova, A., Kazantzis, A. & Kapurniotu, A. Design of a mimic of nonamyloidogenic and bioactive human islet amyloid polypeptide (IAPP) as nanomolar affinity inhibitor of IAPP cytotoxic fibrillogenesis. *Proc. Natl. Acad. Sci. U. S. A.* **103**, 2046-51 (2006). Copyright (2006) National Academy of Sciences, U.S.A.
373. Velkova, A., Tatarek-Nossol, M., Andreetto, E. & Kapurniotu, A. Exploiting cross-amyloid interactions to inhibit protein aggregation but not function: nanomolar affinity inhibition of insulin aggregation by an IAPP mimic. *Angew. Chem. Int. Ed. Engl.* **47**, 7114-8 (2008).
374. Meng, F., Raleigh, D.P. & Abedini, A. Combination of kinetically selected inhibitors in trans leads to highly effective inhibition of amyloid formation. *J. Am. Chem. Soc.* **132**, 14340-2 (2010).
375. Yan, L.M. et al. Selectively N-methylated soluble IAPP mimics as potent IAPP receptor agonists and nanomolar inhibitors of cytotoxic self-assembly of both IAPP and Abeta40. *Angew. Chem. Int. Ed. Engl.* **52**, 10378-83 (2013).
376. Andreetto, E. et al. Identification of hot regions of the Abeta-IAPP interaction interface as high-affinity binding sites in both cross- and self-association. *Angew. Chem. Int. Ed. Engl.* **49**, 3081-5 (2010).
377. Andreetto, E., Yan, L.M., Caporale, A. & Kapurniotu, A. Dissecting the role of single regions of an IAPP mimic and IAPP in inhibition of Abeta40 amyloid formation and cytotoxicity. *Chembiochem* **12**, 1313-22 (2011).
378. Andreetto, E. et al. A Hot-Segment-Based Approach for the Design of Cross-Amyloid Interaction Surface Mimics as Inhibitors of Amyloid Self-Assembly. *Angew. Chem. Int. Ed. Engl.* (2015).
379. Nishi, M. et al. Human islet amyloid polypeptide gene: complete nucleotide sequence, chromosomal localization, and evolutionary history. *Mol. Endocrinol.* **3**, 1775-81 (1989).
380. Schrodinger, LLC. The PyMOL Molecular Graphics System, Version 1.3r1. (2010).
381. Rieping, W. et al. ARIA2: automated NOE assignment and data integration in NMR structure calculation. *Bioinformatics* **23**, 381-2 (2007).
382. Walsh, D.M. et al. A facile method for expression and purification of the Alzheimer's disease-associated amyloid beta-peptide. *FEBS J.* **276**, 1266-81 (2009).
383. Dasari, M. et al. Bacterial inclusion bodies of Alzheimer's disease beta-amyloid peptides can be employed to study native-like aggregation intermediate states. *Chembiochem* **12**, 407-23 (2011).
384. Schagger, H. Tricine-SDS-PAGE. *Nat. Protoc.* **1**, 16-22 (2006).

385. Zagorski, M.G. et al. Methodological and chemical factors affecting amyloid beta peptide amyloidogenicity. *Methods Enzymol.* **309**, 189-204 (1999).
386. Fezoui, Y. et al. An improved method of preparing the amyloid beta-protein for fibrillogenesis and neurotoxicity experiments. *Amyloid* **7**, 166-78 (2000).
387. Helmus, J.J. & Jaroniec, C.P. NmrGlue: an open source Python package for the analysis of multidimensional NMR data. *J. Biomol. NMR* **55**, 355-67 (2013).
388. Goddard, T.D. & Kneller, D.G. SPARKY 3. University of California, San Francisco.
389. Vranken, W.F. et al. The CCPN data model for NMR spectroscopy: development of a software pipeline. *Proteins* **59**, 687-96 (2005).
390. Wishart, D.S. & Sykes, B.D. The ¹³C chemical-shift index: a simple method for the identification of protein secondary structure using ¹³C chemical-shift data. *J. Biomol. NMR* **4**, 171-80 (1994).
391. Wishart, D.S. et al. ¹H, ¹³C and ¹⁵N chemical shift referencing in biomolecular NMR. *J. Biomol. NMR* **6**, 135-40 (1995).
392. Liu, M. et al. Improved WATERGATE Pulse Sequences for Solvent Suppression in NMR Spectroscopy. *J. Magn. Reson.* **132**, 125-129 (1998).
393. Schanda, P. & Brutscher, B. Very fast two-dimensional NMR spectroscopy for real-time investigation of dynamic events in proteins on the time scale of seconds. *J. Am. Chem. Soc.* **127**, 8014-5 (2005).
394. Vuister, G.W. & Bax, A. Resolution enhancement and spectral editing of uniformly ¹³C-enriched proteins by homonuclear broadband ¹³C decoupling. *J. Magn. Reson.* **98**, 428-435 (1992).
395. Schanda, P., Van Melckebeke, H. & Brutscher, B. Speeding up three-dimensional protein NMR experiments to a few minutes. *J. Am. Chem. Soc.* **128**, 9042-3 (2006).
396. Lescop, E., Schanda, P. & Brutscher, B. A set of BEST triple-resonance experiments for time-optimized protein resonance assignment. *J. Magn. Reson.* **187**, 163-169 (2007).
397. Weisemann, R., Ruterjans, H. & Bermel, W. 3D triple-resonance NMR techniques for the sequential assignment of NH and ¹⁵N resonances in ¹⁵N- and ¹³C-labelled proteins. *J. Biomol. NMR* **3**, 113-20 (1993).
398. Wagner, R. & Berger, S. Gradient-Selected NOESY—A Fourfold Reduction of the Measurement Time for the NOESY Experiment. *J. Magn. Reson., Series A* **123**, 119-121 (1996).
399. Bertini, I. et al. On the use of ultracentrifugal devices for sedimented solute NMR. *J. Biomol. NMR* **54**, 123-7 (2012).
400. Morcombe, C.R. & Zilm, K.W. Chemical shift referencing in MAS solid state NMR. *J. Magn. Reson.* **162**, 479-86 (2003).
401. Rienstra, C.M. et al. De novo determination of peptide structure with solid-state magic-angle spinning NMR spectroscopy. *Proc. Natl. Acad. Sci. U. S. A.* **99**, 10260-5 (2002).
402. Metz, G., Wu, X.L. & Smith, S.O. Ramped-Amplitude Cross Polarization in Magic-Angle-Spinning NMR. *J. Magn. Reson.* **110**, 219-227 (1994).
403. Castellani, F., van Rossum, B.J., Diehl, A., Rehbein, K. & Oschkinat, H. Determination of solid-state NMR structures of proteins by means of three-dimensional ¹⁵N-¹³C-¹³C dipolar correlation spectroscopy and chemical shift analysis. *Biochemistry* **42**, 11476-83 (2003).
404. Prade, E. et al. Structural mechanism of the interaction of Alzheimer's disease Aβ fibrils with the NSAID sulindac sulfide. *J. Biol. Chem.*, **290**, 28737-28745 (2015).
405. Mainz, A. et al. The chaperone αB-crystallin uses different interfaces to capture an amorphous and an amyloid client. *Nat. Struct. Mol. Biol.* (2015).
406. Goede, A., Preissner, R. & Frömmel, C. Voronoi cell: New method for allocation of space among atoms: Elimination of avoidable errors in calculation of atomic volume and density. *J. Comput. Chem.* **18**, 1113-1123 (1997).
407. Rother, K., Hildebrand, P.W., Goede, A., Gruening, B. & Preissner, R. Voronoia: analyzing packing in protein structures. *Nucleic Acids Res.* **37**, D393-5 (2009).
408. Tsai, J. & Gerstein, M. Calculations of protein volumes: sensitivity analysis and parameter database. *Bioinformatics* **18**, 985-95 (2002).
409. Zhang, L. & Hermans, J. Hydrophilicity of cavities in proteins. *Proteins* **24**, 433-8 (1996).

410. Sherman, W., Day, T., Jacobson, M.P., Friesner, R.A. & Farid, R. Novel procedure for modeling ligand/receptor induced fit effects. *J. Med. Chem.* **49**, 534-53 (2006).
411. Sherman, W., Beard, H.S. & Farid, R. Use of an induced fit receptor structure in virtual screening. *Chem. Biol. Drug Des.* **67**, 83-4 (2006).
412. Wang, Z.Y., Shimonaga, M., Muraoka, Y., Kobayashi, M. & Nozawa, T. Methionine oxidation and its effect on the stability of a reconstituted subunit of the light-harvesting complex from *Rhodospirillum rubrum*. *Eur. J. Biochem.* **268**, 3375-82 (2001).
413. Zheng, Y.-J. & Ornstein, R.L. A Molecular Dynamics and Quantum Mechanics Analysis of the Effect of DMSO on Enzyme Structure and Dynamics: Subtilisin. *J. Am. Chem. Soc.* **118**, 4175-4180 (1996).
414. Shen, C.L. & Murphy, R.M. Solvent effects on self-assembly of beta-amyloid peptide. *Biophys. J.* **69**, 640-51 (1995).
415. Stine, W.B., Jr., Dahlgren, K.N., Krafft, G.A. & LaDu, M.J. In vitro characterization of conditions for amyloid-beta peptide oligomerization and fibrillogenesis. *J. Biol. Chem.* **278**, 11612-22 (2003).
416. Fandrich, M. Oligomeric intermediates in amyloid formation: structure determination and mechanisms of toxicity. *J. Mol. Biol.* **421**, 427-40 (2012).
417. Kim, S.J., Cegelski, L., Preobrazhenskaya, M. & Schaefer, J. Structures of *Staphylococcus aureus* cell-wall complexes with vancomycin, eremomycin, and chloroeremomycin derivatives by $^{13}\text{C}\{^{19}\text{F}\}$ and $^{15}\text{N}\{^{19}\text{F}\}$ rotational-echo double resonance. *Biochemistry* **45**, 5235-50 (2006).
418. Kanski, J., Varadarajan, S., Aksenova, M. & Butterfield, D.A. Role of glycine-33 and methionine-35 in Alzheimer's amyloid beta-peptide 1-42-associated oxidative stress and neurotoxicity. *Biochim. Biophys. Acta* **1586**, 190-8 (2002).
419. Brunelle, P. & Rauk, A. The radical model of Alzheimer's disease: specific recognition of Gly29 and Gly33 by Met35 in a beta-sheet model of A β : an ONIOM study. *J. Alzheimers Dis.* **4**, 283-9 (2002).
420. Rauk, A. & Armstrong, D.A. Influence of β -Sheet Structure on the Susceptibility of Proteins to Backbone Oxidative Damage: Preference for αC -Centered Radical Formation at Glycine Residues of Antiparallel β -Sheets. *J. Am. Chem. Soc.* **122**, 4185-4192 (2000).
421. Rauk, A., Armstrong, D.A. & Fairlie, D.P. Is Oxidative Damage by β -Amyloid and Prion Peptides Mediated by Hydrogen Atom Transfer from Glycine α -Carbon to Methionine Sulfur within β -Sheets? *J. Am. Chem. Soc.* **122**, 9761-9767 (2000).
422. Harmeier, A. et al. Role of amyloid-beta glycine 33 in oligomerization, toxicity, and neuronal plasticity. *J. Neurosci.* **29**, 7582-90 (2009).
423. Doody, R.S. Therapeutic standards in Alzheimer disease. *Alzheimer Dis. Assoc. Disord.* **13 Suppl 2**, S20-6 (1999).
424. Cole, G.M. et al. Prevention of Alzheimer's disease: Omega-3 fatty acid and phenolic anti-oxidant interventions. *Neurobiol. Aging* **26 Suppl 1**, 133-6 (2005).
425. Biancalana, M. & Koide, S. Molecular mechanism of Thioflavin-T binding to amyloid fibrils. *Biochim. Biophys. Acta* **1804**, 1405-12 (2010).
426. Gullion, T., Baker, D.B. & Conradi, M.S. New, compensated Carr-Purcell sequences. *J. Magn. Reson.* **89**, 479-484 (1990).

Curriculum Vitae

Elke Martha Prade

Festkörper-NMR-Spektroskopie, Dept. Chemie
 Technischen Universität München
 Lichtenbergstr. 4
 85747 Garching, Germany
 elke.prade@tum.de

Research:

- Since Nov 2010 Ph.D. student at Department of Chemistry, Solid-state NMR spectroscopy, TU München and Institute of Structural Biology, Helmholtz-Zentrum Munich, Germany, Supervisor: Prof. Dr. Bernd Reif
 Topic: *Structural Characterization of Interactions between the Alzheimer's Disease Amyloid- β Peptide and Small Molecules and Peptide Inhibitors*
- Jan-Oct 2010 Scientist, Gastroenterology, Klinikum rechts der Isar of the TU München, Germany
- April-Oct 2010 Master student at Gastroenterology, Klinikum rechts der Isar of the TU München, Germany, Supervisor: Prof. Dr. med. Matthias Ebert
 Master Thesis: *Signaling mechanisms of bile acids in esophageal cancer*
 Klinikum rechts der Isar of the TU München, Germany

Education:

- Oct 2007- July 2009 Master of Science in biochemistry, Technical University Munich. Germany
- Aug 2004- July 2007 Bachelor of Science in biochemistry, University of Zurich, Switzerland

Schools:

- 2003-2004 Inter-Community School Zurich, Switzerland
- July 2004 International Baccalaureate Diploma
- 1998-2003 TEDA International School Tianjin, China
- 1997-1998 German School Beijing, China
- 1996-1997 Ehrenbürg Gymnasium Forchheim, Germany
- 1992-1996 Volksschule Eggolsheim, Germany

List of Publications

Parts of this thesis have been published in the following scientific articles:

Prade, E., Bittner, H.J., Sarkar, R., Lopez Del Amo, J.M., Althoff-Ospelt, G., Multhaup, G., Hildebrand, P.W. & Reif, B. Structural mechanism of the interaction of Alzheimer's disease Abeta fibrils with the NSAID sulindac sulfide. *J. Biol. Chem.*, (2015).

Mainz, A., Peschek, J., Stavropoulou, M., Back, K.C., Bardiaux, B., Asami, S., Prade, E., Peters, C., Weinkauff, S., Buchner, J. & Reif, B. The chaperone alphaB-crystallin uses different interfaces to capture an amorphous and an amyloid client. *Nat. Struct. Mol. Biol.* (2015).

Andreetto, E., Malideli, E., Yan, L.M., Kracklauer, M., Farbiarz, K., Tatarek-Nossol, M., Rammes, G., Prade, E., Neumuller, T., Caporale, A., Spanopoulou, A., Bakou, M., Reif, B. & Kapurniotu, A. A Hot-Segment-Based Approach for the Design of Cross-Amyloid Interaction Surface Mimics as Inhibitors of Amyloid Self-Assembly. *Angew. Chem. Int. Ed. Engl.* (2015).

Prade, E., Lopez del Amo, J.M. & Reif, B. CHAPTER 27:NMR Studies of Small Molecules Interacting with Amyloidogenic Proteins. in *Advances in Biological Solid-State NMR : Proteins and Membrane-Active Peptides* (eds. Separovic, F. & Naito, A.) 533-555 (Royal Society of Chemistry, 2014).

The following manuscript is in preparation:

Prade, E., Barucker, C., Sarkar, R., Althoff-Ospelt, G., Lopez del Amo, J.M., Multhaup, G. & Reif, B. Sulindac sulfide drives the Alzheimer's peptide amyloid- β into large oligomeric aggregates, *in preparation*.

Acknowledgements

First of all I would like to thank my Doktorvater Prof. Dr. Bernd Reif for giving me the opportunity to work in his group on many exciting projects. Thank you for your great scientific input, helpful discussions and always taking the time to answer questions or solve problems. You always had an open ear and patience for concerns of any kind, and this was a great support.

I would also like to thank Prof. Dr. Aphrodite Kapurniotu and Prof. Dr. Michael Sattler for agreeing to be on my examination committee, and also for being part of my thesis committee throughout the years of my PhD, guiding me with scientific ideas and input.

Over the years I had to opportunity to collaborate with a lot of great scientists, to whom I would like express my thanks. Prof. Dr. Peter Hildebrand and Heiko Bittner from the Charité in Berlin made essential contributions to my main project with molecular modeling studies. Prof. Dr. Gerd Multhaup from McGill in Montreal initiated my project and Dr. Christian Barucker from his group contributed biochemical assays to make my NMR studies more meaningful. Prof. Dr. Aphrodite Kapurniotu from the TU München in Weihenstephan involved me in her peptide inhibitor studies, and Erika Andreetto and Eleni Malideli from her group provided samples and ideas. Dr. Gerhard Althoff-Ospelt from Bruker BioSpin supported me by recording NMR experiments, which were not possible in Garching. All of my collaborators were a constant support and encouragement! Thank you for making my project a success!

On a more personal level, I would like to thank Riddhiman for assisting me with NMR problems throughout the years. Thank you for your patience, your helpful explanations, and your special tricks to get the spectrometers working. I would also like to acknowledge Juan Miguel, Andi and Tomas for helping me through my first obstacles with A β and NMR. Thank you also to Diana and Manuel, for not only being helpful colleagues, but also friends. Danke auch an dich Matthias, dass du mir immer mit Kaffee und aufmunternden Worten zur Seite gestanden hast, und mich durch

XLVI | ACKNOWLEDGEMENTS

deinen besonderen Charme jeden Tag zum Lachen gebracht hast. My special thanks also goes to Alex and Hamed, who are some of the first friends I found in my time in Garching. We spent a lot of time together, and there a many memories. Hamed, thank you for your constant support and always being there for me, especially throughout this last year, even though there was a long distance between us!

Mein besonderer Dank geht an meine Familie, die mich alle meine Entscheidungen frei haben treffen lassen, und trotzdem immer mit Verständnis und Unterstützung hinter mir gestanden waren. Ohne euch wäre gar nichts möglich gewesen!